

Imperial College London  
Department of Physics

# **Physics and Computational Simulations of Plasma Burn-through for Tokamak Start-up**

Hyun-Tae Kim

Submitted in part fulfilment of the requirements for the degree of  
Doctor of Philosophy in Physics of Imperial College London, July 2013



## Abstract

This thesis will discuss the fundamental process of high temperature plasma formation, consisting of the Townsend avalanche phase and the subsequent plasma burn-through phase. By means of the applied electric field, the gas is partially ionized by the avalanche process. In order for the electron temperature to increase, the remaining neutrals need to be fully ionized in the plasma burn-through phase, as radiation is the main contribution to the electron power loss. The radiated power loss can be significantly affected by impurities resulting from interaction with the plasma facing components. The parallel transport to the surrounding walls is determined by the so called connection length in the plasma.

Previously, plasma burn-through was simulated with the assumptions of constant particle confinement time and impurity fraction. In the new plasma burn-through simulator, called the DYON code, the treatment of particle confinement time is improved with a transonic ambipolar model for parallel transport, by using the effective connection length determined by the magnetic field lines, and Bohm diffusion model for perpendicular transport. In addition, the dynamic evolution of impurity content is calculated in a self-consistent way, using plasma wall interaction models. The recycling of the particles at the walls is also modelled.

For a specific application, the recent installation of a beryllium wall at Joint European Torus (JET) enabled to investigate the effects of plasma facing components on plasma formation and build-up of plasma current in the device. According to the JET experiments the Townsend avalanche phase was not influenced by the replacement of the wall material. However, failures during the plasma burn-through phase, that could occur with a carbon wall, are not observed with a beryllium wall. In order to obtain a deeper insight in these effects this thesis will present detailed modelling of plasma burn-through.

For the first time a quantitative validation of the simulation results to experimental data is documented. The simulation results with the DYON code show consistent good agreement against JET data obtained with the carbon wall as well as the beryllium wall. According to the DYON results, the radiation barrier in a carbon wall is dominated by the carbon radiation. The radiation barrier in the beryllium wall is mainly from the deuterium radiation rather than the beryllium radiation, as far as the radiated power from other impurities (i.e. carbon, nitrogen, etc) is not significant. These issues are of crucial importance for the International

Thermonuclear Experimental Reactor (ITER) where the allowable toroidal electric field for plasma formation is limited to 0.35 V/m, which is significantly lower compared to the typical loop voltage ( 1 V/m) used in the current devices. Using the validated DYON code, predictive simulations for ITER are given, showing a need for RF heating to allow reliable plasma burn-through.

## Supervisors and Examiners

This thesis has been completed under supervision of

- Dr A.C.C. Sips, EFDA-CSU, Culham Science Centre, OX14 3DB, Abingdon, UK
- Dr Wojtek Fundamenski, Department of Physics, Imperial College London, SW7 2AZ, London, UK
- Prof Steven Rose, Department of Physics, Imperial College London, SW7 2AZ, London, UK

Thesis examination committee:

- Dr Brian Lloyd, EURATOM/CCFE, Culham Science Centre, OX14 3DB, Abingdon, UK
- Dr Robert Kingham, Department of Physics, Imperial College London, SW7 2AZ, London, UK



## Acknowledgements

First of all, I would like to thank my supervisor, Dr. A.C.C. Sips. He made enormous contribution to this thesis. His insightful comments, warm encouragement, and active support were invaluable. I would also like to thank my previous supervisor, Dr. Wojtek Fundamenski, who gave me a PhD opportunity and great supervision for the first two years. Also, I appreciate Prof. Steve Rose for allowing me to have generous support from Imperial College. I am grateful to Dr. Peter de Vries for being a great academic adviser in Culham. Discussions with him have been very illuminating.

I would like to express my gratitude to Kwan-Jeong education foundation for their financial support. Also, I would like to thank Prof. Sang-Hee Hong and Prof. Yong-Seok Hwang who first taught me Plasma Physics, and Prof. Oh-Jin Kwon who helped me to find a PhD opportunity in the UK.

I owe a very important debt to my parents-in-law, who have been looking after DYON. Without their devotion, I might not have been able to continue my PhD study. I also wish to thank my parents, grandmothers, and younger brother, who always pray for me.

Finally, I want to express the deepest appreciation to my wife, Jay-Young. Special thanks to her for the great time we have had together. This thesis would not have been possible without her heartfelt encouragement and persistent help.





## Dedication

I confirm that the work presented in this thesis is entirely my own, except where indicated by references in the main text.

Hyun-Tae Kim

July 2013



## Copyright Declaration

The copyright of this thesis rests with the author and is made available under a Creative Commons Attribution Non-Commercial No Derivatives licence. Researchers are free to copy, distribute or transmit the thesis on the condition that they attribute it, that they do not use it for commercial purposes and that they do not alter, transform or build upon it. For any reuse or redistribution, researchers must make clear to others the licence terms of this work.



## List of Publications

The journal papers related to the thesis work are listed below.

1. Hyun-Tae Kim, Wojtek Fundamenski, A.C.C. Sips, and EFDA-JET contributors, Enhancement of plasma burn-through simulations and validation in JET, Nuclear Fusion 52 103016 (2012)
  - Included in chapters 3, 5, and 6 in this thesis.
  
2. Hyun-Tae Kim, A.C.C. Sips, Wojtek Fundamenski, and EFDA-JET contributors, PSI Effects on plasma burn-through in JET, Journal of Nuclear Materials, 438, S1271-S1274 (2013)
  - Included in chapter 5 in this thesis.
  
3. Hyun-Tae Kim, A.C.C. Sips, and EFDA-JET contributors, Physics of plasma burn-through and DYON simulations for the ITER-like wall, Nuclear Fusion, 53 083024 (2013)
  - Included in chapters 4, 5, and 6 in this thesis.
  
4. Hyun-Tae Kim, A.C.C. Sips, P.C. de Vries, and EFDA-JET contributors, Plasma burn-through simulations using the DYON code and predictions for ITER, Plasma Physics and Controlled Fusion, Accepted (2013)
  - Included in chapters 7 and 8 in this thesis.



## List of Main Conferences

The conferences where the thesis work were presented are listed below.

1. (Invited talk) European Physical Society Conference on Plasma Physics, Simulation of plasma formation in magnetized plasmas and the influence of plasma facing components, Espoo, Finland, July 2013
2. IOP Conference on Computational Plasma Physics, Enhancement of plasma burn-through simulation and validation in JET, Brighton, UK, September 2012
3. International Conference on Plasma Surface Interaction, PSI Effects on Plasma Burn-through in JET, Aachen, Germany, May 2012

‘We have generated energy from resources, but now we will generate energy from the knowledge.’

*Steven Cowley, Director of CCFE*



# Contents

<b>Abstract</b>	<b>i</b>
<b>supervisors</b>	<b>iii</b>
<b>Acknowledgements</b>	<b>v</b>
<b>Dedication</b>	<b>v</b>
<b>Copyright Declaration</b>	<b>vii</b>
<b>List of Publications</b>	<b>xi</b>
<b>List of main conferences</b>	<b>xi</b>
<b>1 Introduction</b>	<b>1</b>
1.1 Nuclear Fusion . . . . .	1
1.1.1 Thermonuclear Fusion . . . . .	1
1.1.2 Tokamak . . . . .	2
1.2 ITER and JET . . . . .	8
1.2.1 ITER . . . . .	8
1.2.2 JET and ITER-like wall . . . . .	10

1.3	Brief explanation of tokamak start-up . . . . .	13
1.4	Motivation of plasma burn-through modeling . . . . .	18
1.5	Scope of thesis . . . . .	19
<b>2</b>	<b>Review of electron avalanche</b>	<b>21</b>
2.1	Introduction . . . . .	21
2.2	Townsend avalanche theory . . . . .	22
2.2.1	The first townsend coefficient . . . . .	22
2.2.2	The second townsend coefficient . . . . .	26
2.3	Electron avalanche in tokamaks . . . . .	30
2.4	Discussion . . . . .	33
<b>3</b>	<b>Plasma burn-through simulation</b>	<b>36</b>
3.1	Introduction . . . . .	36
3.2	Basic structure of plasma burn-through simulator . . . . .	37
3.2.1	Circuit equation for plasma current . . . . .	37
3.2.2	Electron energy balance . . . . .	42
3.2.3	Ion energy balance . . . . .	45
3.2.4	Particle balance . . . . .	46
3.3	Review of the previous models . . . . .	48
3.3.1	Confinement time model . . . . .	48
3.3.2	Impurity model . . . . .	49
3.4	New models for plasma burn-through simulation . . . . .	49
3.4.1	Circuit equation for eddy current . . . . .	50

---

3.4.2	Dynamic effective connection length . . . . .	51
3.4.3	Deuterium ion confinement time . . . . .	52
3.4.4	Impurity ion transport model . . . . .	53
3.4.5	Transonic ambipolar transport of impurity ions . . . . .	55
3.4.6	Neutral screening effect deuterium and impurities . . . . .	57
3.4.7	Impurity particle balance model . . . . .	58
3.5	Description of the DYON code . . . . .	60
3.6	Discussion . . . . .	63
<b>4</b>	<b>Physics of deuterium burn-through</b>	<b>65</b>
4.1	Introduction . . . . .	65
4.2	Condition for plasma current ramp-up . . . . .	66
4.3	Criterion for deuterium burn-through . . . . .	70
4.4	Summary and discussion . . . . .	76
<b>5</b>	<b>New models for the carbon wall and the ITER-like wall in JET</b>	<b>77</b>
5.1	Introduction . . . . .	77
5.2	Impurity effects on plasma burn-through at JET with carbon wall and ITER-like wall. . . . .	78
5.2.1	Fractional abundance of impurity in non-coronal equilibrium . . . . .	78
5.2.2	Radiation barrier versus impurity influx in JET . . . . .	80
5.3	Deuterium recycling coefficient and gas fuelling . . . . .	82
5.4	Sputtering models . . . . .	83
5.4.1	Sputtering models in the carbon wall . . . . .	84

5.4.2	Sputtering models for the ITER-like wall . . . . .	86
5.5	Simulation results of the DYON code . . . . .	88
5.6	Summary and discussion . . . . .	92
<b>6</b>	<b>Comparison of experiments and simulations</b>	<b>93</b>
6.1	Introduction . . . . .	93
6.2	Diagnostic tools used for validation . . . . .	94
6.3	DYON simulations for JET with the carbon wall . . . . .	95
6.3.1	Initial conditions for burn-through simulation . . . . .	95
6.3.2	Validation of DYON simulations with the carbon wall . . . . .	97
6.3.3	Effects of the new model of parallel transport . . . . .	101
6.4	DYON simulations for JET with the ITER-like wall . . . . .	106
6.4.1	Validation of the new models . . . . .	106
6.4.2	Beryllium sputtering in ITER-like wall . . . . .	109
6.4.3	Deuterium recycling coefficient . . . . .	112
6.4.4	Gas fuelling . . . . .	113
6.4.5	Initial carbon content . . . . .	114
6.4.6	Effective vessel volume . . . . .	117
6.5	Operation space for plasma burn-through in JET . . . . .	117
6.6	Discussion and Conclusion . . . . .	122
6.6.1	Discussion . . . . .	122
6.6.2	Summary and Conclusion . . . . .	126

<b>7</b>	<b>DYON simulations for ITER</b>	<b>128</b>
7.1	Introduction . . . . .	128
7.2	Circuit system for DYON simulations . . . . .	131
7.3	Ohmic (unassisted) plasma burn-through . . . . .	133
7.4	RF-assisted plasma burn-through . . . . .	137
7.5	Summary and Discussion . . . . .	143
<b>8</b>	<b>Summary and Main Conclusions</b>	<b>144</b>
8.1	Original scope of thesis . . . . .	144
8.2	Summary and Conclusions . . . . .	144
8.3	Future Work . . . . .	150
	<b>List of Tables</b>	<b>153</b>
	<b>List of Figures</b>	<b>155</b>
	<b>Bibliography</b>	<b>164</b>
	<b>Curriculum Vitae</b>	<b>171</b>



# Chapter 1

## Introduction

### 1.1 Nuclear Fusion

#### 1.1.1 Thermonuclear Fusion

Fusion research aims to harness nuclear fusion energy on earth, and has drawn great interest from many physicists all over the world since the early 20th century when the mechanism of energy production in the sun was identified as nuclear fusion reactions. Various merits of nuclear fusion energy, e.g. almost limitless fuel, no long-lived radioactive waste, no carbon emission, and no possibility of use in nuclear weapons, make a nuclear fusion power plant one of the most promising candidates for an alternative energy source. [1]

If a nucleus of deuterium ( $D$ ) has a fusion reaction with a nucleus of tritium ( $T$ ), an  $\alpha$ -particle ( $He^{2+}$ ) and a neutron are released with a total kinetic energy of  $17.6MeV$ ,



The cross section of a fusion reaction is small enough to be ignored when fuel nuclei have low kinetic energy<sup>1</sup>, due to the repulsive Coulomb force resulting from the positive electric charges of the nuclei. In order to generate a fusion reaction, it is necessary for the fuel nuclei to overcome the repulsive force so that they approach each other up to the region where the

---

<sup>1</sup>The required kinetic energy of fuel nuclei for a fusion reactor is around 15keV. [1]

nuclear force is dominant. By heating the fuel nuclei to a sufficiently high temperature, two nuclei of high thermal kinetic energy can have access to such a close region, and then fusion reactions occur at a certain reaction rate. This is called *thermonuclear fusion*.

For a commercial power plant, the generated power by fusion reactions should be high enough to supply the required heating power for sustaining the fusion reactions i.e. *ignition condition*. In order to satisfy the ignition condition, in addition to the requirement of high temperature, the density of fuel nuclei must be high enough to achieve a sufficient fusion reaction rate, and the energy generated by fusion reactions should be maintained sufficiently long in the reactor. Assuming parabolic profile, the quantitative requirement for the ignition condition is [1]

$$\hat{n}\hat{\tau}_E\hat{T} > 5 \times 10^{21} [m^{-3}keVs]. \quad (1.2)$$

where  $\hat{n}$ ,  $\hat{\tau}_E$ , and  $\hat{T}$  are the peak values of particle density, energy confinement time, and the temperature, respectively.<sup>2</sup>

In the sun, the tremendous gravitational force enables such a high density and a long energy confinement time. As an alternative way to confine the fuel nuclei, the concept of *magnetic confinement fusion* has been developed. For the range of temperature and density satisfying the condition for thermonuclear fusion<sup>3</sup>, the fuel gas is fully ionized, consisting of positive ions and electrons. The ionized gas at such a high temperature and density is called a *fusion plasma*. One of the key features of plasmas is that the perpendicular motion of charged particles to magnetic fields is impeded effectively. Hence, we can confine them by using magnetic fields. There are various concepts of magnetic confinement fusion devices. One of the most promising concepts is a toroidal configuration called the *tokamak*; many world leading fusion devices are tokamaks.

### 1.1.2 Tokamak

Figure 1.1 shows the basic structure of a tokamak. The current flowing through toroidal field coils produces a toroidal magnetic field  $B_\phi$  according to Ampere's law (ignoring displacement current),

$$\nabla \times \vec{B} = \mu_0 \vec{J} \quad (1.3)$$

---

<sup>2</sup> $3 \times 10^{21} [m^{-3}keVs]$  for flat profile

<sup>3</sup> $T = 10 \sim 20 [keV]$  and  $n \approx 10^{20} [m^{-3}]$



By surface integration on  $\vec{S}$  of which the normal vector is in  $z$  direction in Figure 1.1, we have

$$\int (\nabla \times \vec{B}) \cdot d\vec{S} = \int \mu_0 \vec{J} \cdot d\vec{S} \quad (1.4)$$

(Stokes theorem)

$$\oint \vec{B} \cdot d\vec{l} = \int \mu_0 \vec{J} \cdot d\vec{S} \quad (1.5)$$

$$2\pi R B_\phi(R) = \mu_0 I_{TF} ,$$

where  $I_{TF}$  is the total current flowing through the toroidal field coils, which is located out of the vessel i.e.  $I_{TF}$  is the same for all radial position  $R$ . Thus, we can have toroidal magnetic field  $B_\phi$  as a function of radial position  $R$  and the toroidal magnetic field at the magnetic axis  $B_\phi(R_0)$  only,

$$2\pi R B_\phi(R) = 2\pi R_0 B_\phi(R_0) \quad (1.6)$$

$$B_\phi(R) = \frac{R_0}{R} B_\phi(R_0) ,$$

where  $R_0$  is the major radius at the magnetic axis. As shown in Equation (1.6), the magnitude of toroidal magnetic field  $B_\phi(R)$  is inversely proportional to the radial position  $R$ .

A current swing in the inner poloidal field coils (primary transformer circuit) generates magnetic flux swing in the iron transformer core, thereby inducing toroidal electric field in the vacuum vessel according to Faraday's law, <sup>4</sup>

$$\nabla \times \vec{E} = -\frac{\partial \vec{B}}{\partial t} . \quad (1.7)$$

By surface integration on  $\vec{S}$  of which the normal vector is in  $z$  direction in Figure 1.1, we have

$$\int (\nabla \times \vec{E}) \cdot d\vec{S} = \int -\frac{\partial \vec{B}}{\partial t} \cdot d\vec{S} . \quad (1.8)$$

Using Stokes theorem for the term in the left-hand side and assuming that the stray magnetic field is not significant for the term in the right-hand side, we can have

$$\oint \vec{E} \cdot d\vec{l} = U_l = -\frac{\partial \phi_{PF}}{\partial t} \quad (1.9)$$

where  $U_l$  is the toroidal loop voltage and  $\phi_{PF}$  is the total magnetic flux within the inner poloidal field coils.  $\phi_{PF}$  can be calculated as a function of the current in the inner poloidal field coils  $I_{PF}$ . It is well known in electromagnetics that the magnetic flux in a solenoid  $\phi_{sol}$  is

$$\phi_{sol} = A_{sol} \mu_0 n_{turn} I_{sol} \quad (1.10)$$

---

<sup>4</sup>Current swing in outer poloidal field coils is also used in some devices e.g. JET.

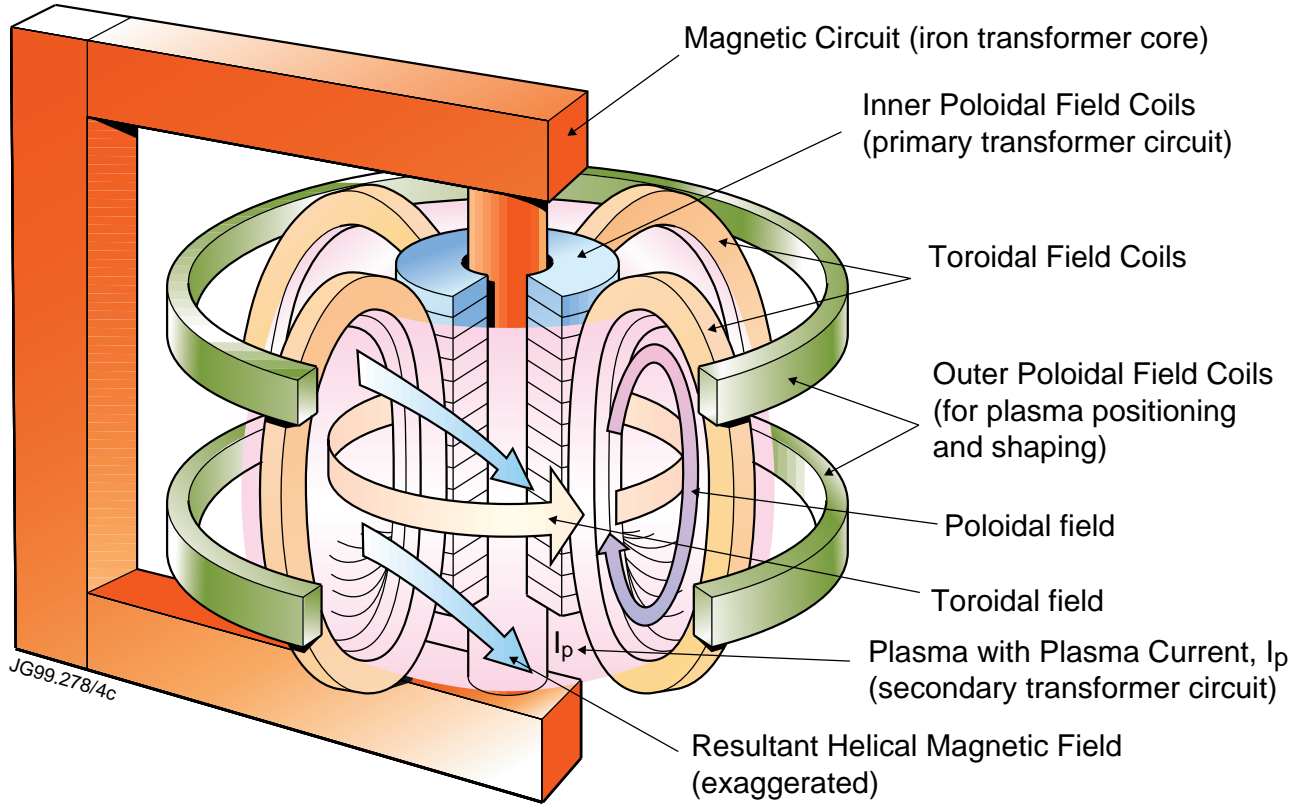


Figure 1.1: *Basic structure of a tokamak with an iron core*

where  $A_{sol}$  is the area of the cross section of the solenoid and  $n_{turns}$  is the number of turns per unit length. Thus,  $\phi_{PF}$  is calculated by

$$\phi_{PF} = A_{PF}\mu_0 n_{turn} I_{PF} \quad (1.11)$$

Substituting  $\phi_{PF}$  in Equation (1.9) with  $\phi_{PF}$  in Equation (1.11), we can have  $U_l$  as a function of  $I_{PF}$ ,

$$U_l = -A_{PF}\mu_0 n_{turn} \frac{\partial I_{PF}}{\partial t} . \quad (1.12)$$

The induced toroidal loop voltage generates plasma break-down (electron avalanche), plasma burn-through (full ionization), the build-up of plasma current  $I_p$ , and the sustainment of  $I_p$  in tokamaks.

The principal magnetic field in tokamaks is the toroidal magnetic field, but if there was only the toroidal magnetic field, then the loss of plasma out of the reactor would be significantly

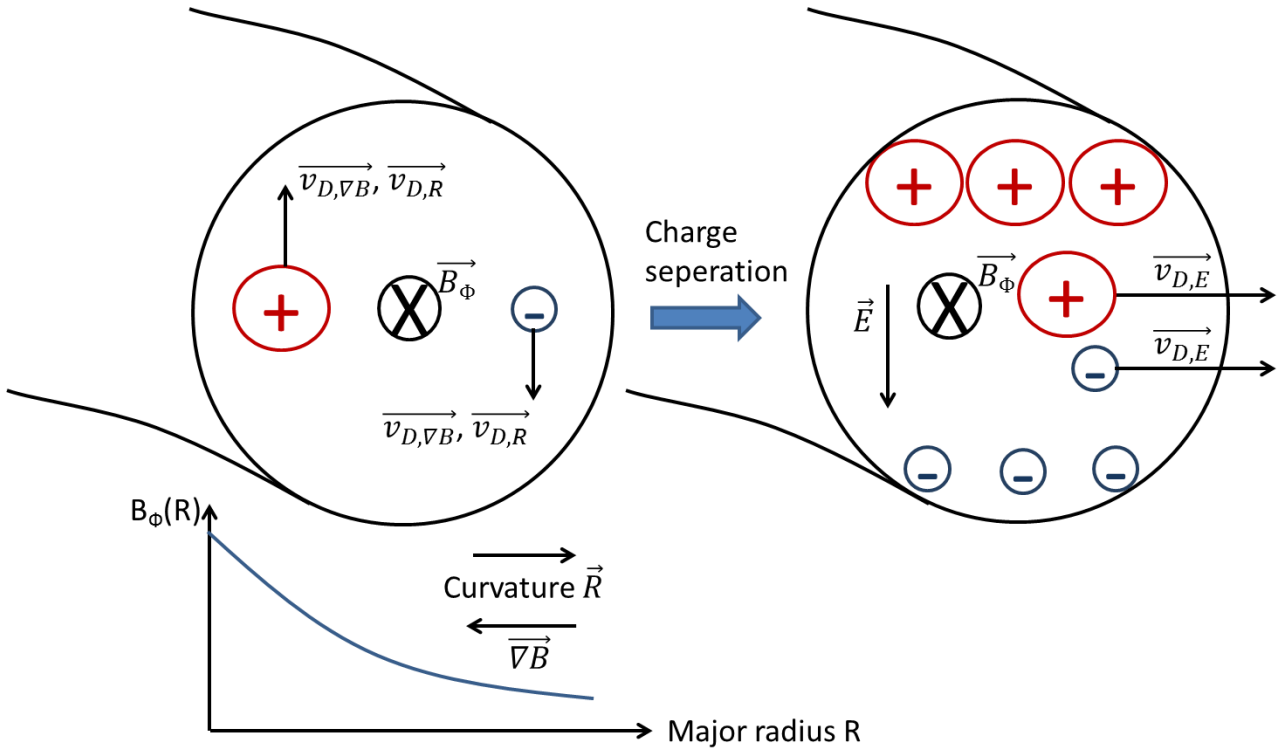


Figure 1.2: Description of the drift motions in tokamaks

large due to the drift motions of particles. As shown in Figure 1.2, the intrinsic gradient and curvature of the magnetic field in tokamaks result in the  $\nabla B$  drift and the curvature drift, and their velocities are calculated as [2][3]

$$\begin{aligned} \text{velocity of } \nabla B \text{ drift } \vec{v}_{D,\nabla B} &= \pm \frac{mv_{\perp}^2}{2eB^3} \vec{B} \times \nabla B \\ \text{velocity of curvature drift } \vec{v}_{D,R} &= \pm \frac{mv_{\parallel}^2}{eB^2 R^2} \vec{R} \times \vec{B}. \end{aligned} \quad (1.13)$$

The resultant drift motion in Equation (1.13) depends on the charge and the direction of magnetic field. With the direction of toroidal magnetic field given in the Figure 1.2, the ions and the electrons drift upward and downward, respectively. The charge separations generate an electric field which is perpendicular to the toroidal magnetic field as shown in Figure 1.2. The perpendicular electric field results in  $E \times B$  drift, thereby making the charged particles drift radially outward with the velocity, regardless of their charge, [2][3]

$$\vec{v}_{D,E} = \frac{\vec{E} \times \vec{B}}{B^2}. \quad (1.14)$$

The  $E \times B$  drift causes significant particle losses in toroidal systems. These are eliminated in a helical configuration of magnetic fields, with so-called toroidally nested magnetic flux surfaces,

so that the charge separations are prevented. In the Tokamak, the helical magnetic fields are formed by the combination of the toroidal magnetic field  $B_\phi$  and the poloidal magnetic field  $B_\theta$ , which are generated by the current in the toroidal field coils and the plasma current  $I_p$ , respectively. The relative magnitude of the two magnetic field components,  $B_\phi$  and  $B_\theta$ , determines the specific helical configuration of the magnetic fields. The configuration of the composite magnetic field lines is described by *safety factor*  $q$ . The safety factor  $q$  indicates how many toroidal trips around the torus are required for a magnetic field line to return to the initial location on the poloidal cross section. The safety factor for a large aspect-ratio (i.e.  $R_0/r \gg 1$ ) tokamak of circular cross-section is calculated with  $r$  the distance from the magnetic axis ( $R_0$ ), as [1]

$$q(r) = \frac{r}{R_0} \frac{B_\phi}{B_\theta}. \quad (1.15)$$

Figure 1.3 shows the stabilization of horizontal displacement of a plasma in tokamaks. The poloidal magnetic field  $B_\theta$  results from plasma currents  $I_p$  flowing along the torus. This makes the inboard poloidal magnetic field  $B_\theta(r_1)$  stronger than the outboard  $B_\theta(r_2)$ . As a result, the net hoop force  $F_{hoop}$  is directed radially outward, i.e.  $\vec{F}_{hoop} \sim \vec{J}_p \times B_\theta(r_1) - \vec{J}_p \times B_\theta(r_2)$ . In addition, the torus shape of a plasma results in a tyre tube force, which makes a plasma ring expand outward. To stabilize the horizontal displacement of a plasma, additional field coils, called outer poloidal field coils (vertical field coil) are installed in tokamaks. The currents flowing in the outer poloidal field coils generate vertical fields  $B_v$ , which compensate the imbalance of the poloidal fields between inboard and outboard. i.e. strengthening the outboard poloidal field and weakening the inboard poloidal field.

Vertical displacement is another important issue since it can result in an abrupt termination of a discharge (disruption). Figure 1.4 shows how to stabilize the vertical displacement. The shifted outer poloidal field coils (P3U and P3L) make the vertical magnetic field bent. This concave vertical magnetic field results in a restoring force on the plasma current i.e.  $\vec{F}_R = \vec{J}_p \times \vec{B}_v$ . The radial component of the concave fields is inward above the midplane, and outward below the midplane. This makes  $\vec{F}_R$  always directed toward the midplane.

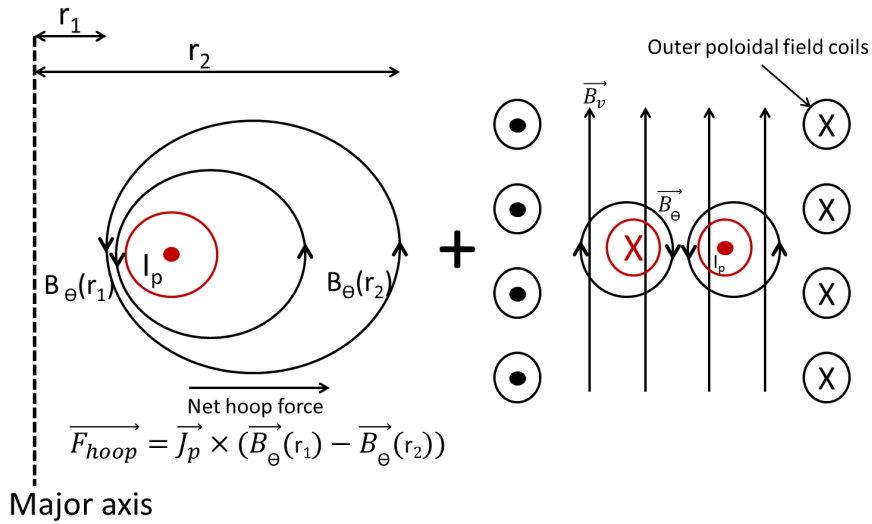


Figure 1.3: *Stabilization of horizontal displacement of a plasma in tokamaks. The imbalance of the poloidal magnetic field ( $B_\theta(r_1) - B_\theta(r_2)$ ) is compensated by the vertical magnetic field  $B_v$ .*

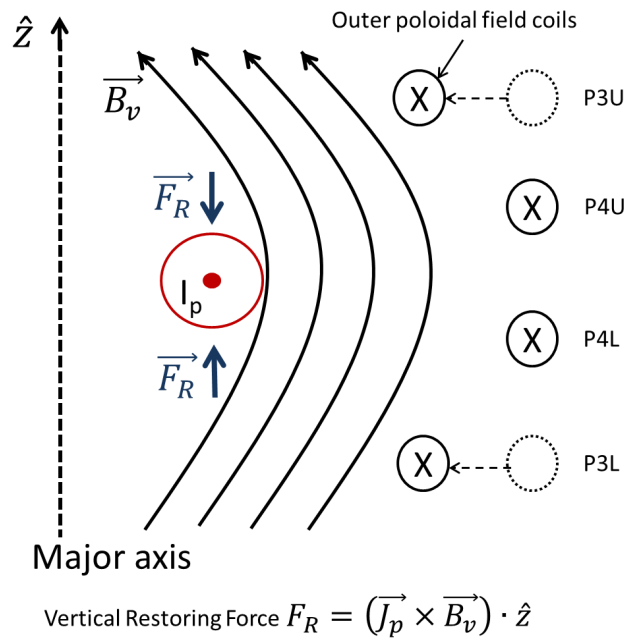


Figure 1.4: *Stabilization of vertical displacement of a plasma in tokamaks. The concave vertical magnetic field, produced by the shifted outer poloidal field coils, generates the restoring force  $\vec{F}_R$ . P3U, P4U, P4L, and P3L correspond to the outer poloidal field coils installed in JET.*

## 1.2 ITER and JET

### 1.2.1 ITER

The International Thermonuclear Experimental Reactor (ITER) is the flagship facility for the world's fusion program for the next twenty years. Seven partners (EU, US, Russia, Korea, Japan, China, and India) signed the ITER Agreement officially on 21 November 2006, and ITER is now under construction in Cadarache<sup>5</sup>, aiming at completion in 2020. The goal of ITER is to demonstrate fusion power output in excess of the required input power, demonstrating the feasibility of a fusion power plant.

For a commercial power plant, output power must be sufficiently higher than the required input power. One of the important parameters determining a fusion reactor's performance is the fusion gain  $Q$ , which is defined by [1]

$$Q = \frac{\text{Fusion power (output power)}}{\text{Heating power (input power)}} = \frac{V_p n_D n_T \langle \sigma v \rangle_{DT} \times 17.6 [\text{MeV}]}{P_H} \quad (1.16)$$

where  $V_p$  is a plasma volume,  $n_D$  is deuterium ion density,  $n_T$  is tritium ion density, and  $\langle \sigma v \rangle_{DT}$  is a rate coefficient for D-T fusion reaction.

In other power plants, such as fossil power plants or nuclear fission power plants, the operation duration available is not a significant issue. However, it is a very important issue for a fusion power plant, in particular the tokamaks, which are operated in pulse mode (at least so far). In tokamaks, a high plasma current is necessary for ohmic heating and confinement of energy and particles. In most present devices, the required plasma current has been generated relying on the inductive loop voltage. This results in short duration of the pulse (10 ~ 20 [sec] in JET, and 1 ~ 2 [sec] in Mega Ampere Spherical Torus (MAST)) due to the intrinsic limitation of magnetic flux swing available in ohmic transformers. It is obvious that such a short pulse duration is not suitable for a power plant. Hence, continuous operation (or at least sufficiently long pulse operation) is one of the key challenges for tokamak research.

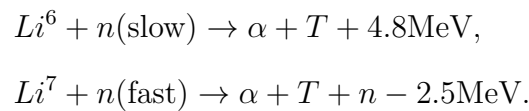
As explained,  $Q$  and operation duration are the two key parameters for tokamak's performance. From the performance's point of view, the ITER experiments aim to achieve two important missions. The primary mission of ITER is to produce a  $Q=10$  plasma being maintained for 400

---

<sup>5</sup>southern France

seconds i.e. stationary operation. In the baseline scenario in ITER, the target plasma current is 15 [MA], and is driven entirely by the ohmic transformer. For the second stage of ITER operation, it is planned to drive plasma current in a non-inductive way using external current drive e.g. Electron Cyclotron Current Drive (ECCD), Lower Hybrid Current Drive (LHCD), and Neutral Beam Injection (NBI). This operation scenario for ITER is called Advanced Tokamak (AT) scenario, and the goal is to produce  $Q=5$  plasma for very long duration i.e. 3000 sec in steady state condition without using ohmic transformer ( $U_l \approx 0$ ).

In addition to the goal in tokamak's performance, important technological issues need to be demonstrated for a fusion power plant. The expected heat load at the plasma facing components in a commercial fusion power plant is much greater than in the present devices. Safe operation scenarios and an effective divertor<sup>6</sup> design to endure the heat load should be demonstrated in ITER. Tritium reproduction is another important issue since it does not exist in nature. Tritium has to be produced by the reaction between lithium and a neutron,



Fortunately, a neutron is one of the fusion products as shown in Equation (1.1). In ITER experiments, it is planned to optimize the Lithium blanket design so that Tritium Breeding Ratio (TBR) is higher than 1. Since we do not have much experience<sup>7</sup> on the tritium injection, extraction, and processing, the tritium treatment is also one of the important technological missions, which have to be demonstrated in ITER.

Another key challenge in ITER is to demonstrate the viability of using large superconducting magnets for all major coils i.e. central solenoid coil, toroidal field coils, and poloidal field coils. In order to reduce the power loss resulting from ohmic heating in the coils, superconducting coils are necessary for a fusion power plant using magnetic confinement. One of the main difficulties arising from use of superconducting coils is that the coil's temperature must be kept below 4 Kelvin ( $-269^{\circ}\text{C}$ ) in order to maintain the superconductivity.

Figure 1.5 shows the structure of the superconducting coil which is planned for the central solenoid in ITER. It should be noted that a bunch of superconducting strands ( $Nb_3Sn$ ) contain copper strands and are enclosed by a copper casing. When voltage is applied to the coil, this

---

<sup>6</sup>Major heat exhauster

<sup>7</sup>Most fusion experiments have been performed using deuterium or hydrogen gas

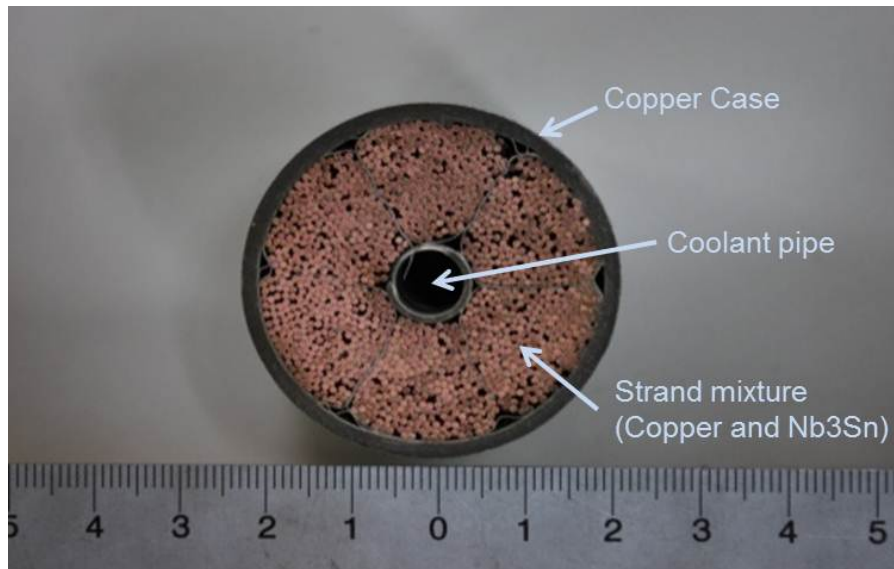


Figure 1.5: *Superconducting central solenoid coil in ITER*

induces current in the copper resulting in ohmic heating. The ohmic heating in the copper can heat the superconducting strands above 4 Kelvin, breaking the superconductivity. This requires a restriction of the current swing  $I_{SC}/dt$  in the superconducting central solenoid, thereby limiting the loop voltage available up to 14[V] at the vacuum vessel centre. [4] [5]

For tokamak start-up, sufficient toroidal loop voltage should be applied. However, the large major radius ( $R_0^{ITER} = 6.2[m]$ ) of ITER makes the allowable toroidal electric field only  $0.35[V/m]$  ( $\approx 14[V]/2\pi R_0^{ITER}[m]$ ). Compared to a typical toroidal electric field for the start-up in the present devices, e.g.  $1[V/m] \approx 18[V]/2\pi R_0^{JET}[m]$  in JET ( $R_0^{JET} = 3[m]$ ), the toroidal electric field available in ITER is thus considerably smaller. Such a restriction of the toroidal electric field available may limit the operation space available, i.e. narrow range of prefill gas pressure, low magnetic error fields, and small impurity content[6]. In order to obtain more confidence in the start-up scenario at ITER, a predictive simulation of tokamak start-up is of crucial importance.

### 1.2.2 JET and ITER-like wall

Figure 1.6 shows the Joint European Torus (JET), the largest tokamak in the world. JET was constructed at Culham<sup>8</sup> in 1983 under the auspices of the Culham Centre for Fusion Energy

<sup>8</sup>Oxfordshire in the UK



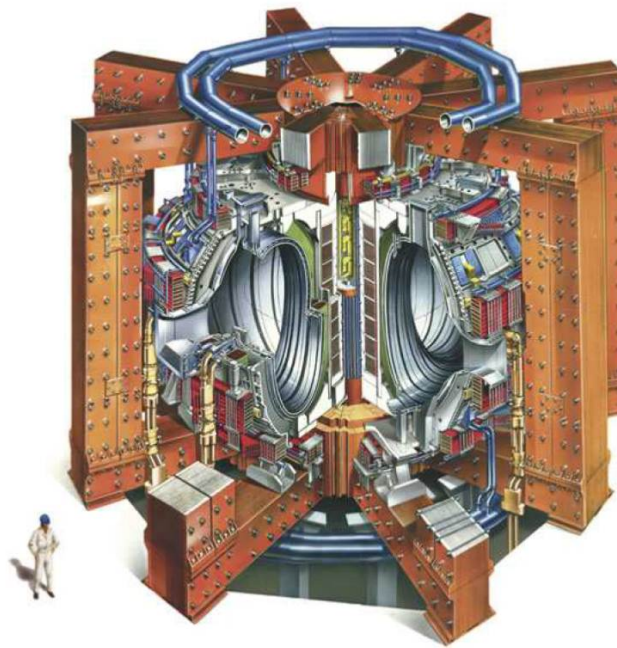


Figure 1.6: *Joint European Torus (JET)*

(CCFE). It is currently operated on behalf of the European Fusion Development Agreement (EFDA) by the United Kingdom Atomic Energy Authority (UKAEA).

Since 1983 when the first plasma was generated, JET has been one of the world-leading fusion devices, making many contributions to fusion research. For example, JET has the world record of the highest fusion power. 16.1 [MW] of fusion power, equivalent to  $Q = 0.62$ , was generated by D-T experiments<sup>9</sup> in JET in 1997 [1]. The D-T experiments in JET showed that the  $\alpha$ -particles were confined and slowed down (i.e. heating the plasma), which was predicted only by theory.

Since the official agreement of ITER construction in 2006, advanced researches for ITER have been the most important priority in the present fusion devices, including JET. One of the critical issues which have to be addressed for ITER is to study Plasma-Wall Interaction (PWI).

Most PWI data accumulated in tokamaks is with a carbon wall. Carbon Fiber Composite (CFC) has been used as components of the first wall<sup>10</sup>, as it does not melt. The carbon wall tends to retain hydrogen isotopes, due to the chemical reactivity. The carbon wall has not caused serious problems for the experiments using deuterium (or hydrogen) gas only. However,

<sup>9</sup>50% – 50% D-T mixture

<sup>10</sup>Previous JET, and other devices such as JT-60U, KSTAR, etc

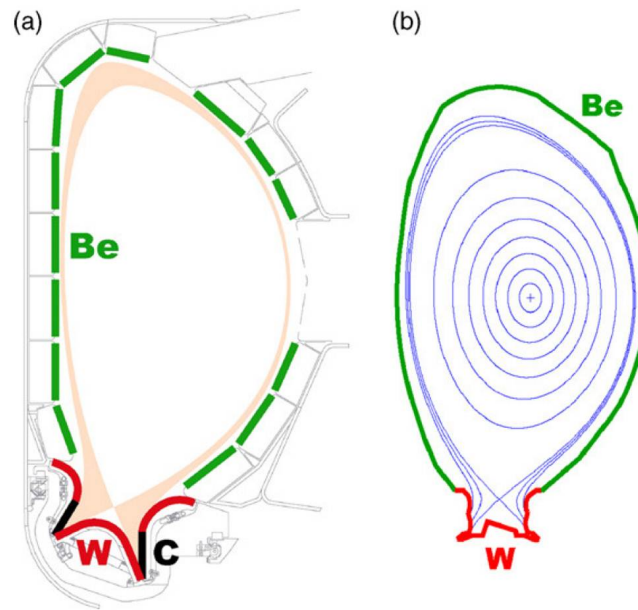


Figure 1.7: (a) *ITER material configuration and (b) material configuration for the JET ITER-like Wall project.* [7]

this would matter when using tritium gas<sup>11</sup>. In ITER, the use of a carbon first wall would lead the in-vessel inventory of tritium to exceed the maximum allowable, limited by regulations on the allowable radioactive material inventory. This requires ITER to be designed using non-carbon material for the first wall. As alternative materials for the first wall, beryllium has been selected in ITER due to the low retention of hydrogen isotope and low radiation level of Be in the plasma [7]. For the divertor, which is a heat exhausting component on the wall, tungsten has been selected due to the high melting temperature and low sputtering yield. (see Figure 1.7 (a))

It is of crucial importance to gain sufficient experimental data on Plasma Facing Components (PFCs) in ITER and to develop operation scenarios compatible with the requirements of the wall. This has motivated the ITER-Like Wall (ILW) project at JET. The CFC tiles in the main chamber wall have been exchanged with beryllium tiles and in parallel a tungsten divertor has been installed as shown in Figure 1.7 (b). [7] [8]

The ILW installation was successfully completed in 2011. Figure 1.8 shows the picture of the completed ILW. Since the operation had been resumed in 2011, JET experiments with the ILW

<sup>11</sup>Tritium transforms to stable non-radioactive helium through the radioactive decay with half-life 12.3 years.

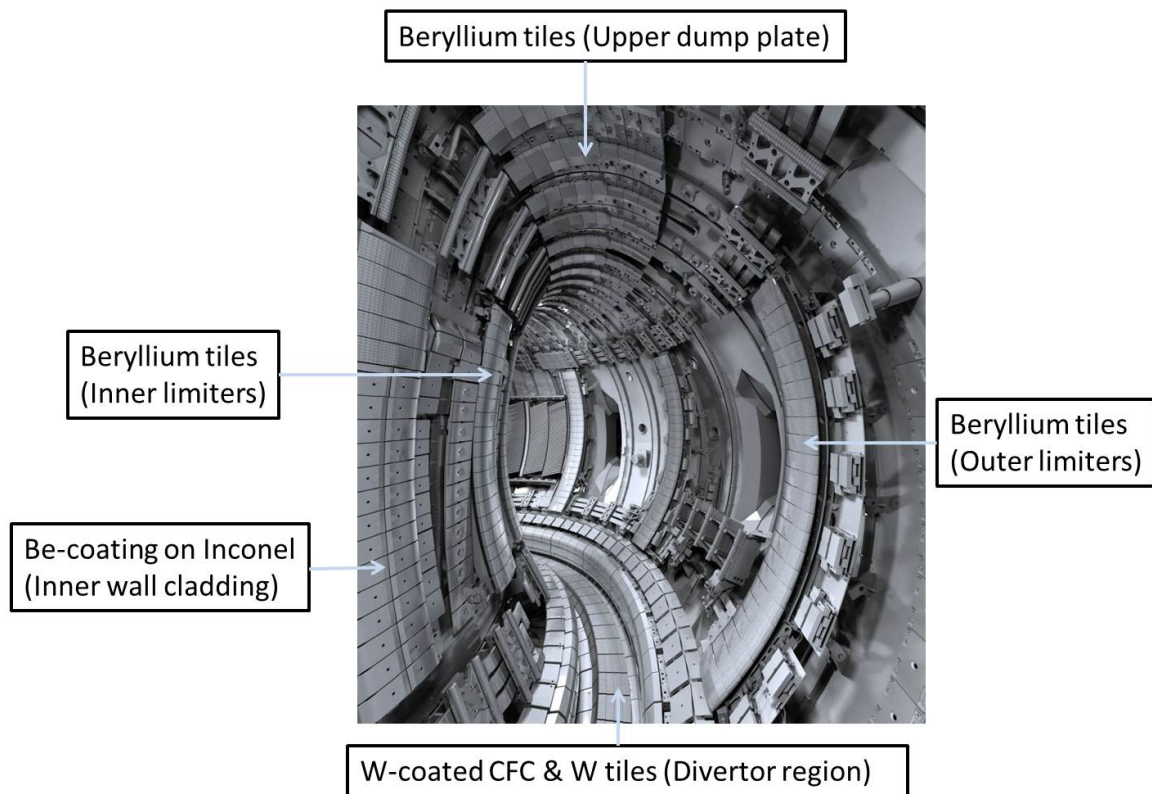


Figure 1.8: *JET chamber with indicated main plasma facing components.* [8]

have produced invaluable information on the wall material's behaviour and a technical basis for the scenario development in ITER.

### 1.3 Brief explanation of tokamak start-up

Tokamak start-up consists of the three phases: 1. Plasma break-down phase (electron avalanche phase), 2. Plasma burn-through phase (full ionization phase), and 3. Plasma current ramp-up phase.

To initiate plasma break-down (electron avalanche) in a given fuel gas, seed electrons existing in the gas must produce one more electrons through collisional ionizations of neutrals before they reach the wall of the surrounding vacuum vessel. In order for electron avalanche to occur, the seed electrons must be sufficiently accelerated by the induced toroidal electric field so that their kinetic energy is high enough to ionize neutrals.

In a tokamak, high toroidal loop voltage  $U_l$  is induced in the toroidal vacuum chamber by the

voltage  $U_{PF}$  in the inner (central solenoid) and outer PF coils. The relation between  $U_l$  and  $U_{PF}$  can be derived as shown following.

In electromagnetics, self-inductance  $L$  of a current loop is defined as

$$L = \frac{N\phi_{loop}}{I_{loop}} \quad (1.17)$$

where  $N_{turns}$  is the total number of turns,  $I_{loop}$  is the current in a loop, and  $\phi_{loop}$  is the magnetic flux penetrating the loop. Substituting  $\phi_{loop}$  in Equation (1.17) with  $\phi_{PF}$  calculated in Equation (1.11), the self-inductance of a inner poloidal field coil  $L_{PF}$  is

$$L_{PF} = \mu_0 n_{turns} N_{turns} A_{PF} \quad (1.18)$$

where  $n_{turns}$  is the number of turns per unit length ( $[m^{-1}]$ ), and  $A_{PF}$  is the area of the cross-section of the inner poloidal field coil. Assuming the dominant voltage in PF coils is consumed by self magnetic induction, ignoring ohmic heating in the coil,

$$\begin{aligned} U_{PF} &= L_{PF} \frac{dI_{PF}}{dt} \\ \frac{dI_{PF}}{dt} &= \frac{U_{PF}}{\mu_0 n_{turns} N_{turns} A_{PF}}, \end{aligned} \quad (1.19)$$

we can substitute  $\frac{dI_{PF}}{dt}$  in Equation (1.12) with the term in the right-hand side in Equation (1.19). Then we can obtain a simple relation between the loop voltage and PF coil voltage,

$$U_l = \frac{-U_{PF}}{N_{turns}}. \quad (1.20)$$

That is, the induced toroidal loop voltage is calculated by dividing the applied voltage in the coil with the number of turns in the coils. For example, for a typical plasma break-down in JET, the toroidal loop voltage is induced by the current swing in the central solenoid coil (P1) and outer PF coil (P4). Then, the induced toroidal loop voltage is calculated as

$$U_l = \frac{U_{P1}}{710} + \frac{U_{P4}}{122} \quad (1.21)$$

where the number of coil turns is 710 in the central solenoid and 122 in the outer PF coils, respectively.

In addition to high electric field, for electron avalanche (plasma break-down) the traveling length of electrons has to be long enough to ensure sufficient collisions with neutrals. Since the electron's motion is guided by a magnetic field line, magnetic field lines in tokamaks define the

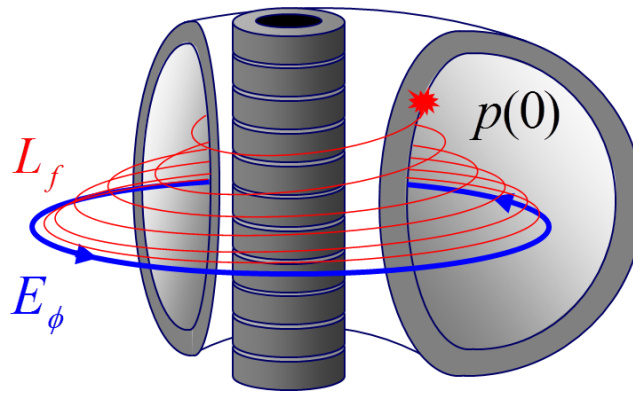


Figure 1.9: *Schematic description of effective connection length  $L_f$*

traveling length of seed electrons. The average length of magnetic field lines is defined by effective connection length  $L_f$ . Hence, ensuring sufficiently long  $L_f$  is one of the key requirements for tokamak start-up. The quantitative requirement on  $L_f$  can be calculated by the *Townsend criterion*<sup>12</sup>.

If there was only toroidal magnetic field during the tokamak start-up phase, the  $L_f$  would be infinity, which is ideal for plasma break-down. However, in the tokamak experiments, there can be significant stray magnetic field, thereby reducing the effective connection length  $L_f$  i.e. open magnetic field lines (see Figure 1.9). In some tokamaks such as JET, an iron transformer core is installed to reduce the stray magnetic fields (see Figure 1.1). However, most present devices do not have an iron core due to the space limitation. In addition to the stray magnetic field, further decrease in  $L_f$  results from the error magnetic field generated by eddy currents in passive structures. This requires optimization of magnetic field configuration with a combination of PF coil currents. Figure 1.10 shows a hexapolar null configuration of poloidal magnetic fields, which is usually used for plasma break-down in JET. Sufficiently long  $L_f$  is obtained at the null point, and this enables plasma break-down near the centre of the vacuum vessel.

Electron avalanche is not the only requirement for tokamak start-up. To achieve the configuration of closed flux surfaces, which is required for high performance in JET, the plasma current must increase at least up to 0.1 [MA]. In order for plasma current to increase, background gas must be fully ionized during the subsequent phase, which is called the *plasma burn-through* phase.

<sup>12</sup>Townsend criterion will be explained in the next section in detail

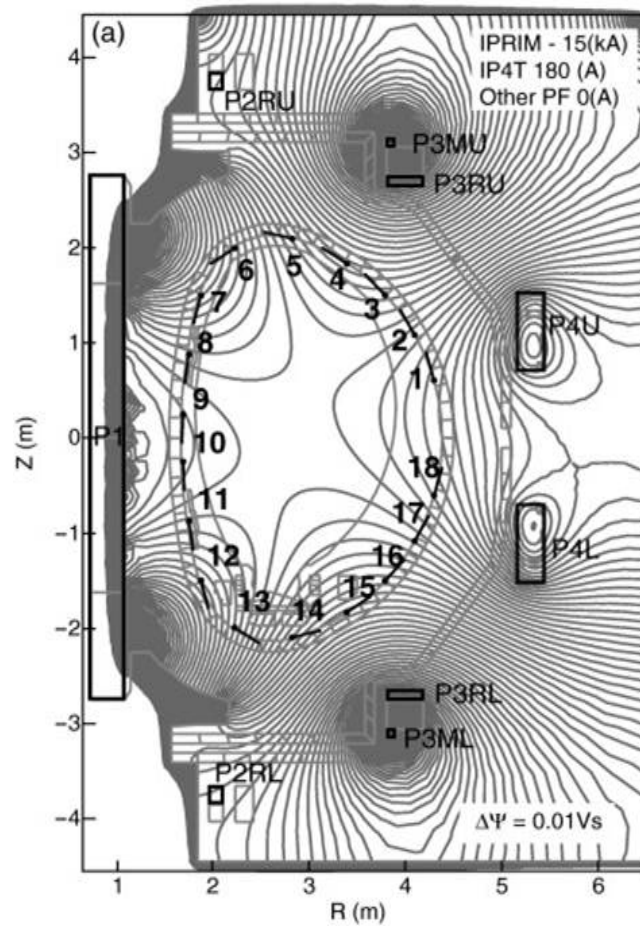


Figure 1.10: *Hexapolar null configuration for plasma break-down in JET [9]*

Figure 1.11 shows typical experimental data of the plasma burn-through phase in JET. In this phase, the majority of the total power loss results from radiation and ionization. Since the total power loss of the plasma is significantly high until full ionization of the background gas and impurities, high loop voltage is pre-programmed for plasma burn-through during the early phase ( $0 \sim 100[msec]$ ), as shown in Figure 1.11(b). The applied loop voltage accelerates electrons, thereby increasing the electron density through collisional ionization of deuterium atoms. Figure 1.11(c) shows interferometry data indicating the increase in electron density during the plasma burn-through phase. The measured line radiations in Figure 1.11(d), (e), and (f) are emitted from the background gas ( $D^0$ ) and impurities ( $Be^{1+}$  and  $C^{2+}$ ) in the plasma, respectively. The decay after their peak implies that all are ionized to higher charge states. Once the plasma is fully ionized, then the plasma current can increase even with reduced loop voltage, as shown in Figure 1.11 (a) and (b).

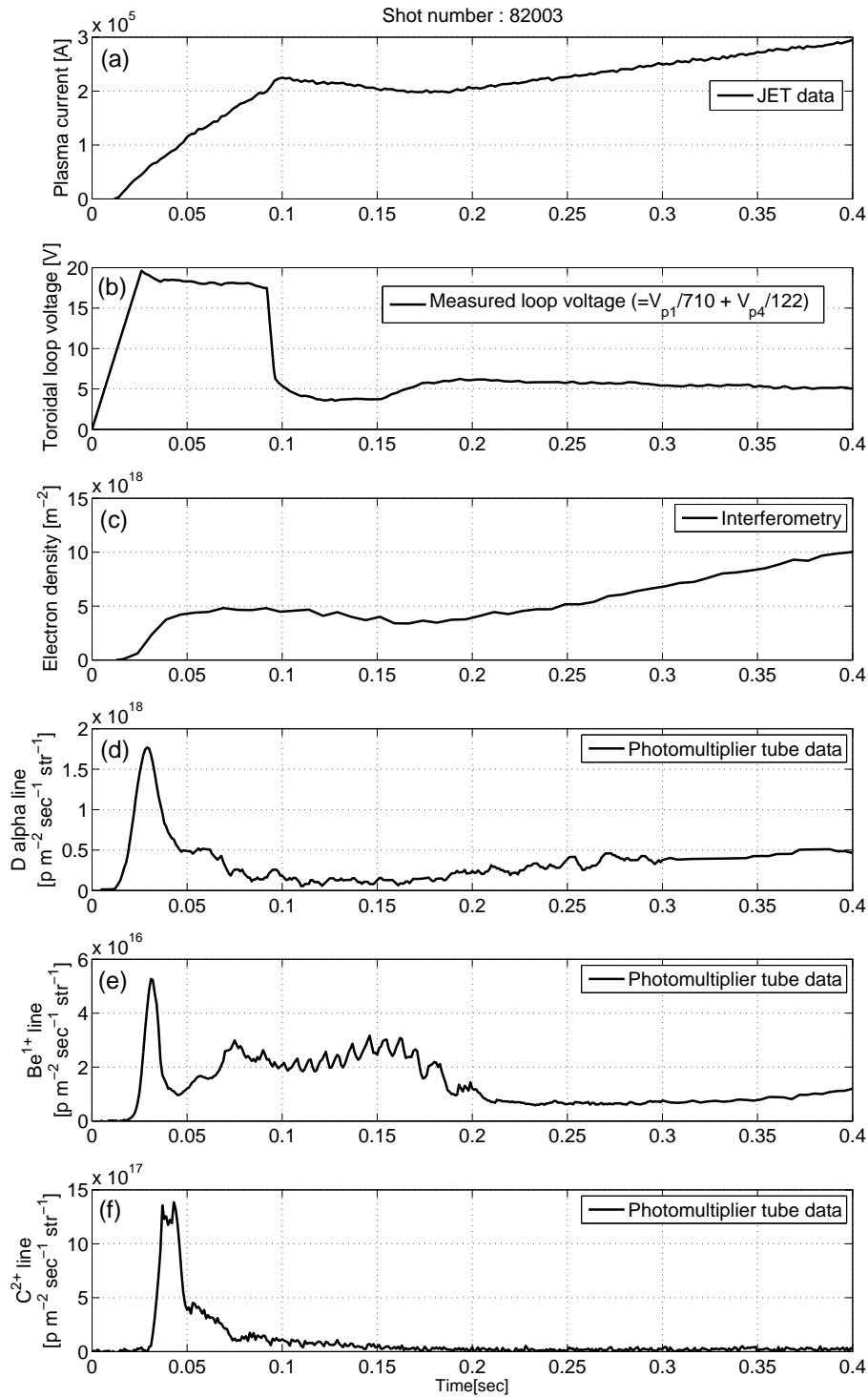


Figure 1.11: Typical experimental data during the plasma burn-through phase measured in JET(#82003); (a) plasma current, (b) toroidal loop voltage, (c) electron density, (d) D alpha line emission, (e)  $\text{Be}^{1+}$  line emission, and (f)  $\text{C}^{2+}$  line emission

## 1.4 Motivation of plasma burn-through modeling

In order to calculate the required electric field for electron avalanche ( $E_{avalanche}$ ) at a given prefill gas pressure  $p$  and effective connection length  $L_f$ , the Townsend avalanche theory [10][11] is generally used as shown below <sup>13</sup>,

$$E_{avalanche}[V/m] \geq \frac{1.25 \times 10^4 p[Torr]}{\ln(510 p[Torr] L_f[m])}. \quad (1.22)$$

The required  $E_{avalanche}$  for plasma initiation in the International Thermonuclear Experimental Reactor (ITER) has also been calculated using Equation (1.22) as presented in the ITER Physics Basis[4].

However, the Townsend avalanche theory is not sufficient to explain all non-sustained breakdown discharges. In order for plasma current to increase, sufficient ionization of the prefill gas (deuterium) and impurities, i.e. plasma burn-through, is necessary. Otherwise, most heating power is lost through radiation and ionizations of the remaining neutrals, so that it prevents electron temperature from increasing in the ramp-up phase of plasma current [10]. A number of start-up failures in current devices result from the failure of plasma burn-through. For experiments with the carbon wall in the Joint European Torus (JET), more than 85% of all non-sustained breakdown failures occurred during the plasma burn-through phase [12]. These start-up failures could be reduced by understanding key physics aspects of the plasma burn-through phase.

Furthermore, due to the engineering issues in ITER, resulting from the use of superconducting central solenoid coils, the maximum toroidal electric field on-axis is limited up to 0.35 [V/m] [5], which is much lower than the typical toroidal electric field used for plasma burn-through in current devices, e.g.  $\sim 1$  [V/m] in JET. Tokamak start-up using such a low electric field limits the operation space available for the range of prefill gas pressure, magnetic error fields, and impurity content [6]. This leads to urgent need of a predictive simulation for plasma burn-through in ITER.

For reliable start-up using a low electric field, RF-assisted start-up using Electron Cyclotron Heating (ECH)[13][14][15] or Ion Cyclotron Heating (ICH)[16][17] is planned in ITER [5]. However, launching excessive RF power into the vacuum vessel without a plasma or at a very low

---

<sup>13</sup>Equation (1.22) will be derived in the next chapter.



plasma temperature can result in serious damage to the diagnostic systems, due to the low absorption efficiency of RF power. Hence, in order to estimate the minimum required ECH power, understanding the plasma burn-through conditions (or requirements) is also important.

In most tokamaks, when determining an operational scenario for the first plasma, the required parameters have been found through trial and error methods, rather than a computational simulation approach. As a result, our understanding of tokamak start-up and our prediction abilities are very limited, even after 30 years of research. In order to approach a commercial fusion power plant, tokamak start-up should not remain as ‘kitchen physics’. We should be able to predict the required operational conditions using computational simulations. A comprehensive understanding of plasma burn-through is also necessary for non-inductive start-up, which is of crucial importance for a compact design of spherical torus. The plasma burn-through modeling will make a contribution to deepen our understanding of the start-up in a spherical torus, thereby establishing a basis of research on non-inductive tokamak start-up.

Although the plasma burn-through phase has been modelled before [6][18][19][20], important physics models such as impurity treatment and particle (or energy) confinement time were overly simplified. Furthermore, the previous simulation results have not been validated against any experimental data. This has motivated development of a new plasma burn-through simulator, the DYON code, introduced in this thesis.

## 1.5 Scope of thesis

This thesis will first review the electron avalanche physics (Townsend avalanche theory) in chapter 2. The following research questions are addressed.

1. Can we simulate plasma burn-through, and can we improve the simulations performed previously?
2. Impurities have a significant influence on plasma burn-through. Then, how can we simulate impurity evolution?
3. Can we validate the simulation against experimental data?

The basic structure of plasma burn-through modeling is introduced in chapter 3. Fundamental physics of deuterium burn-through is investigated in chapter 4. Chapter 5 explains the new models developed in the DYON code for impurity treatment in detail. In chapter 6, for the first time, the simulation results are compared with the experimental data in JET, and the influence of a carbon wall and a beryllium wall are discussed. In chapter 7, the predictive simulations of ITER, obtained by the DYON code, is provided. In chapter 8, main conclusion of the thesis is presented.

# Chapter 2

## Review of electron avalanche

### 2.1 Introduction

*Electron avalanche* implies an abrupt increase in electron density in a gas. By the electron avalanche process, a gas is transferred to a plasma. Hence, electron avalanche is also called plasma break-down or plasma formation. It should be noted that during the electron avalanche phase the degree of ionization in this phase is low initially. One of the important consequences of a low degree of ionization is that the dominant mechanism for electrons' collisions is electron-neutral collision (i.e. billiard-ball collision) rather than the collisions between charged particle (i.e. coulomb collision) [10]. Hence, the electron dynamics is mainly determined by the electron-neutral collision. This makes many concepts of general plasma physics such as Debye shielding inapplicable.

The physical mechanism in the electron avalanche phase can be described by the *Townsend avalanche theory*, which is well validated for laboratory plasmas. The Townsend avalanche theory is also applicable to tokamaks, and it is used to estimate the operation parameters for tokamak start-up [4][11][6]. In order to understand the requirements for tokamak start-up, it is worth reviewing the Townsend avalanche theory.

In Section 2.2, the concept of the Townsend avalanche theory is reviewed, focusing on two important coefficients, i.e. the Townsend first coefficient  $\alpha$  and the second Townsend coefficient  $\gamma$ . In Section 2.3, the application to the electron avalanche in tokamaks is introduced. The

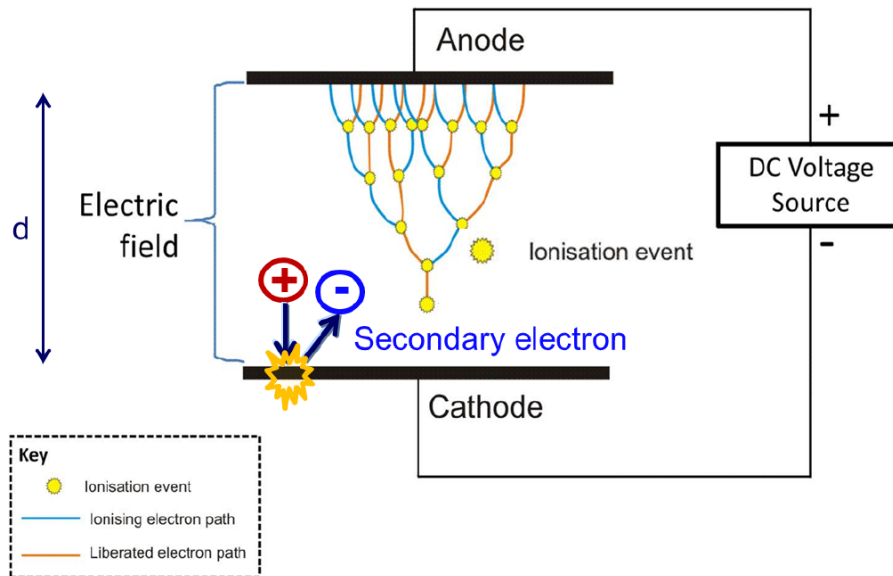


Figure 2.1: *Visualisation of an electron avalanche, also known as a Townsend discharge. The applied electric field accelerates seed electrons to collide with other neutrals and release further electrons, causing an avalanche. - from WIKIPEDIA*

operational parameters for electron avalanche in tokamaks is discussed in Section 2.4.

## 2.2 Townsend avalanche theory

### 2.2.1 The first townsend coefficient

Electrons can be created naturally in a gas by ionization caused by cosmic x-ray background radiation or beta decay, though the amount is extremely small. Electrons can also be artificially generated by the exposure of UV light at the cathode<sup>1</sup>. Such electrons play an important role as seed electrons to trigger the electron avalanche process, thereby generating a plasma.

In a DC plasma, a seed electron is accelerated to the anode by the electric field between electrodes. If the seed electron is accelerated sufficiently to the ionization energy of background neutrals, it can create other electrons by collisional ionizations. The electrons produced by the collisional ionizations are also accelerated by the electric field, and they make further collisional

<sup>1</sup>Photoelectric effect

ionizations. This results in electron avalanche, as can be seen in Figure 2.1.

Flowing from the cathode at  $z = 0$  to the anode at  $z = d$ , the electron flux  $\Gamma_e$  increases exponentially. By defining  $\alpha$  as the number of the electrons produced by an electron in unit distance, we can calculate the increase in the electron flux by a differential equation below,

$$\frac{dn_e}{dz} = \alpha n_e . \quad (2.1)$$

$\alpha$  is called *the first Townsend coefficient*. The physical meaning of  $\alpha$  is how many collisional ionizations can be made by an electron per unit distance. In order for an electron to make a collisional ionization, the electron must collide with a neutral as well as have sufficient energy to ionize the neutral. Hence,  $\alpha$  is the product of ‘the probability for an electron to collide with a neutral over a unit distance ( $P_{collision}$ )’ and ‘the probability for an electron to have higher energy than ionization energy ( $P_{acceleration}$ )’,

$$\alpha = P_{collision} \times P_{acceleration} . \quad (2.2)$$

$P_{collision}$  is inversely proportional to the average traveling length of an electron between collisional events with neutrals. We define  $\lambda_e$  as the mean free path of an inelastic collision by which an electron excites or ionizes a neutral, using kinetic energy. Then, the collisional probability can be expressed as

$$P_{collision} = \frac{1}{\lambda_e} . \quad (2.3)$$

In order for an electron to have the ionization energy, the electron must be sufficiently accelerated, traveling a certain distance without undergoing any inelastic collision. If an electron collides with neutrals before having the ionization energy, the electron loses the kinetic energy resulting in collisional excitation of the neutrals without ionization.

$P_{acceleration}$  is the fraction of sufficiently accelerated electrons, of which the kinetic energy is higher than the ionization energy, to the total electrons, i.e.  $P_{acceleration} = n_e^{iz}/n_e^{total}$ . Then, we can calculate  $P_{acceleration}$  using  $\lambda_e^{-1}$  in Equation (2.3). For this calculation, we should define  $n_e^{virgin}(z)$  as the number density of the electrons which have not experienced any inelastic collision at a position  $z$ , i.e. the number density of ‘virgin electrons’ at  $z$ . The rate of decrease in  $n_e^{virgin}$  along the traveling path,  $dn_e^{virgin}/dz$ , can be calculated using  $\lambda_e^{-1}$  and  $n_e^{virgin}$ ,

$$\frac{dn_e^{virgin}}{dz} = -\lambda_e^{-1} \times n_e^{virgin}(z) , \quad (2.4)$$

where the minus symbol means that the number of ‘virgin’ electrons decreases traveling along  $z$  direction toward the anode.  $\delta_{iz}$  is the required traveling length for an electron to obtain the ionization energy  $\varepsilon_{iz}$  for a given electric field  $E$ , i.e.  $\varepsilon_{iz} = \delta_{iz}qE$ .<sup>2</sup> The number of virgin electrons which will survive after traveling  $\delta_{iz}$  from a random position  $z_1$  is the number of the electrons which will have  $\varepsilon_{iz}$  i.e.  $n_e^{iz}(z_1) = n_e^{virgin}(z_1 + \delta_{iz})$ . The electron density at  $z_1$ ,  $n_e^{virgin}(z_1)$ , is the total electron density at  $z_1$ ,  $n_e^{total}(z_1)$ , since no electron has experienced any collision yet between  $z_1$  and  $z_1 + \delta_{iz}$ .

$$\begin{aligned} \frac{1}{n_e^{virgin}} dn_e^{virgin} &= -\frac{1}{\lambda_e} dz \\ [\ln n_e^{virgin}]_{n_e^{virgin}(z_1)}^{n_e^{virgin}(z_1+\delta_{iz})} &= \left[-\frac{z}{\lambda_e}\right]_{z=z_1}^{z=z_1+\delta_{iz}} \\ [\ln n_e^{virgin}]_{n_e^{total}}^{n_e^{iz}} &= -\frac{\delta_{iz}}{\lambda_e} \\ P_{acceleration} &= \frac{n_e^{iz}}{n_e^{total}} = \exp\left(-\frac{\delta_{iz}}{\lambda_e}\right) \end{aligned} \quad (2.5)$$

By substituting  $P_{collision}$  and  $P_{acceleration}$  in Equation (2.2) using Equation (2.3) and Equation (2.5), we can have  $\alpha$  as a function of  $\lambda_e$  and  $\delta_{iz}$ ,

$$\alpha = \frac{1}{\lambda_e} \exp\left(-\frac{\delta_{iz}}{\lambda_e}\right).$$

By substituting  $\delta_{iz}$  with  $\varepsilon_{iz}/E$ , we can obtain the *first Townsend coefficient*  $\alpha$  expressed as a function of the prefill gas pressure  $p$  and the electric field  $E$ ,

$$\begin{aligned} \alpha &= \frac{1}{\lambda_e} \exp\left(-\frac{E\delta_{iz}}{\lambda_e e E}\right) \\ &= \frac{1}{\lambda_e} \exp\left(-\frac{\varepsilon_{iz}/p}{\lambda_e E/p}\right) \\ &= pA \exp\left(-\frac{B}{E/p}\right), \end{aligned} \quad (2.6)$$

where  $A$  and  $B$  are

$$A = \frac{1}{p\lambda_e}, \quad B = \frac{\varepsilon_{iz}}{p\lambda_e}. \quad (2.7)$$

$\lambda_e$  equals  $(n_n\sigma_e)^{-1}$  where  $n_n$  is the number density of neutrals and  $\sigma_e$  is the cross section of an inelastic collision. Within a certain range of  $E/p$ , it is reasonable to assume  $\sigma_e$  as a constant [21]. The prefill gas pressure  $p$  is  $n_n T_n$ .<sup>3</sup> Since the temperature of a prefill gas for plasma

<sup>2</sup>For a hydrogen molecule  $H_2$ , effective  $\varepsilon_{iz} = 25 \sim 30$  eV.

<sup>3</sup>The temperature unit is Joule

Gas	A [ $cm^{-1} Torr^{-1}$ ]	B [ $V cm^{-1} Torr^{-1}$ ]	Range of $E/p$ [ $Vcm^{-1} Torr^{-1}$ ]
<i>He</i>	2.8	77	30 ~ 250
<i>Ne</i>	4.4	111	100 ~ 400
<i>Ar</i>	11.5	176	100 ~ 600
<i>Kr</i>	15.6	220	100 ~ 1000
<i>Xe</i>	24	330	200 ~ 800
<i>H<sub>2</sub></i>	5.1	125	15 ~ 600
<i>N<sub>2</sub></i>	11.8	325	100 ~ 600
<i>O<sub>2</sub></i>	6.5	190	50 ~ 130
<i>CH<sub>4</sub></i>	17	300	150 ~ 1000
<i>CF<sub>4</sub></i>	11	213	25 ~ 200

Table 2.1: Constants  $A$  and  $B$  in the Equation (2.6) at the range of  $E/p$  [21]

experiments is about room temperature (300 K), the prefill gas pressure is only subject to the neutral density  $n_n$ . Therefore, it is probable to treat  $p\lambda_e$  as a constant, so that both of  $A$  and  $B$  in Equation (2.7) are constants. The intrinsic  $\varepsilon_{iz}$  and  $\sigma_e$  of the background neutrals determine the constant  $A$  and  $B$ . Table 2.1 shows the list of  $A$  and  $B$  of various gas at a range of  $E/p$ .

Equation (2.6) reveals an important relationship between the prefill gas pressure and the first townsend coefficient  $\alpha$ . The blue solid line in Figure 2.2 shows that there is an optimum pressure range for high  $\alpha$ . This can be explained by the different behaviour of  $P_{collision}$  and  $P_{acceleration}$  with  $p$ . Since  $\lambda_e^{-1}$  is proportional to  $n_n(\propto p)$ ,  $P_{collision}$  is simply proportional to the prefill gas pressure  $p$  as indicated by the red solid line in Figure 2.2. For a given electric field,  $P_{acceleration}$  is  $\exp(-constant \times p)$  as shown by the black solid line. That is, at an extremely low pressure, even though an electron is easily accelerated due to the rare inelastic collisions with neutrals, it is difficult to trigger electron avalanche due to the small number of collision events. In contrast, at a high pressure, it is also difficult to generate collisional ionizations since the collision frequency is too high to accelerate an electron.

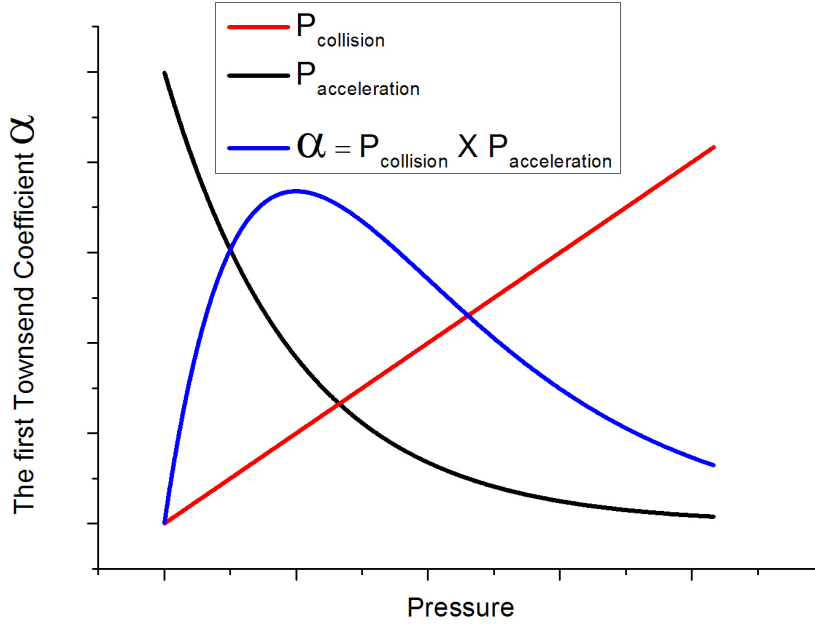


Figure 2.2: *Townsend first coefficient  $\alpha$*

## 2.2.2 The second townsend coefficient

Electric field  $E$  is a constant for a vacuum region before plasma break-down. Thus,  $\alpha$  is a constant between the electrodes. By using Equation (2.1), we have the electron density at  $z$  as

$$\begin{aligned}
 \frac{dn_e}{dz} &= \alpha n_e \\
 \frac{1}{n_e} dn_e &= \alpha dz \\
 \ln \frac{n_e(z)}{n_e(0)} &= \alpha z \\
 n_e(z) &= n_e(0) e^{\alpha z} .
 \end{aligned} \tag{2.8}$$

From (2.8), we can see an electron starting from the cathode at  $z = 0$  would be multiplied to  $e^{\alpha d}$  electrons, approaching the anode at  $z = d$ . During the avalanche process,  $e^{\alpha d} - 1$  ions are generated if the atomic number of the background neutrals is 1. The ions are accelerated to the cathode by the electric field. The energetic ions collide with the cathode, and secondary electrons are emitted from the cathode by the ion impact. Figure (2.3) describes the secondary electron emission from a cathode.

For plasma break-down without any UV light or additional electron source, the number of



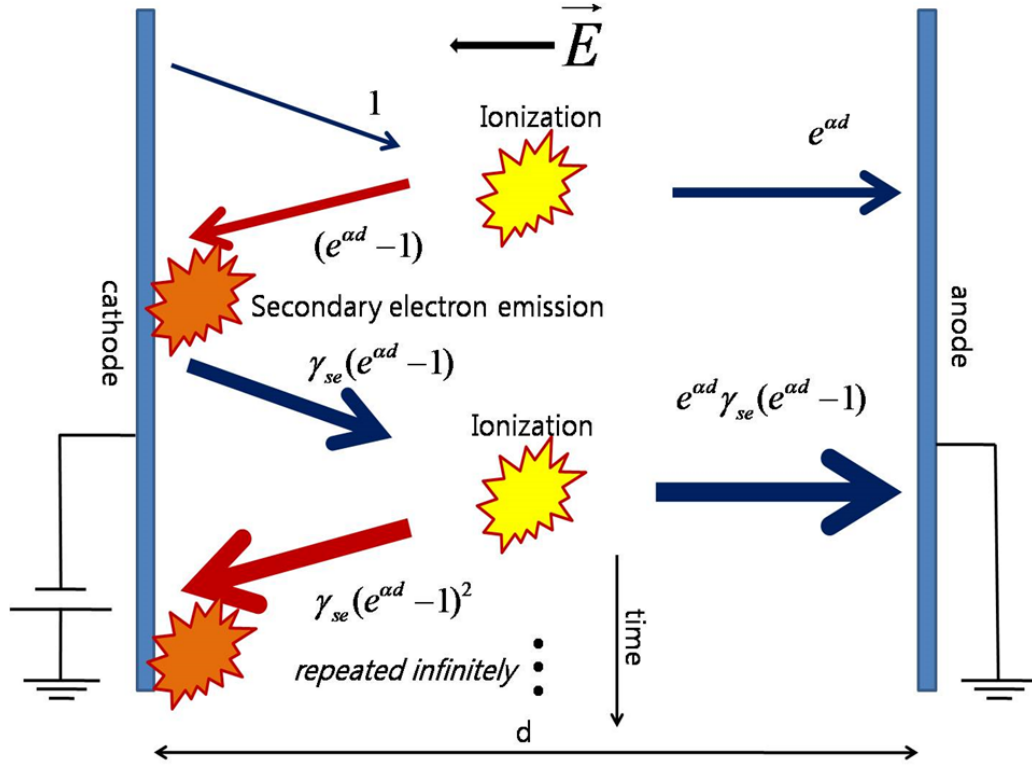


Figure 2.3: Secondary electron emission

generated electrons must be high enough to be self-sustaining. That is, the electrons have to be generated in sufficient numbers by the ion-cathode collisions. The *second Townsend coefficient*  $\gamma_{se}$  is defined as the number of secondary electrons emitted by the impact of an energetic ion at the cathode.

The number of secondary electrons, resulting from  $e^{\alpha d} - 1$  ion-impacts, is  $\gamma_{se}(e^{\alpha d} - 1)$ . The secondary electrons also experience collisions with neutrals and are multiplied to  $e^{\alpha d} \gamma_{se}(e^{\alpha d} - 1)$  at the anode. It should be noted that the number of electrons arriving at the anode increases with a ratio  $\eta$ ,

$$\eta = \frac{e^{\alpha d} \gamma_{se}(e^{\alpha d} - 1)}{e^{\alpha d}}. \quad (2.9)$$

The number of ions arriving at the cathode also increases by the ratio of  $\eta$ . Therefore, we can have the total amount of electrons flowing to the anode through the repeated processes,

$$n_e^\infty(d) = n_e(0)e^{\alpha d} + n_e(0)e^{\alpha d}\eta + n_e(0)e^{\alpha d}\eta^2 + \dots = \begin{cases} n_e(0)e^{\alpha d}/(1 - \eta) & \text{if } \eta < 1 \\ \infty & \text{if } \eta \geq 1 \end{cases} \quad (2.10)$$

Finite number of electrons arriving at the anode through the (infinitely) repeated process implies the electron current would vanish after a certain number of repeated process. For a steady

Solid	Ion	Energy [eV]	$\gamma_{se}$
W	He <sup>+</sup>	100	0.263
W	Ar <sup>+</sup>	10	0.096
W	Ar <sup>+</sup>	100	0.095
W	H <sub>2</sub> <sup>+</sup>	100	0.029
W	N <sub>2</sub> <sup>+</sup>	100	0.025
W	O <sub>2</sub> <sup>+</sup>	100	0.015
Mo	He <sup>+</sup>	100	0.274
Mo	Ar <sup>+</sup>	10	0.115
Mo	N <sub>2</sub> <sup>+</sup>	100	0.032
Mo	O <sub>2</sub> <sup>+</sup>	100	0.026

Table 2.2: Secondary electron emission coefficients  $\gamma_{se}$  [21]

current,  $I(t) = \bar{I}$ , the total amount of electrons  $n_e^\infty$  must be infinite value as can be seen by

$$n_e^\infty = \int_0^\infty I(t)dt = \int_0^\infty \bar{I}dt = \infty . \quad (2.11)$$

Therefore,  $\eta$  should be higher than (or equal to) 1 for a self-sustaining discharge. We can define the condition for plasma break-down as  $\eta = 1$ ,

$$\gamma_{se}(e^{\alpha d} - 1) = 1 . \quad (2.12)$$

Then, we can have the requirement on  $\alpha d$

$$\alpha d = \ln \left( 1 + \frac{1}{\gamma_{se}} \right) . \quad (2.13)$$

By substituting  $\alpha$  with Equation (2.6) and setting the break-down voltage  $U_b = Ed$ , the required voltage for plasma breakdown is obtained,

$$Apd \exp \left( - \frac{Bpd}{U_b} \right) = \ln \left( 1 + \frac{1}{\gamma_{se}} \right) \quad (2.14)$$

$$U_b = \frac{Bpd}{\ln Apd - \ln \left( \ln(1 + 1/\gamma_{se}) \right)} . \quad (2.15)$$

As can be seen in Equation (2.15), the break-down voltage  $U_b$  is a function of the product  $pd$  as well as the *second Townsend coefficient*  $\gamma_{se}$ . Table 2.2 gives a list of the *secondary electron*

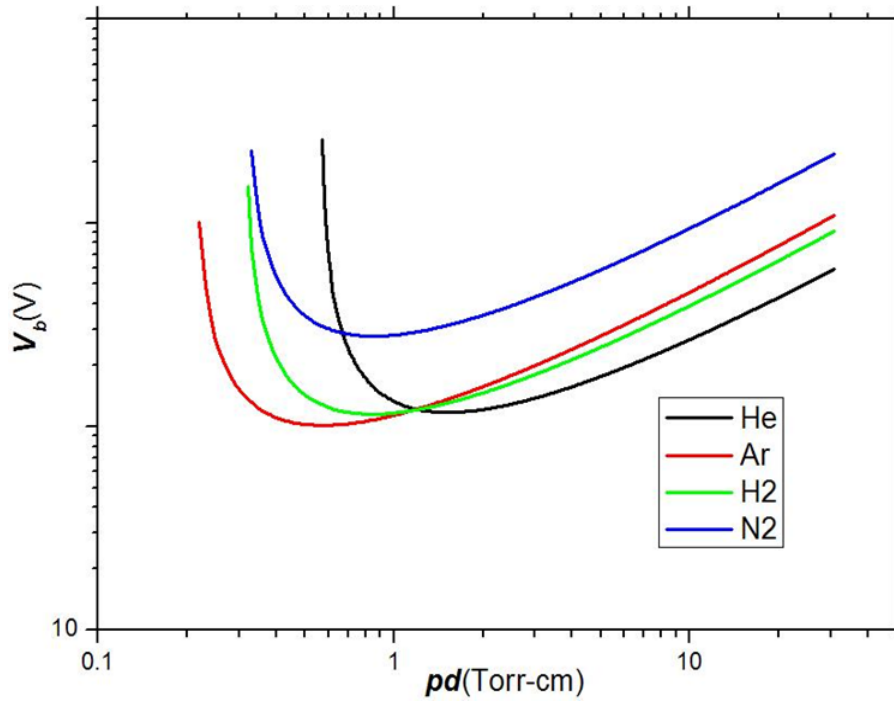


Figure 2.4: Analytical drawing of Equation (2.15); gas : He, Ar, H<sub>2</sub>, N<sub>2</sub>, cathode : W

*emission coefficients*. By using Table 2.1 and Table 2.2, we can find the required voltage for plasma break-down as a function of  $pd$ . Figure 2.4 shows  $U_b(pd)$  drawn analytically using Equation (2.15). In Figure 2.4, the cathode material was assumed to tungsten, and the ions assumed to be singly ionized ( $Z = 1$ ).

The curve of  $U_b(pd)$  is called *Paschen curve*, and we can understand the characteristic of DC plasma break-down by the curve. In the range of high  $pd$ , the required  $U_b$  increases almost linearly with  $pd$ . At a high prefill gas pressure, electrons experience too frequent collisions to obtain sufficient energy from electric field for background gas ionization. Accordingly, a high electric field is required for electrons to be sufficiently accelerated between the frequent electron-neutral collisions. Electron avalanche is also difficult to initiate in the range of small  $pd$ . This is due to the fact that electrons rarely collide with neutrals at a low prefill gas pressure. Moreover, if the distance between electrodes  $d$  is also too small, then the collision scarcity would be more severe since the electron's traveling length is too short. For electron avalanche to occur with the 'scarce collision probability', the applied voltage should accelerate a high fraction of electrons over ionization energy of the neutrals. This results in steep increase in the break-down voltage  $U_b$  at a low  $pd$  regime.

As can be seen by Figure 2.4, the break-down voltage has a minimum at some intermediate value  $pd = (pd)_{min}$ . By differentiating Equation (2.15) for  $pd$ , we can find  $(pd)_{min}$ , with which the required voltage for plasma break-down is a minimum.

$$\left. \frac{dU_b}{d(pd)} \right|_{pd=(pd)_{min}} = 0 \quad (2.16)$$

Simplifying by substituting  $\ln(1 + 1/\gamma_{se})$  with a constant  $C$ , we have

$$\begin{aligned} \left. \frac{d(Bpd)}{d(\ln(Apd/C))} \right|_{pd=(pd)_{min}} &= 0 \\ \left. \frac{B \ln(Apd/C) - B}{(\ln(Apd/C))^2} \right|_{pd=(pd)_{min}} &= 0 \\ \ln(A(pd)_{min}/C) &= 1 \\ (pd)_{min} &= \frac{eC}{A} = \frac{e}{A} \left( \ln(1 + 1/\gamma_{se}) \right). \end{aligned} \quad (2.17)$$

The value of  $(pd)_{min}$  is a function of the gas and a weak function of the cathode material.

## 2.3 Electron avalanche in tokamaks

Electrons in a tokamak are accelerated by the toroidally induced electric field. We define  $\nu_{iz}$  as the ionization rate of an electron i.e. the number of ionizations in a second by an electron.  $\nu_{iz}$  is calculated by the product of the neutral density  $n_n$  and the rate coefficient of ionization  $\langle \sigma v \rangle_{iz}$  i.e.  $\nu_{iz} = n_n \langle \sigma v \rangle_{iz}$ .  $\beta_{loss}$  is defined as the transport loss rate of an electron i.e.  $\beta_{loss} = 1/\tau_e$  where  $\tau_e$  is the mean time for an electron to arrive at the vessel wall. The evolution of electron density can be calculated using  $\nu_{iz}$  and  $\beta_{loss}$  as

$$\frac{dn_e}{dt} = (\nu_{iz} - \beta_{loss})n_e \quad (2.18)$$

During the electron avalanche phase, the degree of ionization in the avalanche phase is only a few percent, and the electron velocity is quickly saturated by collisions with the neutrals. Hence, it is reasonable to assume that the neutral density  $n_n$  and the rate coefficients for ionization  $\langle \sigma v \rangle_{iz}$  are constant. Since operation parameters determining the particle loss (the prefill gas pressure, the induced toroidal electric field, and magnetic field) do not change significantly during the avalanche phase, particle loss rate  $\beta_{loss}$  can also be assumed as constant. Then, we

have

$$\begin{aligned}\frac{1}{n_e} dn_e &= (\nu_{iz} - \beta_{loss}) dt \\ \ln\left(\frac{n_e(t)}{n_e(0)}\right) &= (\nu_{iz} - \beta_{loss}) t \\ n_e(t) &= n_e(0) \exp(\nu_{iz} - \beta_{loss}) t.\end{aligned}\tag{2.19}$$

Equation (2.19) shows that if  $\nu_{iz}$  exceeds  $\beta_{loss}$ , the electron density  $n_e$  increases exponentially i.e. electron avalanche.

The requirement for electron avalanche can be found by  $\nu_{iz} = \beta_{loss}$ . In order to find the criterion for electron avalanche, we have to calculate  $\nu_{iz}$  and  $\beta_{loss}$ , respectively. This ionization process in tokamaks is described by the *Townsend avalanche theory*[22]. One of the key features of the Townsend avalanche theory is that the mean velocity of electrons  $u$  [m/s] is a function of  $E/p$ , where  $E$  is the induced electric field and  $p$  is the prefill gas pressure (as long as  $E/p$  is smaller than  $2 \times 10^4$  [Vm<sup>-1</sup>torr<sup>-1</sup>] i.e. the limitation of run-away electron production).<sup>4</sup> According to the Townsend avalanche theory, we can have the electron mean velocity  $u_e$  as a function of  $E/p$ , [11]

$$u_e \approx 43 \frac{E \text{ [V/m]}}{p \text{ [Torr]}}.\tag{2.20}$$

The *first townsend coefficient*  $\alpha$  [m<sup>-1</sup>] in tokamak experiments using the hydrogen isotope as prefill gas can be found by Equation (2.6), where  $A = 510$  [m<sup>-1</sup>torr<sup>-1</sup>],  $B = 1.25 \times 10^4$  [Vm<sup>-1</sup>torr<sup>-1</sup>], [11]

$$\alpha = p 510 \exp\left(-\frac{1.25 \times 10^4}{E/p}\right).\tag{2.21}$$

Therefore, the ionization rate of an electron  $\nu_{iz}$  can be obtained as a function of electric field  $E$  and prefill gas pressure  $p$  by using (2.20) and (2.21),

$$\begin{aligned}\nu_{iz} &= \alpha u_e \\ &\approx 43 \frac{E}{p} \times p 510 \exp\left(-\frac{1.25 \times 10^4}{E/p}\right) \\ &\approx 21930 \times E \times \exp\left(-\frac{1.25 \times 10^4}{E/p}\right).\end{aligned}\tag{2.22}$$

---

<sup>4</sup>If the  $E/p$  is higher than  $2 \times 10^4$  [Vm<sup>-1</sup>torr<sup>-1</sup>], (Equation (2.20)) is not valid due to the run away electrons produced in higher  $E/p$  range.

Equation (2.22) shows  $\nu_{iz}$  is about  $20000[s^{-1}]$  for typical operation parameters in JET i.e.  $E \sim 1[V/m]$  and  $p \sim 10^{-5}[Torr]$ .

The majority of electron losses during the electron avalanche phase are due to the drift motion and the stray (or error) magnetic fields [11].

The drift loss results from the intrinsic  $\nabla B$  and curvature of the magnetic fields in a torus. The vertical drift velocity  $v_d$  is calculated by Equation (1.13),

$$v_d = \vec{v}_{\nabla B} + \vec{v}_R = \frac{m}{qB^2} [v_{\parallel}^2 \frac{\vec{R} \times \vec{B}}{R^2} + \frac{v_{\perp}^2}{2} (\frac{\vec{B}}{B} \times \nabla B)] . \quad (2.23)$$

Assuming typical parameters for JET ( $B_{\phi} = 2[T]$ ,  $R = 3[m]$ ,  $a = 1[m]$   $T_e \approx 10[eV]$  and  $v_{\parallel}^2 \approx v_{\perp}^2 \approx \frac{3kT_e}{2m}$ ), we can estimate  $v_d$  as  $3.7[m/s]$ . Then, the characteristic time of vertical drift loss  $\tau_d$  is

$$\tau_d = \frac{a}{v_d} \approx 270[ms] . \quad (2.24)$$

During the electron avalanche phase, the magnetic field has the open field configuration, due to the stray (or error) magnetic fields. The parallel transport of the particles along the open magnetic field lines, which are connected to the vacuum vessel, result in significant particle losses. The effective connection length  $L_f$  in tokamaks is calculated as [10]

$$L_f \equiv 0.25 \frac{aB_{\phi}}{B_{\perp}} \quad (2.25)$$

where 0.25 is a correction factor to take into account the distance between the actual avalanche position and the wall.  $a$  is a plasma minor radius, and  $B_{\phi}$  and  $B_{\perp}$  are the toroidal and perpendicular magnetic fields, respectively. The electron loss due to the parallel transport can be estimated using the effective connection length  $L_f$  and the mean electron velocity  $u_e$  in Equation (2.20). Assuming typical parameters for JET ( $B_{\phi} = 2[T]$ ,  $B_{\perp} \approx$  vertical magnetic field  $B_z = 0.001[T]$ ,  $a = 1[m]$   $E \approx 1[V/m]$  and,  $p \sim 10^{-5}[Torr]$ ) we can estimate  $\tau_z$  as  $0.12[ms]$ ,

$$\tau_z = \frac{L_f}{u_e} \approx 0.12[ms] . \quad (2.26)$$

Comparison of  $\tau_d$  in Equation (2.24) and  $\tau_z$  in Equation (2.26) shows that the drift loss in JET is small enough to neglect compared to the parallel transport loss. Thus, the total particle loss

rate  $\beta_{loss}$  can be approximated to  $\beta_z$ ,

$$\beta_z[sec^{-1}] \approx \frac{u_e}{L_f} . \quad (2.27)$$

It is necessary for electron avalanche that the ionization rate  $\nu_{iz}$  exceeds the electron loss rate  $\beta_z$ . The electron loss rate  $\beta_z (= 1/\tau_e = 1/0.00012)$  is about  $8333[s^{-1}]$ , which is smaller than the ionization rate  $\nu_{iz} \sim 20000[s^{-1}]$  calculated using Equation (2.22). This is consistent with the fact that the operation parameters assumed for the calculation are the typical values generating electron avalanche in JET.

By substituting  $\nu_{iz} = \beta_z$  with Equation (2.22) and Equation (2.27), we can have the required condition for electron avalanche in tokamaks,

$$\alpha L_f = 1 . \quad (2.28)$$

$\alpha$  is the number of ionization by an electron in a unit distance, and  $L_f$  is the traveling length of an electron since the electron motion are guided toward the wall by the open magnetic field lines.

The first townsend coefficient  $\alpha$  in (2.28) is substituted with (2.6), and the minimum electric field for electron avalanche can be obtained as,

$$Ap \exp\left(\frac{-B}{E/p}\right)L_f = 1$$

$$E_{min}[V/m] = \frac{Bp}{\ln(ApL_{eff})} . \quad (2.29)$$

Substituting constant  $A$  and  $B$  with  $A = 510[m^{-1}torr^{-1}]$ ,  $B = 1.25 \times 10^4[Vm^{-1}torr^{-1}]$  assuming hydrogen isotope as prefill gas, we can have

$$E_{min}[V/m] = \frac{1.25 \times 10^4 p[torr]}{\ln(510 \times p[torr]L_f[m])} . \quad (2.30)$$

Equation (2.30) was used to calculate the required electric field for electron avalanche in ITER. Figure 2.5 is the operation space for various effective connection length  $L_f$ , provided in the ITER physics basis [4] published in 1999.

## 2.4 Discussion

Figure 2.5 indicates that there is an optimum intermediate range of prefill gas pressure to minimize the required electric field for electron avalanche. In addition, Figure 2.5 shows that

the required electric field decreases as  $L_f$  increases. This implies that in ITER, where the toroidal electric field available is very low, it is important to reduce the stray (or error) magnetic field so that the effective connection length is maximized.

Although Equation (2.30) indicates the required electric field as a function of  $p$  and  $L_f$ , it is difficult to predict the accurate value of  $E_{min}$  due to the uncertainty of  $L_f$ , resulting from the eddy currents. To obtain accurate values of eddy currents needs calculations, using all three dimensional passive structures in tokamaks.

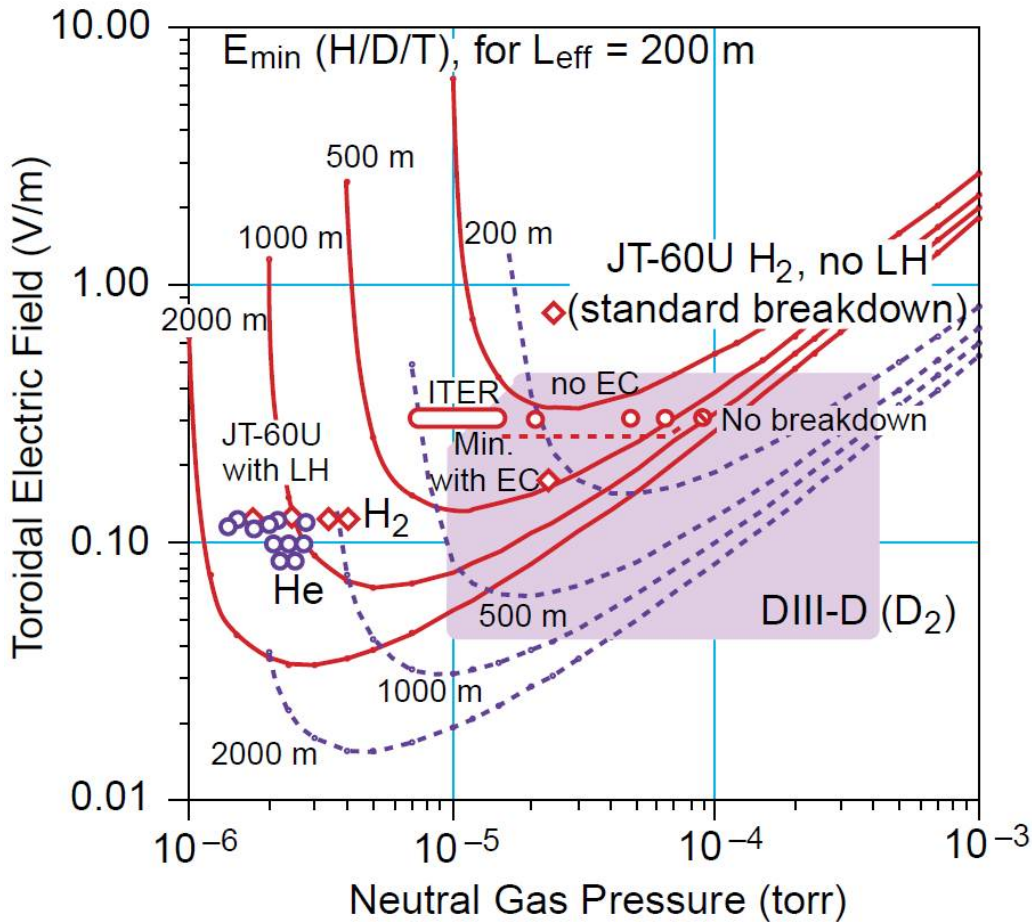


Figure 2.5: Minimum electric fields for electron avalanche in hydrogen isotope gas (solid lines) and in helium (dashed lines), for various effective connection length  $L_f$ . The experimental data for unassisted (ohmic) and RF-assisted start-up in DIII-D [11] and JT-60U [23] are superposed. Proposed parameters for ITER start-up are also indicated. The shaded domain represent the typical parameters for DIII-D start-up. The red dashed line labelled ‘Min.’ is the lowest electric field at which unassisted start-up in DIII-D is possible.[4]



It is well known that pre-ionization using external RF power in a gas enables electron avalanche with a low electric field [11]. In order to ensure a reliable tokamak start-up in ITER even for a pessimistic  $L_f$ , ECH<sup>5</sup>-assisted start-up [5] (or ICH<sup>6</sup>-assisted start-up [16][17]) has been proposed.

---

<sup>5</sup>Electron Cyclotron Heating

<sup>6</sup>Ion Cyclotron Heating

# Chapter 3

## Plasma burn-through simulation

### 3.1 Introduction

It has been observed that most failures in tokamak start-up occur during the plasma burn-through phase. However, our understanding of plasma burn-through is limited, and tokamak start-up has relied on trial and error methods without investigation on the physics of plasma burn-through. The plasma burn-through modelling is a very useful tool to understand the key physics aspects in the burn-through phase, and it will make a contribution to ensuring a reliable tokamak start-up and can be used in reducing flux consumption of the ohmic transformer at the start of the plasma discharge in tokamaks. Plasma burn-through modelling can also be a basis for the research on non-inductive start-up (or solenoid-free start-up), which are of crucial importance for a fusion power plant.

In ITER, the allowable toroidal electric field for start-up is limited up to  $0.35[V/m]$  due to the engineering issues explained in section 1.2. Since tokamak start-up using such a low  $E$  field is only possible for a narrow range of prefill gas pressure, low magnetic error fields, and low impurity content, RF-assisted start-up [5] has been proposed in ITER. In order to estimate the required RF power, plasma burn-through in ITER was modelled [6] [20]. However, the previous models were overly simplified, and furthermore, they have never been validated against experimental data. In this section, the basic structure of plasma burn-through modelling and the enhancement in the DYON code are introduced. The validation of the models and simulations

with experimental data is presented in chapter 6 (section 6.3).

The detailed explanation on plasma burn-through modelling is provided in section 3.2, and key features of the previous models are reviewed in section 3.3. Section 3.4 presents the new models in detail. Section 3.5 describes the plasma burn-through simulator, the DYON code. Section 3.6 discusses the underlying assumptions in the DYON code.

## 3.2 Basic structure of plasma burn-through simulator

In this chapter, all physical quantities are expressed in SI units except for the prefill gas pressure. A prefill gas pressure is indicated in [Torr]. Temperatures in the equations are written in [Joules]. Whenever the temperature given is in [eV], this is explicitly stated.

### 3.2.1 Circuit equation for plasma current

Assuming a plasma as a circular current loop, the plasma current  $I_p$  can be calculated using the circuit equation.

$$U_l = I_p R_p + L_p \frac{dI_p}{dt} \quad (3.1)$$

where  $U_l$  is a toroidal loop voltage, induced by the external coil voltage. In this section, the self-inductance  $L_p$  and electric resistance  $R_p$  of a plasma are derived, respectively.

#### Plasma inductance

Inductance can be calculated from the relation of electric current and the stored magnetic energy in electromagnetics,

$$\frac{1}{2} L I^2 = \int_V \frac{B^2}{2\mu_0} dV \quad (3.2)$$

Derivation of inductance requires surprisingly lengthy calculations depending on the coil geometry, but it is well known that the electric inductance of a circular current loop is

$$L = \mu_0 R \left( \ln \frac{8R}{a} - 2 + Y \right), \quad (3.3)$$

where  $a$  is a minor radius,  $R$  is a major radius, and  $Y$  is a function of the current profile in the coil (plasma cross-section)<sup>1</sup>.  $Y$  represents how much magnetic energy ( $= B^2/2\mu$ ) is stored within the coil. When the electric current is uniformly distributed over the surface of the coil (no magnetic energy within the coil),  $Y = 0$ .

Equation (3.3) can be applied to calculate the inductance  $L_p$  of the plasma current.  $L_p$  can be separated into two parts,

$$L_p = L_e + L_i. \quad (3.4)$$

$L_e$  is external inductance which is related to the magnetic energy stored in the external volume (outside the coil),

$$L_e = \mu_0 R \left( \ln \frac{8R}{a} - 2 \right). \quad (3.5)$$

The inductance  $L_i$  represents the stored magnetic energy within the plasma volume, and is defined as

$$L_i = \mu_0 R Y. \quad (3.6)$$

$Y$  (and in turn  $L_i$ ) for a plasma current can be derived using Equation (3.2),

$$\frac{1}{2} L_i I_p^2 = \int_{\text{plasma volume}} \frac{B_\theta(x, y, z)^2}{2\mu_0} dx dy dz, \quad (3.7)$$

where  $B_\theta$  is the poloidal magnetic field, produced by a plasma current. In order to integrate  $B_\theta$  over the plasma volume, which is a torus, we should change the rectangular coordinate to be suitable for the integration of the torus volume,

$$\begin{aligned} (x, y, z) &\rightarrow (R\phi, r, \theta) \\ dx dy dz &\rightarrow R d\phi dr r d\theta \end{aligned} \quad (3.8)$$

where  $\phi$  and  $\theta$  are the toroidal and poloidal angle, and  $R$  and  $r$  are the length in directions of major radius and minor radius, respectively. Then, assuming toroidal symmetry,  $dB_\theta(R\phi, r, \theta)/d\phi = 0$ , we can have

$$\begin{aligned} \frac{1}{2} L_i I_p^2 &= \int_0^a \int_0^{2\pi} \int_0^{2\pi} \frac{B_\theta(R\phi, r, \theta)^2}{2\mu_0} R r d\phi dr d\theta \\ &= 2\pi \int_0^a \int_0^{2\pi} \frac{B_\theta(r, \theta)^2}{2\mu_0} R r dr d\theta. \end{aligned} \quad (3.9)$$

---

<sup>1</sup><http://en.wikipedia.org/wiki/Inductance>

We assume a plasma current in a circular cross-section and assume poloidal symmetry i.e.  $dB_\theta(r, \theta)/d\theta = 0$ . Then, Equation (3.9) is

$$\frac{1}{2}L_i I_p^2 = 4\pi^2 \int_0^a \frac{B_\theta(r)^2}{2\mu_0} R r dr . \quad (3.10)$$

Using Ampere's law, i.e.  $\nabla \times B_\theta = \mu_0 J_p$ , we can substitute  $I_p$  in Equation (3.10) with

$$I_p = \frac{2\pi a B_\theta(a)}{\mu_0} , \quad (3.11)$$

then,  $L_i$  and  $Y$  can be obtained as

$$\begin{aligned} L_i &= \mu_0 R \times \frac{\int_0^a B_\theta(r)^2 r dr}{a^2 B_\theta^2(a)} \\ Y &= \frac{\int_0^a B_\theta(r)^2 r dr}{a^2 B_\theta^2(a)} \end{aligned} \quad (3.12)$$

In plasma physics, it is conventional to express the plasma inductance  $L_p$  using a dimensionless normalized plasma inductance  $l_i^2$ ,

$$L_p = \mu_0 R \left( \ln \frac{8R}{a} - 2 + \frac{l_i}{2} \right) \quad \text{where} \quad l_i = \frac{2 \int_0^a B_\theta(r)^2 r dr}{a^2 B_\theta^2(a)} . \quad (3.13)$$

In the case of a flat profile of the plasma current,  $B_\theta(r)$  can be substituted using the constant plasma current density  $J_p$ ,

$$B_\theta(r) = \frac{\mu_0 J_p \pi r^2}{2\pi r} . \quad (3.14)$$

Then,  $l_i$  for a uniform plasma current is

$$l_i = \frac{2 \int_0^a \left( \frac{\mu_0 J_p \pi r^2}{2\pi r} \right)^2 dr}{a^2 \left( \frac{\mu_0 J_p \pi a^2}{2\pi a} \right)^2} = \frac{2 \int_0^a r^3 dr}{a^4} = 0.5 . \quad (3.15)$$

## Plasma resistance

We can derive the plasma resistance  $R_p$  assuming that coulomb collisions are dominant compared to electron-neutral collisions. The derivation begins from the fluid equation of motion for electrons,

$$m_e n_e \frac{d\vec{u}_e}{dt} = -en_e (\vec{E} + \vec{u}_e \times \vec{B}) - \nabla p_e + \vec{F}_{e-i} \quad (3.16)$$

---

<sup>2</sup>In tokamak research,  $l_i$  is often called internal inductance.

where  $\vec{F}_{e-i}$  is the friction force, which results from collisional transfer of momentum between electron and ion, and  $\vec{u}_e$  is the fluid velocity of electrons ( $\vec{u}_i$  is ion fluid velocity). Defining momentum transfer frequency of an electron  $\nu_{e-i}^m$ ,  $\vec{F}_{e-i}$  can be expressed as

$$\vec{F}_{e-i} = m_e n_e (\vec{u}_i - \vec{u}_e) < \nu_{e-i}^m >, \quad (3.17)$$

where  $< \nu_{e-i}^m >$  is an average value of  $\nu_{e-i}^m$  in the fluid. Assuming uniform electron pressure ( $\nabla p_e = 0$ ), parallel fluid velocity to the electric field and the magnetic field ( $\vec{u}_e \parallel \vec{u}_i \parallel \vec{E}$ ,  $\vec{u}_e \times \vec{B} = 0$ ), and small electron inertia term ( $m_e n_e \frac{d\vec{u}_e}{dt} = 0$ ), Equation (3.16) can be reduced to

$$en_e E = m_e n_e (u_i - u_e) < \nu_{e-i}^m > \quad (3.18)$$

The electric resistivity is a function of the electric current and the electric field,  $\eta = \frac{E}{J}$ . Substituting J and E with  $en_e(u_i - u_e)$  and Equation (3.18), the electric resistivity  $\eta_{e-i}$  due to the e-i collisions can be obtained,

$$\eta_{e-i} = \frac{E}{J} = \frac{m_e < \nu_{e-i}^m >}{e^2 n_e}. \quad (3.19)$$

For a deuterium plasma,  $\nu_{e-i}^m$  is a product of  $n_i$  (ion density),  $\sigma_{e-i}^m$  (cross-section for collisional momentum transfer), and  $v_e$  (velocity of an electron),

$$\nu_{e-i}^m = n_i \sigma_{e-i}^m v_e. \quad (3.20)$$

$\sigma_{e-i}^m$  can be calculated with the impact parameter  $b_0$  which is defined as a distance between an electron and an ion when electrons have a 90 scattering coulomb collision.<sup>3</sup>

$$b_0 = \frac{e^2}{4\pi\epsilon_0 m_e (v_e)^2}. \quad (3.21)$$

Then,  $\sigma_{e-i}^m$  equals  $\pi b_0^2 \times (4 \ln \Lambda)$ ,

$$\sigma_{e-i}^m = \pi \left( \frac{e^2}{4\pi\epsilon_0 m_e (v_e)^2} \right)^2 \times 4 \ln \Lambda \quad (3.22)$$

where  $(4 \ln \Lambda)$  is a correction factor to include the cumulative effect of many small-angle deflections. The coulomb logarithm  $\ln \Lambda$  is insensitive to plasma parameters ( $\ln \Lambda \approx 10$ ), and is defined by  $\ln(\lambda_D/b_0)$ .<sup>4</sup>

Substituting  $\sigma_{e-i}^m$  in Equation (3.20) with Equation (3.22), we can have

$$\begin{aligned} \nu_{e-i}^m &= n_i \times \pi \left( \frac{e^2}{4\pi\epsilon_0 m_e (v_e)^2} \right)^2 \times 4 \ln \Lambda \times v_e \\ &= \frac{n_i e^4 \ln \Lambda}{4\pi\epsilon_0^2 m^2 v_e^3}. \end{aligned} \quad (3.23)$$

<sup>3</sup>The derivation of  $b_0$  can be found in standard textbooks in classical mechanics.

<sup>4</sup> $\lambda_D$  is the Debye length.

Since  $\nu_{e-i}^m$  is a function of  $v_e^{-3}$ ,  $\langle \nu_{e-i}^m \rangle$  must be calculated using a distribution function. The detailed derivation of  $\langle \nu_{e-i}^m \rangle$  using Equation (3.23) for a Maxwellian distribution is well described in [24]. Defining  $v_e^{th} = \sqrt{T_e/m_e}$ , the average value of the momentum collision frequency  $\langle \nu_{e-i}^m \rangle$  is

$$\langle \nu_{e-i}^m \rangle = \frac{n_i e^4 \ln \Lambda}{6\sqrt{2}\pi^{3/2}\epsilon_0^2 m^{1/2} (T_e)^3}. \quad (3.24)$$

The plasma resistivity  $\eta_{e-i}$  can be calculated by substituting the momentum transfer frequency  $\nu_{e-i}^m$  in Equation (3.19) with Equation (3.24),

$$\begin{aligned} \eta_{e-i} &= \frac{m_e \langle \nu_{e-i}^m \rangle}{e^2 n_e} = \frac{m_e}{e^2 n_e} \times \frac{n_i e^4 \ln \Lambda}{6\sqrt{2}\pi^{3/2}\epsilon_0^2 m_e^{1/2} (T_e)^3} \\ &= \frac{m_e^{1/2} e^2 \ln \Lambda}{6\sqrt{2}\pi^{3/2}\epsilon_0^2 (T_e)^{3/2}}. \end{aligned} \quad (3.25)$$

In order to calculate an accurate plasma resistivity, e-e collisions should also be considered. Spitzer and co-workers have found the correction factor for this as 0.51. Hence, accurate resistivity in a deuterium plasma i.e. *Spitzer resistivity*  $\eta_s$  is

$$\begin{aligned} \eta_s &= 0.51 \frac{m_e^{1/2} e^2 \ln \Lambda}{6\sqrt{2}\pi^{3/2}\epsilon_0^2 (T_e)^{3/2}} \\ &\approx 5 \times 10^{-5} \times \ln \Lambda \times T_e^{-3/2} [eV]. \end{aligned} \quad (3.26)$$

In the case of impurities in a plasma,  $\eta_s$  should be modified to  $Z_f \eta_s$  where  $Z_f$  is an effective charge, defined as [1]

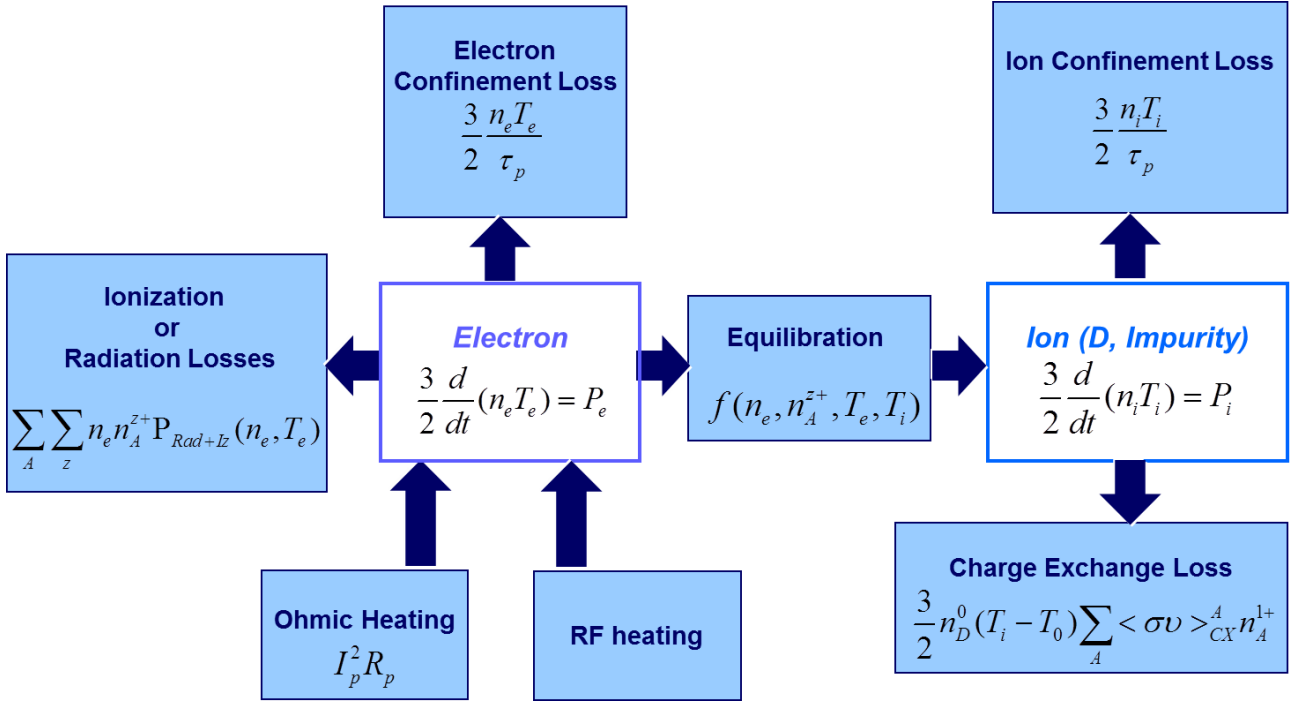
$$Z_f = \frac{\sum_A \sum_z n_A^{z+} z^2}{\sum_A \sum_{z \geq 1} n_A^{z+} z} \quad (3.27)$$

where subscript  $A$  represents deuterium or an impurity.  $z$  means an ionic charge state. Accordingly,  $n_A^{z+}$  indicates deuterium ion density  $n_D^{1+}$  or impurity ion densities  $n_I^{z+}$  with charge state  $z$ .

Plasma resistance  $R_p$  is a function of plasma resistivity  $\eta_s$  and the size of the current loop (cross-section  $A$  and length  $l$ ),

$$\begin{aligned} R_p &= Z_f \eta_s \frac{l}{A} = Z_f \eta_s \frac{2\pi R}{\pi a^2} \\ &= 5 \times 10^{-5} \times \ln \Lambda \times Z_f \times \frac{2R}{a^2} \times T_e^{-3/2} [eV] \end{aligned} \quad (3.28)$$

where  $R$  and  $a$  are the major and minor radius of the plasma.

Figure 3.1: *Energy flow in a plasma*

### 3.2.2 Electron energy balance

It should be noted that plasma resistance  $R_p$  is a function of electron temperature  $T_e$  and effective charge  $Z_f$ . In order to calculate  $I_p$  with (3.1),  $T_e$  and  $Z_f$  should be obtained by solving the energy and particle balance equations.

Figure 3.1 shows how energy flows in a plasma through various heating and loss channels. The net heating power i.e.  $P_{heating} - P_{loss}$  remains as the internal energy of the plasma,  $\frac{3}{2}n_e T_e$  and  $\frac{3}{2}n_i T_i$ . Assuming a uniform plasma density and temperature, we can calculate the electron energy balance equation,

$$\frac{3}{2} \frac{d(n_e T_e)}{dt} = P_{oh} + P_{aux} - (P_{iz} + P_{rad}) - P_{equi} - P_{conv}^e \quad (3.29)$$

where  $P_{oh}$  and  $P_{aux}$  are ohmic heating and auxiliary heating such as ECH or ICH. Electron power losses in Equation (3.29) consist of collisional ionization power loss  $P_{iz}$ , radiation power loss  $P_{rad}$ , equilibration power loss  $P_{equi}$ , and convective transport power loss  $P_{conv}^e$ . Each term is explained below in detail.



### Electron heating power

Ohmic heating  $P_{oh}$  is the main electron heating source, and all ohmic heating power is assumed to be absorbed by electrons without ion heating. Ohmic heating power per unit volume is

$$P_{oh} = \frac{I_p^2 R_p}{V_p}, \quad (3.30)$$

where  $V_p$  is the plasma volume [6].

Since most simulations in this thesis are for ohmic start-up cases (no RF assist), we set  $P_{aux} = 0$ . In order to provide more input power to ensure robust tokamak start-up, auxiliary heating such as Electron cyclotron Heating (ECH) or Ion Cyclotron Heating (ICH) is planned for ITER. The auxiliary heating power  $P_{aux}$  to the plasma is a complicated function of various plasma parameters. For RF-assisted start-up for ITER, we will assume  $P_{aux}$  as a constant (in time and over the plasma volume) absorbed heating power.

### Electron power losses

The collisional ionization process is a power loss mechanism from an electron point of view since a free electron loses their kinetic energy as much as the binding energy of an electron in an atom [6]. Therefore, collisional ionization power loss  $P_{iz}$  is

$$P_{iz} = \frac{V_n^A}{V_p} \sum_A \langle \sigma v \rangle_{A,iz}^{0 \rightarrow 1+} W_A^{0 \rightarrow 1+} n_e n_A^0 + \sum_A \sum_{z \geq 1} \langle \sigma v \rangle_{A,iz}^{z+ \rightarrow (z+1)+} W_A^{z+ \rightarrow (z+1)+} n_e n_A^{z+} \quad (3.31)$$

where  $W_A^{z+ \rightarrow (z+1)+}$  is the ionization energy required to ionize an atom or a non-fully ionized ion from  $z+$  to an  $(z+1)+$ . Here  $V_n^A$  represents a neutral volume of species  $A$  within a plasma volume. Since the ionization reaction of neutrals can occur only in the neutral volume within a plasma volume, the different volume occupied by neutrals or ions must be taken into account. The first term on the right-hand-side in Equation (3.31) is the electron power loss required to ionize neutrals. The second term is for further ionization of non-fully ionized ions to higher charge states. The detailed explanation for  $V_n^A$  (the neutral screening effect) will be discussed in section 3.4.6.

$\langle \sigma v \rangle_{A,iz}^{0 \rightarrow 1+}$  and  $\langle \sigma v \rangle_{A,iz}^{z+ \rightarrow (z+1)+}$  are ionization rate coefficients. In this thesis, the reaction rate coefficients and power coefficients are expressed as  $\langle \sigma v \rangle$ . Their superscript indicates

the change of the ion charge in the atomic reaction, the subscripts represent the species of the reaction particle and the kind of the reaction. For example,  $\langle \sigma v \rangle_{A,rec}^{z+\rightarrow(z-1)+}$  indicates a recombination rate coefficient of species  $A$  of which the ionic charge transits to  $(z-1)+$  from  $z+$  through a recombination reaction. In the case of charge exchange reaction, the subscript is  $cx$ .  $\langle \sigma v \rangle_{A,line}^{z+}$  is a power coefficient for line radiation and  $\langle \sigma v \rangle_{A,RB}^{z+\rightarrow(z-1)+}$  is a power coefficient for Recombination and Bremsstrahlung radiation. The rate coefficients and power coefficients used in the burn-through simulation are obtained from Atomic Data and Analysis Structure (ADAS) package<sup>5</sup>. The ADAS atomic rate coefficients are based on the generalised collisional-radiative theory, and the data can cover various range of plasmas e.g. space plasma, industrial plasma, and the thermonuclear fusion plasma in current devices. It is assumed in the ADAS data that the free electrons have a Maxwellian velocity distribution and the dominant populations of impurities are in the quasi-equilibrium i.e. the ground and metastable states. Further information about the rate and power coefficients in ADAS is available in H. P. Summers's paper published in 2006 [25].

If there is a collisional excitation of an atom or an ion, a free electron also loses its kinetic energy. In the case of optically thin plasma (no reabsorption of photons in the plasma), which is assumed in this thesis, the amount of the electron power loss for collisional excitations is equal to the subsequent line radiation power [6]. The electron power loss resulting from the electron deceleration due to the background ions is also equal to the Bremsstrahlung radiation power loss [6]. However, in the case of recombination, the radiation power loss is greater than the electron power loss for the recombination reactions since the potential energy in an atom or an ion is included in the total recombination radiation power [6]. Therefore, this amount must be subtracted from the total recombination radiation power in order to calculate the electron power loss. The total electron power loss through radiation is

$$P_{rad} = \sum_A \frac{V_n^A}{V_p} \langle \sigma v \rangle_{A,line}^0 n_e n_A^0 + \sum_A \sum_{z \geq 1} (\langle \sigma v \rangle_{A,line}^{z+} + \langle \sigma v \rangle_{A,RB}^{z+\rightarrow(z-1)+} - \langle \sigma v \rangle_{A,rec}^{z+\rightarrow(z-1)+} W_A^{(z-1)+ \rightarrow z+}) n_e n_A^{z+}. \quad (3.32)$$

As in Equation (3.31), the first term and the second term in Equation (3.32) indicates the line radiation power losses from the neutral and the non-fully ionized ions, respectively.

Electrons also lose energy through elastic coulomb collisions with ions, i.e. the equilibration

---

<sup>5</sup><http://open.adas.ac.uk>

process. The equilibration power loss  $P_{equi}$  is a power loss term from electron's point of view for  $T_e > T_i$ , which is typical for the plasma formation phase. The formula for  $P_{equi}$  is well known as

$$P_{equi} = 7.75 \times 10^{-34} (T_e[eV] - T_i[eV]) \frac{n_e \ln \Lambda}{T_e^{3/2}[eV]} \left( \sum_A \sum_{z \geq 1} \frac{n_A^{z+} z^2}{M_A} \right) \quad (3.33)$$

where  $M_A$  is ion mass of each species in *amu* [6].

When electrons are transported out of a plasma, they take their kinetic energy to the surrounding wall i.e. convection loss. Electron convective transport power loss  $P_{conv}^e$  can be calculated using the confinement time of electrons  $\tau_e$  as

$$P_{conv}^e = \frac{3 n_e T_e}{2 \tau_e}. \quad (3.34)$$

In the model, ambipolar transport to the wall is assumed. Hence,  $\tau_e$  is equal to deuterium confinement time  $\tau_D$  in the model. The details of particle confinement time will be discussed in section 3.4.3.

### 3.2.3 Ion energy balance

Ions are assumed to be heated only by equilibration with electrons and lose energy through charge exchange reactions and ion convective transport [6]. The ion energy balance equation is [6]

$$\frac{3}{2} \frac{d(n_i T_i)}{dt} = P_{equi} - P_{CX} - P_{conv}^i. \quad (3.35)$$

where the ion density  $n_i$  and temperature  $T_i$  are defined to be

$$n_i = n_D^{1+} + \sum_I \sum_{z \geq 1} n_I^{z+} \quad (3.36)$$

$$T_i = T_D^{1+} = T_I^{z+}. \quad (3.37)$$

where  $n_D^{1+}$  and  $n_I^{z+}$  are deuterium ion density and impurity ion density with charge stage  $z+$ .  $T_D^{1+}$  and  $T_I^{z+}$  are deuterium ion temperature and impurity ion temperature with charge stage  $z+$ .

The ion energy loss in a charge exchange reaction is equal to the energy difference between the energetic ion (a deuterium ion or an impurity ion) and the lower-energy deuterium atom [6],

which is assumed to be at room temperature, i.e.  $T_0 = 0.026[eV]$ . In this model, deuterium is assumed to be the only electron donor for charge exchange reactions. Therefore, charge exchange reactions occur only in a deuterium neutral volume within a plasma volume,  $V_n^D$ . Accordingly, the ion power loss due to a charge exchange reaction is

$$P_{cx} = \frac{V_n^D}{V_p} \left( \frac{3}{2} n_D^0 (T_i - T_0) \sum_A \langle \sigma v \rangle_{A,cx}^{1+\rightarrow 0} n_A^{1+} \right). \quad (3.38)$$

As in Equation (3.34), the ion convective transport power loss  $P_{conv}^i$  can be calculated as

$$P_{conv}^i = \sum_A \sum_{z \geq 1} \frac{3}{2} \frac{n_A^{z+} T_i}{\tau_D}, \quad (3.39)$$

where  $\tau_D$  is the ion confinement time.

### 3.2.4 Particle balance

As shown in Equations (3.31) to (3.39), there are many density terms in the computations of electron energy balance and ion energy balance. This requires the particle balance equations to be solved simultaneously. Figure 3.2 shows how particles flow in a plasma. The deuterium neutrals are injected into a vacuum vessel by gas fuelling. In the model, we assume full dissociated deuterium gas as an initial condition. The deuterium atoms are ionized by the induced toroidal electric field. The deuterium ions are transported out of the plasma, generating recycling or sputtering at the wall. The deuterium neutrals released from the wall are ionized in the plasma. Deuterium ions also capture free electrons (i.e. recombination) or bound electrons from other deuterium atoms (i.e. charge exchange). The impurities resulting from the plasma wall interaction are also important, but the particle balance is more complicated due to the various charge states. The particle balance of impurities will be given in section 3.4.7.

#### Deuterium atom particle balance

Deuterium atoms are supplied by gas fuelling or generated by recombination. The deuterium atoms are ionized by collisional ionizations or charge exchange with impurities. Since we assume

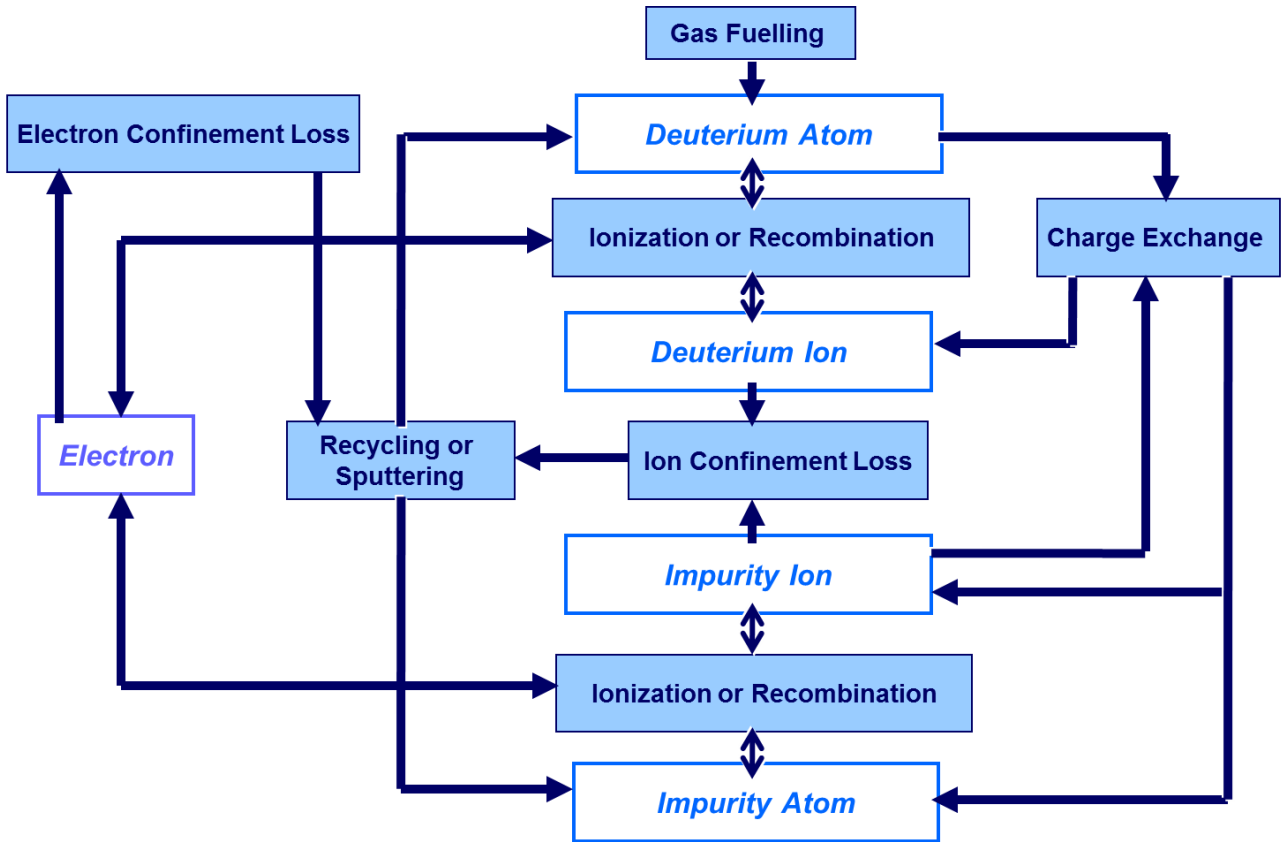


Figure 3.2: Particle flow in a plasma

the backscattering coefficient of a deuterium atom at the wall is 1, the transport term is not included in the deuterium atom particle balance.

The particle balance equation of neutral deuterium atoms is given by:

$$\frac{dn_D^0}{dt} = \frac{1}{\gamma_n^D V_V} (V_p \langle \sigma v \rangle_{D,rec}^{1+\rightarrow 0} n_e n_D^{1+} - V_n^D \langle \sigma v \rangle_{D,iz}^{0\rightarrow 1+} n_e n_D^0 - V_n^D \sum_I \sum_{z \geq 1} \langle \sigma v \rangle_{I,cx}^{z+\rightarrow (z-1)+} n_D^0 n_I^{z+}) + \frac{\Gamma_{D,in}^{total}}{\gamma_n^D V_V}, \quad (3.40)$$

where the total influx of deuterium atoms  $\Gamma_{D,in}^{total}$  is

$$\Gamma_{D,in}^{total} = V_p \frac{Y_D^D n_D^{1+}}{\tau_D}. \quad (3.41)$$

In Equation (3.40),  $\gamma_n^D$  is a neutral volume coefficient.  $\gamma_n^D V_V$  is the total neutral deuterium volume including the neutral volume within the plasma volume. The formula of  $\gamma_n^D$  is given in section 3.4.6.

### Deuterium ion particle balance

Deuterium ions are produced by ionization or charge exchange between deuterium atoms and impurity ions. Ion transport to the wall and recombination are ion particle losses. The particle balance equation of deuterium ions is given by:

$$\begin{aligned} \frac{dn_D^{1+}}{dt} = & \frac{V_n^D}{V_p} \langle \sigma v \rangle_{D,iz}^{0 \rightarrow 1+} n_e n_D^0 - \langle \sigma v \rangle_{D,rec}^{1+ \rightarrow 0} n_e n_D^{1+} \\ & + \frac{V_n^D}{V_p} \sum_I \sum_{z \geq 1} \langle \sigma v \rangle_{I,cx}^{z+ \rightarrow (z-1)+} n_D^0 n_I^{z+} - \frac{n_D^{1+}}{\tau_D}. \end{aligned} \quad (3.42)$$

### Electron particle balance

On the condition of charge neutrality, an electron density is calculated using each ion density [6],

$$n_e = \sum_A \sum_{z \geq 1} z n_A^{z+}. \quad (3.43)$$

## 3.3 Review of the previous models

The zero dimensional energy and particle balance model for a burn-through simulation has been presented by [6], [19], and [20]. However, the simpler confinement time and impurity models were deployed in earlier work.

### 3.3.1 Confinement time model

In the 0D code [6], the energy confinement time  $\tau_E$  was calculated with the INTOR scaling law, in which  $\tau_E$  was simply proportional to electron density  $n_e$ , i.e.  $\tau_E[s] \equiv 5 \times 10^{-21} \tau_0 n_e [m^{-3}]$  where  $\tau_0$  is a multiplier ( $\tau_0 \approx 0.2 \sim 2$ ). In addition, the particle confinement time  $\tau_p$  was treated as a constant parameter ( $\tau_p \approx 5 \sim 50 [ms]$ ).

### 3.3.2 Impurity model

The impurity content, which is one of the important parameters determining the burn-through criterion, was assumed to be constant in the 0D code used in [6]. The evolution of an impurity content in a plasma was treated in the SCENPLINT code [5][19][20] with an exponentially growing function, i.e. for carbon impurities,  $n_c/n_e \equiv 0.013 + 0.03((1 - \exp(-t[s]/0.25)))$ .

## 3.4 New models for plasma burn-through simulation

The models used in the simulations for plasma burn-through have been extended. One of the crucial features, which must be taken into account to calculate the particle confinement time in the burn-through phase, is the transition of magnetic field configuration, i.e. the change from the open field line configuration to the closed flux surfaces (CFS). This transition results in the change of dominant particle loss mechanism, i.e. the change of dominant particle loss to perpendicular transport from parallel transport, hence, the dynamics of effective connection length must be modelled as well.

In the new burn-through simulations, it is assumed that a parallel particle loss in the burn-through phase is dominated by a convective transonic ambipolar flow along a magnetic field line to the vessel wall as used in divertor-SOL plasma simulations [26]. Accordingly, parallel transport losses are calculated with a finite effective connection length  $L_f$  and an ion sound speed  $C_s$ . Regarding the perpendicular particle loss, the Bohm diffusion model is adopted. The particle confinement time is calculated by combining these transport mechanisms.

In the case of JET, it is generally observed that magnetic configuration forms closed magnetic surfaces at around 100 [kA] plasma current. According to this, the evolution of an effective connection length is modelled with an exponential term approaching an infinite value from 100 [kA] of plasma current. In addition, once a toroidal electric field is induced for plasma break-down, there can be significant eddy currents, thereby decreasing the effective connection length. In JET, most eddy currents in this phase flow through the support ring of the divertor tiles (MK2) due to its relatively low electric resistance. This effect is considered with a two ring model, i.e. plasma current ring and MK2 current ring. The details of the calculation will be presented in section 3.4.2.

Secondly, the previous treatments of impurities were overly simplified. The impurity content in the plasma is significantly affected by the wall material and ion transport. Therefore, *Plasma Wall Interaction (PWI)* must be included with more sophisticated models. In order to model the impurity evolution in the burn-through phase, new models of particle transport and PWI have been added to B. Lloyd's model.

Plasma Wall Interaction is modelled with a wall-sputtering yield according to the type of incident ions. In a carbon-wall (used up to 2009 in JET), chemical sputtering is dominant, a carbon sputtering yield due to a deuterium ion or an oxygen ion is assumed to be constant, based on experimental data [27]. In the ITER-like wall (with a *Be* first wall), physical sputtering is dominant, and the formula for physical sputtering yield is presented in [28] and [29].

The recycling coefficient of incident deuterium ions is modelled with an exponential saturation function to take into account the dynamic behaviour of the deuterium recycling coefficient. The recycling coefficients of impurities are assumed to be constant according to their volatility. Detailed explanations on PWI models in the carbon wall and ITER-like wall are given in chapter 5.

Another important feature in the burn-through phase is a low electron temperature, less than 100 [eV]. This requires sophisticated calculations of atomic reactions in each ionic charge state of deuterium and impurities. By using the ADAS rate and power coefficients [25], energy and particle balance equations in each ionic charge state of deuterium and impurities are solved in a matrix form.

As the electron density increases in the burn-through phase, the mean free path for neutral ionization decreases, thereby reducing the neutral volume within a plasma. This neutral screening effect is taken into account according to particle species. These more sophisticated energy and particle balance equations for impurities will be presented in section 3.4.7.

### 3.4.1 Circuit equation for eddy current

When a loop voltage is applied by a transformer action in tokamaks, an eddy current is induced in the vessel since the electric resistance of the vessel is comparable with that of plasma column. Until the plasma resistance becomes much smaller than the vessel's electric resistance, the effect



	$L[H]$	$M[H]$	$R[\Omega]$
Plasma	$6.09 \times 10^{-6}$	$2.49 \times 10^{-6}$	$R_p(T_e, Z_f)$
MK2	$9.1 \times 10^{-6}$	$2.49 \times 10^{-6}$	$7.5 \times 10^{-4}$

Table 3.1: *Inductances and resistances of a plasma current ring and a MK2 current ring for JET*

of eddy current can be significant. In the case of JET, the MK2 ring, which is the mechanical support structure for the divertor, has the lowest electric resistance. The MK2 current  $I_{MK2}$  and plasma current  $I_p$  can be modelled with a two ring model,

$$\begin{aligned}
 U_l &= I_p R_p + L_p \frac{dI_p}{dt} + M \frac{dI_{MK2}}{dt} \\
 U_l &= I_{MK2} R_{MK2} + L_{MK2} \frac{dI_{MK2}}{dt} + M \frac{dI_p}{dt}
 \end{aligned}
 \tag{3.44}$$

where  $U_l$  is an applied loop voltage.  $L_p$  and  $L_{MK2}$  are self-inductances of a plasma current ring and the MK2 current ring. Similarly,  $R_p$  and  $R_{MK2}$  indicate their resistances, respectively.  $M$  represents a mutual inductance between the two current rings. The value of the inductances and the resistances for JET systems are summarized in Table 3.1.

### 3.4.2 Dynamic effective connection length

The effective connection length without a plasma current is calculated using [11]

$$L_f = 0.25 \times a \frac{B_\phi}{B_z}. \tag{3.45}$$

However, this should be modified as a function of plasma current to simulate the burn-through phase as one of the important features in this phase is the formation of closed magnetic flux surfaces i.e. a significant change of the effective connection length  $L_f$ . Since the mechanism of the dominant particle loss, i.e. a parallel or perpendicular transport, is subject to  $L_f$ , the dynamic model of  $L_f$  is of crucial importance.

It is generally accepted that a magnetic field configuration becomes closed with increasing plasma current, thereby overcoming the stray magnetic field. To suppress the stray field, the plasma current must exceed the the eddy current on the vessel wall. In the case of JET, the resistance of MK2 structure where most eddy current flows is  $7.5 \times 10^{-4}[\text{ohm}]$ , and the typical

loop voltage during the burn-through phase in JET is about 25 [V]. Hence, the eddy current on MK2 structure is calculated to be about 33 [kA]. Based on this, we assume that the plasma current from which the field transition occurs is around  $I_{ref} = 100$  [kA], and the  $L_f$  is modelled as a function of plasma current as shown below.

$$L_f = 0.25 \times a(t) \frac{B_\phi}{B_z(t)} \exp\left(\frac{I_p(t)}{I_{ref}}\right) \quad (3.46)$$

where  $B_\phi$  and  $B_z(t)$  are a toroidal magnetic field and a magnetic field in z direction, respectively.  $B_z(t)$  is composed of vertical field  $B_v$  and error field  $B_{eddy}$  (which is due to the eddy current in a vacuum vessel in JET),

$$B_z(t) = \sqrt{B_v^2 + B_{eddy}^2(t)}, \quad (3.47)$$

The mean vertical field  $B_v$  at JET is approximately  $10^{-3}$ [T] at  $t = 0$ [s]. The contribution of  $B_{eddy}(t)$  near the middle point between the centre of a plasma column and the position of the MK2 structure can be approximately calculated as,

$$B_{eddy}(t) = \frac{\mu_0}{\pi l_{MK2}} I_{MK2}(t), \quad (3.48)$$

where  $l_{MK2}$  is the distance between the centre of a plasma column and the position of the MK2 structure.

### 3.4.3 Deuterium ion confinement time

For an open field configuration, the parallel transport loss can be assumed as a transonic ambipolar flow along a magnetic field line toward the vessel wall. Analogous to the plasma in the *Scrape-Off-Layer (SOL)*, the deuterium confinement time due to the parallel particle loss  $\tau_{D,\parallel}$  is calculated by dividing effective connection length  $L_f$  with the deuterium ion sound speed  $C_s$ ,

$$\tau_{D,\parallel} = \frac{L_f}{C_s}, \quad (3.49)$$

where

$$C_s = \sqrt{\frac{T_e + T_i}{m_D}}, \quad (3.50)$$

where  $m_D$  is deuterium ion mass,  $2 \times 1.66 \times 10^{-27}$  [kg].

While perpendicular particle loss is small enough to be ignored when  $L_f$  is sufficiently short, the perpendicular particle transport becomes dominant as field lines are closed. In this model, Bohm diffusion is used to calculate the perpendicular particle transport [30]. The Bohm diffusion velocity is presented in [31],

$$v_{Bohm}(t) = \frac{2D_{Bohm}(t)}{a(t)} \quad (3.51)$$

where

$$D_{Bohm}(t) = \frac{1}{16} \frac{T_e[eV]}{B_\phi}. \quad (3.52)$$

Accordingly, the particle confinement time due to the perpendicular transport is

$$\tau_{D,\perp} = \frac{a(t)}{v_{Bohm}(t)} \quad (3.53)$$

The confinement time of a deuterium ion  $\tau_D$  is then obtained with Equation (3.49) and Equation (3.53) as

$$\frac{1}{\tau_D} = \frac{1}{\tau_{D,\parallel}} + \frac{1}{\tau_{D,\perp}}. \quad (3.54)$$

Figure 3.3 shows a simulation result of confinement time in a typical JET discharge where plasma current increases with time. As shown, the resultant confinement time  $\tau_p$  is dominated by parallel (before 0.1 second) or perpendicular (after 0.2 second) confinement time, which implies the dominant transport mechanism is changed from the parallel transport to the perpendicular transport as closed magnetic flux surfaces form. Not including transport on open field lines would greatly over estimate the energy and particle confinement before  $t = 0.15$  sec in JET.

#### 3.4.4 Impurity ion transport model

The parallel flow velocity of impurities at sheath entrance  $v_z$  during the burn-through phase is assumed to be the deuterium ion sound speed  $C_s$ . Justification of this assumption is given in section 3.4.5. According to the assumption, impurity confinement time due to parallel transport  $\tau_{I,\parallel}$  is also equal to  $\tau_{D,\parallel}$  in the model, i.e.  $\tau_{I,\parallel} = \tau_{D,\parallel}$ .

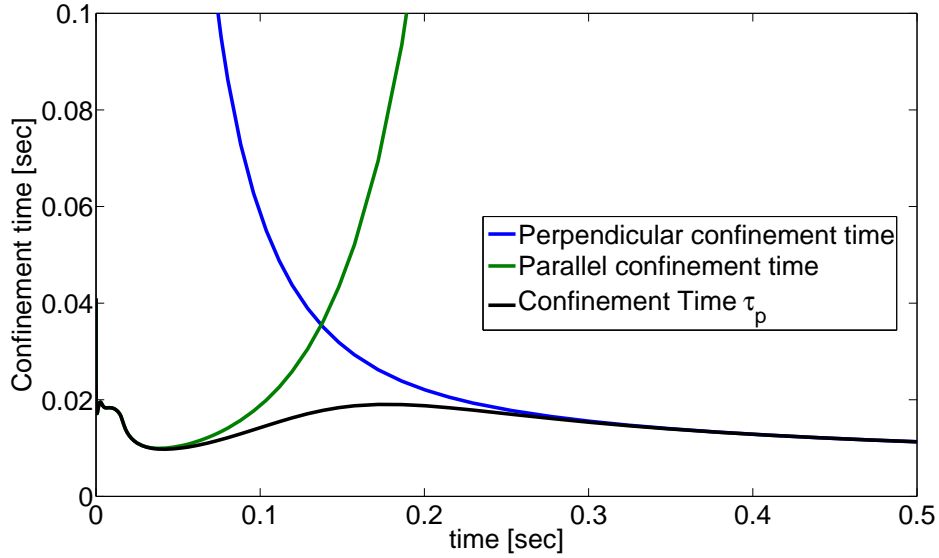


Figure 3.3: *DYON* simulation result of confinement time for a typical discharge in JET. The green line is the parallel confinement time (by Equation (3.49)), and the blue line is perpendicular confinement time (by Equation (3.53)). The black line is a resultant particle confinement time calculated by Equation (3.54).

Since the Bohm diffusion coefficient  $D_{Bohm}$  is only dependent on an electron temperature, it is valid for impurities as well. Using the Bohm diffusion model, the perpendicular diffusion particle loss of impurities is the same with the deuterium ion's, i.e.  $\tau_{I,\perp} = \tau_{D,\perp}$ . Therefore, the resulting impurity confinement time is equal to the deuterium confinement time in the model, i.e.

$$\tau_I = \tau_D. \quad (3.55)$$

In the model, all influx of impurity atoms result from wall sputtering or recycling due to the outflux of deuterium and impurity ions toward the wall, i.e. no impurity gas pumping and puffing. The total influx of neutral impurity atoms  $\Gamma_{I,in}^0$  [# of atoms per second] and the total outflux of ions  $\Gamma_{A,out}^{z+}$  [# of ions per second] are defined to be

$$\begin{aligned} \Gamma_{I,in}^0 &= V_p \sum_A \sum_{z \geq 1} \frac{Y_A^I n_A^{z+}}{\tau_A} \\ \Gamma_{A,out}^{z+} &= V_p \left( \frac{n_A^{z+}}{\tau_A} \right), \end{aligned} \quad (3.56)$$

where  $Y_A^I$  is the sputtering yield (or the recycling coefficient) of impurity  $I$  due to the bombardment of incident ion  $A$  as defined above. (Superscript  $I$  is the sputtered neutral impurity atom, and  $A$  is the incident ion, including deuterium and impurities.)

### 3.4.5 Transonic ambipolar transport of impurity ions

The parallel forces  $F_z$  on an impurity ion for tokamak start-up can be calculated using the parallel force equation. The details of the equation can be found in [26].

$$F_z = -\frac{1}{n_z} \frac{dp_z}{ds} + m_z \frac{v_D - v_z}{\tau_{\parallel}} + zeE + \alpha_e \frac{dT_e}{ds} + \beta_i \frac{dT_i}{ds} \quad (3.57)$$

where  $v_D$  and  $v_z$  are flow velocities of deuterium and impurities, respectively. Based on Spitzer's analysis of the coulomb collision frequency [32],  $\tau_{\parallel}$  is defined as a parallel collisional diffusion time,

$$\tau_{\parallel} \cong \frac{1.47 \times 10^{13} M_z [amu] T_z [eV] (T_D [eV] / M_D [amu])^{0.5}}{n_D z^2 \ln \Lambda} \quad (3.58)$$

where  $M_z$  is in  $[amu]$  and  $T$  is in  $[eV]$ .  $\alpha_e$  and  $\beta_i$  are coefficients for the electron temperature gradient force and the ion temperature gradient force, respectively [26], and they are given as a function of  $z^2$  [33] [34] [35],

$$\alpha_e \cong 0.71z^2 \quad (3.59)$$

$$\beta_i \cong 2.6z^2. \quad (3.60)$$

In order to simplify Equation (3.57), we define the following assumptions.

1. The temperatures of electrons, deuterium and impurities decrease toward the vessel wall.

The values of their gradients are approximated to be

$$\begin{aligned} \frac{dT_e}{ds} &\cong -\frac{T_e}{L_f} \\ \frac{dT_i}{ds} &= \frac{dT_z}{ds} \cong -\frac{T_i}{L_f}. \end{aligned} \quad (3.61)$$

2. The impurity density  $n_z$  decreases toward the vessel wall and the value of the gradient are approximated to be

$$\frac{dn_z}{ds} \cong -\frac{n_z}{L_f} \quad (3.62)$$

$T_e$	$10[eV] \cong 1.602 \times 10^{-18}[\text{Joules}]$
$T_D = T_z$	$3[eV] \cong 4.806 \times 10^{-19}[\text{Joules}]$
$n_D$	$10^{18}[m^{-3}]$
$L_f$	$1000[m]$
$\ln \Lambda$	$15$

Table 3.2: Assumed parameters for the justification of ambipolar transport model for impurities

3. The flow velocity of background deuterium ions is the ion sound speed  $C_s$
4. The electric field acting on impurities is determined by the pre-sheath potential drop.

$$E = \frac{0.7T_e}{eL_f} \quad (3.63)$$

5. Collisionality is strong enough so that the impurity inertial term can be ignored,

$$m_z \frac{dv_z}{dt} \cong 0. \quad (3.64)$$

By substituting each term in Equation (3.57) with the assumptions above, the impurity velocity  $v_z$  can be derived

$$v_z = C_s + \frac{\tau_{\parallel}}{m_z L_f} (2T_z + 0.7zT_e - 0.71z^2T_e - 2.6z^2T_i). \quad (3.65)$$

During the burn-through phase in JET, typical plasma parameters and effective connection length  $L_f$  are shown in Table 3.2. With the given values, the first term  $C_s$ , and the second term in Equation (3.65) are calculated to be

$$C_s \cong 25000 [m/s]$$

$$\frac{\tau_{\parallel}}{m_z L_f} (2T_z + 0.7zT_e - 0.71z^2T_e - 2.6z^2T_i) \cong -5.173 + \frac{2.43}{z} + \frac{2.08}{z^2} [m/s]$$

As shown above, the first term,  $C_s$ , in Equation (3.65) dominates the second term. Therefore, for the tokamak start-up phase, impurity flow velocity  $v_z$  can be assumed to be background ion's sound speed  $C_s$ ,

$$v_z \cong C_s.$$

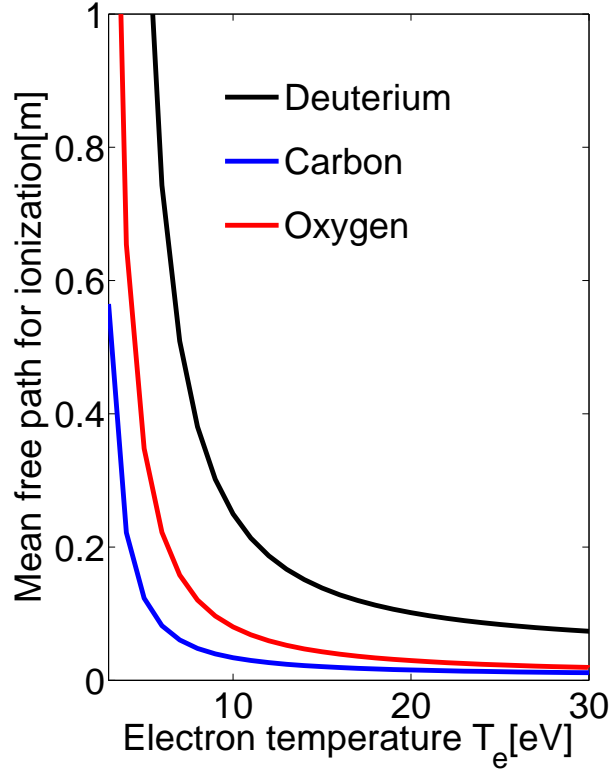


Figure 3.4: Mean free path for ionization for Deuterium, Carbon, and Oxygen.  $\lambda_{iz} = v_n / (n_e < \sigma v >_{iz})$

### 3.4.6 Neutral screening effect deuterium and impurities

As electron temperature (or density) increases, the ionization mean-free-path of neutrals,  $\lambda_{A,iz}$ , is reduced, thereby preventing neutrals from penetrating into a plasma column, i.e. decrease in the neutral volume within a plasma column,  $V_n^A$ . Figure 3.4 shows that  $\lambda_{A,iz}$  for deuterium, carbon, and oxygen decrease as the electron temperature increases.

The different  $\lambda_{A,iz}$  (i.e. different neutral screening effect) requires sophisticated particle balance equations. For example, a charge exchange reaction is only available in a deuterium neutral volume within a plasma volume,  $V_n^D$ , since a deuterium atom is assumed to be the only electron donor in this thesis. In addition, ionization and excitation of neutral  $A$  are limited to  $V_n^A$  which contains neutral  $A$ .

The neutral screening effect has been modelled in B. Lloyd's model [6]. However, the different neutral volume between impurities was not explicitly taken into account in the model. In

addition,  $V_n^A$  is likely to be a function of the cross-section of a neutral volume as shown in Figure 3.5 rather than a simple proportional function of  $\lambda_{A,iz}$ , assumed in [6]. We define the neutral volume within a plasma volume as

$$V_n^A = \begin{cases} 2\pi R(\pi\kappa a^2 - \pi\kappa(a - \lambda_{A,iz})^2) & \text{if } \lambda_{A,iz} \leq a \\ V_p & \text{if } \lambda_{A,iz} > a \end{cases}$$

where  $\kappa$  is the elongation of plasma cross-section.

For the sake of a compact expression, the neutral volume coefficient is defined as  $\gamma_n^A$ ,

$$\gamma_n^A = 1 - \frac{V_p - V_n^A}{V_V}, \quad (3.66)$$

i.e. the total neutral volume including the volume within a plasma is  $\gamma_n^A V_V$ .

### 3.4.7 Impurity particle balance model

The general form of the modified impurity particle balance equations including the neutral screening effect, sputtering, and recycling effects at the wall is shown below. The transport of impurity neutrals is not modelled in the impurity particle balance since the backscattering coefficient of impurity neutrals is implicitly assumed to be 1 (no loss).

For the neutral density we use :

$$\begin{aligned} \frac{dn_I^0}{dt} = & -\frac{V_n^I}{\gamma_n^I V_V} \langle \sigma v \rangle_{I,iz}^{0 \rightarrow 1+} n_e n_I^0 + \frac{V_p}{\gamma_n^I V_V} \langle \sigma v \rangle_{I,rec}^{1+ \rightarrow 0} n_e n_I^{1+} \\ & + \frac{V_n^D}{\gamma_n^I V_V} \langle \sigma v \rangle_{I,cx}^{1+ \rightarrow 0} n_D^0 n_I^{1+} + \frac{\Gamma_{I,in}^0}{\gamma_n^I V_V} \end{aligned} \quad (3.67)$$

For the 1+ ionization stage :

$$\begin{aligned} \frac{dn_I^{1+}}{dt} = & \frac{V_n^I}{V_p} \langle \sigma v \rangle_{I,iz}^{0 \rightarrow 1+} n_e n_I^0 - \langle \sigma v \rangle_{I,iz}^{1 \rightarrow 2+} n_e n_I^{1+} + \langle \sigma v \rangle_{I,rec}^{2+ \rightarrow 1+} n_e n_I^{2+} - \langle \sigma v \rangle_{I,rec}^{1+ \rightarrow 0} n_e n_I^{1+} \\ & + \frac{V_n^D}{V_p} \langle \sigma v \rangle_{I,cx}^{2+ \rightarrow 1+} n_D^0 n_I^{2+} - \frac{V_n^D}{V_p} \langle \sigma v \rangle_{I,cx}^{1+ \rightarrow 0} n_D^0 n_I^{1+} - \frac{n_I^{1+}}{\tau_I} \end{aligned} \quad (3.68)$$

For further ionization stages :

$$\begin{aligned} \frac{dn_I^{z+}}{dt} = & \langle \sigma v \rangle_{I,iz}^{(z-1)+ \rightarrow z+} n_e n_I^{(z-1)+} - \langle \sigma v \rangle_{I,iz}^{z+ \rightarrow (z+1)+} n_e n_I^{z+} + \langle \sigma v \rangle_{I,rec}^{(z+1)+ \rightarrow z+} n_e n_I^{(z+1)+} \\ & - \langle \sigma v \rangle_{I,rec}^{z+ \rightarrow (z-1)+} n_e n_I^{z+} + \frac{V_n^D}{V_p} \langle \sigma v \rangle_{I,cx}^{(z+1)+ \rightarrow z+} n_D^0 n_I^{(z+1)+} \\ & - \frac{V_n^D}{V_p} \langle \sigma v \rangle_{I,cx}^{z+ \rightarrow (z-1)+} n_D^0 n_I^{z+} - \frac{n_I^{z+}}{\tau_I} \end{aligned} \quad (3.69)$$



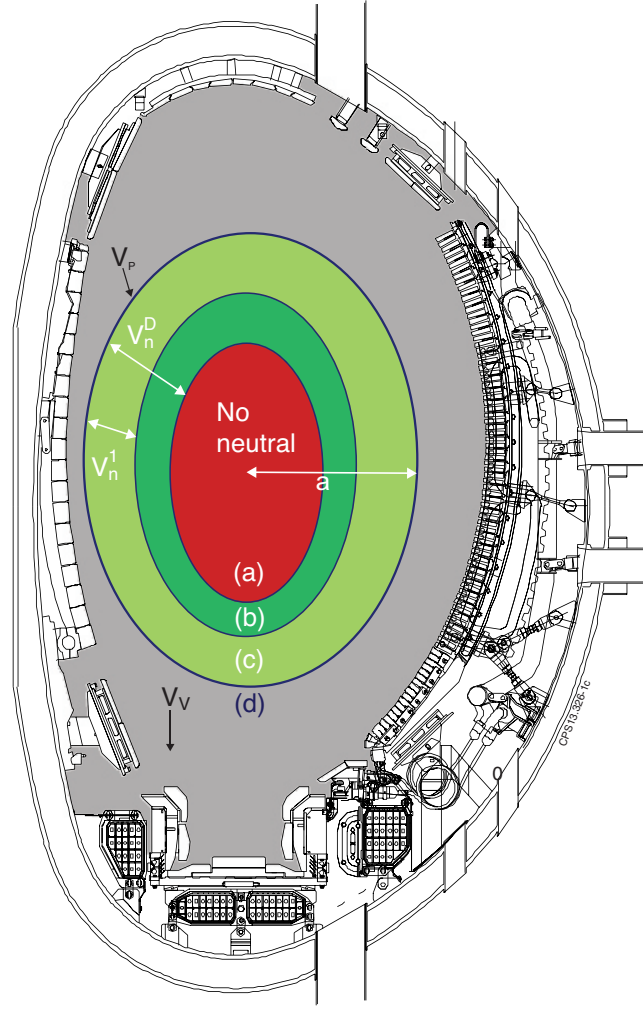


Figure 3.5: The areas of green and yellow-green indicate a neutral volume of deuterium within a plasma volume  $V_n^D$ . The neutral volume of an impurity is indicated by  $V_n^I$ , i.e. yellow-green region. The red region represents no neutral region into which neutrals cannot penetrate. The sum of the two green regions and the red area equals the total plasma volume  $V_p$ . : (a) ions (b) ions and deuterium neutrals (c) ions and neutrals of an impurity and deuterium (d) neutrals of impurities and deuterium. The grey region (d) represents the vessel volume  $V_v$ .

The corresponding matrix for impurity particle balance is shown below.

$$\frac{d}{dt} \begin{pmatrix} n_I^0 \\ n_I^{1+} \\ n_I^{2+} \\ \vdots \end{pmatrix} = \begin{pmatrix} A & B & 0 & 0 & \dots \\ C & D & E & 0 & \dots \\ 0 & F & G & H & \dots \\ \vdots & \vdots & \vdots & \ddots & \dots \end{pmatrix} \begin{pmatrix} n_I^0 \\ n_I^{1+} \\ n_I^{2+} \\ \vdots \end{pmatrix} + \begin{pmatrix} \frac{\Gamma_{I,in}^0}{\gamma_n^I V_v} \\ 0 \\ 0 \\ \vdots \end{pmatrix} \quad (3.70)$$

where

$$\begin{aligned}
\mathbb{A} &= -\frac{V_n^I}{\gamma_n^I V_V} \langle \sigma v \rangle_{I,iz}^{0 \rightarrow 1+} n_e \\
\mathbb{B} &= \frac{V_p}{\gamma_n^I V_V} \langle \sigma v \rangle_{I,rec}^{1+ \rightarrow 0} n_e + \frac{V_n^D}{\gamma_n^I V_V} \langle \sigma v \rangle_{I,cx}^{1+ \rightarrow 0} n_D^0 \\
\mathbb{C} &= \frac{V_n^I}{V_p} \langle \sigma v \rangle_{I,iz}^{0 \rightarrow 1+} n_e \\
\mathbb{D} &= -\langle \sigma v \rangle_{I,iz}^{1+ \rightarrow 2+} n_e - \langle \sigma v \rangle_{I,rec}^{1+ \rightarrow 0} n_e - \frac{V_n^D}{V_p} \langle \sigma v \rangle_{I,cx}^{1+ \rightarrow 0} n_D^0 - \frac{1}{\tau_I} \\
\mathbb{E} &= \langle \sigma v \rangle_{I,rec}^{2+ \rightarrow 1+} n_e + \frac{V_n^D}{V_p} \langle \sigma v \rangle_{I,cx}^{2+ \rightarrow 1+} n_D^0 \\
\mathbb{F} &= \langle \sigma v \rangle_{I,iz}^{1+ \rightarrow 2+} n_e \\
\mathbb{G} &= -\langle \sigma v \rangle_{I,iz}^{2+ \rightarrow 3+} n_e - \langle \sigma v \rangle_{I,rec}^{2+ \rightarrow 1+} n_e - \frac{V_n^D}{V_p} \langle \sigma v \rangle_{I,cx}^{2+ \rightarrow 1+} n_D^0 - \frac{1}{\tau_I} \\
\mathbb{H} &= \langle \sigma v \rangle_{I,rec}^{3+ \rightarrow 2+} n_e + \frac{V_n^D}{V_p} \langle \sigma v \rangle_{I,cx}^{3+ \rightarrow 2+} n_D^0
\end{aligned}$$

### 3.5 Description of the DYON code

The DYON code solves the circuit equation (plasma current and eddy current in MK2), energy balance (electron and ion), and particle balance (electron, D atom, D ion, and impurities). In the DYON code, it is assumed that the plasma during the burn-through phase has uniform plasma current, density and temperature i.e. flat profile assumption. The DYON code is comprised of the system of ordinary differential equations in time without any spatial variation. The differential equation system is shown below.

- Circuit equations

$$\begin{aligned}
\frac{dI_p}{dt} &= \frac{I_p R_p - I_{MK2} R_{MK2} + (M - L_{MK2}) \frac{dI_{MK2}}{dt}}{M - L_p} \\
\frac{dI_{MK2}}{dt} &= \frac{I_{MK2} R_{MK2} - I_p R_p + (M - L_p) \frac{dI_p}{dt}}{M - L_{MK2}}
\end{aligned} \tag{3.71}$$

- Energy balance equations

$$\begin{aligned}\frac{dT_e}{dt} &= \frac{2 P_e}{3 n_e} - \frac{T_e}{n_e} \frac{dn_e}{dt} \\ \frac{dT_i}{dt} &= \frac{2 P_i}{3 n_e} - \frac{T_i}{n_i} \left( \frac{dn_D^{1+}}{dt} + \sum_I \sum_{z \neq 0} \frac{dn_I^{z+}}{dt} \right)\end{aligned}\quad (3.72)$$

- Particle balance equations

Electron :

$$\frac{dn_e}{dt} = \frac{dn_D^{1+}}{dt} + \sum_I \sum_{z \neq 0} z \frac{dn_I^{z+}}{dt}$$

Deuterium ion :

$$\begin{aligned}\frac{dn_D^{1+}}{dt} &= \frac{V_n^D}{V_p} \langle \sigma v \rangle_{D,iz}^{0 \rightarrow 1+} n_e n_D^0 - \langle \sigma v \rangle_{D,rec}^{1+ \rightarrow 0} n_e n_D^{1+} \\ &+ \frac{V_n^D}{V_p} \sum_I \sum_{z \geq 1} \langle \sigma v \rangle_{I,cx}^{z+ \rightarrow (z-1)+} n_D^0 n_I^{z+} - \frac{n_D^{1+}}{\tau_D}\end{aligned}\quad (3.73)$$

Deuterium atom :

$$\begin{aligned}\frac{dn_D^0}{dt} &= \frac{1}{\gamma_n^D V_V} (V_p \langle \sigma v \rangle_{D,rec}^{1+ \rightarrow 0} n_e n_D^{1+} - V_n^D \langle \sigma v \rangle_{D,iz}^{0 \rightarrow 1+} n_e n_D^0 \\ &- V_n^D \sum_I \sum_{z \geq 1} \langle \sigma v \rangle_{I,cx}^{z+ \rightarrow (z-1)+} n_D^0 n_I^{z+}) + \frac{\Gamma_{D,in}^{total}}{\gamma_n^D V_V}\end{aligned}$$

Impurity atom and ions :

$$\frac{dn_I^{z+}}{dt} = [\text{Equation(3.70)}] \quad (C \times 7, Be \times 5, O \times 9, \text{ and } N \times 8 \text{ differential equations}).$$

In the simulations, C, Be, O, and N are modelled. Hence, the impurity particle balance in each charge stage comprise of 29 differential equations.

In order to make the differential equations suitable for numerical calculations, the energy balance for electron and ion are rearranged to the differential equations for temperature as

$$\begin{aligned}\frac{3}{2} \frac{d(n_e T_e)}{dt} &= P_{oh} + P_{aux} - (P_{iz} + P_{rad}) - P_{equi} - P_{conv}^e \equiv P_e \\ \frac{3}{2} (T_e \frac{dn_e}{dt} + n_e \frac{dT_e}{dt}) &= P_e \\ \frac{dT_e}{dt} &= \frac{2 P_e}{3 n_e} - \frac{T_e}{n_e} \frac{dn_e}{dt}\end{aligned}\quad (3.74)$$

Input	Output
Prefill gas pressure $p(0)$ ,	Plasma temperature $T_e(t)$ , $T_i(t)$ ,
Loop voltage $U_l(t)$ ,	Plasma density $n_e(t)$ , $n_D^0(t)$ , $n_D^{1+}(t)$ ,
Toroidal magnetic field $B_\phi$ ,	Impurity density in each charge state $n_I^{z+}(t)$ ,
Vertical magnetic field $B_v(0)$	Plasma current $I_p(t)$ , eddy current in MK2 $I_{MK2}(t)$ ,
Major radius $R(t)$ , Minor radius $a(t)$	Effective connection length $L_f(t)$

Table 3.3: *Input and output in the DYON code.*

and

$$\begin{aligned}
\frac{3}{2} \frac{d(n_i T_i)}{dt} &= P_{equi} - P_{CX} - P_{conv}^i \equiv P_i \\
\frac{3}{2} \left( T_i \frac{dn_i}{dt} + n_i \frac{dT_i}{dt} \right) &= P_i \\
\frac{dT_i}{dt} &= \frac{2 P_i}{3 n_i} - \frac{T_i}{n_i} \frac{dn_i}{dt} = \frac{2 P_i}{3 n_i} - \frac{T_i}{n_i} \left( \frac{dn_D^{1+}}{dt} + \sum_I \sum_{z \neq 0} \frac{dn_I^{z+}}{dt} \right).
\end{aligned} \tag{3.75}$$

Table 3.3 shows the input and output variables of the DYON code. The input data can be obtained by using the JET data. The prefill gas pressure  $p(0)$  is measured by the pressure gauge at  $t = 0$  [sec]. The loop voltage  $U_l(t)$  is calculated by Equation (1.21) using the measured poloidal coil voltage. Plasma major  $R(t)$  and minor radius  $a(t)$  is obtained from Experimentally Constrained Equilibrium Fit (EFIT) data. The toroidal magnetic field  $B_\phi$  is constant during the discharge, and it is obtained from the JET data. The vertical magnetic field  $B_v$  at 0 second is assumed to be 1 [mT] for JET simulations. With the given input data, the DYON code simulates the evolution of plasma parameters during the plasma burn-through phase. The simulations are typically for 1 second, from 0 to 1 [sec] of the plasma discharge in JET.

The DYON code is written in MATLAB R2012a<sup>6</sup>. Since the density terms ( $n_e$ ,  $n_D^{z+}$ , and  $n_I^{z+}$ ) during the early burn-through phase ( $\sim 50$  msec) increase much faster than the other plasma parameters ( $T_e$ ,  $T_i$ ,  $I_p$ , and  $I_{MK2}$ ), the differential equation set is a stiff system requiring an implicit numerical method. ODE15s is an implicit ordinary differential equation solver, which is a built-in function in MATLAB R2012a. ODE15s uses the numerical differentiation formulas (NDFs), which is a multistep solver using the Backward differences (BDF) combined with the

<sup>6</sup><http://www.mathworks.co.uk/products/matlab/>

additional term as shown below,

$$\underbrace{\sum_{m=1}^k \frac{1}{m} \nabla^m y_{n+1} - hF(t_{n+1}, y_{n+1})}_{BDF} - \underbrace{\kappa \gamma_k (y_{n+1} - \sum_{m=0}^k \nabla^m y_n)}_{\text{additional term}} = 0$$

where

$$F(t, y) = \frac{dy}{dt}$$

$$h = \Delta t$$

(3.76)

Order k	1	2	3	4	5
NDF coefficient $\kappa$	-0.185	-1/9	-0.0823	-0.0415	0

$$\gamma_k = \sum_{j=1}^k \frac{1}{j}$$

$$\nabla^m y_n = \nabla^{m-1} y_n - \nabla^{m-1} y_{n-1} \text{ and } \nabla^1 y_n = y_n - y_{n-1}.$$

The NDFs is more efficient than BDF since it can have bigger time step size than BDF with the same truncation error. The truncation error and stability of the NDF can be compromised by changing order  $k$  indicated in Equation (3.76). The higher order  $k$  has the smaller truncation error, but worse stability. In ODE15s, by changing the  $k$  during the computation process, the time step size is maximized under a certain limitation of truncation error, maintaining the numerical stability. Using ODE15s for DYON simulation, a typical computation time for JET discharge during 0 ~ 1 second takes less than 10 minutes with a normal laptop computer (2.5 GHz CPU and 4 GB RAM).

## 3.6 Discussion

In this section, the governing equations for plasma burn-through modelling, summary of the previous models, and description of the new models and the DYON code are presented in detail.

Plasma burn-through modelling, including the DYON code, assumes uniform plasma parameters i.e. 0D model. This assumption is reasonable during the plasma burn-through phase since the closed magnetic flux surfaces, which make a major contribution to the gradient of plasma parameters, are not yet fully formed due to the low plasma current during the early start-up phase.

For plasma resistance, Spitzer resistivity is used assuming that coulomb collisions are dominant. This assumption can be justified by giving a sufficient initial degree of ionization for which coulomb collisions are dominant over electron-neutral collisions. The quantitative calculation for the initial degree of ionization is given in Section 6.3 of this thesis.

We assume room temperature for the neutral energy without calculation of neutral energy balance. In JET experiments, deuterium gas at room temperature is injected into the vessel, and the cross-section for momentum transfer through billiard-ball collision is much smaller than coulomb collision.

We assume fully dissociated D gas, and this is a reasonable assumption for  $T_e(0) = 1$  [eV], the initial condition in the simulation. The dissociation energy per D atom  $P_{dis}$  is just 2.26 [eV]. Compared to D ionization energy 13.6 [eV], this is small. Moreover, radiation power loss is much greater than D ionization energy i.e.  $P_{rad} > P_{iz} > P_{dis}$ . This has been checked in the simulations by adding 2.26 [eV] to D ionization energy; the simulation results did not show any visible difference. Hence, the D dissociation energy can be ignored in the simulation.

The two ring model used in the DYON code is a simplified model for JET. This is a reasonable model for JET due to the iron core which reduces the stray field significantly. The iron core enables the loop voltage calculation for plasma current and MK2 current using Equation (1.21). Hence, it should be noted that for applications to other tokamaks, a 2D (or 3D) electromagnetic code should be incorporated into the model to compute the stray fields.

Even though one of the key improvements in the DYON code is impurity treatment using sputtering models at the wall, the PWI models are not introduced in this chapter. The detailed explanation on the PWI models are given in chapter 5.

# Chapter 4

## Physics of deuterium burn-through

### 4.1 Introduction

The criterion for plasma burn-through in tokamaks was firstly published by Hawlyruk [18]. The minimum loop voltage for plasma burn-through was computed for TFTR, the tokamak at the Princeton Plasma Physics Laboratory in USA, using a 0D model. For a deuterium plasma, it was qualitatively discussed that the criterion of the plasma burn-through increases with the prefill gas pressure and the impurity content. Although the basic physics of plasma burn-through was described in [18], the following points should be improved.

The paper gives no physical explanation of the Radiation and Ionization Barrier (RIB), which determines the criterion for plasma burn-through. The RIB will be explained using a concept of critical degree of ionization in this chapter. Furthermore, the magnitude of the RIB and the required electric field to overcome the RIB,  $E_{RIB}$ , will be derived in an analytical way.

Impurities during the plasma burn-through phase result from complex plasma wall interactions. This makes analytical investigation on plasma burn-through extremely complicated. To gain an insight into the key physics aspects in the plasma burn-through phase, it is worth starting the investigation of a pure deuterium plasma. Furthermore, according to recent observations in JET with the ITER-like wall, deuterium radiation can be critical for plasma burn-through with a beryllium wall. Hence, this chapter describes the burn-through process of a pure deuterium plasma. We discuss the required condition for plasma current ramp-up in section 4.2. Then,

the requirements for plasma burn-through is discussed in section 4.3. The effects of impurities, which constitute the wall materials in tokamaks such as carbon and beryllium, on the burn-through criterion will be discussed in the next chapter (chapter 5).

## 4.2 Condition for plasma current ramp-up

Assuming no eddy current in the passive structure, the plasma current  $I_p$  in tokamaks can be calculated with the circuit equation

$$I_p = \frac{1}{R_p}(U_l - L_p \frac{dI_p}{dt}) \quad (4.1)$$

where  $R_p$ ,  $U_l$ , and  $L_p$  are plasma resistance, loop voltage, and plasma inductance, respectively. In order for  $I_p$  to increase continuously for a given  $U_l$ , which is approximately constant in the  $I_p$  ramp-up phase,  $R_p$  must be decreasing continuously. According to Spitzer resistivity,  $R_p$  decreases with increasing electron temperature  $T_e$  [1], i.e.  $R_p \propto T_e^{-\frac{3}{2}}$ . Therefore,

$$\frac{dT_e}{dt} > 0 \quad (4.2)$$

is a necessary condition for  $I_p$  ramp-up ( $\frac{dI_p}{dt} > 0$ ).

Whether or not  $T_e$  increases is determined by the equation of electron energy balance,

$$P_e = \frac{3}{2} \frac{d(n_e k T_e)}{dt} = \frac{3}{2} k T_e \frac{dn_e}{dt} + \frac{3}{2} n_e \frac{dk T_e}{dt}, \quad (4.3)$$

where  $P_e$  is the net electron heating power, determined by the ohmic heating power  $P_{Oh}$  (for cases without assist from additional heating) and the total electron power loss  $P_{Loss}$ , i.e.  $P_e = P_{Oh} - P_{Loss}$ . As separated into the two terms in Equation (4.3), the net electron heating power  $P_e$  is consumed by increasing  $n_e$  or  $T_e$ , i.e.  $\frac{3}{2} k T_e \frac{dn_e}{dt} > 0$  or  $\frac{3}{2} n_e \frac{dk T_e}{dt} > 0$ .

The diagrams used in this section are obtained by DYON simulations for a pure deuterium plasma (Figure 4.1, 4.2, 4.4, and 4.5) or by using an analytical formula (Figure 4.3). The plasma parameters assumed in the DYON simulations are given in Table 4.1. In order to simulate the cases of successful and failed plasma burn-through, two different prefill gas pressures are assumed,  $5 \times 10^{-5}$ [Torr](Success), and  $7 \times 10^{-5}$ [Torr](Failure) in Figures 4.1, 4.2, and 4.4. In 4.5, a wider range of prefill gas pressures ( $1 \times 10^{-5}$ ,  $3 \times 10^{-5}$ ,  $5 \times 10^{-5}$ , and  $7 \times 10^{-5}$ [Torr]) is used to show the effects of prefill gas pressure on plasma burn-through.



The change of the electron power balance during the plasma burn-through phase is described in Figure 4.1 using DYON simulation results : (a) the power consumption for successful  $I_p$  ramp-up (blue) and failed case (red), and (b) the corresponding plasma currents. As shown,  $P_e$  is positive for the successful case, and goes to zero in the failed case during the  $I_p$  ramp-up phase. Whereas the power consumed by the increasing  $n_e$  (chain lines) is dominant in the plasma burn-through phase (i.e.  $t = 0 \sim 0.015$ [sec]), it is small enough to be ignored in the

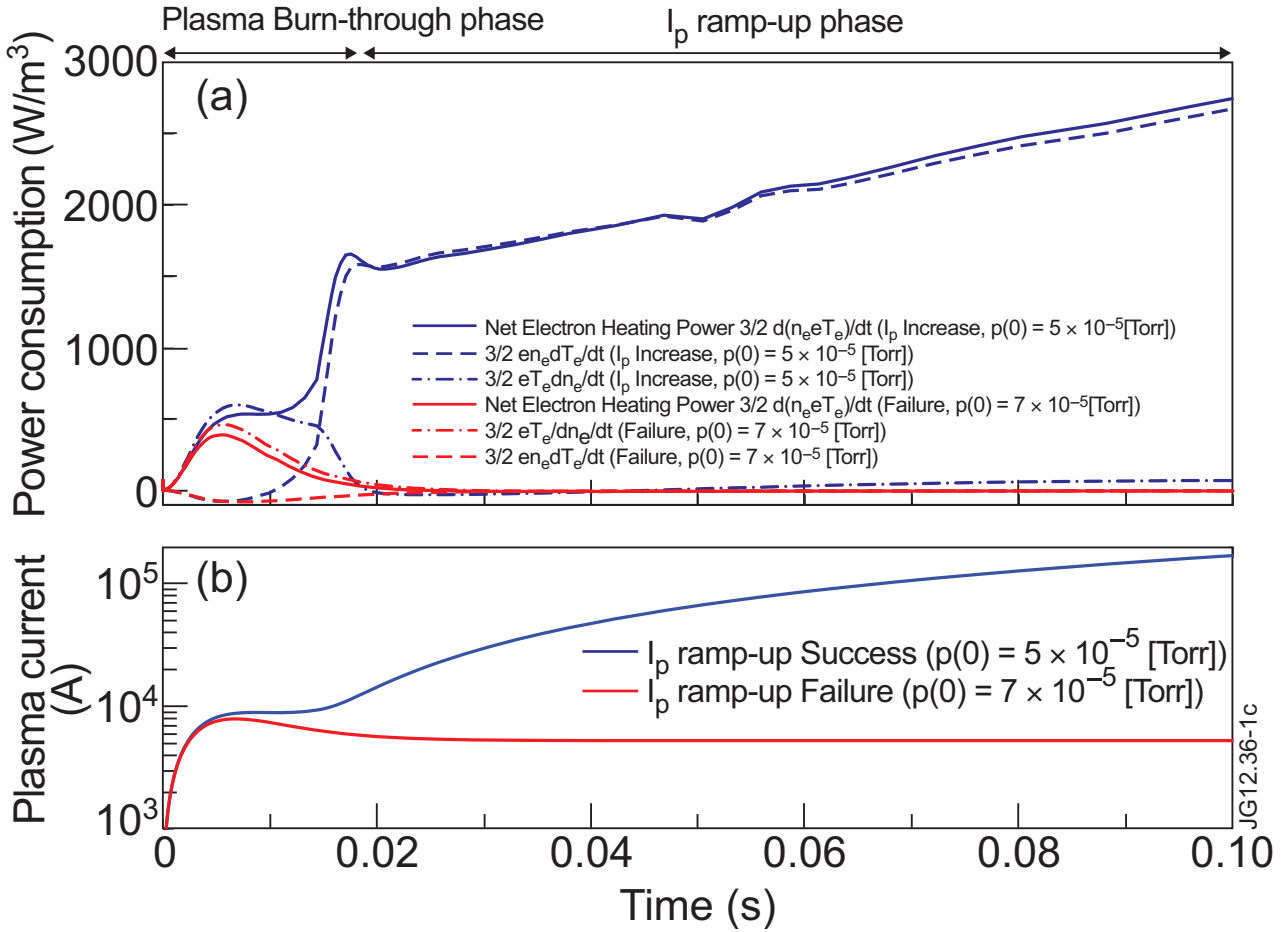


Figure 4.1: DYON simulation results for pure deuterium plasmas for two different prefill pressures  $5 \times 10^{-5}$  [Torr] (success) and  $7 \times 10^{-5}$  [Torr] (failure). The colors of lines in (a) and (b) indicate successful  $I_p$  ramp-up (blue) and failure (red). The solid lines represent the net electron heating power  $P_e$ . The dashed lines and the chain lines are the amount of  $P_e$  consumed by increasing  $T_e$  and increasing  $n_e$ , respectively. The corresponding plasma currents  $I_p$  are represented by the blue solid line ( $I_p$  ramp-up) and the red solid line (non-sustained break-down) in (b). In order for  $I_p$  to increase,  $P_e$  must be positive in the  $I_p$  ramp-up phase.

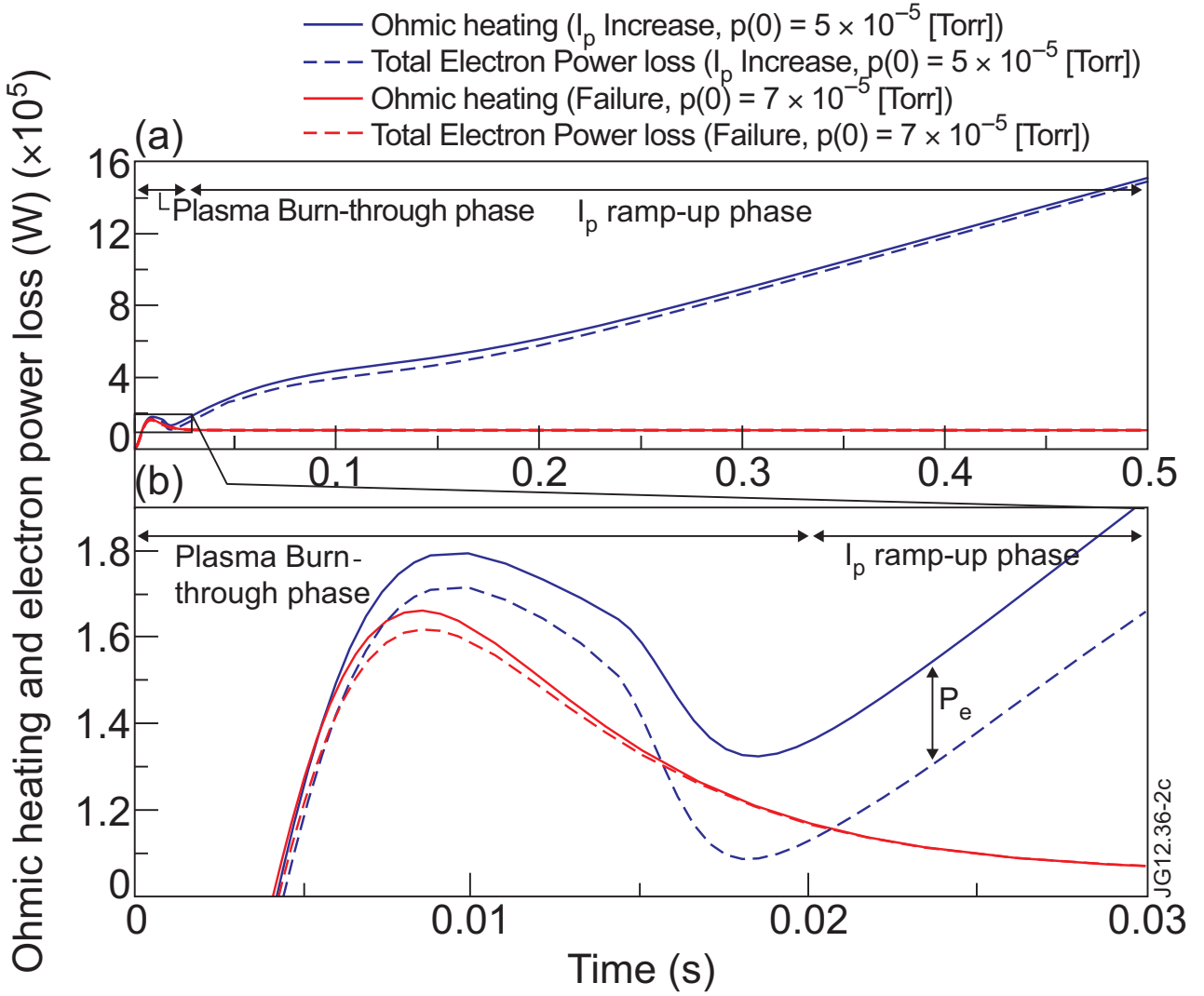


Figure 4.2: *DYON* simulation results for pure deuterium plasmas for two different prefill pressures  $5 \times 10^{-5}$  [Torr] (success) and  $7 \times 10^{-5}$  [Torr] (failure). The solid lines and the dashed lines in (a) show  $P_{Oh}$  and  $P_{Loss}$  in successful (blue) and failure (red) cases, respectively. (b) is an expanded figure from the burn-through phase in (a). It is determined by  $P_e$  during the plasma burn-through phase whether  $P_e$  is positive for the  $I_p$  ramp-up phase.

$I_p$  ramp-up phase (i.e.  $t > 0.015$ [sec]) as shown in Figure 4.1 (a) i.e. blue solid line  $\approx$  blue dashed line. Therefore,  $P_e$  in the  $I_p$  ramp-up phase can be approximated to be  $P_e \approx \frac{3}{2}n_e \frac{dkT_e}{dt}$ . Accordingly, in order for  $T_e$  increases,  $P_e$  must be positive in the  $I_p$  ramp-up phase, i.e.

$$P_e > 0. \quad (4.4)$$

In this simulation, the deuterium recycling coefficient  $Y_D^D$  is assumed as 1. In the case that  $Y_D^D$

Plasma parameters	Input values
Toroidal magnetic field $B_\phi$	2.3 [Tesla]
Vertical magnetic field $B_v$	0.001 [Tesla]
Initial plasma current density $J_p(0)$	$382.5 \times E(= U_l/2\pi R) = 405.8 [A m^{-2}]$
Initial Eddy current $I_{MK2}(0)$	0 [A]
Initial electron temperature $T_e(0)$	1 [eV]
Initial ion temperature $T_i(0)$	0.03 [eV]
Prefilled gas pressure $p(0)$	Figures 4.1, 4.2, and 4.4 : $5$ and $7 \times 10^{-5}$ [Torr] Figure 4.5 : $1, 3, 5,$ and $7 \times 10^{-5}$ [Torr]
Initial D atom density $n_D^0(0)$	$2.78 \times 10^{22} \times p(0)$ [Torr]
Initial degree of ionization $\gamma_{iz}(0)$	0.002
Initial Be content $n_{Be}^0(0)$	0
Initial C content $n_C^0(0)$	0
Initial O content $n_O^0(0)$	0
Initial N content $n_N^0(0)$	0
$Y_D^D$	1
Fuelling efficiency	No additional fuelling
Plasma major radius $R$	3 [m]
Plasma minor radius $a$	0.5 [m]
Internal inductance $l_i$	0.5
Loop voltage $U_l$	20 [V]
Vacuum vessel volume	100 [m <sup>3</sup> ]

Table 4.1: Plasma parameters assumed for DYON simulations. (Figure 4.1, 4.2, 4.4, and 4.5)

is higher than 1, the power consumed by the increasing  $n_e$  would not be 0. However, Equation (4.4) is still a necessary condition for the increase in  $T_e$  unless the power consumed by the increasing  $n_e$  becomes significant.

Figure 4.2 shows DYON simulation results of  $P_{oh}$  and  $P_{Loss}$  in the cases of  $I_p$  ramp-up success

(blue) and failure (red), respectively. In the successful case,  $P_{Oh}$  (blue solid line) exceeds  $P_{Loss}$  (blue dashed line), i.e. positive  $P_e$  in the  $I_p$  ramp-up phase. However,  $P_{Oh}$  (red solid line) and  $P_{Loss}$  (red dashed line) overlap in the failed case, hence  $P_e$  is zero. Figure 4.2(b), which is enlarged from Figure 4.2 (a), shows that the behaviour of  $P_e$  in the burn-through phase are clearly different in the two cases. It is determined by the behaviour of  $P_e$  during the plasma burn-through phase whether  $P_e$  in the  $I_p$  ramp-up phase is positive. Hence,  $P_e$  during the plasma burn-through phase should be investigated to derive the requirement of  $I_p$  ramp-up, i.e. the criterion of plasma burn-through.

### 4.3 Criterion for deuterium burn-through

The total electron power loss,  $P_{Loss}$  consists of the three power loss terms, i.e. radiation and ionization power loss  $P_{rad+iz}$ , equilibration power loss  $P_{equi}$ , and convective transport power loss  $P_{conv}^e$ .<sup>1</sup> In the case of a pure deuterium plasma assumed in this section, they are calculated as shown below [6][36].

$$\begin{aligned}
 P_{Loss} &= P_{rad+iz} + P_{equi} + P_{conv}^e \\
 P_{rad+iz} &= V_p \times \langle \sigma v \rangle_{rad+iz} (T_e) n_e n_D^0 \\
 P_{equi} &= V_p \times 7.75 \times 10^{-34} (T_e - T_i) \frac{n_e n_D^{1+} \ln \Lambda}{T_e^{3/2} M_D}, \\
 P_{conv}^e &= V_p \times \frac{3 n_e k T_e}{2 \tau_e},
 \end{aligned} \tag{4.5}$$

where  $n_D^0$  is a deuterium atom density,  $n_D^{1+}$  is a deuterium ion density,  $V_p$  is a plasma volume,  $M_D$  is a deuterium ion mass in [amu],  $\tau_e$  is the electron particle confinement time, and  $\langle \sigma v \rangle_{rad+iz} (T_e)$  is the power loss coefficient due to the radiation and ionization, obtained from ADAS package [25].

In contrast to  $P_{equi}$  and  $P_{conv}^e$ , which monotonically increase with  $n_e$ ,  $P_{rad+iz}$  has a maximum value at a certain degree of ionization since  $n_D^0$  decreases as  $n_e$  increases. In this section, we define the peak value of  $P_{rad+iz}$  as the *Radiation and Ionization Barrier* (RIB), and the degree of ionization at the RIB is defined to be the *Critical Degree of Ionization* for plasma burn-through,  $\gamma_{iz}(t_{RIB})$ .

---

<sup>1</sup>The details on each term are explained in chapter 3.

The RIB is of crucial importance since the required  $P_{Oh}$  for  $I_p$  ramp-up is mainly determined by the RIB. As will be shown, the magnitude of  $P_{rad+iz}$  is dominant in  $P_{Loss}$  during the plasma burn-through phase. This implies that  $P_{Loss}$  also has the maximum value at  $\gamma_{iz}(t_{RIB})$ . Hence, once the  $P_{Oh}$  exceeds the  $P_{Loss}$  maximum,  $P_{Loss}$  decreases significantly as ionizations proceed. This enables  $T_e$  to increase, so that ionizations continue to increase up to 100%, i.e. full ionization.

During the plasma burn-through phase, the density of deuterium atoms  $n_D^0(t)$  decreases, thereby increasing  $n_e(t)$ . When the deuterium atom density within a plasma volume decreases, neutral particles flow into the plasma volume from the ex-plasma volume, giving a dynamic fuelling effect. This effect maintains a neutral density within a plasma volume as much as the ratio of plasma volume to total neutral volume (= Effective vessel volume  $V_V$ , in which all neutrals are accessible to the plasma). The effective reduction of neutral density in  $V_p$  is  $\frac{V_p}{V_V}n_e(t)$ . Hence, in the case that the deuterium recycling coefficient  $Y_D^D$  is 1 and there is no gas pumping or puffing,  $n_D^0(t)$  is a function of  $n_e(t)$ ,

$$n_D^0(t) = n_D^0(0) - \frac{V_p}{V_V}n_e(t), \quad (4.6)$$

where  $n_D^0(0)$  indicates the initial density of deuterium atoms, which is proportional to the prefill gas pressure. By substituting  $n_D^0$  in  $P_{rad+iz}(t)$  in Equation (4.5) with  $n_D^0(t)$  in Equation (4.6),  $P_{rad+iz}(t)$  can be written as a quadratic function of  $n_e(t)$ ,

$$\begin{aligned} P_{rad+iz}(t) &= V_p \langle \sigma v \rangle_{rad+iz} (T_e) n_e(t) n_D^0(t) \\ &= V_p \langle \sigma v \rangle_{rad+iz} (T_e) n_e(t) \left( n_D^0(0) - \frac{V_p}{V_V} n_e(t) \right) \\ &= V_p \langle \sigma v \rangle_{rad+iz} (T_e) \left( \frac{V_V n_D^0(0)^2}{4V_p} - \frac{V_p}{V_V} \left( n_e(t) - \frac{V_V n_D^0(0)}{2V_p} \right)^2 \right) \end{aligned} \quad (4.7)$$

Therefore, as ionizations proceed,  $n_e(t)n_D^0(t)$  in Equation (4.7) has a maximum value. Figure 4.3 (a) indicates the change of  $n_e(t)n_D^0(t)$  with the normalized  $n_e(t)$ , i.e.  $(n_e(t)V_p)/(n_D^0(0)V_V)$ . As shown in Figure 4.3 (a),  $n_e(t)n_D^0(t)$  has the maximum value,

$$\frac{V_V n_D^0(0)^2}{4V_p} \quad (4.8)$$

when  $n_e(t)$  is equal to

$$\frac{V_V n_D^0(0)}{2V_p}. \quad (4.9)$$

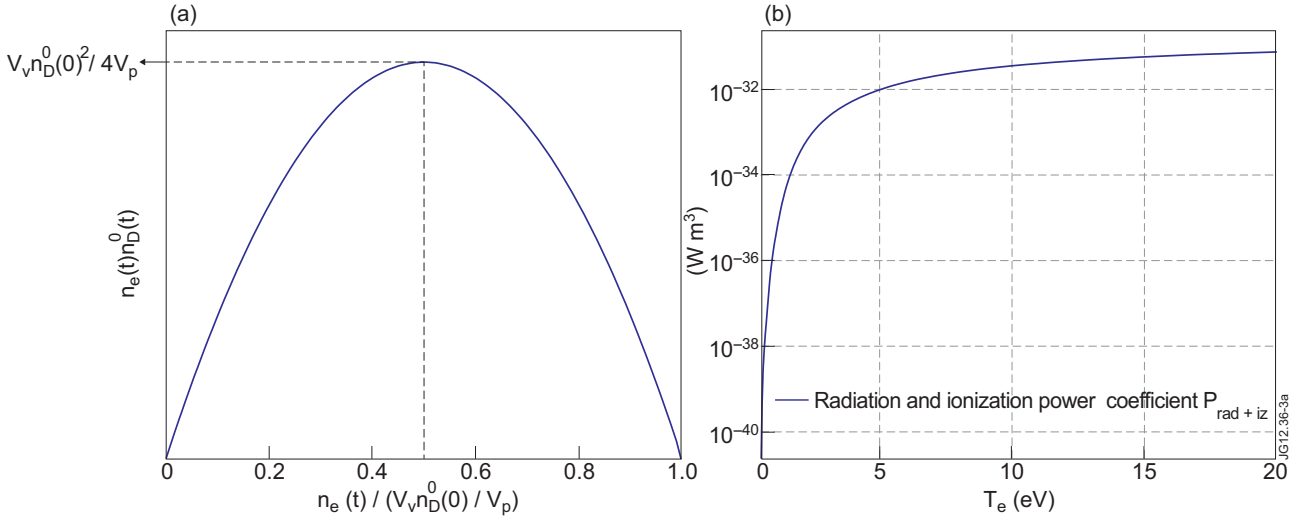


Figure 4.3: (a) shows the change of  $n_e(t)n_D^0(t)$  with the normalized  $n_e$ . Since  $n_e(t)n_D^0(t)$  can be substituted by  $n_e(t)(n_D^0(0) - n_e(t))$  in the case of a recycling coefficient (= 1.0), it has a maximum value as  $n_e(t)$  approaches Equation (4.9). (b) indicates electron power loss coefficient due to the radiation and ionization of deuterium,  $\langle \sigma v \rangle_{rad+iz}$ , obtained from ADAS.  $\langle \sigma v \rangle_{rad+iz}$  is strongly dependent on  $T_e$  only.

The power coefficient  $\langle \sigma v \rangle_{rad+iz}(T_e)$  is a function of  $T_e$ . Figure 4.3 (b) shows  $\langle \sigma v \rangle_{rad+iz}(T_e)$  obtained from ADAS [25]. The product of  $n_e(t)n_D^0(t)$  and  $\langle \sigma v \rangle_{rad+iz}(T_e)$  results in the change of  $P_{rad+iz}$ , thereby the change of  $P_{Loss}$  in Figure 4.2. The increase in  $P_{Loss}$  during the  $I_p$  ramp-up phase in Figure 4.2 results from the increase in  $\langle \sigma v \rangle_{rad+iz}(T_e)$ .

The degree of ionization in the plasma burn-through phase can be calculated using

$$\gamma_{iz}(t) = \frac{n_e(t)}{n_e(t) + n_D^0(t)}. \quad (4.10)$$

The degree of ionization at the RIB,  $\gamma_{iz}(t_{RIB})$ , is then obtained by substituting  $n_D^0(t)$  and  $n_e(t)$  using Equation (4.6) and Equation (4.9) as shown below.

$$\begin{aligned} \gamma_{iz}(t_{RIB}) &= \frac{\frac{V_v n_d^0(0)}{2V_p}}{\frac{V_v n_d^0(0)}{2V_p} + \left( n_D^0(0) - \frac{V_p \frac{V_v n_d^0(0)}{2V_p}}{V_V} \right)} \\ &= \frac{V_V}{V_V + V_p} \end{aligned} \quad (4.11)$$

The plasma volume is limited by the vessel volume, i.e.  $V_p \leq V_V$ . This implies that  $\gamma_{iz}(t_{RIB})$  is always higher than 50%. In the case of JET, where  $V_V$  is  $\sim 100[m^3]^2$  and initial plasma volume

<sup>2</sup>Further explanation on  $V_V$  is provided in section 6.4.6.

$V_p = 14.8 \sim 59.2[m^3]$  (major radius  $R = 3[m]$  and minor radius  $a = 0.5 \sim 1[m]$ ), the critical degree of ionization  $\gamma_{iz}(t_{RIB})$  is  $87.1 \sim 62.8\%$ , respectively.

The DYON simulation results of  $P_{rad+iz}$  are shown in Figure 4.4(a).  $P_{rad+iz}$  in the successful  $I_p$  ramp-up case (blue) has a maximum and decreases immediately after the peak. This is consistent with Equation (4.7), since  $n_e n_D^0$  decreases with increasing  $n_e$  after the peak point as shown in Figure 4.3(a).  $P_{rad+iz}$  falls with increasing degree of ionization from  $0.008[s]$ ,  $t_{RIB}$ , when the critical degree of ionization is achieved. Accordingly,  $T_e$  begins to increase from  $t_{RIB}$ , and the increase becomes steep after  $P_{rad+iz}$  falls sufficiently around  $0.015[s]$  as shown in Figure 4.4(c). Because the neutral particles are strong sinks of electron energy, the increase in  $T_e$  is impeded ( $T_e \sim \text{constant}$ ) until the neutrals are fully ionized.

As shown in Figure 4.4 (b) the degree of ionization in the successful case (blue) approaches 100% which is larger than the  $\gamma_{iz}(t_{RIB})$  87.1%, calculated using Equation (4.11) where  $a$  is  $0.5[m]$ , as assumed in the DYON simulations. On the other hand, the degree of ionization in the failed case does not exceed 87.1%. Hence,  $P_{rad+iz}$  does not fall abruptly, and  $P_e$  approaches 0, thereby resulting in the failure of the  $I_p$  ramp-up.

Figure 4.5 shows DYON simulation results of (a) plasma current, (b) degree of ionization, and (c) electron power losses for different prefill gas pressures. The  $I_p$  ramp-up is delayed until almost 100% degree of ionization is achieved in the low prefill gas pressure cases ( $1 \times 10^{-5}$ ,  $3 \times 10^{-5}$ , and  $5 \times 10^{-5}[Torr]$ ), and the delay is extended with increasing prefill gas pressures. The  $I_p$  ramp-up fails at a prefill gas pressure over  $7 \times 10^{-5}[Torr]$ . This indicates that above a prefill gas pressure of  $7 \times 10^{-5}[Torr]$  the given loop voltage is not sufficient to achieve the critical degree of ionization,  $\gamma_{iz}(t_{RIB})$ , as shown in Figure 4.5 (b). That is, the maximum prefill gas pressure available for plasma burn-through with the given  $20[V]$  loop voltage exists between  $5 \times 10^{-5}[Torr]$  and  $7 \times 10^{-5}[Torr]$ .

For the low prefill gas pressure cases, the corresponding peak values of  $P_{rad+iz}$  in Figure 4.5(c) indicate the RIB. As shown in Figure 4.5 (c),  $P_{iz+rad}$  is dominant in  $P_{Loss}$  during the plasma burn-through phase, and the peak of  $P_{Loss}$  coincides with the RIBs. Therefore, the required electric field for plasma burn-through is mainly determined by the  $P_{iz+rad}$ . It should be noted that the RIB rises as prefill gas pressure increases in Figure 4.5 (c). This is due to the fact that neutrals are strong energy sinks. That is, the larger number of neutrals at a high prefill gas pressure results in higher  $P_{rad}$ . In addition, there are more neutrals to be ionized at a high

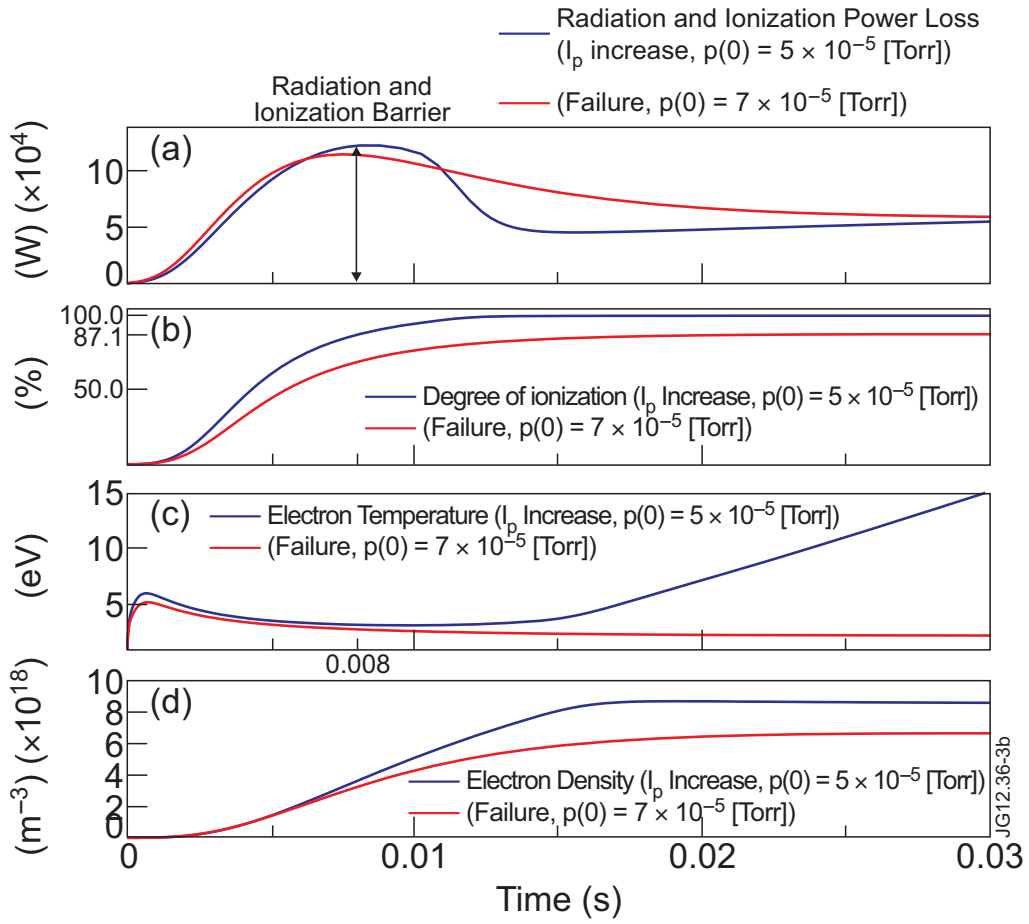


Figure 4.4: *DYON* simulation results for pure deuterium plasmas for two different prefill pressures  $5 \times 10^{-5}$  [Torr] (success) and  $7 \times 10^{-5}$  [Torr] (failure). The blue line and the red line indicate the case of successful  $I_p$  ramp-up and failed ramp-up, respectively. (a) shows  $P_{rad+iz}$ . The corresponding degree of ionization is indicated in (b). The critical degree of ionization  $\gamma_{iz}(t_{RIB})$  is 87.1% as calculated using Equation (4.11) where minor radius  $a$  is assumed to be  $0.5[m]$ . Whether or not a degree of ionization can go over  $\gamma_{iz}(t_{RIB})$  is critical for  $I_p$  ramp-up. (c) and (d) show electron temperature and density, respectively.

prefill gas pressure, thereby increasing  $P_{iz}$ .

The increase in RIB can also be seen in Equation (4.7). Equation (4.7) indicates that the maximum  $P_{rad+iz}(t_{RIB})$  is

$$P_{rad+iz}(t_{RIB}) = \frac{V_V \langle \sigma v \rangle_{rad+iz} (T_e) n_D^0(0)^2}{4}. \quad (4.12)$$

$n_D^0(0)$  is proportional to the prefill gas pressure  $p(0)$ . Hence,  $P_{rad+iz}(t_{RIB})$  also increases proportionally with the square of  $p(0)$ , if  $T_e$  is identical at the  $t_{RIB}$ . Since  $T_e$  during the plasma



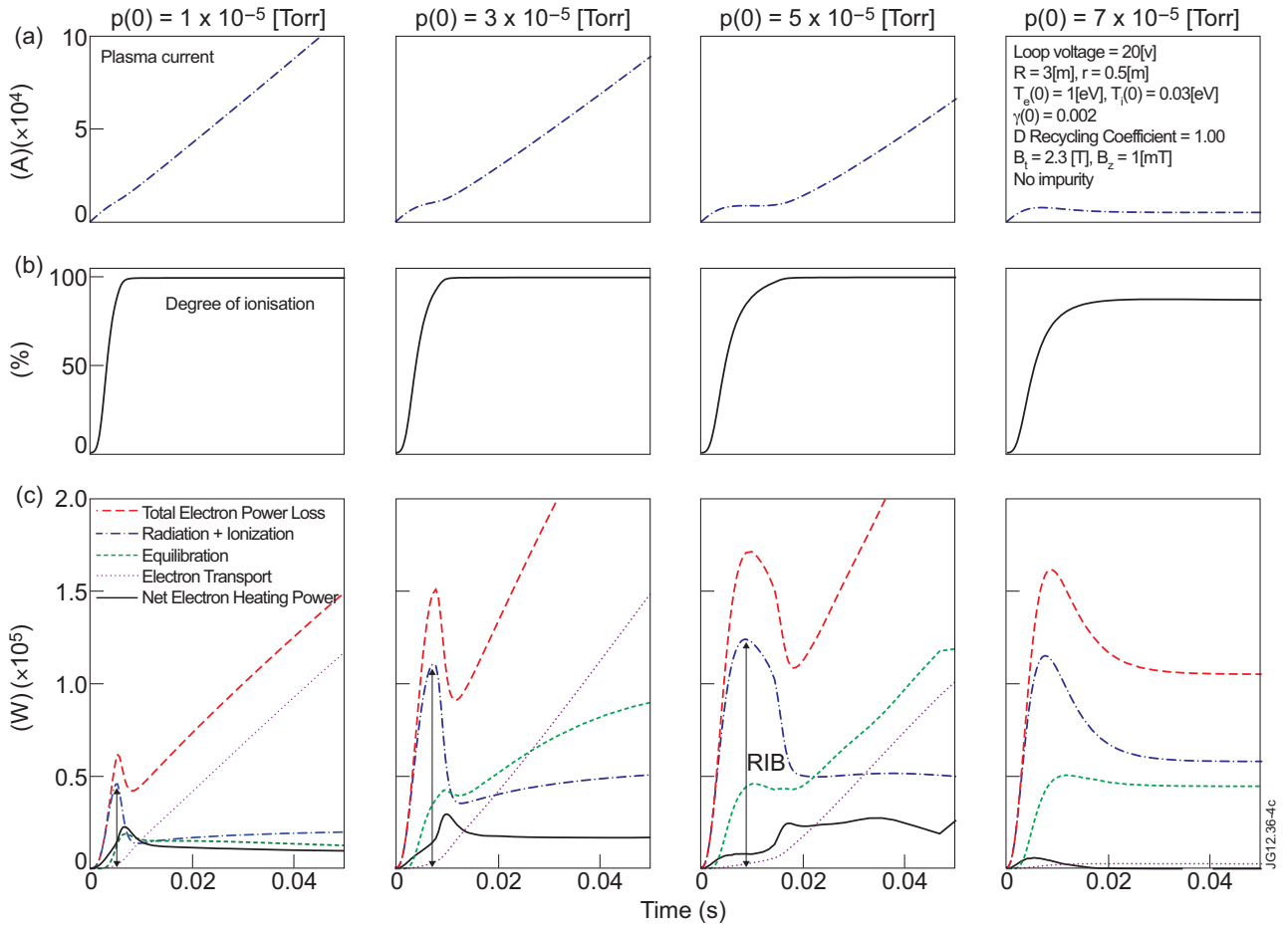


Figure 4.5: *DYON* simulation results for a pure deuterium plasma for various prefill pressures. The figures show (a) the plasma current, (b) the degree of ionization, and (c) various electron power losses at different prefill gas pressures,  $1 \times 10^{-5}$ ,  $3 \times 10^{-5}$ ,  $5 \times 10^{-5}$ , and  $7 \times 10^{-5}$  [Torr]. The assumed loop voltage and plasma parameters are shown in Table 4.1. Under the given condition, a critical prefill gas pressure for  $I_p$  ramp-up exists between  $5 \times 10^{-5}$  and  $7 \times 10^{-5}$  [Torr]. Prefill gases are almost fully ionized in the cases of successful  $I_p$  ramp-up while they are not fully ionized in the cases of failure. The colored lines in (c) indicate  $P_{Loss}$  (dashed red),  $P_{equi}$  (dashed green),  $P_{conv}^e$  (dotted cyan), and  $P_{rad+iz}$  (chain blue), respectively. As shown in (c),  $P_{rad+iz}$  is dominant in  $P_{Loss}$  during the burn-through phase, and its peak values coincide the RIB. The RIB increases with prefill gas pressure, thereby increasing  $P_{Loss}$  maximum. That is, the higher the prefill gas pressure, the larger the  $P_{Loss}$  maximum.

burn-through phase does not vary significantly as shown in Figure 4.4 (c), Equation (4.12) is another indication for the increase in RIB with prefill gas pressure.

The required electric field to overcome the RIB,  $E_{RIB}$ , can also be calculated using Equation (4.12), i.e.  $P_{Oh} = P_{rad+iz}(t_{RIB})$ . Since the ohmic heating power  $P_{Oh}$  is  $V_p(E^2/\eta_s)$ , the required electric field  $E_{RIB}$  is

$$E_{RIB}^2 = \frac{\eta_s V_V \langle \sigma v \rangle_{rad+iz} (T_e) n_D^0(0)^2}{4V_p} \quad (4.13)$$

$$E_{RIB} = 0.011 \sqrt{\frac{V_V \langle \sigma v \rangle_{rad+iz} (T_e)}{V_p T_e^{3/2}}} \times n_D^0(0)$$

where  $\eta_s$  is Spitzer resistivity, i.e.  $\eta_s = 5 \times 10^{-4} \times T_e^{-3/2} [eV][1]$ . These results will be used in chapter 6 of the thesis (section 6.5), which describes the operation space for plasma burn-through at JET.

## 4.4 Summary and discussion

In this chapter, key physics aspects in the plasma burn-through phase for pure deuterium are investigated with the DYON code. The criterion for plasma burn-through is explained with the Radiation and Ionization Barrier (RIB) and the critical degree of ionization  $\gamma_{iz}(t_{RIB})$ .

It is shown that  $dT_e/dt > 0$  is necessary for  $I_p$  ramp-up in the current ramp-up phase. In order for  $T_e$  to increase, the background gas must be fully ionized i.e. plasma burn-through. The requirements for plasma burn-through are investigated using the DYON simulations assuming a pure deuterium plasma, and the required electric field is derived in an analytical way.

It should be noted that impurities resulting from the plasma wall interaction at the wall can influence the requirement of plasma burn-through. Significant impurity content would require higher toroidal loop voltage. The effects of impurities are modelled in the DYON code. The PWI models for the carbon wall and the ITER-like wall in JET are introduced in chapter 5, and the operation space obtained by Equation (4.13) are compared with the DYON simulation results in chapter 6.

# Chapter 5

## New models for the carbon wall and the ITER-like wall in JET

### 5.1 Introduction

In order to achieve the required degree of ionization during the plasma burn-through phase, the total heating power of the plasma (ohmic heating) must exceed the maximum of the total electron power loss. The electron power loss in the burn-through phase is dominated by the radiation and ionization power losses. Since the impurities can result in significant radiation and ionization power loss until they are fully ionized [4], not only the burn-through of the prefill gas (Deuterium) but also the burn-through of the impurities from the first wall is very important. In section 5.2, the experimental results obtained in JET are analyzed to show the effects of the different first wall on the Radiation and Ionization Barrier (RIB).

Previously, the effect of impurities on plasma burn-through in ITER has been simulated assuming a constant content of carbon and beryllium [6]. In order to simulate the impurity effects in the burn-through phase, the evolution of impurity densities should be calculated considering Plasma Wall Interaction (PWI) effects. In this chapter, we present the new models for the carbon wall and the ITER-like wall (Be/W) in JET. The dynamic recycling coefficient model and additional gas fuelling model are introduced in section 5.3. The sputtering models for the different wall conditions are explained in section 5.4.1 (carbon wall) and section 5.4.2 (beryl-

lithium wall), respectively. The DYON simulation results for the different walls are compared in section 5.5.

## 5.2 Impurity effects on plasma burn-through at JET with carbon wall and ITER-like wall.

The ionization power loss and the radiated power loss are functions of the product of electron and deuterium atom densities, i.e.  $n_e n_d^0$ . Hence, both power loss terms change as ionization proceeds. The radiation barrier, which is defined as the maximum of the radiated power loss during the plasma burn-through phase, is directly measurable using bolometry. Hence, the radiation barrier is very useful to see the dependency of total electron power loss on the impurity from the wall. In this section, the effects of impurity influx on the radiation barrier in the carbon wall JET and the beryllium wall JET are compared.

In order to calculate the impurity influx, we need to know the electron temperature  $T_e$  since the inverse photon efficiency is a function of  $T_e$ . The  $T_e$  at the peak of a specific line emission can be obtained by using the fractional abundance in non-coronal equilibrium. In section 5.2.1, the details about this method are explained. In section 5.2.2, the correlation between the impurity influx and the radiation barrier in JET is presented.

### 5.2.1 Fractional abundance of impurity in non-coronal equilibrium

The impurity influx  $\Gamma_I^{z+}[m^{-2}s^{-1}]$  can be calculated using a specific line emission from the impurity,  $I^{\lambda[nm]}[photons\ m^{-2}s^{-1}]$ , and the corresponding inverse photon efficiency  $SXB(T_e)$ ,

$$SXB(T_e) = \frac{\langle \sigma v \rangle_{iz}}{b_r \langle \sigma v \rangle_{exc,lm}} \quad (5.1)$$

where  $\langle \sigma v \rangle_{iz}$  and  $\langle \sigma v \rangle_{exc,lm}$  are the ionization rate coefficient and the excitation rate coefficient for transition from state  $l$  to  $m$ , resulting in the subsequent release of a specific line emission, and  $b_r$  is the branching ratio for the particular optical transition, i.e.  $SXB = \text{ionizations/photon}$ . Hence, the particle influx into the charge state can be calculated by photomultiplier tube data measuring a specific line emission, i.e.  $\Gamma_I^{z+}[m^{-2}s^{-1}] =$

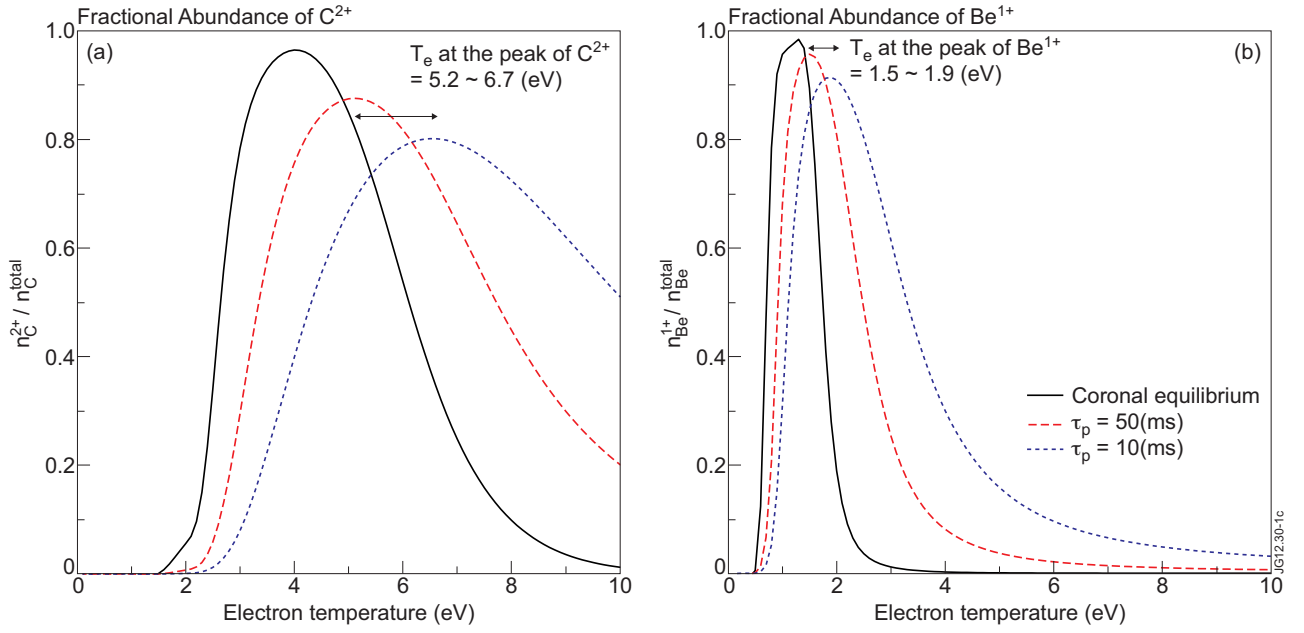


Figure 5.1: (a) and (b) show the fractional abundance of  $C^{2+}$  and  $Be^{1+}$ , respectively. In both figures, each line indicates the assumed equilibrium or particle confinement time : solid black (Coronal equilibrium), dashed red ( $\tau_p = 50$ [ms]), and dashed blue ( $\tau_p = 10$ [ms]).

$I^{\lambda[nm]}[\text{photons } m^{-2}s^{-1}] \times SXB^{\lambda[nm]}(T_e)$  [26]. The photomultiplier tube data measures the number of photons, integrated along a line of sight. In this section, the averaged value of the photomultiplier tube data measured along two orthogonal lines of sight, i.e. vertical and horizontal lines of sight, is used for the impurity influx calculation. The values of SXB used in this thesis are adopted from the Atomic Data and Analysis Structure(ADAS) package [25].

In order to calculate the impurity influx at a specific moment, the corresponding electron temperature  $T_e$  is required as SXB is a function of  $T_e$ . However, the measurement of  $T_e$  during the burn-through phase is not accurate due to the significant diagnostic errors in this phase. During the plasma burn-through phase, the dominant charge state of the impurity rises as  $T_e$  increases. This results in a maximum in time (peak) of a specific line emission of the impurity. In coronal equilibrium, the fractional abundance of the charge state of the impurity is determined by  $T_e$ . Hence, the corresponding  $T_e$  at the peak of the photon emission can be obtained using the fractional abundance. However, in the case of the plasma burn-through phase, coronal equilibrium is not valid due to the significant particle transport along the open magnetic field lines. In order to estimate the correct  $T_e$  at the peak of the line emission, the

fractional abundance should be calculated by the particle balance of each charge state including particle transport. For this calculation, we assume that all neutrals are backscattered and ions are recycled to neutrals at the wall with 1 recycling coefficient. According to this assumption, neutral influx is only from ion recycling, and the particle balance equation can be simplified as shown below.

$$0 = - \langle \sigma v \rangle_{I,iz}^0 n_I^0 + \langle \sigma v \rangle_{I,rec}^{1+} n_I^{1+} + \sum_z \frac{n_I^{z+}}{n_e \tau_p} \quad (5.2)$$

$$0 = \langle \sigma v \rangle_{I,iz}^{(z-1)+} n_I^{(z-1)+} - \langle \sigma v \rangle_{I,iz}^{z+} n_I^{z+} + \langle \sigma v \rangle_{I,rec}^{(z+1)+} n_I^{(z+1)+} - \langle \sigma v \rangle_{I,rec}^{z+} n_I^{z+} - \frac{n_I^{z+}}{n_e \tau_p}$$

where  $\tau_p$  is the particle confinement time for ions, and  $\langle \sigma v \rangle_{I,iz}^{z+}$  and  $\langle \sigma v \rangle_{I,rec}^{z+}$  indicate the rate coefficients for ionization and recombination, respectively. The confinement time  $\tau_p$  during the burn-through phase can be approximately calculated as shown below.

$$\tau_p[sec] = \frac{L_f[m]}{C_s[m/sec]} \quad (5.3)$$

where  $L_f$  is an effective connection length[10],

$$L_f[m] = 0.25 \times a[m] \times \frac{B_\phi[T]}{B_\perp[T]}, \quad (5.4)$$

and  $C_s$  is the sound speed,

$$C_s[m/sec] = \sqrt{\frac{T_e[Joule]}{m_D[kg]}}. \quad (5.5)$$

$m_D$  is the mass of deuterium. In the case of the burn-through phase in JET, we can assume that the minor radius  $a = 0.8[m]$ , the toroidal magnetic field  $B_\phi = 2.3[T]$ , the stray magnetic field  $B_\perp = 10^{-3}[T]$ , and  $T_e = 5 \sim 10[eV]$ . The resultant  $\tau_p$  is  $29[msec]$  when  $T_e = 5[eV]$  and  $21[msec]$  when  $T_e = 10[eV]$ . According to this, it can be justified that  $\tau_p$  during the burn-through phase in JET is between 10 and  $50[msec]$ .

Figure 5.1 shows the fractional abundances of  $C^{2+}$  and  $Be^{1+}$  for  $\tau_p$  values of  $10[msec]$  and  $50[msec]$ . Compared to the case of coronal equilibrium ( $\tau_p = \infty$ ), the peaks of  $C^{2+}$  and  $Be^{1+}$  are shifted to higher  $T_e$  due to the transport effect. According to Figure 5.1, the range of  $T_e$  at the peak of  $C^{2+}$  and  $Be^{1+}$  are  $5.2 \sim 6.7[eV]$  and  $1.5 \sim 1.9[eV]$ , respectively.

## 5.2.2 Radiation barrier versus impurity influx in JET

The influx of  $C^{2+}$  and  $Be^{1+}$  are calculated by using photomultiplier tube data ( $465[nm]$  of  $C^{2+}$  and  $527[nm]$  of  $Be^{1+}$ ) and SXB values. Based on the range of  $T_e$  in Figure 5.1,  $T_e$  at each peak

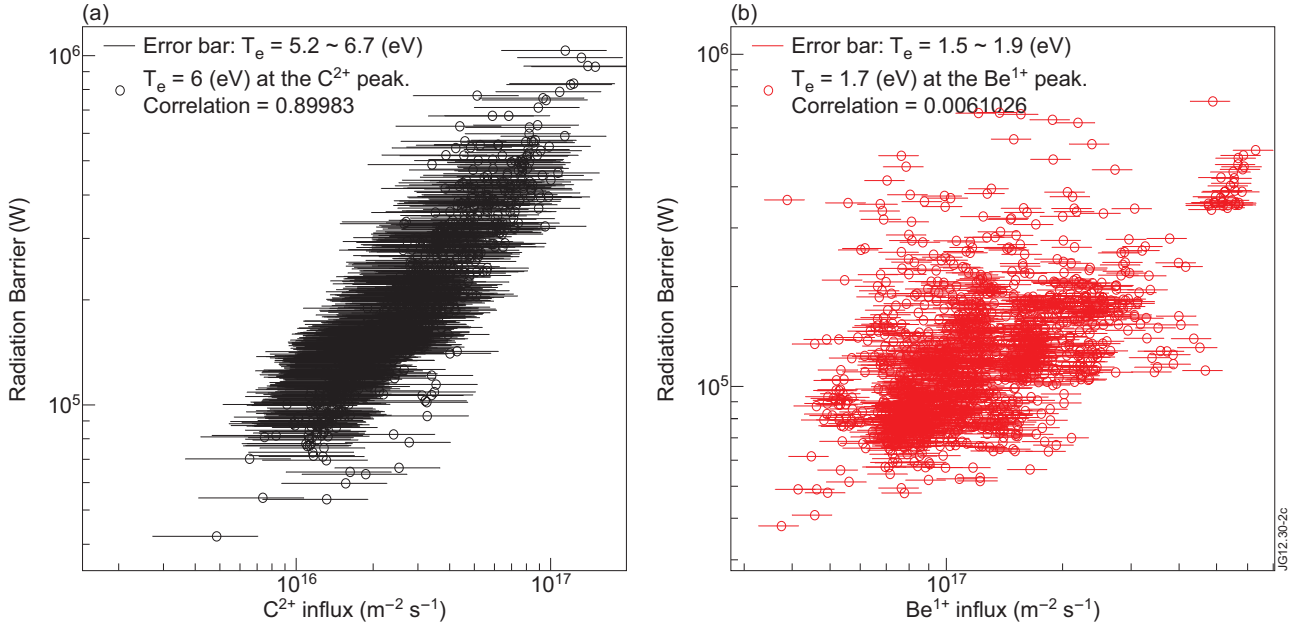


Figure 5.2: (a) shows the radiation barrier at different  $C^{2+}$  influx calculated by the  $T_e(t_{C^{2+}peak}) = 6[eV]$  in the carbon wall JET. The error bars of  $C^{2+}$  influx are for  $T_e(t_{C^{2+}peak}) = 5.2$  or  $6.7[eV]$ . (b) indicates the radiation barrier at different  $Be^{1+}$  influx calculated by the  $T_e(t_{Be^{1+}peak}) = 1.7[eV]$  in the ITER-like wall. The error bars of  $Be^{1+}$  influx are for  $T_e(t_{Be^{1+}peak}) = 1.5$  or  $1.9[eV]$ . The linear correlation coefficients for the carbon wall and the ITER-like wall are  $0.89983$  and  $0.0061026$ , respectively.

of the line emission are assumed as the mean values,  $6[eV]$  ( $C^{2+}$ ) and  $1.7[eV]$  ( $Be^{1+}$ ).

$$\Gamma_C^{2+}[m^{-2}sec^{-1}] = I^{465[nm]}[photons\ m^{-2}s^{-1}] \times SXB^{465[nm]}(6[eV]) \quad (5.6)$$

$$\Gamma_{Be}^{1+}[m^{-2}sec^{-1}] = I^{527[nm]}[photons\ m^{-2}s^{-1}] \times SXB^{527[nm]}(1.7[eV]) \quad (5.7)$$

In this calculation,  $n_e$  is assumed to be  $10^{18}[m^{-3}]$ , however the dependence of SXB on  $n_e$  is small enough to be ignored. The calculated impurity influx and the radiation barrier measured by bolometry in JET are presented in Figure 5.2. The error bars in Figure 5.2 correspond to the range of  $T_e$  obtained in Figure 5.1.

It should be noted that the linear correlation coefficient in the carbon wall JET is  $0.9$  while it is only  $0.0061$  for the ITER-like wall. This implies that the radiation barrier was strongly affected by the carbon influx in the carbon wall JET, but the effect of beryllium influx is not important in the ITER-like wall.

### 5.3 Deuterium recycling coefficient and gas fuelling

Once deuterium ions arrive at the vessel wall, they are retained or they release deuterium atoms from the wall. The fraction of the deuterium atom influx to the deuterium ion outflux is defined by the deuterium recycling coefficient  $Y_D^D$ . In the burn-through phase, this deuterium recycling coefficient can be higher than 1 if the wall is saturated from the previous discharges. However, if the deuterium retention at the wall is not saturated, the incident deuterium ions are retained rather than being recycled, i.e.  $Y_D^D$  is lower than 1. The deuterium recycling coefficient, which was somewhat higher or smaller than 1, approaches 1 as Plasma Wall Interaction (PWI) processes proceed. In order to take this change of deuterium recycling coefficient into account, an exponential saturation function is used as shown below.

$$Y_D^D(t) = c_1 - c_2(1 - \exp(-\frac{t}{c_3})) \quad (5.8)$$

According to Equation (5.8), the dynamic behaviour of the deuterium recycling coefficient  $Y_D^D(t)$  is adjusted by the combination of constants  $c_1$ ,  $c_2$ , and  $c_3$ . The initial value of the deuterium recycling coefficient  $Y_D^D(t=0)$  is determined by  $c_1$ , and  $Y_D^D(t)$  approaches  $c_1 - c_2$  as  $t$  increases. The temporal change of  $Y_D^D(t)$  is adjusted by  $c_3$ .

It is observed at JET experiments that during the plasma burn-through phase the carbon wall releases deuterium atoms into the plasma, while the beryllium wall pumps them out from the plasma [12]. Figure 5.3 (a) shows the differences in deuterium recycling coefficient used in the DYON simulations for the carbon wall and the ITER-like wall. For DYON simulations with the carbon wall, the exponential decay model was used. However, for DYON simulations with the ITER-like wall, the exponential growing model is used.

Figure 5.3 (b) indicates the gas fuelling used in the simulations for the carbon wall and the ITER-like wall. There was no gas fuelling model in the simulations for the carbon wall, conforming with the JET experiments with the carbon wall. However, deuterium gas is injected around 0.1 [sec] in JET experiments with the ITER-like wall. This additional fuelling is modelled in the DYON simulation for the ITER-like wall. In the simulation the efficiency of the gas dosing to fuel the plasma can be adjusted to provide a match to the measured plasma density rise.

The  $D$  recycling and additional gas fuelling influence the particle balance of deuterium atoms



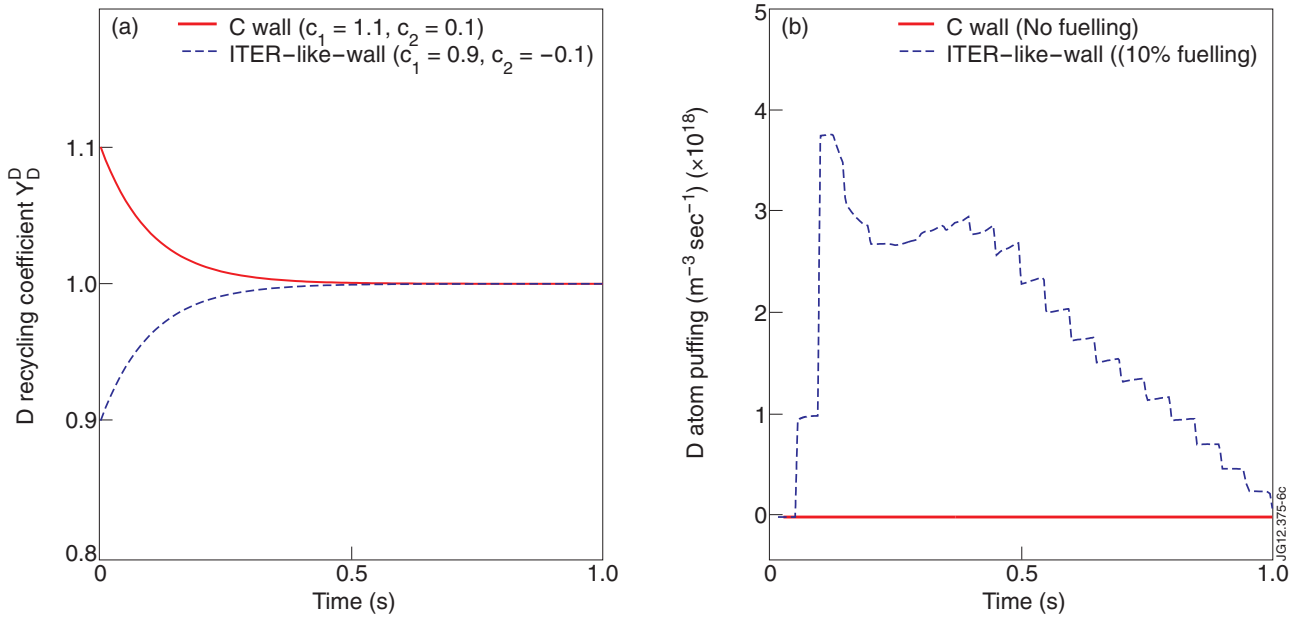


Figure 5.3: (a)  $D$  recycling coefficient and (b) Gas fuelling used in the DYON simulations with a carbon wall or ITER-like wall

as shown below [36],

$$\begin{aligned} \frac{dn_D^0}{dt} = & \frac{1}{\gamma_n^D V_V} (V_p \langle \sigma v \rangle_{D,rec}^{1+\rightarrow 0} n_e n_D^{1+} \\ & - V_n^D \langle \sigma v \rangle_{D,iz}^{0\rightarrow 1+} n_e n_D^0 - V_n^D \sum_I \sum_{z \geq 1} \langle \sigma v \rangle_{I,cx}^{z+\rightarrow (z-1)+} n_D^0 n_I^{z+}) + \frac{\Gamma_{D,in}^{total}}{\gamma_n^D V_V}. \end{aligned} \quad (5.9)$$

The total influx of deuterium atoms  $\Gamma_{D,in}^{total}$  is

$$\Gamma_{D,in}^{total} = V_p \frac{Y_D^D n_D^{1+}}{\tau_D} + \Gamma_{D,in}^{eff} \quad (5.10)$$

where on the right hand side the first and second terms are  $D$  recycling and additional gas fuelling, respectively.

## 5.4 Sputtering models

Figure 5.4 shows the particle balance including plasma wall interactions. A prefill gas of the vacuum chamber provides deuterium (D) atoms. The D atoms are ionized, and D ions recombine with free electrons to return to neutrals. Deuterium ions are also transported to the wall, resulting in recycling of D atoms or sputtering of impurity atoms. Impurity atoms are ionized,

and can recombine with free electrons reducing their charge state. Impurity ions are also transported to the wall; the impurity wall-sputtering generates additional impurity atoms. [26].

The electron power losses due to the radiations and ionizations, i.e.  $P_{rad} + P_{iz}$ , are dominant in the total electron power loss during the plasma burn-through phase. Since  $P_{rad} + P_{iz}$  are significantly affected by impurity content [5], a treatment for impurity evolution is of crucial importance. In order to take them into account, impurity transport and PWI effects are included in the DYON code. In this section,  $Y_{incident}^{sputtered\ or\ recycled}$  represents an impurity sputtering yield (or a recycling coefficient) due to deuterium ion or impurity ion bombardment. Here, the superscript indicates the sputtered (or recycled) impurity, and the subscript represents an incident ion, including deuterium and impurities.

### 5.4.1 Sputtering models in the carbon wall

For sputtering, the species of the dominant impurity is determined by the wall material. In JET experiments with the carbon-wall, hydrocarbon such as  $CD_4$  is a major impurity [26].

While a physical sputtering yield is a function of incident ion energy [26], a chemical sputtering yield is weakly dependent on incident ion energy. For the carbon wall, chemical sputtering dominates physical sputtering when incident deuterium ion energy is lower than  $100[eV]$  [27], which is a typical ion temperature in the burn-through phase. In addition, in laboratory plasma experiments the carbon sputtering yield due to the low-energy deuterium ion bombardment,  $Y_D^C$ , has been measured to be less than 0.03 [27] when a substrate temperature is around  $500[K]$  [27], which is similar to the wall temperature in JET. Based on this,  $Y_D^C$  in the burn-through simulation of the carbon-wall JET is assumed to be a constant and equal to 0.03.

Oxygen is another primary intrinsic impurity in tokamaks. Oxygen is not only a strong radiator in a plasma, but it can also lead to a high level of carbon content [26]. When there is oxygen bombardment on a carbon surface with an energy of a several tens of  $eV$ , carbon monoxide  $CO$  is dominantly emitted with sputtering yield about 1.0 [37]. Therefore, it is assumed that an oxygen atom and a carbon atom are ejected from the wall by oxygen ion bombardment, i.e.  $Y_O^O \equiv 1.0$  and  $Y_O^C \equiv 1.0$ .

Once impurity ions arrive at the vessel wall, they are assumed to be recycled to a neutral impurity according to their recycling coefficient  $Y_I^I$  which is assumed to be the same for all ionic charge states. The oxygen recycling coefficient,  $Y_O^O$ , and the carbon recycling coefficient,  $Y_C^C$ , are assumed to be 1 and 0, respectively, according to their volatility. Figure 5.5 describes the sputtering model used for the carbon wall. The sputtering yields and recycling coefficients used in the model are summarized in Table 5.1.

The DYON simulation results using the wall-sputtering model for the carbon wall have shown good agreement with the experimental data of JET with the carbon wall as will be presented in section 6.3.2 [36]. However, it should be noted that the chemical sputtering model used was

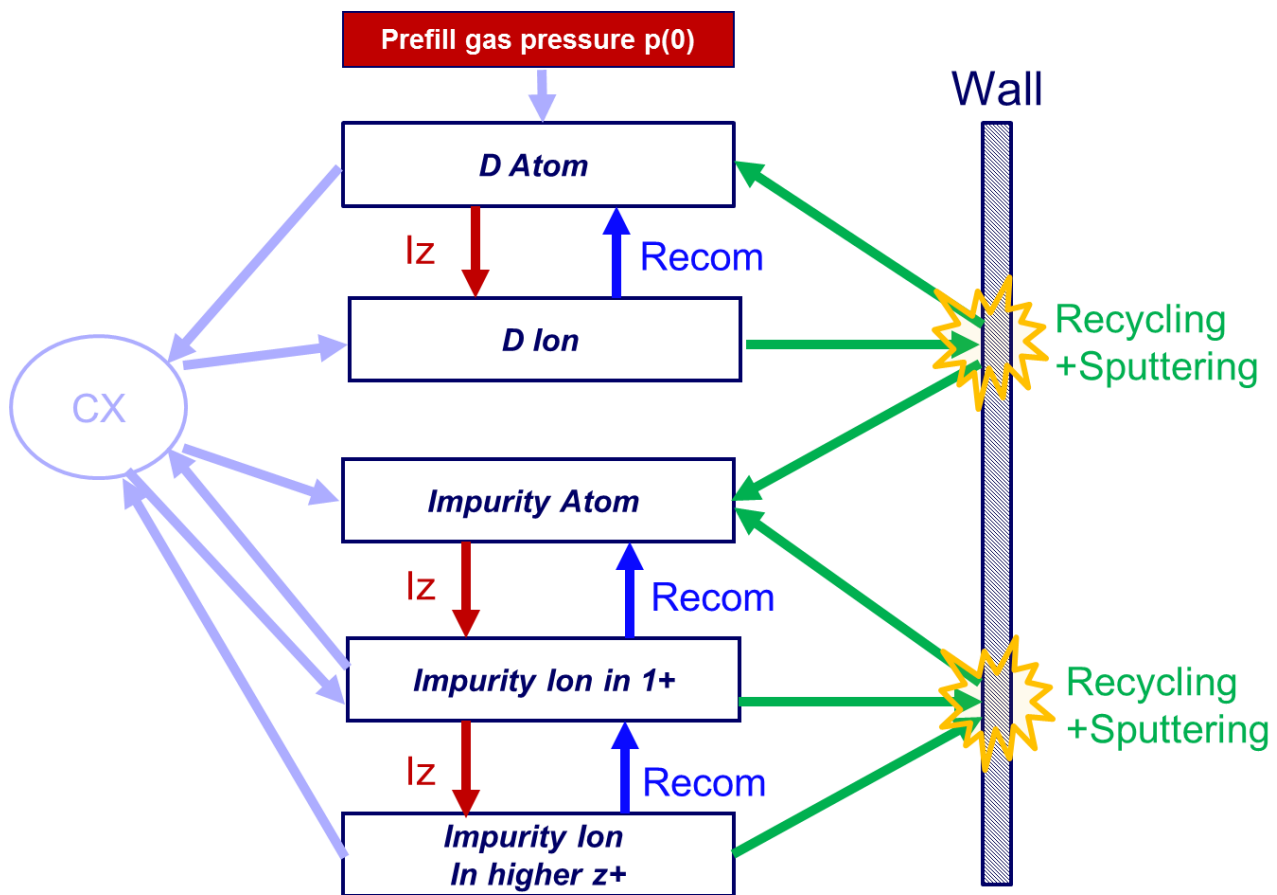


Figure 5.4: Particle balance in a plasma during the plasma burn-through phase. *CX* is charge exchange reaction between *D* atoms and impurity ions; it is assumed that only *D* atoms are an electron donor in charge exchange reactions. *Iz* is impact ionization by free electrons, and *Recom* is Recombination reaction. *Wall* is the surrounding plasma facing component; in this study the wall material is carbon or beryllium.

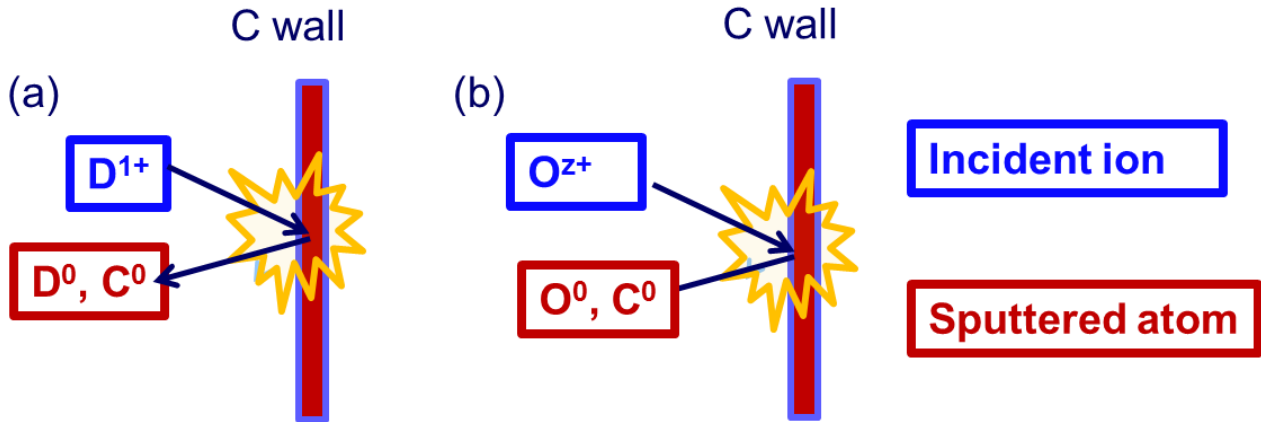


Figure 5.5: PWI models used in the DYON simulations with a carbon wall.

Sputtered(recycled) atom \ incident ion	$D^{1+}$	$C^{z+}$	$O^{z+}$
$D^0$	Equation (5.8)	$Y_C^D = 0$	$Y_O^D = 0$
$C^0$	$Y_D^C = 0.03$	$Y_C^C = 0$	$Y_O^C = 1$
$O^0$	$Y_D^O = 0$	$Y_C^O = 0$	$Y_O^O = 1$

Table 5.1: Sputtering yields and recycling coefficients.

a simplified model, without considering some issues such as chemical sputtering by neutrals, physical sputtering, and a-CH film formation on the wall surface. These can increase the carbon sputtering yield.

#### 5.4.2 Sputtering models for the ITER-like wall

One of the main differences of the beryllium wall compared to the carbon wall is that physical sputtering is dominant due to its low threshold energy [38]. It is well known that a physical sputtering yield is a function of incident ion energy. The Bohdansky formula for physical sputtering yield has been given as [28],[29]

$$Y = Q \times S_n(\epsilon) \times g(\delta) \quad (5.11)$$

where  $Q$  is a yield factor and  $S_n$  is nuclear stopping cross-section which is given by

$$S_n = \frac{3.441\sqrt{\epsilon} \ln(\epsilon + 2.718)}{1 + 6.355\sqrt{\epsilon} + \epsilon(6.882\sqrt{\epsilon} - 1.708)}. \quad (5.12)$$

$\epsilon$  is defined to be  $E_0/E_{TF}$  where  $E_0$  and  $E_{TF}$  are the ion wall-impact energy and the Thomas-Fermi energy, respectively [28],[29]. Assuming a typical sheath formation of negative potential at the wall [26], the ion wall-impact energy  $E_0$  can be calculated as  $2kT_i + 3kT_e$ , i.e. ion's energy gain within a sheath is approximately  $3kT_e$ . The function  $g(\delta)$  is defined to be

$$g(\delta) = (1 - \delta^{2/3})(1 - \delta)^2, \quad (5.13)$$

where  $\delta$  is defined to be  $E_{th}/E_0$  [26].  $E_{th}$  indicates the threshold energy for physical sputtering.

Although there was a small air leak ( $\sim 1.5 \times 10^{-6}$  [Torr  $m^3/sec$ ]) in JET during the 2011/2012 experimental campaigns with the ITER-like wall, the oxygen level in the residual gas in the vacuum vessel remained lower than in JET with the carbon wall [39]. This implies the oxygen in the air forms a BeO monolayer on the wall. Figure 5.6 describes the wall-sputtering models used in the DYON simulation for the ITER-like wall. Deuterium, carbon, oxygen, and beryllium ions are modelled to be incident ions on the BeO wall (or pure Be wall), resulting in Be (and O) sputtering due to the wall erosion. Since the threshold energy of the tungsten divertor significantly exceeds the range of incident ion energy during the burn-through phase, (e.g.  $E_{th}$  of tungsten is 220[eV] with D ion bombardment. [26]), tungsten sputtering is not taken into account here. The physical sputtering yield is subject to the oblique angle of incident ions. However, it is difficult to find the effective oblique incidence angle for 0D simulations. In addition, a rapid evolution of the field line angles or even the magnetic geometry during plasma formation from open to closed field lines makes it difficult to assess the incidence angle. For a starting point of this study, we assume normal incidence. In this case, the Bohdansky formulae agrees well with more sophisticated models, such as TRIM [40].

The BeO layer contacting the plasma would be eroded by the plasma. It is assumed that the surface of the Be wall is oxidized first, and the BeO layer is removed by ion bombardments after a certain erosion period, changing the BeO wall to the pure Be wall. Including the effects

of the BeO layer erosion, the impurity influx due to the physical sputtering is modelled as

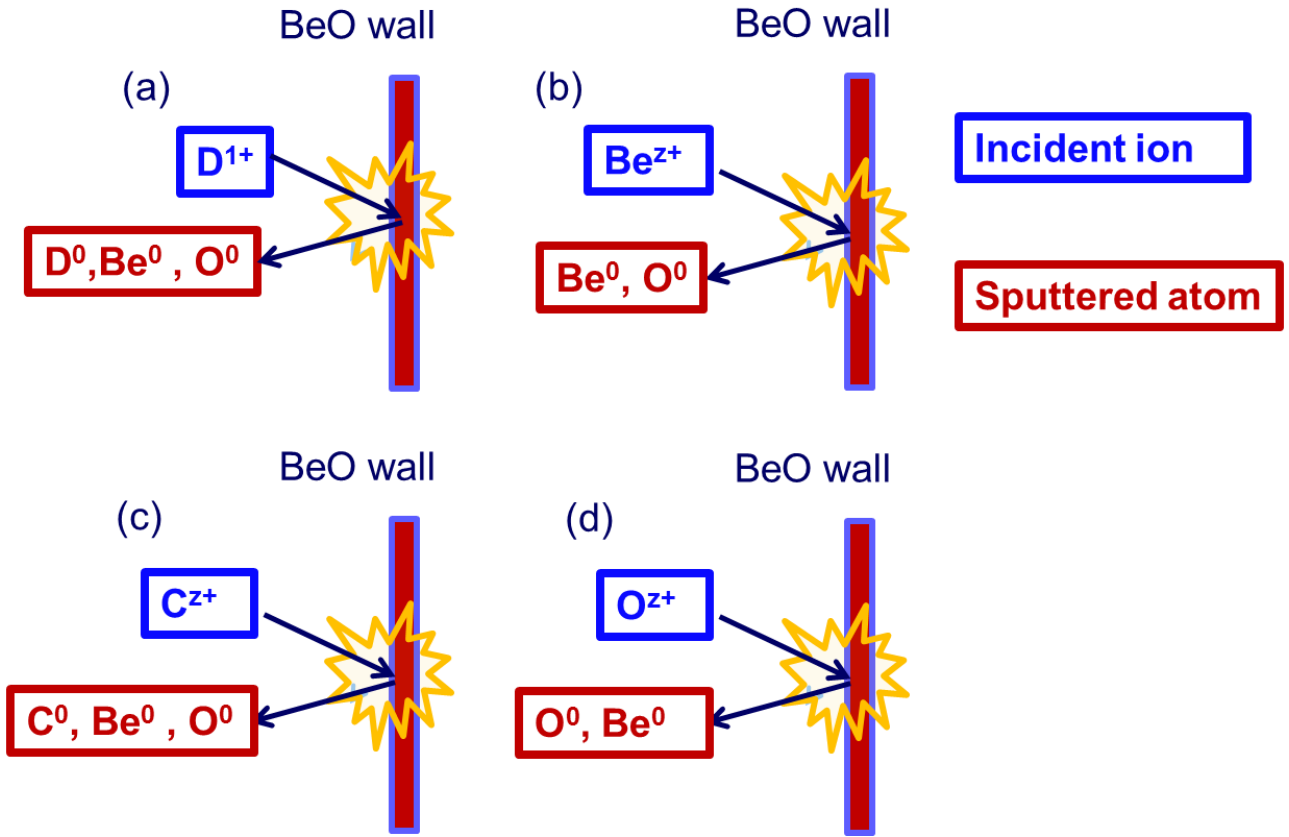
$$\begin{aligned}
\Gamma_{Be,in}^0 &= V_p \sum_A \sum_{z \geq 1} (C_{BeO} Y_A^{BeO} + (1 - C_{BeO}) Y_A^{Be}) \frac{n_A^{z+}}{\tau_p} \\
\Gamma_{O,in}^0 &= V_p \sum_A \sum_{z \geq 1} C_{BeO} Y_A^{BeO} \frac{n_A^{z+}}{\tau_p} \\
\Gamma_{D,in}^0 &= V_p Y_D^D \frac{n_D^{1+}}{\tau_p} \\
\Gamma_{C,in}^0 &= V_p \sum_{z \geq 1} Y_D^D \frac{n_C^{z+}}{\tau_p}
\end{aligned} \tag{5.14}$$

where superscript and subscript of  $Y$  indicate the sputtered (or recycled) species and an incident ion, respectively. For example,  $Y_D^{BeO}$  is BeO sputtering yield due to D ion bombardment.  $C_{BeO}$  is defined as the BeO erosion coefficient, which is used to model the transition from BeO wall to Be wall at the end of the BeO layer erosion time  $\tau_{erosion}$ .  $C_{BeO}$  is 1 before  $\tau_{erosion}$  and decreases to 0 after  $\tau_{erosion}$ .  $\tau_{erosion}$  is adjusted to be 60 [msec] based on obtaining agreement of the synthetic data for bolometry and  $Be^{1+}$  photomultiplier tube signals against the measured data. The parameters required to calculate physical sputtering yields of the BeO wall (or pure Be wall) are given in Table 5.2.

The incident ions are also recycled as neutrals at the wall with a fraction, called the recycling coefficient. It is observed at JET that during the plasma burn-through phase the carbon wall releases deuterium into the plasma, while the beryllium wall pumps them from the plasma [12]. Hence, (as given in section 5.3) for DYON simulations with the carbon wall, an exponential decay model was used i.e.  $Y_D^D = 1.1 \rightarrow 1$ . However, the deuterium recycling coefficient with the ITER-like wall is modelled to grow and approach 1 during the plasma burn-through phase. That is, the exponential growing model is used for DYON simulations with the ITER-like wall i.e.  $Y_D^D = 0.9 \rightarrow 1$ . This is consistent with the outgassing observed after discharges with the ITER-like wall [41].

## 5.5 Simulation results of the DYON code

In order to investigate the PWI effects on the Radiation and Ionization Barrier, plasma burn-through in the carbon wall and the beryllium wall is simulated using the DYON code [36]. Identical conditions (prefill gas pressure =  $5 \times 10^{-5}$ [Torr], loop voltage = 25[V]) are used for

Figure 5.6: *PWI models used in DYON simulations with ITER-like wall*

Incident ion / target	$D^{1+} / \text{Be}$	$D^{1+} / \text{BeO}$	$\text{Be}^{z+} / \text{Be}$	$C^{z+} / \text{Be}$	$O^{z+} / \text{Be}$
$E_{th}[\text{eV}]$	10	29	23	40	70
$E_{TF}[\text{eV}]$	282	444	2208	4152	6970
$Q$	0.22	0.13	0.77	1.6	1.3

Table 5.2: *Parameters for physical sputtering yield of beryllium in the ITER-Like Wall [26],[42]*

the simulations except the wall sputtering models. Since chemical sputtering yield is not subject to an incident ion energy, the sputtering yield in the carbon wall is assumed to be constant as described in section 5.4.1. In the case of beryllium wall, the PWI effects are dominated by physical sputtering [38]. The physical sputtering yield is a function of  $T_e$  and  $T_i$ . The formula for physical sputtering given in section 5.4.2 is used for the simulation. Figure 5.7 shows the simulation results in the carbon wall (left) and the pure beryllium wall (right). The sputtering yields in the simulation are shown in Figure 5.7 (e).

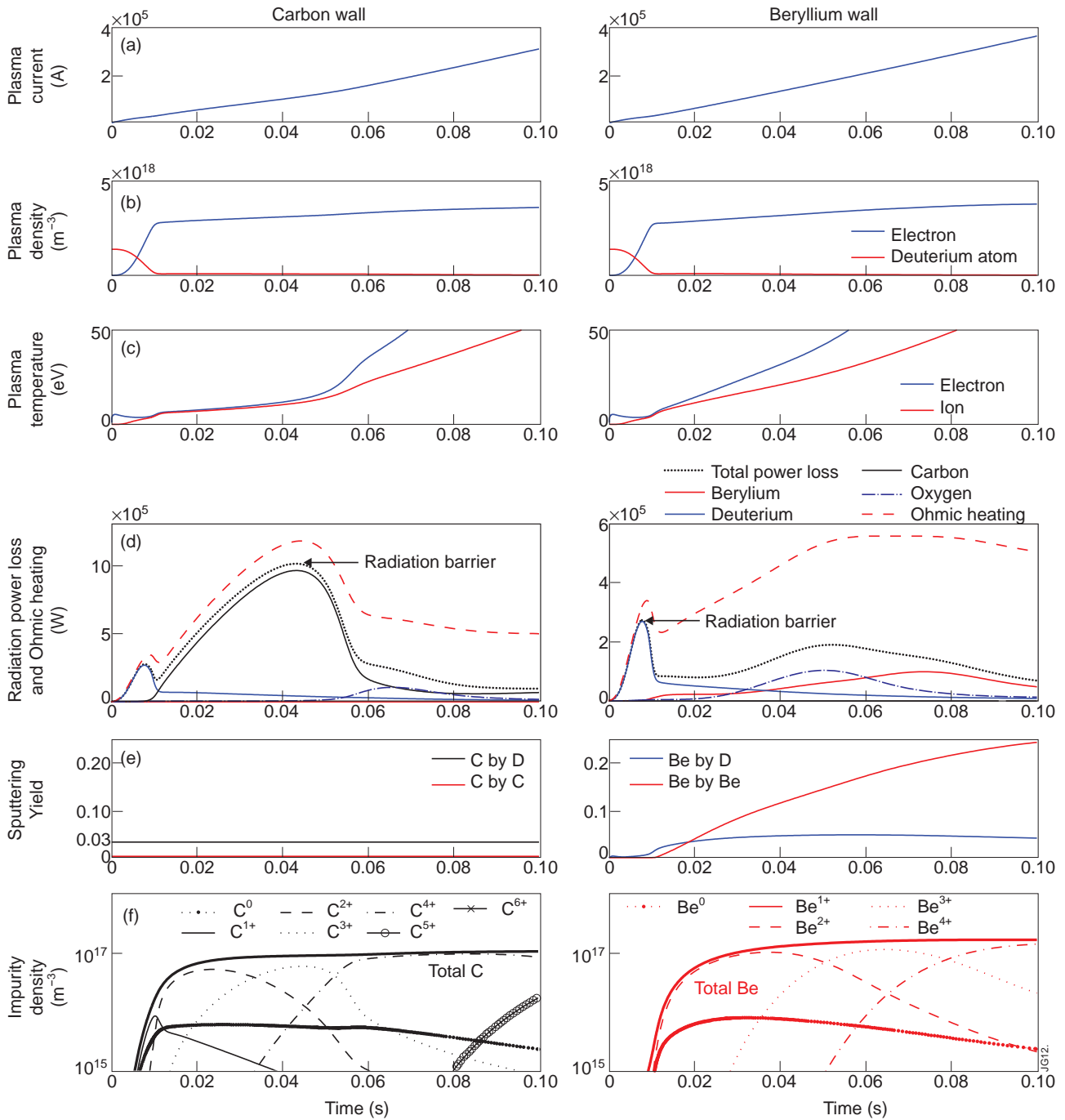


Figure 5.7: Simulation results in the carbon wall and the beryllium wall under the identical conditions are presented: (a) Plasma current, (b) electron density (blue) and deuterium atom density (red), (c) electron temperature (blue) and ion temperature (red), (d) radiation power losses and ohmic heating power (dotted black: total radiation power loss, solid blue: deuterium radiation, solid red: beryllium radiation, solid black: carbon radiation, dashed blue: oxygen radiation, and dashed red: ohmic heating power), (e) sputtering yield (solid black: carbon sputtering due to incident deuterium ion, solid blue: beryllium sputtering due to incident deuterium ion, solid red: self-sputtering yield), (f) impurity densities in each charge state.



Sputtered \ incident	$D^{1+}$	$Be^{z+}$	$C^{z+}$	$O^{z+}$	$N^{z+}$
$D^0$	Equation (5.8)	0	0	0	0
$Be^0$	Equation (5.11)	Equation (5.11)	Equation (5.11)	Equation (5.11)	0
$C^0$	0	0	1	0	0
$O^0$ (BeO wall)	Equation (5.11)	Equation (5.11)	Equation (5.11)	Equation (5.11)	0
$O^0$ (Pure Be wall)	0	0	0	0	0
$N^0$	0	0	0	0	1

Table 5.3: *Sputtering yields and recycling coefficients assumed for the plasma burn-through simulation in the ITER-Like Wall*

As shown in Figure 5.7 (d), for both the the carbon wall and the beryllium wall, ohmic heating power is comparable to the total radiation power loss until the radiation barrier is overcome. Consistently, it is not until the radiation barrier is overcome that  $T_e$  begins to increase, since the significant radiated power losses impede  $T_e$  from increasing. As can be seen in Figure 5.7 (c), it is only after 0.05[sec] and 0.01[sec] that  $T_e$  rises steeply in the carbon wall and the beryllium wall, respectively. This implies that the corresponding radiation barrier are located at 0.05[sec] and 0.01[sec] as indicated in Figure 5.7 (d). The radiation barrier in the carbon wall JET is dominated by the carbon radiation (solid black) whereas it is mainly from the deuterium radiation (solid blue) in the beryllium wall rather than the beryllium radiation (solid red). In other words, the radiation barrier in the beryllium wall is not dependent on the beryllium content whereas it does depend on the carbon for the carbon wall. It should be noted that these simulation results are consistent with the experimental results presented in Figure 5.2.

The maximum radiation from carbon is about 10 times higher than that of beryllium in Figure 5.7 (d), while  $n_e$  and total impurity content do not differ much as shown in Figure 5.7 (b) and (f). The significant difference in the radiation power losses results from the different radiation power coefficients of carbon and beryllium during the burn-through phase.

## 5.6 Summary and discussion

The influx of  $C^{2+}$  and  $Be^{1+}$  during the plasma burn-through phase are calculated from experimental observations assuming non-coronal equilibrium at the each peak of the line emission of the impurities. The observed impurity influx in the carbon wall has a strong linear correlation with the radiation barrier, but such a correlation does not appear in the ITER-like wall at JET. This result is explained with the simulation results of the DYON code using the different PWI models for the carbon wall and the beryllium wall. The radiation barrier in the carbon wall is dominated by the carbon radiation. However, in the beryllium wall, the deuterium radiation is dominant in the radiation barrier. For the beryllium wall, the beryllium impurities from the first wall do not seriously influence on the plasma burn-through. This implies that the required ohmic heating power for plasma burn-through will be lower in the ITER-like wall compared to the carbon wall in cases where the prefill gas pressures are identical.

# Chapter 6

## Comparison of experiments and simulations

### 6.1 Introduction

Even though the plasma burn-through has been simulated previously [6][19][43], quantitative validation of the models against experimental data has not been published extensively. One of the main limitations are the available diagnostic data in tokamak experiments, together with an adequate model to provide the simulations. In order to test whether the model incorporates the key aspects of plasma burn-through physics, its validation process is necessary. Validation of the model is also important for further applications such as ECRH heating power modulation for ECRH-assisted start-up [44] and ferromagnetic effects in superconducting tokamak start-up [45], all of which are based on the burn-through simulation.

The diagnostic system used for validation is introduced in section 6.2. Validation of the new burn-through model against JET experimental data with the carbon wall will be presented in section 6.3. The significance of the new models introduced in chapter 3 will be shown by the simulation results without these new models. In section 6.3.3, simulation results when the parallel transport model or the MK2 current ring model is removed from the DYON code are presented.

The Plasma Wall Interaction (PWI) models for the ITER-Like Wall in JET were introduced

in chapter 5. The recent installation of the ITER-like wall (a combination of beryllium and tungsten protection tiles) at JET [46] enabled us to validate the DYON simulations with experimental results with the beryllium first wall. In section 6.4, the simulation results using the PWI models for the beryllium first wall are compared to JET data with the ITER-like wall.

In order to perform the DYON simulations, values for the initial impurity content, deuterium recycling coefficient, and fuelling efficiency must be specified. However, the information about these parameters is not available. To treat this problem, the effects of those parameters on simulation results will be investigated through parameter scanning, and the results will be discussed. The effects of the parameters assumed in the DYON simulation, i.e. initial impurity content, deuterium recycling coefficient, and fuelling efficiency, are investigated in section 6.4.

In section 6.5, the operation space in JET, defined by the requirement to obtain a Townsend avalanche and plasma burn-through, is presented. The computed (and derived using Equation (4.13)) criterion for plasma burn-through for a pure deuterium plasma, a carbon wall, and a beryllium wall are compared, and the operation space in JET is discussed. A discussion and conclusions are given in section 6.6.

## 6.2 Diagnostic tools used for validation

Figure 6.1 shows EFIT (Equilibrium FITting code) data for the plasma equilibrium and the lines of sight of the diagnostic tools, which are used for validation of the DYON code in JET. The total radiation power loss is obtained from bolometry measurements. Thomson scattering data is used to obtain the volume-averaged value of electron temperature and density. Interferometry data is used for the volume-averaged value of the electron density. The emission rate of photons which have a specific wavelength (465[nm] for  $C^{2+}$ , 656[nm] for  $D\ alpha$ , and 527[nm] for  $Be^{1+}$ ) are measured by photomultiplier tubes of which the lines of sight are vertical and horizontal, respectively, as shown in Figure 6.1. The photomultiplier tube data is averaged using the two measurements of the different lines of sight.

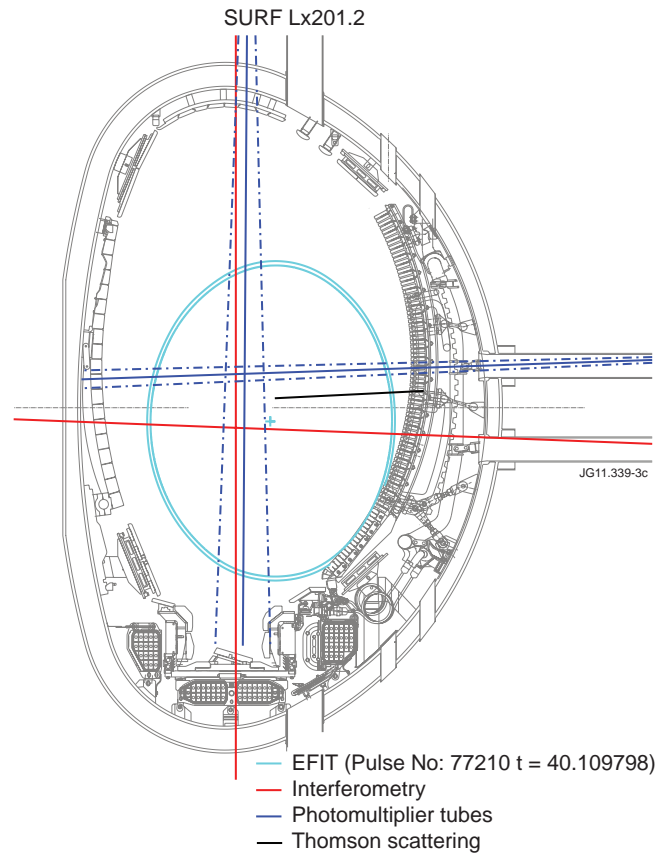


Figure 6.1: (a) cyan circle: The outermost flux surface obtained with EFIT at 109[ms] after plasma initiation, (b) red solid lines: line of sight for interferometry, (c) blue solid lines: line of sight for photomultiplier tubes, (d) black solid line: line of sight for Thomson scattering.

## 6.3 DYON simulations for JET with the carbon wall

### 6.3.1 Initial conditions for burn-through simulation

In order to perform DYON simulations, initial conditions should be given at the starting point of the burn-through phase, i.e. the end of the electron avalanche. R. Papoular [22] has defined electron avalanche (plasma break-down) as the realization of a critical electron density  $n_{ec}$ , from which coulomb collisions dominate atomic and molecular collisions. Based on this, the initial values required for the burn-through simulation in JET are given for the plasma parameters at the transition of the dominant collisions.

According to the definition of the electron avalanche, the degree of ionization at the transition

can be calculated:

$$n_{ec}\sigma_{e-i} = (n_a - n_{ec})\sigma_{e-a} \quad (6.1)$$

where  $n_a$  is the neutral density, and  $n_{ec}$  is the electron density at the transition. The cross-section for electron-ion collision  $\sigma_{e-i}$  and electron-atom collision  $\sigma_{e-a}$  are [22]

$$\sigma_{e-i} \approx 1.5 \times 10^{-16} T_e^{-2} [eV] \quad (6.2)$$

$$\sigma_{e-a} \approx 3 \times 10^{-19} T_e^{-0.5} [eV]. \quad (6.3)$$

Using Equation (6.1), the relation between  $n_{ec}$ ,  $n_a$ , and  $T_{ec}$  can be obtained,

$$\frac{n_{ec}}{n_a - n_{ec}} = \frac{\sigma_{e-a}^{cr}}{\sigma_{e-i}^{cr}} \approx \frac{3 \times 10^{-19} T_{ec}^{-0.5} [eV]}{1.5 \times 10^{-16} T_{ec}^{-2} [eV]} = 2 \times 10^{-3} T_{ec}^{\frac{3}{2}} [eV] \quad (6.4)$$

where the  $T_{ec}$  is the electron temperature at which the critical electron density  $n_{ec}$  is achieved.

If we assume  $T_{ec}$  is approximately 1 [eV], then the consistent degree of ionization  $\gamma_c$  is

$$\frac{\gamma_c}{1 - \gamma_c} \approx \gamma_c \approx 0.002 \quad (6.5)$$

where  $\gamma_c = n_{ec}/n_a$ . Since the neutrals are assumed to be a room temperature ( $\approx 0.03[eV]$ ),  $n_{ec}$  is calculated with the initial prefill gas pressure  $p$ ,

$$n_{ec} = 0.002 n_a \approx 0.002 \times 2.78 \times 10^{22} p [Torr] \quad (6.6)$$

where  $n_a \approx 2.78 \times 10^{22} p [Torr]$ .  $n_{ec}$  enables us to calculate the plasma current density at the transition point with the electron drift speed  $v_{De} (\approx 43E/p)$  [11],

$$J_c = en_{ec} \times \left(43 \frac{E}{p}\right) \approx 382.5 \times E [V/m]. \quad (6.7)$$

Table 6.1 summarizes the initial conditions for the burn-through simulation. The time to achieve this initial condition in JET is short enough to be ignored [10]. Hence, the simulation result can be directly compared to the JET data from  $t=0$ .

In order to compare the simulation results against one of the typical burn-through shots in JET performed with the carbon wall, measured data from # 77210 are used as an input data in the simulation. That is, measured loop voltage  $V_{loop}(t)$  (shown in Figure 6.2(b)) and EFIT data such as major radius  $R(t)$ , minor radius  $a(t)$ , and plasma cross-section  $A_p(t)$  of a plasma column in # 77210 are input data for the simulation. For the deuterium recycling coefficient  $Y_D^D$  in Equation (5.8),  $c1$ ,  $c2$ , and  $c3$  are assumed to be 1.1, 0.09, and 0.1, respectively. These constants are optimized to match the simulation results with data from # 77210.

Plasma parameters	Initial values
Electron temperature $T_e(0)$	1[eV]
Ion temperature $T_i(0)$	0.03[eV]
Deuterium atom density $n_d^0(0)$	$2.78 \times 10^{22} p[\text{Torr}]$
Electron density $n_e(0)$	$5.56 \times 10^{19} p[\text{Torr}]$
Carbon atom density $n_c^0(0)$	0
Oxygen atom density $n_o^0(0)$	$0.01 n_d^0(0)$
plasma current density $J_p(0)$	$382.5 \times E[\text{V/m}]$
Eddy current density $I_{MK2}(0)$	0

Table 6.1: *Initial conditions for the burn-through simulation in JET.*

### 6.3.2 Validation of DYON simulations with the carbon wall

Figure 6.2 shows JET data and the simulation results between 0 and 0.5 second in #77210. The plasma current in the simulation and JET data start to increase with the loop voltage applied from  $t = 0$  [sec] onwards. Both simulated and experimental  $I_p$  approaches 0.8 [MA] at  $t = 0.5$  [sec] showing very good agreement.

One of the important features in the burn-through phase is the radiation peak (barrier), which results from the change of the total radiation power as shown in the bolometry data [47]. It should be noted that the synthetic data for bolometry  $P^{Bol}$  (i.e. the total radiated power loss) is not the same quantity as  $P_{rad}$ , the total electron power loss due to radiation calculated using Equation (3.32). Charge exchange radiation is not included in  $P_{rad}$  since it is not the power loss of electrons. The potential difference in atomic structure is the source of charge exchange radiation.  $P^{Bol}$  consists of line radiation  $P_{line}^{BOL}$ , radiation due to Recombination and

Bremsstrahlung  $P_{RB}^{BOL}$ , and radiation due to charge exchange  $P_{cx}^{BOL}$ ,

$$P^{Bol} = V_p P_{line}^{BOL} + V_p P_{RB}^{BOL} + V_n^D P_{cx}^{BOL}$$

where

$$\begin{aligned} P_{line}^{BOL} &= \sum_A \frac{V_n^A}{V_p} n_e n_A^0 \langle \sigma v \rangle_{A,line}^0 + \sum_A \sum_{z \geq 1} n_e n_A^{z+} \langle \sigma v \rangle_{A,line}^{z+} \\ P_{RB}^{BOL} &= \sum_A \sum_{z \geq 1} n_e n_A^{z+} \langle \sigma v \rangle_{A,RB}^{z+ \rightarrow (z-1)+} \\ P_{cx}^{BOL} &= \sum_I \sum_{z \geq 1} n_D^0 n_I^{z+} \langle \sigma v \rangle_{I,cx}^{z+ \rightarrow (z-1)+} . \end{aligned} \quad (6.8)$$

Here,  $V_p$  is a plasma volume and  $V_n^D$  is a deuterium neutral volume within the plasma, which is explained in section 3.4.6. Since it is assumed in the DYON simulation that only deuterium atoms are the electron donors for charge exchange, the charge exchange reactions are only available in  $V_n^D$  where deuterium atoms and impurity ions coexist.

Using Equation (6.8), the bolometry data is reproduced and compared with the measured value in Figure 6.2. The simulated radiation barrier has a similar magnitude with the measured. In addition, the total radiation power around the radiation barrier has a similar FWHM. These imply that the model incorporates key physics aspects of the radiation power during the burn-through phase.

The electron temperature and density indicated by the red solid lines in Figure 6.2 (d) and (e) are measured by Thomson scattering [48]. The simulated electron temperature and density approach similar values with the Thomson scattering data, showing reasonable agreement. However, the simulated electron temperature and density have a discrepancy before around 0.15 seconds. Probably, this is due to the error of the EFIT data, which is used to calculate volume averaged value with the raw Thomson scattering data. There can be significant errors in the EFIT data in the early phase of discharge such as the burn-through phase. This would result in errors in the volume-averaged values. In addition, during the early phase, the signal for Thomson scattering measurement is very weak, thereby resulting in significant errors in data analysis. The red dotted line in Figure 6.2 (e) is the electron density measured by interferometry [49] in JET. Its discrepancy with the Thomson scattering data implies that there are errors in the diagnostic data.

Figure 6.3 (a) shows the number of photons emitted by  $C^{2+}$ . The red solid line is the measured values and the blue solid line is the synthetic data, which is calculated from the simulated



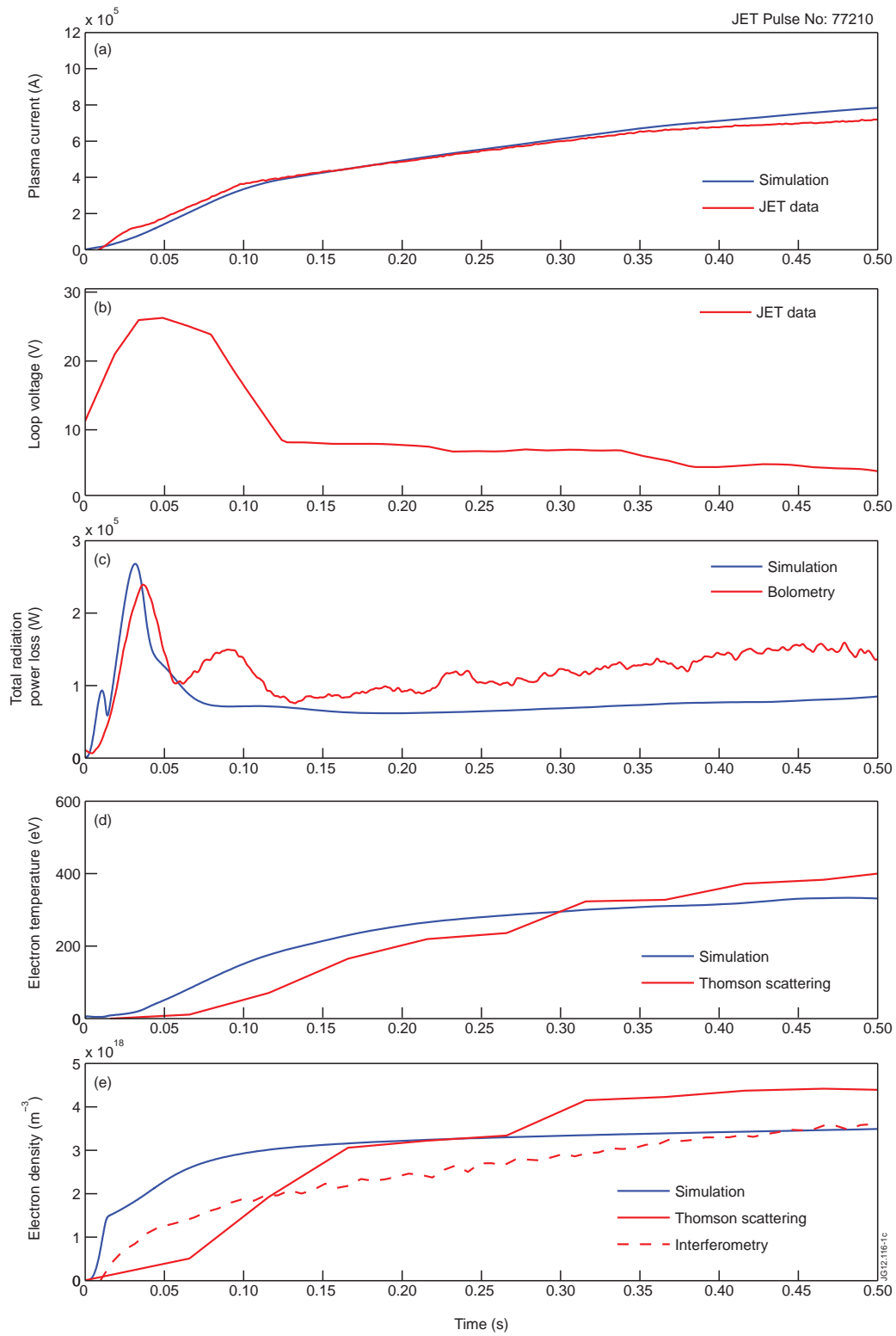


Figure 6.2: Each figure show simulation results and JET data of (a) Plasma current, (b) Loop voltage, (c) Total radiation power, (d) Plasma temperature, and (e) Plasma density. In all figures, red solid lines indicate JET experimental data and blue solid lines describe the simulation results. The red dotted line in (e) represent electron density measured by interferometry.

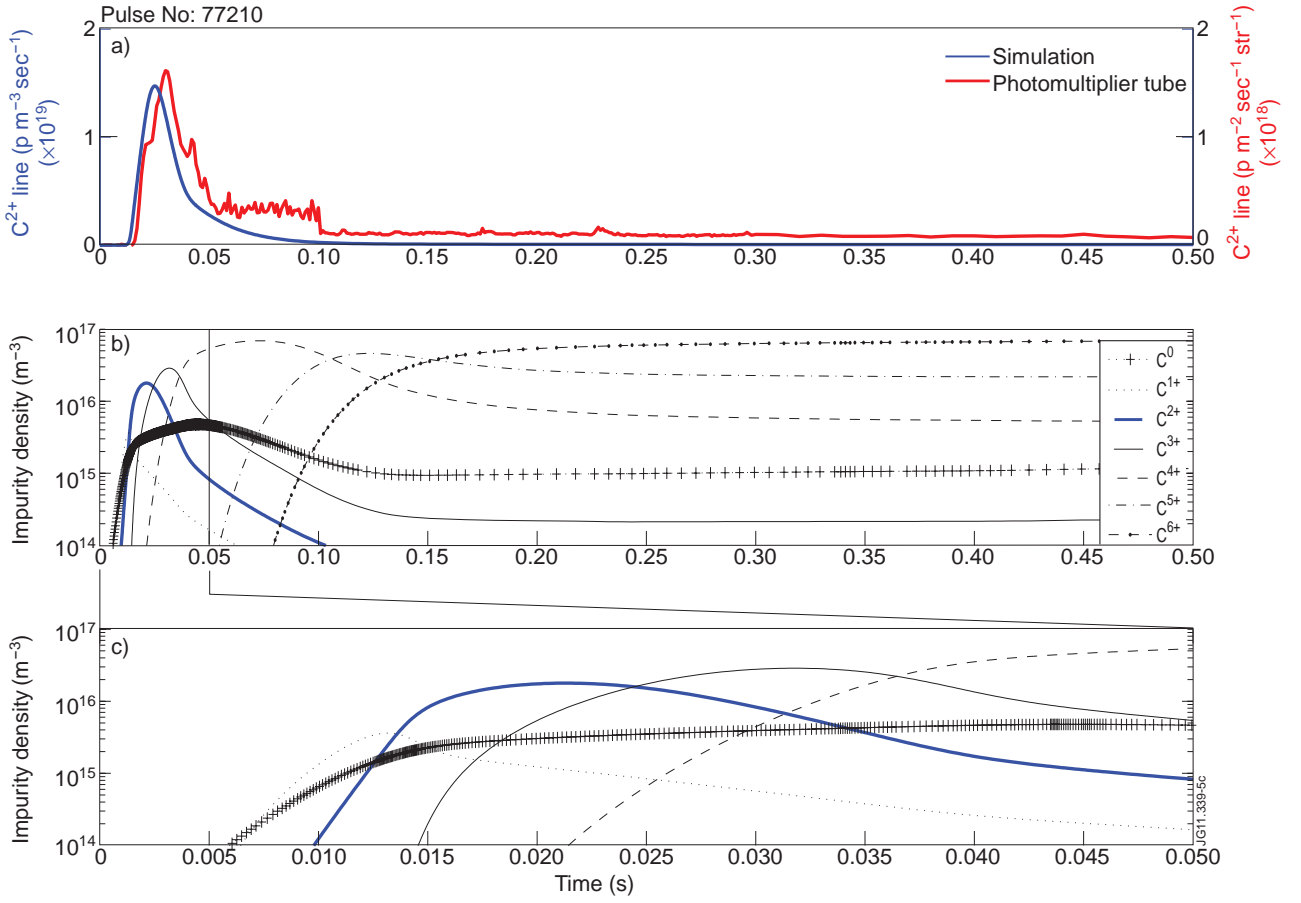


Figure 6.3: The blue solid line in (a) indicates the synthetic data of C<sup>2+</sup> line(465[nm]) emission. The red solid line in (a) shows C<sup>2+</sup> line(465[nm]) emission measured with the photomultiplier tube in JET. The different units in the simulated data([p m<sup>-3</sup>sec<sup>-1</sup>]) and the measured data([p m<sup>-2</sup>sec<sup>-1</sup>str<sup>-1</sup>]) are indicated in the left and right y-axis, respectively. The change of C<sup>2+</sup> line in the simulation results and the measured data show good agreement, thereby implying that the DYON code computes the impurity evolution reasonably well. (b) shows the simulational evolution of carbon, and (c) represents the enlarged figure between 0 and 0.05 second in (b).

plasma parameters, i.e.  $n_e$ ,  $T_e$ , and  $n_c^{2+}$  in Figure 6.3. The calculation of the synthetic data uses

$$I_{Az^+} = n_e n_A^{z^+} \mathcal{P} \mathcal{E} \mathcal{C}_{A,z^+}(n_e, T_e) [p m^{-3} sec^{-1}] \quad (6.9)$$

where  $\mathcal{P} \mathcal{E} \mathcal{C}_{A,2^+}(n_e, T_e)$  is a photon emissivity coefficient, which is a function of electron density and temperature.  $A$  and  $z^+$  indicate the corresponding particle species and the charge state.

Here,  $A$  and  $z_+$  are C and  $2+$ . The photon emissivity coefficient of  $C^{2+}$  (465[nm] wavelength) is obtained from ADAS [25].

As can be seen in Equation (6.9), the growth and decay of  $C^{2+}$  line emission result from the change of  $n_c^{2+}$ . Hence, the change of the photon emission rate can give us important information about the  $n_c^{2+}$  evolution. The peak value of  $C^{2+}$  line emission and its decrease after the peak point indicate that the maximum amount of  $n_c^{2+}$  exists at around this time and most  $C^{2+}$  are ionized to higher charge states after the peak. The synthetic photon emission rate of the  $C^{2+}$  line shows a similar time scale of growth and decay with those of the measured value. It should be noted that the change of the synthetic  $C^{2+}$  line emission is available only with an adequate model for impurity evolution. The similar behaviour of the synthetic data implies the simulation can compute the evolution of  $C^{2+}$  with good accuracy.

In JET, observation of the carbon evolution in the burn-through phase is limited to  $C^{2+}$  due to the lack of diagnostic data available for this phase. The burn-through simulation can provide information of the impurities in other charge states. The simulated evolution of carbon ions is presented in Figure 6.3 (b). As explained above, the peak of  $C^{2+}$  density is coincident with that of the synthetic  $C^{2+}$  line.  $C^{3+}$  density increases as  $C^{2+}$  density decreases, and so on. Through ionization of carbon ions,  $C^{6+}$  density becomes dominant from 0.15[s] onwards, indicating that most carbon ions are fully ionized from that time. Figure 6.3 (c), enlarged from Figure 6.3 (b), describes the process of carbon burn-through in detail.

### 6.3.3 Effects of the new model of parallel transport

One of the new features of the DYON code is the modelling of the particle losses parallel to the magnetic field lines. During the plasma burn-through phase, the magnetic field lines can be open. In that case, the parallel transport loss dominates the transport mechanism. Figure 6.4 shows a simulation result of the DYON code for #77210, showing the transition from parallel transport to perpendicular transport. Hence, the simulation results are significantly changed if the parallel transport model is removed from the DYON code.

Figure 6.5 shows the difference between the simulation results with and without the parallel transport model. Particularly, the radiation barrier is significantly reduced. The decrease in the radiation power loss is due to the decrease in the deuterium outflux to the wall, thereby

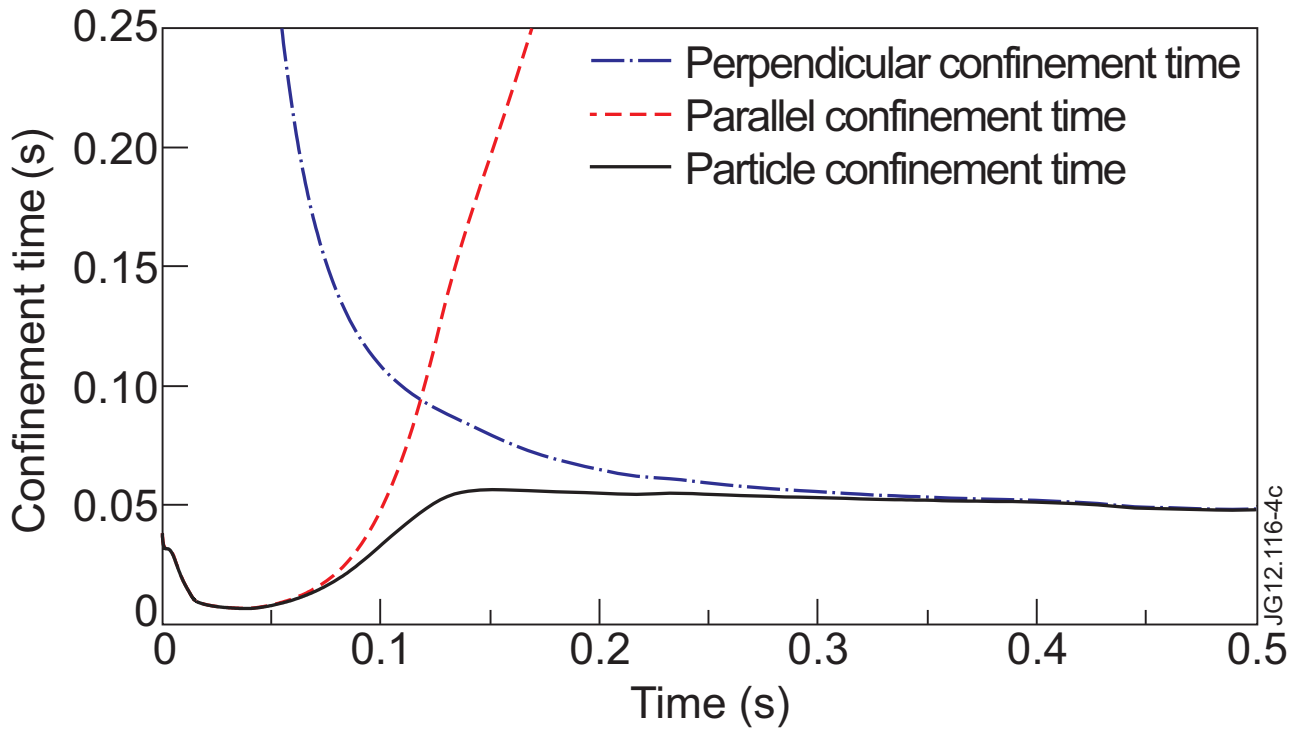


Figure 6.4: The blue chain line and the red dashed line indicate the perpendicular confinement time, Equation (3.53), and the parallel confinement time, Equation (3.49), respectively. The resultant particle confinement time is shown by the black line, Equation (3.54).

reducing the amount of the sputtered carbon. As the impurity evolution is computed including the PWI effects in the DYON code, the change of the radiation power loss due to the change of the particle transport is apparent. This is another important feature of the DYON code compared to simulations using fixed impurity content or fraction. Consistently, Figure 6.5 (e) shows that the line emission of  $C^{2+}$  significantly decreases without the parallel transport model. The reduced radiation power loss results in an increase in the electron temperature (red solid line in Figure 6.5 (b)). The decrease in the deuterium outflux to the wall also reduces the deuterium recycling from the wall, and this results in the decrease in electron density (red solid line in Figure 6.5 (c)). The plasma current does not show significant discrepancy since it is a less sensitive parameter due to the self inductance term  $L_p \frac{dI_p}{dt}$  in Equation (3.1).

Due to the low electron temperature during the plasma burn-through phase, the vessel resistance can be comparable to the plasma resistance. This results in significant eddy currents, reducing the effective connection length. In the DYON code, the error fields are calculated with the eddy currents flowing on the MK2 support structure, i.e. current ring model for MK2 current. Figure

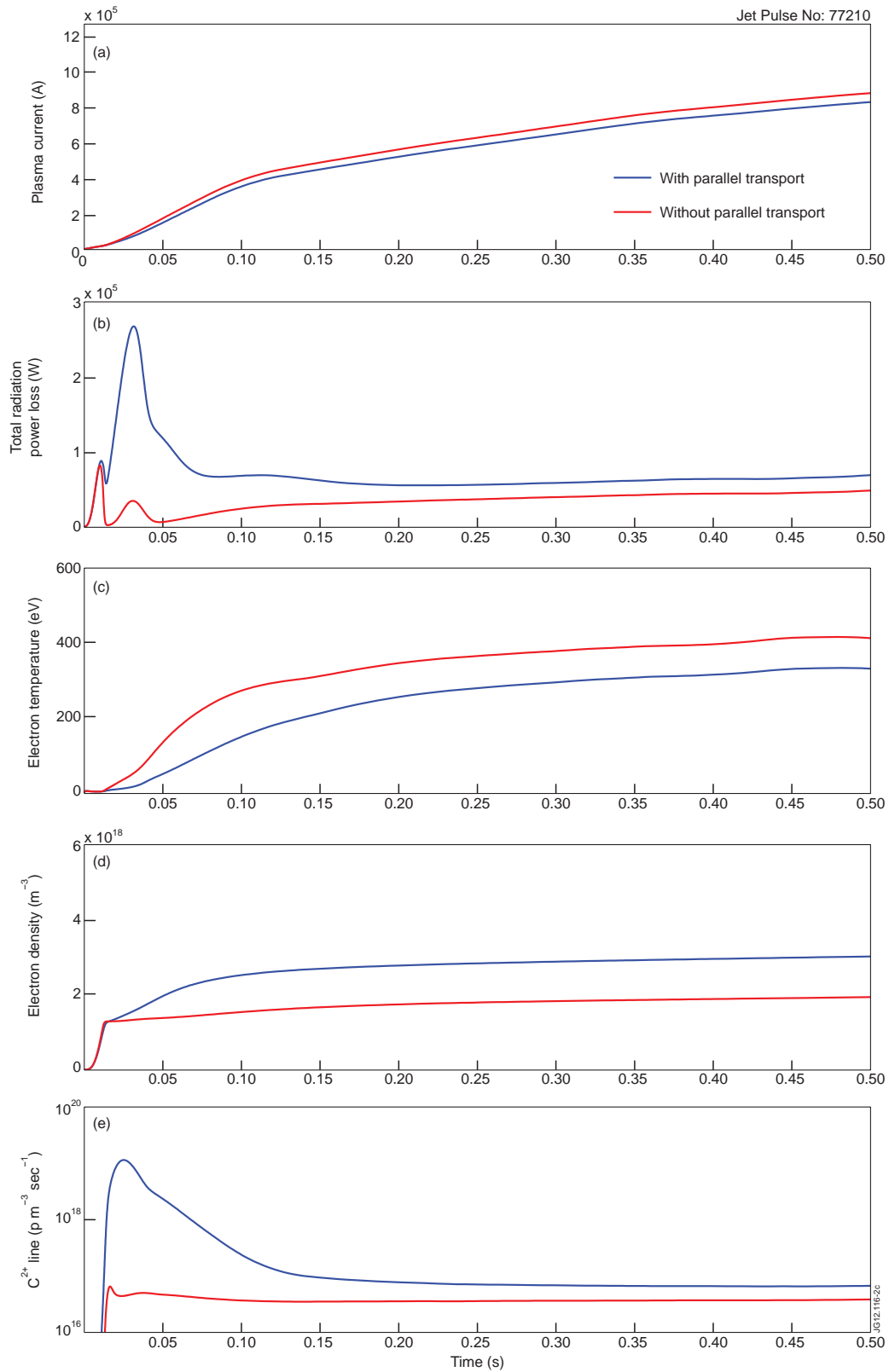


Figure 6.5: The red solid lines in each figure show simulation results without the parallel transport model: (a) Plasma current, (b) Total radiation power, (c) Plasma temperature, (d) Plasma density, and (e) the synthetic data of  $C^{2+}$  line(465[nm]) emission. In all figures, the blue solid lines describe the simulation results with the parallel transport model, which is compared with the JET data in Figure 6.2 and 6.3.

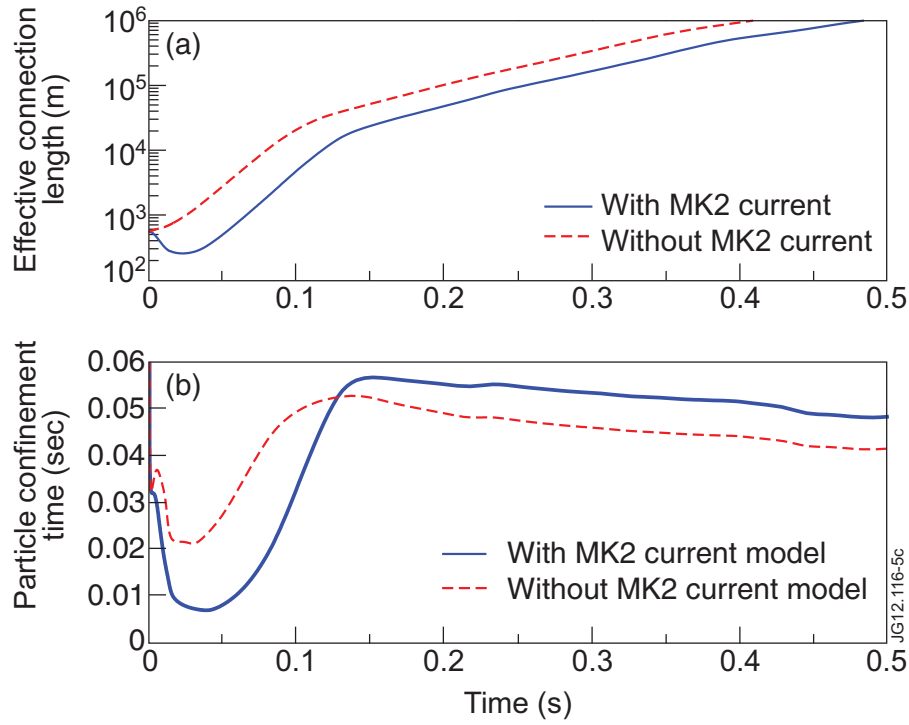


Figure 6.6: In (a), the red dashed line shows the effective connection length without the MK2 current model (i.e. single plasma current ring) in the DYON code, and the blue solid line describe the effective connection length with the MK2 current model, i.e. two ring model (plasma current and MK2 current). The red dashed line and the blue solid line in (b) show the particle confinement with and without the MK2 current model, respectively.

6.6 and 6.7 shows how significant the effect of the eddy currents is. As shown in Figure 6.6 (a), the effective connection length without MK2 current model is much longer. The increase in the effective connection length without the MK2 model results in the decrease in the parallel transport, which is the dominant transport mechanism during the plasma burn-through phase ( $0 \sim 0.1$ [sec]). Hence, the resultant particle confinement time during the burn-through phase is longer when the MK2 current model is removed than when it is included, as shown in Figure 6.6 (b). As a result, the simulation results in Figure 6.7 are changed, following similar trend as the simulation results without the parallel transport model.

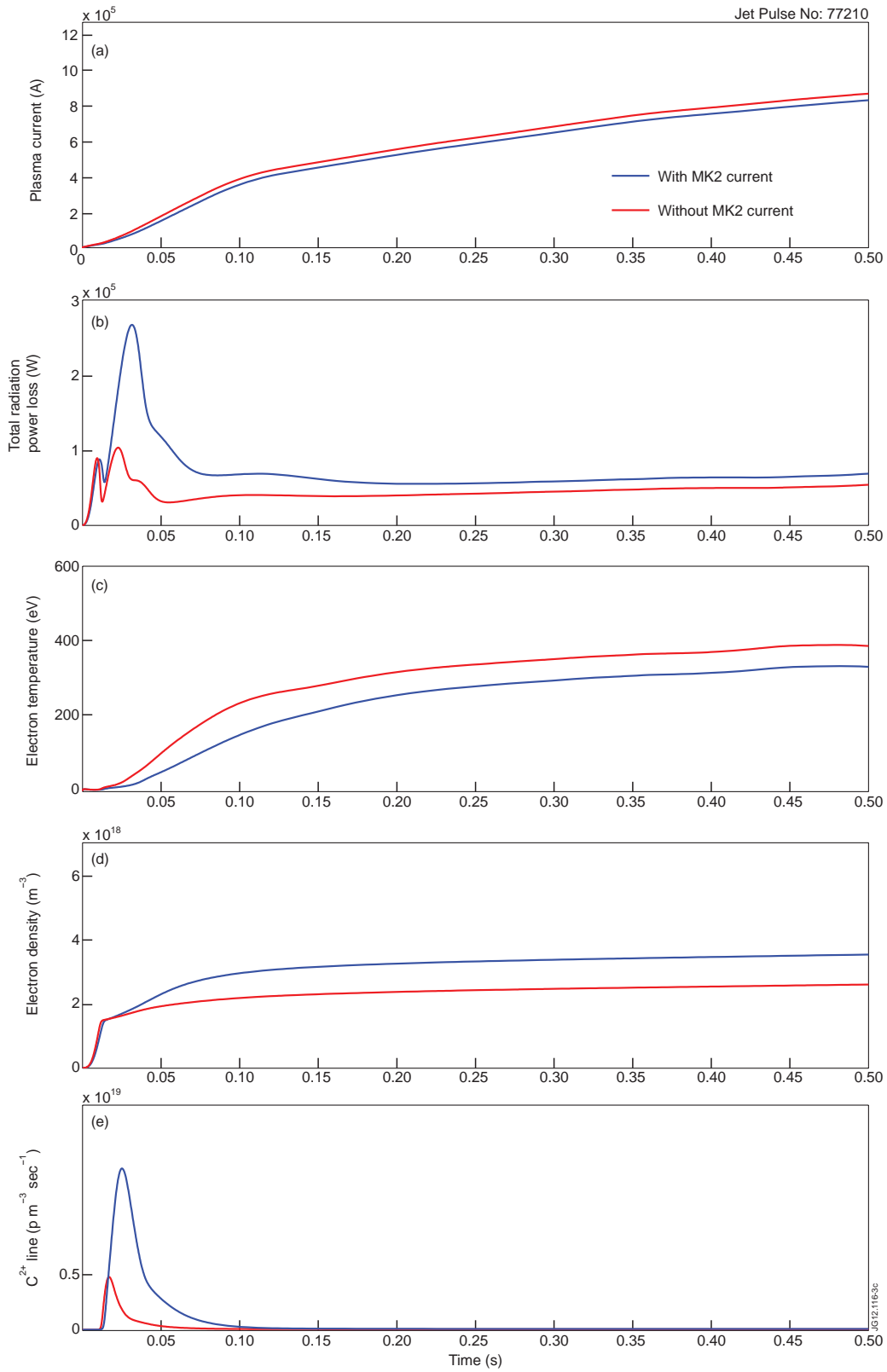


Figure 6.7: The red solid lines in each figure show simulation results without the MK2 current (i.e. single plasma current ring): (a) Plasma current, (b) Total radiation power, (c) Plasma temperature, (d) Plasma density, and (e) the synthetic data of  $C^{2+}$  line (465[nm]) emission. In all figures, the blue solid lines describe the simulation results with the two ring model (plasma current and MK2 current), which is compared with the JET data in Figure 6.2 and 6.3.

## 6.4 DYON simulations for JET with the ITER-like wall

### 6.4.1 Validation of the new models

The recent installation of the ITER-like wall at JET enables us to validate the new models for PWI at the beryllium wall. For the validation of the new models, one typical discharge in JET has been selected (#82003), and compared to the DYON simulation results. Figure 6.8 shows the DYON simulation results and the JET data with the ITER-like wall. The required input parameters for the DYON simulation, i.e. prefill gas pressure, loop voltage, plasma major and minor radius, toroidal magnetic field, and additional fuelling, are obtained from the measured data. The parameters given to perform the simulation are summarized in Table 6.2.

The plasma current in the DYON simulation is in good agreement with the JET data. As shown in Figure 6.8 (b), the toroidal loop voltage decreases abruptly at 0.1 second due to the pre-programmed use of a switching network to reduce the voltage from the ohmic transformer, a typical operation scenario at JET. This results in the sharp decrease in the  $I_p$  ramp-up rate around 0.1 second in Figure 6.8 (a). The measured loop voltage is used as an input for the simulations.

Figure 6.8 (c) shows the total radiation power loss. In the simulations, the temporal behaviour of the radiation barrier is used to adjust  $\tau_{erosion}$ , the transition time of a  $BeO$  wall to a pure  $Be$  wall. The synthetic bolometry data can be well reproduced with  $\tau_{erosion}(=60$  [msec]). For this simulation, the initial carbon content  $n_C^0(0)$  is assumed to be 0.5% of prefill deuterium atoms  $n_D^0(0)$ . As will be discussed later, the assumption of  $n_C^0(0)$  has a small contribution to the magnitude of the radiation barrier. Also, both  $\tau_{erosion}$  and  $n_C^0(0)$  do not have a significant influence on the evolution of other plasma parameters i.e.  $I_p(t)$ ,  $T_e(t)$ , and  $n_e(t)$ .

The  $T_e$  and  $n_e$  in the simulations and the measured Thomson Scattering data approach similar values, but they have a discrepancy before 0.3 [sec]. The discrepancy is due to the limitations of the Thomson Scattering diagnostic, which can have significant error bars during the low density phase such as the plasma burn-through phase. The interferometry data show a better agreement with the density in the simulations during this early phase, as shown in Figure 6.8(e).

As ionization of deuterium and impurities proceeds, the photomultiplier tube data has a peak



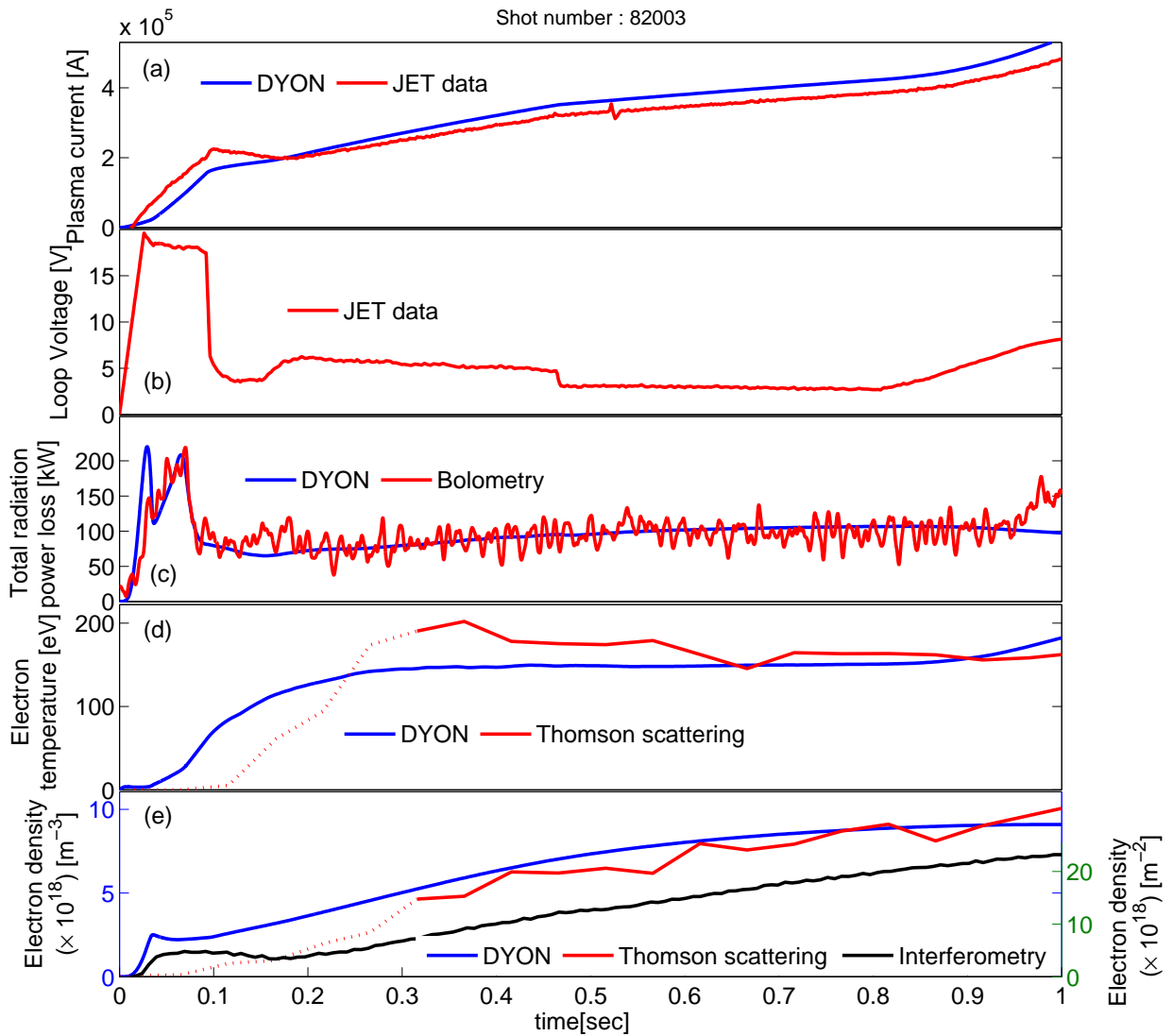


Figure 6.8: *DYON* simulation results with the new models for the ITER-like wall and JET data. (a) Plasma current, (b) Loop voltage, (c) Total radiation power (Bolometry), (d) Electron temperature (Thomson scattering), (e) Electron density (Thomson scattering and Interferometry). The red lines (and the black line in (e)) indicate JET data for #82003, and the blue lines are the corresponding *DYON* simulation results. The condition given for the simulations is in Table 6.2.

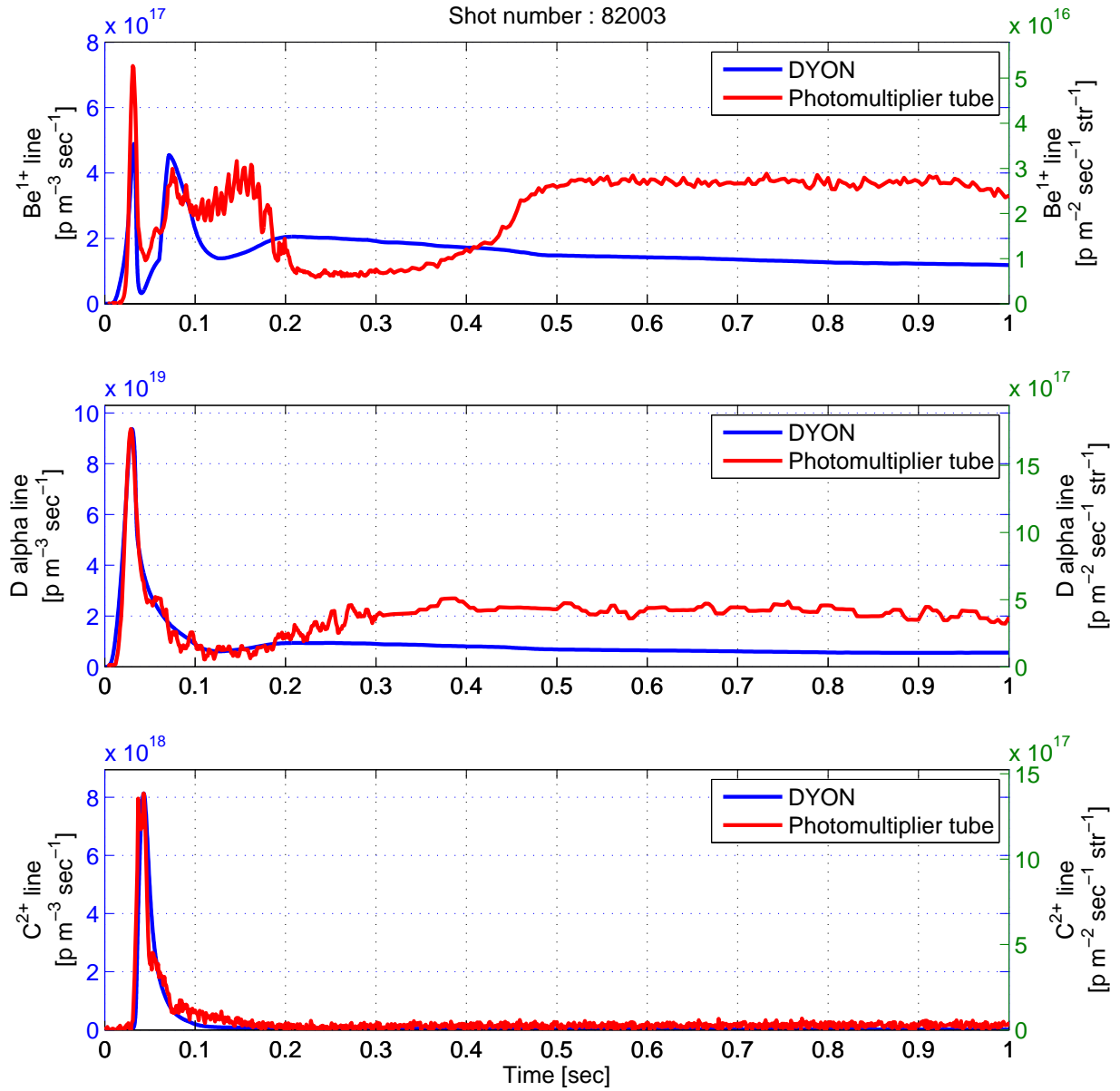


Figure 6.9: The measured photomultiplier tube data and the synthetic photomultiplier tube data: (a) number of photons emitted from  $Be^{1+}$  (527[nm]), (b) number of photons emitted from  $D^0$  (D alpha), and (c) number of photons emitted from  $C^{2+}$  (465[nm]). The red lines are the photomultiplier tube data in JET for #82003, and the blue lines are the synthetic data, calculated by DYON simulations.

for each specific line emission, which is emitted from the deuterium atom or impurity ions in a certain charge state. The synthetic volume emission of  $Be^{1+}$  (527[nm]),  $D^0$  (Dalpha), and  $C^{2+}$  (465[nm]) are calculated using Equation (6.9), and compared with the measured photon flux in Figure 6.9 (a), (b), and (c). The temporal behaviour of the peaks in the synthetic data is coincident with the measured data. This implies that the ionization process of deuterium and impurities is reproduced correctly in the DYON simulations.

### 6.4.2 Beryllium sputtering in ITER-like wall

In the DYON simulations, the first radiation peak for  $Be^{1+}$  is reproduced showing a very good temporal agreement with the photomultiplier tube data in Figure 6.10 (a). However, the first radiation peak is removed when the initial beryllium content is not assumed in the simulations, as shown by the dashed black line in Figure 6.10 (b). This implies that the first radiation peak results from the initial beryllium content rather than physical sputtering. These particles are probably the beryllium atoms bonded weakly at the wall due to the migrations of beryllium during previous experiments.

The secondary radiation peak in the photomultiplier tube data for  $Be^{1+}$  is observed at around 0.07 [sec], as shown in Figure 6.9 (a). It should be noted that such a secondary radiation peak does not appear for  $D^0$  and  $C^{2+}$  in Figure 6.9 (b) and (c). This is because the secondary radiation peak results from the wall-sputtering rather than the initial impurity content. Wall-sputtering can occur only if the incident ion energy exceeds the threshold energy. This implies that the beryllium sputtering is delayed until the wall-impacting energy,  $2kT_i + 3kT_e$ , exceeds the threshold energy. The secondary radiation peak is reproduced with the physical sputtering model, showing a good temporal agreement in Figure 6.10 (a). The solid black line in Figure 6.10 (b) shows the DYON simulation result without the physical sputtering model. The secondary radiation peak does not appear without the physical sputtering model.

It is observed in many laboratory plasmas that the surface of beryllium tiles are easily oxidized [7],[42],[50]. The high affinity of Be to O tends to result in the BeO layer on the wall, which has higher surface binding energy than the pure beryllium wall [42]. In Table 5.2, the threshold energy of a deuterium incident ion for the physical sputtering on the BeO layer is 29[eV], which is much higher than that on a pure beryllium wall, 10[eV]. The higher surface binding energy

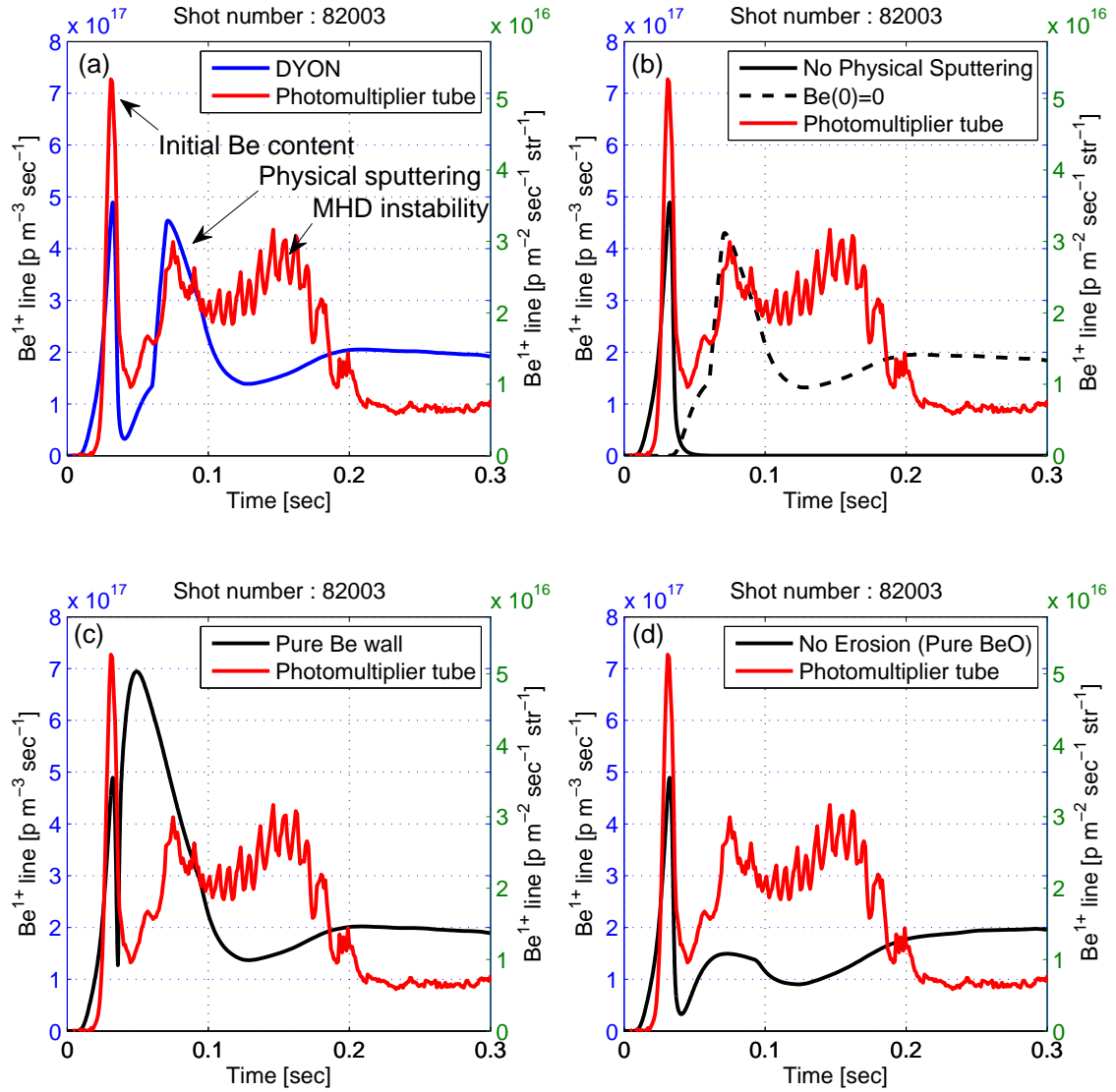


Figure 6.10: These figures compare the photomultiplier tube data ( $Be^{1+}$  (527[nm])) between the measured data and the synthetic data, and show the significance of the new models used in the DYON simulations. The red solid lines are the photomultiplier tube data in JET for #82003. The blue solid line in (a) is the synthetic data with the condition given in Table 6.2 (i.e. with physical sputtering model on BeO layer, erosion model of BeO layer, and initial Be content). The black dashed line and solid line in (b) are without initial Be content or any physical sputtering model, respectively. The black solid line in (c) is for pure Be wall. The black solid line in (d) is without erosion model of BeO layer i.e. continuous BeO layer.

Plasma parameters	Input values
Toroidal magnetic field $B_\phi$	2.7[Tesla]
Vertical magnetic field $B_v$	0.001[Tesla]
Initial plasma current density $J_p(0)$	$382.5 \times E[V/m]$
Initial Eddy current $I_{MK2}(0)$	0[A]
Initial electron temperature $T_e(0)$	1[eV]
Initial ion temperature $T_i(0)$	0.03[eV]
Prefilled gas pressure $p(0)$	$4.3135 \times 10^{-5}[Torr]$
Initial Deuterium atom density $n_D^0(0)$	$2.78 \times 10^{22} \times p(0)[Torr]$
Initial degree of ionization $\gamma_{iz}(0)$	0.002
Initial Be content $n_{Be}^0(0)$	$0.01 \times n_D^0(0)[m^{-3}]$
Initial C content $n_C^0(0)$	$0.005 \times n_D^0(0)[m^{-3}]$
Initial O content $n_O^0(0)$	$0.001 \times n_D^0(0)[m^{-3}]$
Initial N content $n_N^0(0)$	$0.001 \times n_D^0(0)[m^{-3}]$
$Y_D^D$	$c_1 = 0.9, c_2 = -0.1, c_3 = 0.1$ in Equation (5.8)
Fuelling efficiency	10%
PWI model	physical sputtering with BeO wall
Plasma major radius $R(t)$	EFIT ( $R(0) = 3.0381[m]$ )
Plasma minor radius $a(t)$	EFIT ( $a(0) = 0.08519[m]$ )
Internal inductance $l_i$	0.5
Loop voltage $V_l(t)$	Measured in JET
Effective vacuum vessel volume	100[m <sup>3</sup> ]

Table 6.2: Plasma parameters assumed for the plasma burn-through simulation (#82003) in the ITER-Like Wall

in the BeO layer makes the physical sputtering more difficult than in the pure beryllium wall. The simulation results using the different parameters for BeO and Be are compared in Figure 6.10 (a) and (c). The secondary radiation peak in Figure 6.10 (c) occurs much earlier, showing a deviation from the measured value.

Due to the erosion of BeO layer, the BeO sputtering model is switched to the Be sputtering at  $\tau_{erosion} (\approx 60[msec])$ . Figure 6.10(d) shows BeO sputtering without switching to Be sputtering i.e. no BeO erosion model. The secondary peak shows a reasonable temporal agreement with the measured, but it decreases slowly, without the sharp peak observed in the measured and the simulated with the erosion model. Moreover, in this case the radiation resulting from oxygen would be much higher than measured.

Based on the frequency of the fluctuating radiation, it is found that the third peak around  $100 \sim 200[msec]$  in the photomultiplier tube data for  $Be^{1+}$  is probably due to an MHD instability in the plasma, which is not modelled in the DYON simulation. Since a detailed investigation on the MHD instabilities is beyond the scope of this thesis, this is not discussed further here.

### 6.4.3 Deuterium recycling coefficient

As shown in Equation (5.8),  $Y_D^D(t)$  is adjusted by the combination of constants  $c_1$ ,  $c_2$ , and  $c_3$ . In order to test whether  $Y_D^D$  is growing or decaying during the plasma burn-through phase, the constants are assumed to be  $c_1 = 0.9$ ,  $c_2 = -0.1$ , and  $c_3 = 0.1$  for the growing model, and  $c_1 = 1.1$ ,  $c_2 = 0.1$ , and  $c_3 = 0.1$  for the decaying model.

Figure 6.11 shows the different simulation results between the two sets of parameters used. The decay model implies additional release of deuterium atoms during the plasma burn-through phase. This results in a too high electron density in the simulation compared to the Thomson scattering data in Figure 6.11 (a). The discrepancy is reduced by the growing model as indicated with the blue solid lines in Figure 6.11 (a). This implies that some portion of incident deuterium ions are retained at the wall rather than being recycled. Based on this, the growing model for recycling is used for the simulations with the ITER-like wall in Figure 6.8. It should be noted that for the carbon wall simulations the DYON simulation results with the decay model showed better agreement with the JET data [36].

Figure 6.11 (b) gives another indication that the growing model is required for the ITER-like wall. The synthetic data for the D alpha line using the growing model shows very good agreement against the measured value for  $0 \sim 0.2[sec]$ . However, with the decay model, the synthetic data deviates significantly from the measured value as shown in Figure 6.11 (b). This

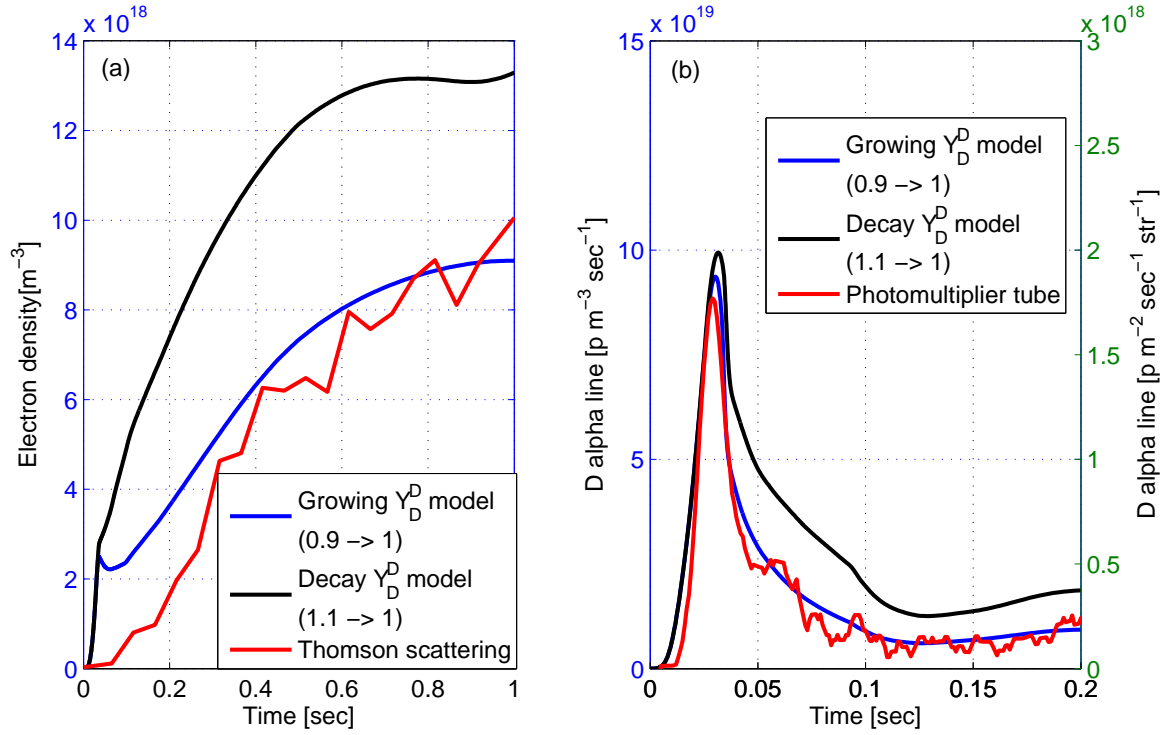


Figure 6.11: The figures show the effects of the deuterium recycling coefficients. (a) electron density (b) number of photons emitted from  $D^0$  ( $D$  alpha) (465[nm]). The red lines are (a) Thomson scattering data (b) the measured photomultiplier tube data in JET (#82003). The blue and black lines are the DYON simulation results with the growing model or decay model of  $Y_D^D$ , respectively.

gives a confidence on the fact that such additional release of deuterium atoms during the plasma burn-through phase is not probable in the ITER-like wall.

#### 6.4.4 Gas fuelling

One of the main differences in the JET operation scenario with the ITER-like wall is the use of additional gas fuelling around 0.1[sec]. This is to compensate for the gas pumping effect at the wall as seen with the new wall ( $Y_D^D < 1$  before  $t = 0.2$ [sec]) [12]. The first term in Equation (5.10) is the influx of the deuterium atoms recycled at the wall, and the second term is the additional gas fuelling  $\Gamma_{D,in}^{eff}$ , which was not included (i.e.  $\Gamma_{D,in}^{eff} = 0$ ) for the carbon wall

simulations. In the simulations for the ITER-like wall,  $\Gamma_{D,in}^{eff}$  is modelled as

$$\Gamma_{D,in}^{eff} = \psi_{puffing} \Gamma_{D,in}^{GIM}, \quad (6.10)$$

where  $\Gamma_{D,in}^{GIM}$  is obtained from the data of the Gas Injection Modules in JET [51] and  $\psi_{puffing}$  is a fuelling efficiency. The gas injection module used for the fuelling at 0.1[sec] is located on the top of the vacuum vessel in JET. The 4 main pumping ports, 2 Neutral Beam Injection (NBI) ports, and 1 Lower Hybrid (LH) ports are on the outer midplane of the vessel. Since a significant fraction of the injected gas is pumped out immediately rather than being ionized, the fuelling efficiency must be evaluated for the effective influx of deuterium atoms. Figure 6.12 shows the differences in the simulation results when assuming different values for  $\psi_{puffing}$  between 30% and 0%. Since gas injection is applied from 0.1[sec] as can be seen in Figure 6.12 (a), the simulation results does not show discrepancy until then. However, the electron density with 30% fuelling efficiency increases excessively from 0.1[sec] onwards as shown in Figure 6.12 (b). In contrast, without the fuelling model i.e. 0% fuelling efficiency, the electron density in Figure 6.12 (b) is much lower than Thomson scattering data. Scanning of the fuelling efficiency, it has been found that the simulation results with 10% fuelling efficiency agree well with the JET data. Based on this, 10% fuelling efficiency is assumed for the simulations in Figure 6.8 and Figure 6.9.

### 6.4.5 Initial carbon content

Although all CFC tiles have been removed from the plasma facing components in the ITER-like wall, the  $C^{2+}$  line emission is still observed in the JET data with ITER-like wall as shown in Figure 6.9 (c). This requires the assumption of an initial (or residual) carbon content  $n_C^0(0)$  for the ITER-like wall simulations.

The total carbon content assumed at plasma initiation is between 0 ~ 1% of the prefill deuterium atom density  $n_D^0(0)$ ;  $n_C^0(0) \sim 10^{16} [m^{-3}]$ . This value is lower than the carbon content during the main heating phase of JET plasmas, which is reported [52] as 0.1 ~ 0.2% of the plasma density (in the range of  $10^{19} \sim 10^{20} [m^{-3}]$ ) during the heating phase. Figure 6.13 (a) shows the total radiation power loss in the simulations with  $n_C^0(0)$ . Here, the initial carbon content  $n_C^0(0)$  is assumed to be 0%, 0.5% or 1% of the initial deuterium atom density  $n_D^0(0)$ ,



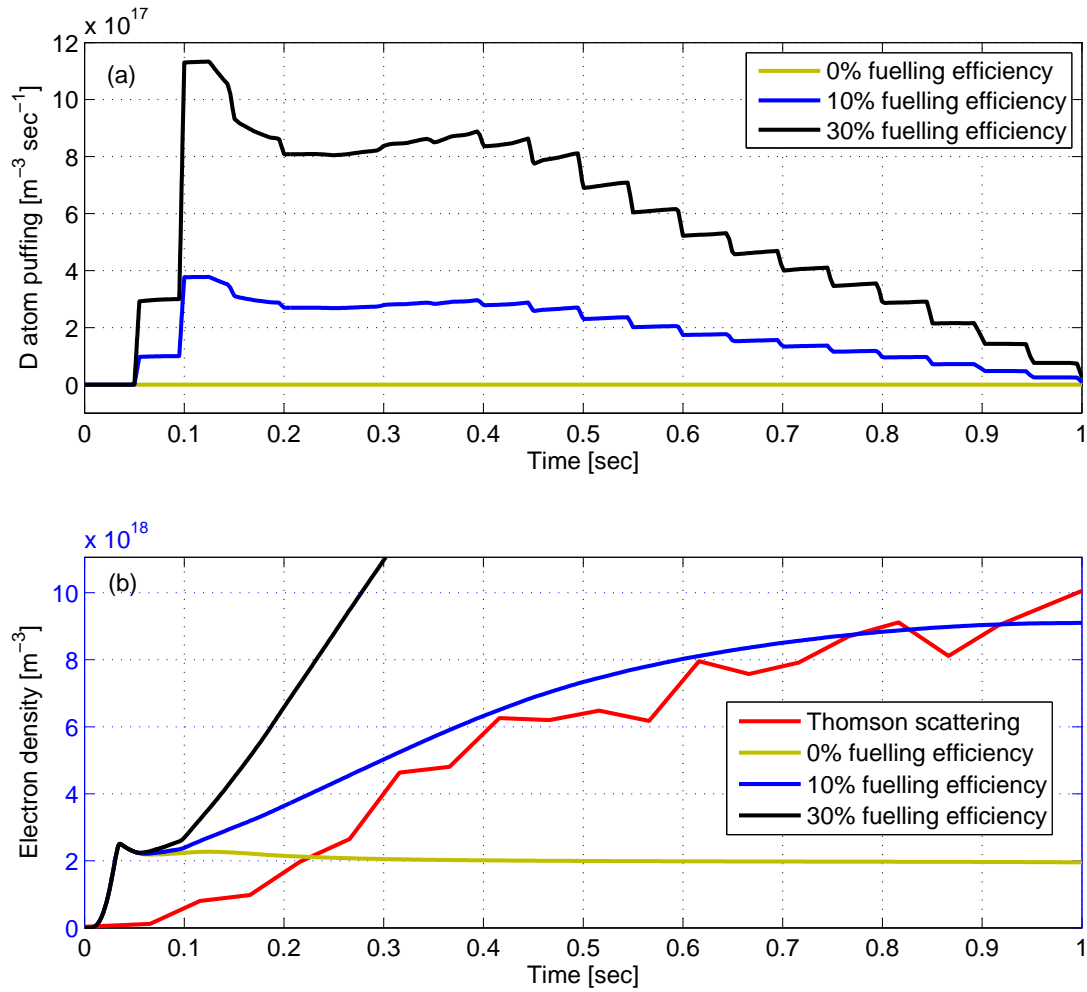


Figure 6.12: The figures show the effects of deuterium fuelling efficiency applied after 100 [msec]. (a) D atom puffing with the assumed fuelling efficiency (black 30%, blue 10%, and green 0%), (b) electron densities, obtained by DYON simulation (black 30%, blue 10%, and green 0%) and measured by Thomson scattering (red) in JET (#82003).

respectively. As shown in Figure 6.13 (a), without  $n_C^0(0)$ , the synthetic radiation barrier deviates from (below) the bolometry data. The magnitude of the total radiation power loss in the simulation with 1%  $n_C^0(0)$  exceeds the peak of the bolometry data. However, in the case of the simulation with 0.5%  $n_C^0(0)$ , the radiation barrier shows good agreement. Based on this, 0.5%  $n_C^0(0)$  is assumed in the simulations.

Figure 6.13 (b) shows the constituent radiated power losses in the case of the simulation with

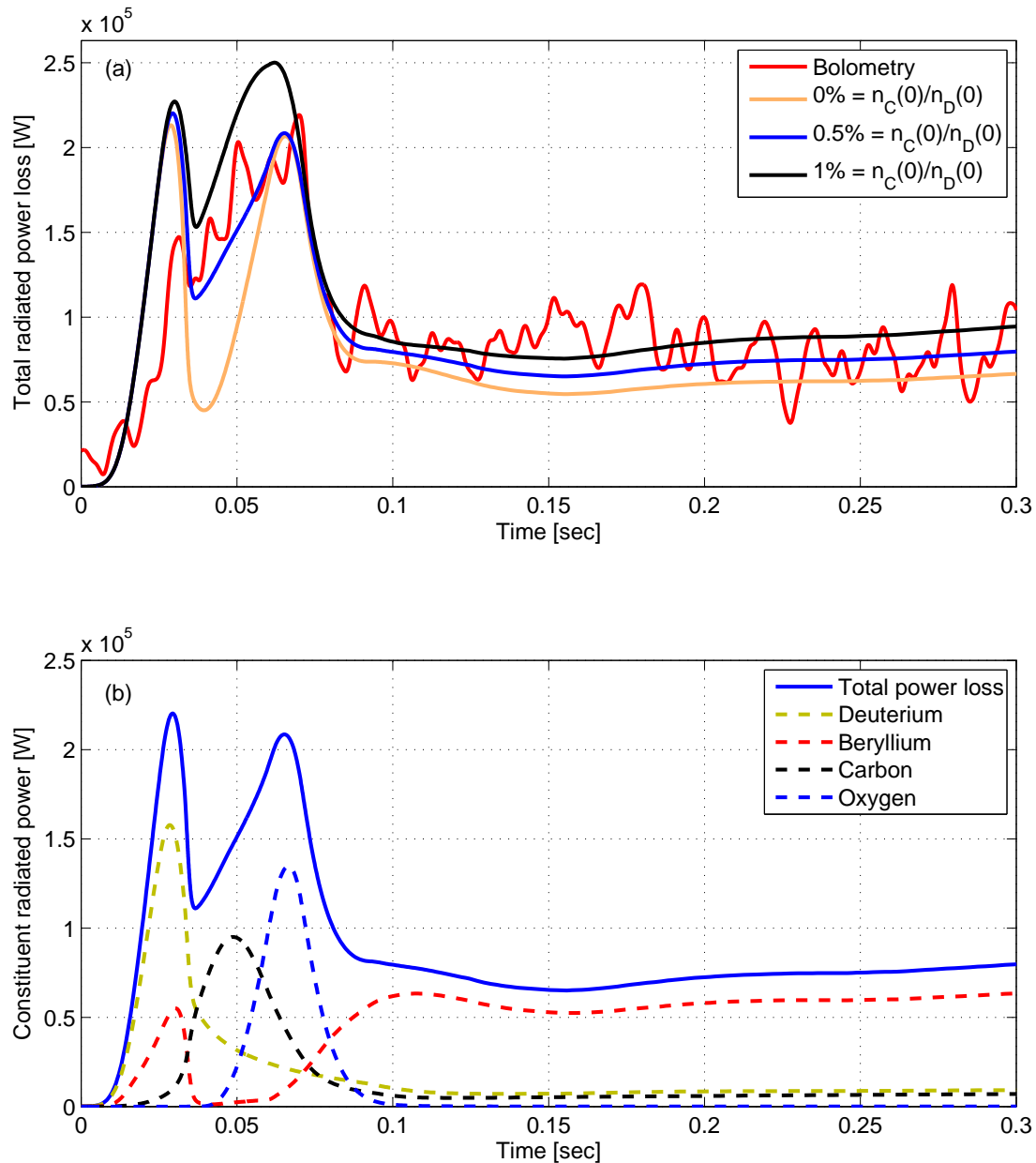


Figure 6.13: The figures show the effects of  $n_c^0(0)$  on the radiation barrier and the constituent radiated power. (a) bolometry data (red) in JET (#82003), and the simulated radiated power in the DYON simulations (solid black 1%, solid blue 0.5%, and solid green 0% of  $n_c^0(0)$ ). (b) the constituent radiated power (solid blue: total radiated power, dashed red: Be, dashed green: D, dashed black: C, dashed blue: O). For the simulation in (b), the  $n_c^0(0)$  is assumed to be 0.5%, as given for the simulation in Figure 6.8 and 6.9.

0.5%  $n_C^0(0)$ . It can be seen that the radiation is dominated in turn by the radiated power loss from deuterium, carbon, oxygen, and beryllium. The radiated power loss due to beryllium is not significant in the radiation barrier during the plasma burn-through phase.

### 6.4.6 Effective vessel volume

One of the underlying assumptions in the simulations is that all deuterium atoms are accessible to the plasma. This implies that the vessel volume determines the neutral influx into the plasma. However, deuterium atoms in large ports for diagnostics or additional heating and near pumping ports are impeded to approach the plasma. For example, the neutral particles in the cryogenic pumping chamber for NBI system (i.e.  $V_{NBI}$ ) cannot access to the main plasma. Hence,  $V_{NBI}$  should not be included in  $V_V$ . The initial peak of bolometry data is proportional to the number of deuterium atoms in the vessel. Comparing the reproduced bolometry data with the measured, we could find the effective vessel volume  $V_V$  is around 100 [ $m^3$ ] in JET, although the total volume of the vacuum vessel is 189 [ $m^3$ ].

Figure 6.14 shows the simulation results with the actual vessel volume i.e.  $V_V = 190$  [ $m^3$ ]. Otherwise identical conditions were used i.e. input data from Table 6.2 except for  $V_V$ . As a result, all plasma parameters are significantly deviated from the measured values. As shown in Figure 6.13 (b), the initial peak in the bolometry data is due to D radiation. The large initial peak in the total radiation power loss in the simulation (see Figure 6.14 (b)) implies that D fuelling from ex-plasma volume is excessive as shown in Figure 6.14 (d). In the simulations, this results in much smaller electron temperature than the measured (and excessively high plasma resistance), and the simulated plasma current is significantly deviated from the JET data (see Figure 6.14 (a) and (c)).

## 6.5 Operation space for plasma burn-through in JET

Figure 6.15 compares the Townsend criterion and the criterion for plasma burn-through. The cyan dashed lines in Figure 6.15 are the minimum electric field for electron avalanche  $E_{avalanche}$  for various effective connection lengths  $L_f$  in JET, computed analytically by using the Townsend criterion in Equation (1.22). The Townsend criterion shows that there is an optimum range

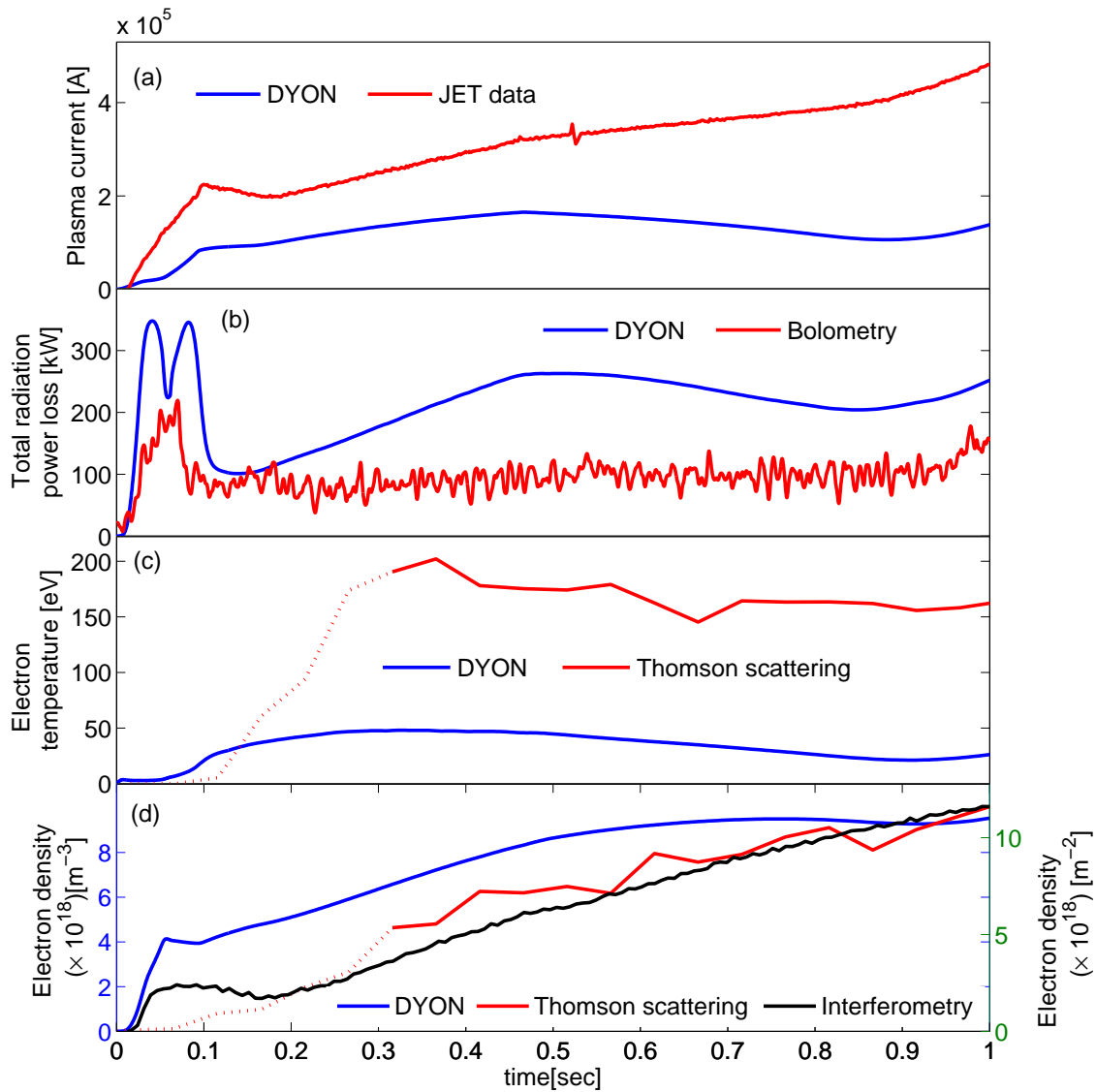


Figure 6.14: *DYON* simulation results using the vessel volume  $V_V = 190$  [m $^3$ ].

of the prefill gas pressure at which the lowest toroidal electric field is available for electron avalanche. However, for successful tokamak start-up, operation space is not only determined by the Townsend criterion, but also by the criterion for plasma burn-through. The black solid, red dotted, and blue dashed lines in Figure 6.15 represent the required electric field for plasma burn-through  $E_{Burn}$  without or with impurities, obtained using *DYON* simulation results. The wall-sputtering models described in section 5.3 and 5.4 are used for the *DYON* simulations. Plasma parameters assumed for the *DYON* simulation are indicated in Table 4.1.

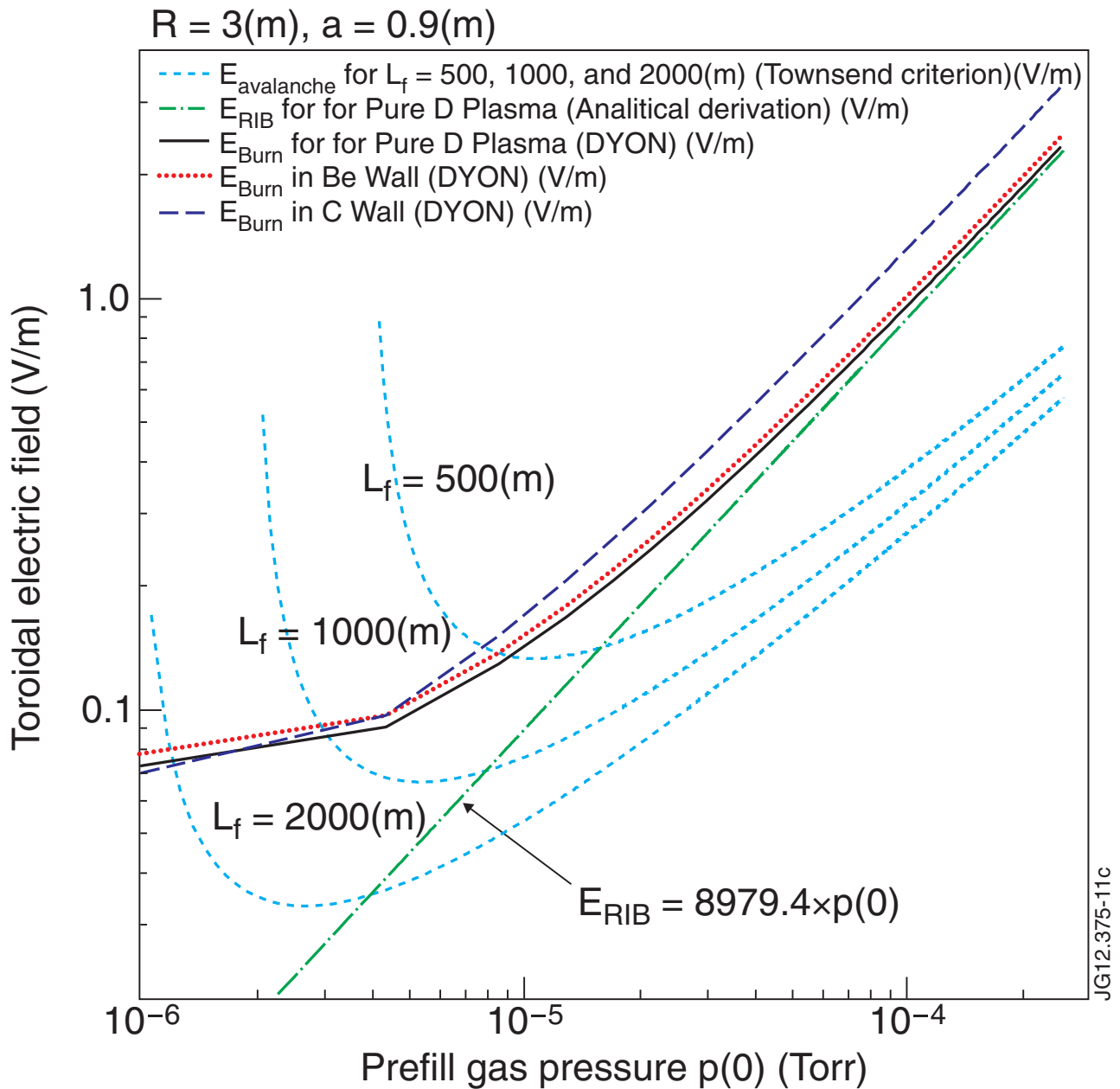


Figure 6.15: The cyan dashed lines show the Townsend criterion at different effective connection lengths, as indicated with 500, 1000, and 2000[m], respectively. The black solid, red dotted, and blue dashed lines indicate the criterion for plasma burn-through, i.e. the minimum electric field for plasma burn-through in the case of a pure deuterium plasma (black solid), beryllium wall (red dotted), and carbon wall (blue dashed), respectively. The wall-sputtering models described in section 5.4 are used for the simulations, and the required plasma parameters are given by Table 4.1. The green chain line indicates the criterion for deuterium burn-through, calculated analytically by Equation (6.12). The area above both the burn-through criterion and Townsend criterion represents the operation space available for successful start-up in JET.

The criterion for plasma burn-through is computed from the numerical simulations using several assumptions, subject to wall conditions and operation scenario. However, the simulation results provide informative insight on the operation space. As shown in Figure 6.15, the required electric field for plasma burn-through increases monotonically as prefill gas pressure rises since the RIB is greater at a higher prefill gas pressures. This monotonic increase with prefill gas pressure is consistent with Equation (4.13), which is analytically derived for deuterium burn-through. In order to compare Equation (4.13) quantitatively to the DYON simulation results, the electron temperature at the RIB,  $T_e(t_{RIB})$ , is assumed to be  $3[eV]$ , based on DYON simulation results. The effective vessel volume, major radius, and minor radius of a plasma are given by the same values assumed in the simulations, i.e.  $R = 3$  and  $a = 0.9[m]$ . The corresponding  $P_{rad+iz}(T_e(t_{RIB}))$  is obtained from ADAS[25], i.e.  $P_{rad+iz}(3) = 2.15 \times 10^{-33}[Wm^3]$ . Then, the required electric field  $E_{RIB}$  is calculated as

$$E_{RIB} = 3.23 \times 10^{-19} \times n_D^0(0). \quad (6.11)$$

With the assumption of a room temperature ( $\approx 0.03[eV]$ ) for deuterium atoms,  $E_{RIB}$  is represented as a function of prefill gas pressure  $p(0)$ ,

$$\begin{aligned} E_{RIB} &= (3.23 \times 10^{-19}) \times (2.78 \times 10^{22}) \times p(0)[Torr] \\ &= 8979.4 \times p(0)[Torr]. \end{aligned} \quad (6.12)$$

The green line in Figure 6.15 indicates  $E_{RIB}$  obtained using Equation (6.12). The  $E_{RIB}$  obtained by the analytical derivation shows good agreement with that obtained by DYON simulations for a pure deuterium plasma at a high prefill gas pressure. The discrepancy at a low prefill gas pressure is probably due to the convective transport which is neglected in the analytical derivation for Equation (6.11).

If the effects of the impurities from the wall are included, the required electric field for plasma burn-through increases, thereby reducing the operation space available. As can be seen in Figure 6.16, the RIB for carbon burn-through is much greater than for deuterium burn-through. Hence, the required loop voltage for the carbon wall is significantly higher than for a pure deuterium plasma. This results in the smaller operation space available in the carbon wall as shown in Figure 6.15. However, the RIB for beryllium burn-through is not significant as shown in Figures 6.16. With the beryllium wall, the critical RIB to be overcome is for deuterium rather than for beryllium as long as other impurities are not significant. This implies that lower loop

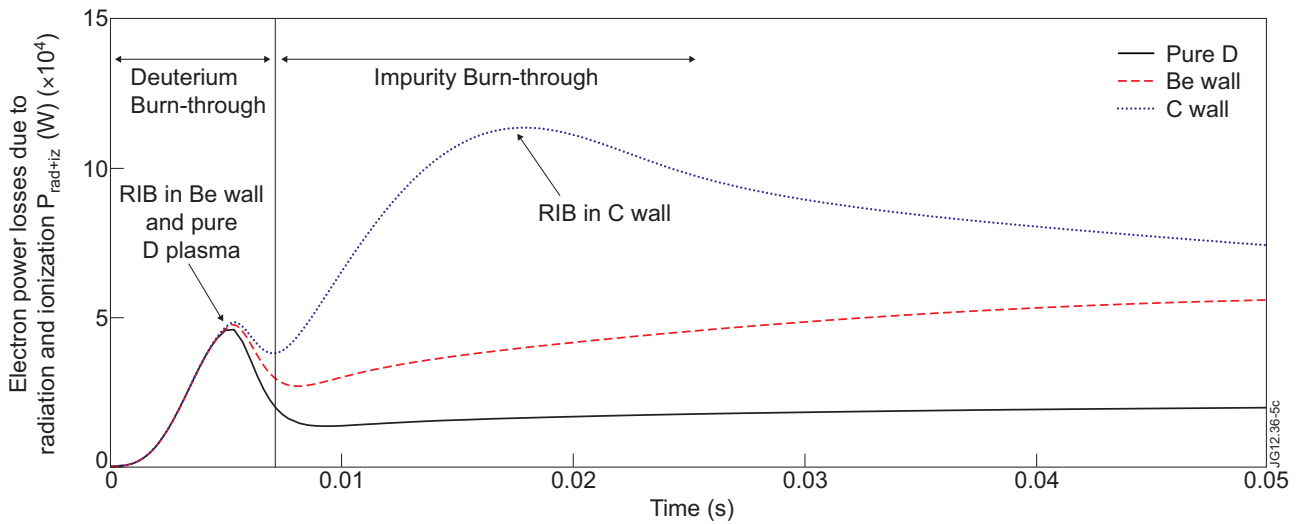


Figure 6.16: *DYON* simulation results for a pure deuterium plasma or with PWI models i.e. carbon wall or beryllium wall. Each line indicates the electron power losses due to the radiation and ionization: carbon wall(dotted blue), beryllium wall(dashed red), and pure deuterium plasma(solid black). In the case of a carbon wall, the first RIB (mainly from deuterium radiation) is much smaller than the second peak, which results from carbon impurities.

voltage can be used for plasma burn-through in the ITER-like wall i.e. larger operation space available compared to the carbon wall as shown in Figure 6.15.

These predictions are compared to experimental data in Figure 6.17. The majority of the experimental data points with the C wall (blue circles) and the Be wall (red circles) lie above (or near) the simulated minimum electric field required for a C wall (blue line) and a Be wall (red line) again showing good agreement of the simulations with the experiments, over a wide range of conditions. It should be noted that in previous studies determining operation space in tokamaks, only the Townsend criterion was used [4]. Since the  $L_f$  can decrease during the electron avalanche phase due to the eddy current, pessimistic value (200 [m]) and reasonable value (500 [m]) of  $L_f$  are used for Townsend criterion in Figure 6.17. As can be seen in Figure 6.17, the operation at low prefill gas pressure is limited by the Townsend criterion. However, at high prefill gas pressure, the limitation is set by the burn-through criterion rather than the Townsend criterion.

It was observed that the Be wall tends to absorb the fuel at the wall. This can reduce the prefill gas pressure or initial plasma density, thereby resulting in slow electric avalanche (which is not

favorable for operation) or run-away electron generation. Hence, the prefill gas pressure used for start-up with the Be wall in JET is higher than that of the C wall as shown in Figure 6.17.

It should be noted that the criterion for plasma burn-through in Figures 6.15 and 6.17 change with different assumptions in the DYON code. That is, the increase in required loop voltage with increasing prefill gas pressure is steeper for higher recycling coefficient (or sputtering yield) or for higher  $V_V/V_p$ . In tokamaks, the recycling coefficients and the sputtering yields vary due to the effects of deuterium retention and impurity migration in the wall. In addition, the ratio of the effective vessel volume to the plasma volume, which is related to dynamic neutral gas fuelling from the ex-plasma volume, is also varying according to the operation scenario. Hence, to find the precise operation space using the simulations, the information on the wall conditions and operation scenario in each shot should be specified.

## 6.6 Discussion and Conclusion

### 6.6.1 Discussion

A model validation using the five subsequent discharges (#77211 ~ 77215) has been performed. The simulations of the radiated power, electron density evolution, and  $C^{2+}$  line emission show similar agreement with the measured data as shown for #77210 in Figure 6.2 and 6.3. However, the plasma current rise is slightly overestimated in these discharges. The plasma current after the burn-through phase depends on the loop voltage available. The time evolution of the loop voltage available for the plasma current build-up would require detailed information of the magnetic equilibrium. This is not used in the model (only external measurement is used), hence the agreement with the measured plasma current rise could be improved.

The investigation of plasma burn-through has been published only with 0D simulations [6][18][19][36]. Since closed flux surfaces (CFSs) are not established yet during the plasma burn-through phase at low plasma current, a 2D approach of numerical simulation is extremely difficult. Fortunately, the results of DYON simulations (also 0D) show good agreement with JET data. This implies the assumption of a uniform temperature and density in a numerical simulation is reasonable to compute the gross energy and particle balances during the plasma burn-through



phase. Probably, this is due to the open field configurations during the plasma burn-through phase. With the open magnetic field lines, the parallel thermal conduction and particle diffusion would be significant. Quantitative investigations on the profile effects of temperature and density will be interesting to confirm this. Regarding the profile of plasma current, a flat current profile is assumed i.e.  $l_i = 0.5$ . According to a scan of  $l_i$  with the DYON code, the

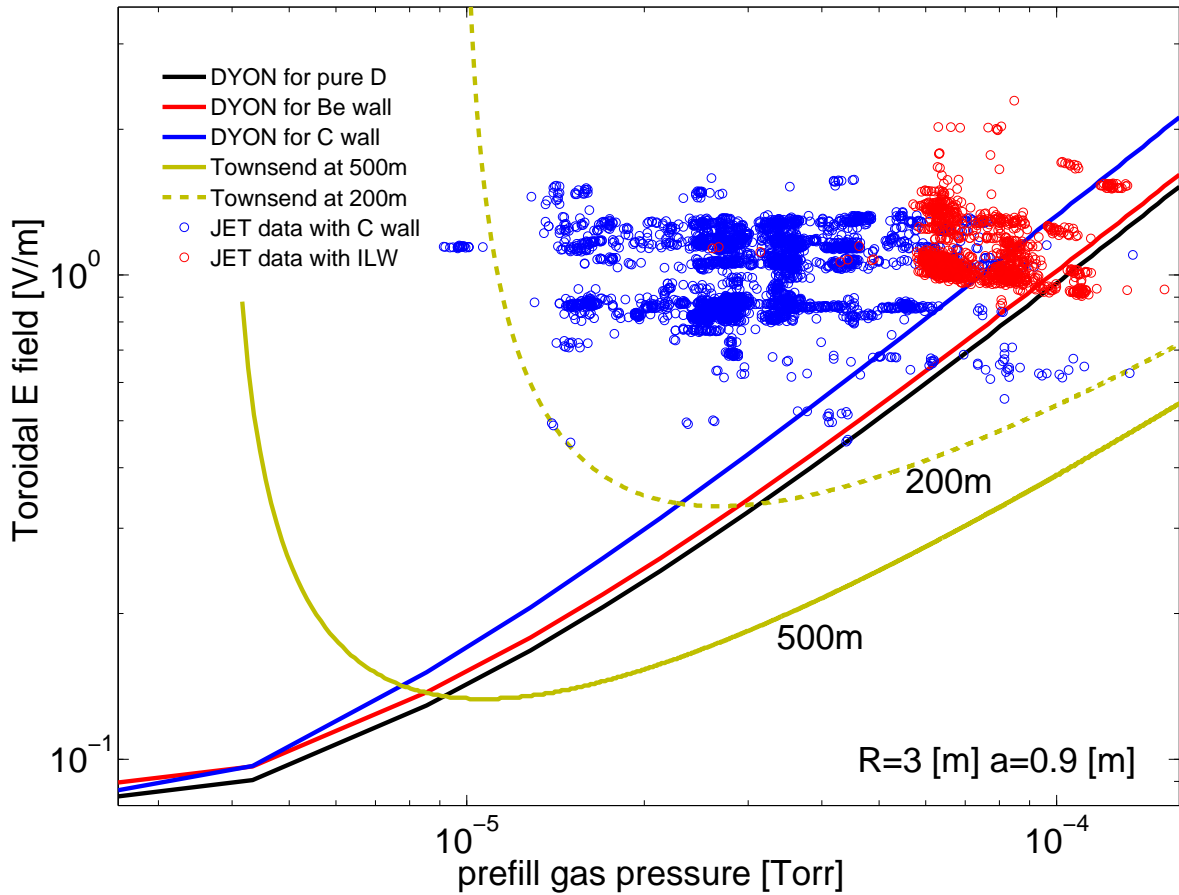


Figure 6.17: Operation space for JET start-up. The green lines indicate the Townsend criterion for electron avalanche with an effective connection length of 200m (pessimistic) and 500m (reasonable), respectively. The black line is the required electric field for pure deuterium burn-through, computed using the DYON code. The red (Be wall) and blue (C wall) lines are the corresponding burn-through criterion and including the different wall models. The circles correspond to the successful plasma burn-through in JET experiments with the ITER-like wall (#80239 ~ #82905, red circles) and the C wall (#70988 ~ #78805, blue circles).

internal inductance does not have significant effect on the simulation results since most of the power is consumed by ohmic heating.

The synthetic PM tube data is not dependent on the initial electron temperature ( $T_e(0)$ ) assumed in the simulations.  $T_e(t)$  quickly saturates to the same value in a few millisecond regardless of the assumed value of  $T_e(0)$ . This has been checked in the simulations, starting with  $T_e(0) = 1, 3, \text{ and } 5$  [eV].

The formula for impact ion energy (i.e.  $E_0 = \gamma_i kT_i + 3kT_e$  where  $\gamma_i = 2$ ) is good enough for the scope of this thesis, and the simulation results match well with experimental data. However, it should be noted that the formula does not include all physical processes for computing the impact ion energy. Due to the pre-sheath acceleration, the ions at the sheath edge might not have maxwellian velocity distribution. This results in different  $\gamma_i$  depending on the model assumed ( $\gamma_i \approx 1.5 \sim 2.93$ ) [53]. For more accurate calculation of  $\gamma_i$  it would be needed to solve full kinetic equations using the distorted energy distribution of the ions. However, the calculation has not been well established yet. The pre-sheath energy gain is ignored in the adopted formula since it is assumed to be small compared to the uncertainty of  $\gamma_i$  and the sheath energy gain. However, the wall impact energy of impurities can be higher than the value calculated using the adopted formula if impurity flow velocity is equal to the ion sound speed  $C_s$  ( $= \sqrt{\frac{T_e + T_i}{m_D}}$ ). For example, in the case of  $Be^{1+}$  in isothermal plasma ( $T_e = T_i$ ), the wall impact energy is

$$E_0^{Be^{1+}} = 0.5kT_e + \frac{1}{2}m_{Be}C_s^2 + (2kT_i + 3kT_e) \approx 10kT_e \quad (6.13)$$

where the first term is due to pre-sheath acceleration, the second term is due to the sound speed equilibrium, and the third term is due to temperature equilibration plus sheath-acceleration. The result is almost twice higher than the formula ( $E_0 = 2kT_i + 3kT_e$ ). Fortunately, the formula used in the simulations is still valid since the majority of impacting ions are deuterium in the simulation.

The deuterium recycling coefficient has a significant influence on plasma burn-through and the dynamics of deuterium recycling coefficient is different for the carbon wall and the ITER-like wall. This probably results from the different retention of deuterium at the wall. In the carbon wall, deuterium is retained especially after disruptions, so that the simulation results using decay model of  $Y_D^D$  match well with JET data [36]. However, in the ITER-like wall, the DYON

results using the growing model of  $Y_D^D$  shows good agreement with JET data. This might be due to the fact that most of attached deuterium, even after disruption event, are easily removed by pumping between discharges [54] (typically 30 ~ 40 minutes in JET).

Deuterium fuelling has a significant effect, and it should be confirmed for ITER simulations. However, it might not be a critical issue for plasma burn-through if the fuelling is pre-programmed after the plasma burn-through is completed as shown in Figure 6.12.

As shown in Figure 6.13 (b), the radiation barrier in the ITER-like wall simulations is dominated by deuterium, carbon, and oxygen. The simulation results with 0.5%  $n_C^0(0)$  show good agreement with experimental data. However, the simulation results with 0% and 1%  $n_C^0(0)$  still show reasonable agreement in the other plasma parameters, i.e.  $I_p(t)$ ,  $T_e(t)$ , and  $n_e(t)$ . This implies that, although the radiation barrier is subject to  $n_C^0(0)$ , it might not be deleterious to the energy and particle balances for the plasma. This is consistent with the recent observation in JET experiments with the ITER-like wall where failures during the plasma burn-through phase are hardly observed, for a wide range of experimental conditions [12].

Plasma initiation in JET experiments with the ITER-like wall is very reliable. According to an experimental characterisation of plasma formation with the ITER-like wall [12], the failures during the plasma burn-through phase, that usually occurred with the carbon wall (mostly after disruptions), were not observed with the ITER-like wall. This implies that the plasma parameters during the burn-through phase, including the radiated power losses from impurities, are not likely to vary significantly in each shot, even after disruption events. Hence, the validation of #82003 is representative of plasma burn-through simulations for other shots with the ITER-like wall.

In ITER, oxidation of beryllium surface might be much less than in JET, due to the much longer plasma pulses. Also, the initial carbon content would be much reduced if the first divertor is made solely of tungsten. On the other hand, due to the use of seeding gases, there should be various impurities e.g. Ar, Ne, or N. Hence, modelling impurity seeding in the simulations would be interesting for predictive simulations of ITER. In DYON simulations, RF heating is not included as no RF heating was used for the simulated pulse (# 82003), but RF-assisted start-up is planned in ITER. In order to apply the DYON code to such operations, it is required for development of an RF-heating module.

## 6.6.2 Summary and Conclusion

In this chapter, quantitative validation of the models against the JET data is provided for the first time. The simulation results using the PWI models are compared to JET data with the carbon wall and the ITER-like wall. Good agreement of plasma current and the total radiated power is shown between the simulation results and JET data.

Due to the uncertainties or errors in the measured data in the early burn-through phase, it is difficult to compare the simulated electron temperature and density. However, the simulation result and the measured densities approach the similar value with time, showing reasonable agreement for the evolution in time. The measured photon emission rate of impurities are compared with the synthetic data calculated with the simulated plasma parameters. The peaks of the synthetic data are consistent with the observed peaks in the measured data.

The results of parameter scanning in DYON simulations provide important information for the ITER-like wall experiments. The deuterium recycling coefficient significantly influences the gross energy and particle balance, and the simulation results with the growing model of  $Y_D^D$  show good agreement. This implies that during the plasma burn-through phase deuterium is pumped out by the beryllium wall. Second, the physical sputtering model using the BeO layer erosion model (i.e. transition of a BeO wall to a pure Be wall at  $\tau_{erosion}$ ) agrees well with the photomultiplier tube data. Third, the radiation barrier in the ITER-like wall is dominated by deuterium and other impurities rather than beryllium. The initial carbon content does not influence other plasma parameters significantly in the simulation results. Fourth, in the case of JET with the ITER-like wall, plasma burn-through is not affected by gas fuelling if the fuelling is pre-programmed after 100 [msec]. Lastly, effective vessel volume should be used for simulations since not all neutrals are accessible to the plasma.

The required electric field for deuterium burn-through is calculated by the DYON code as well as an analytical derivation, and it is compared to the Townsend avalanche criterion. The limitations set by the burn-through criterion will reduce the operational space with respect to those only based on the Townsend criterion for an electron avalanche.

The operation space available for JET is computed for the carbon wall and the ITER-like wall. The impurity effects result in a reduced operation space for the carbon wall compared to a pure deuterium plasma. However, the RIB in the ITER-like wall is not much higher than in a

pure deuterium plasma. This results in larger operation space available for successful plasma initiation in the ITER-like wall than in the carbon wall.

The similarity of the simulation results and JET data implies that the new burn-through models contain the essential physics in the burn-through phase, and the significance of the new models is shown by comparing the simulation results with and without the new models. Based on this, we suggest that the DYON code can be used to investigate the burn-through criterion in ITER.

# Chapter 7

## DYON simulations for ITER

### 7.1 Introduction

Reliable plasma burn-through in ITER is of crucial importance. However, as detailed in chapter 1, the toroidal electric field available is limited to 0.35 [V/m], which is very small compared to the value used in current devices e.g. 1 [V/m] in JET. The limitation on toroidal electric field also reduces the range of other operation parameters available (e.g.  $p$ ,  $U_l$ ,  $L_f$ ,  $n_I$ , and  $P_{RF}$ ). For reliable start-up in ITER, additional RF heating is planned to assist plasma burn-through. In order to ensure the operation scenario for robust start-up, predictive simulations of plasma burn-through in ITER, including the estimation of the required RF power, are required.

Previously, plasma burn-through simulations for ITER were attempted to evaluate the required RF power. Simulations of old ITER (major radius  $R = 10[m]$  and vessel volume  $2000[m^3]$ ) were published in [6], reporting that i) without RF assist, operation parameters are significantly restricted; very low prefill gas pressure  $p(0)$  is required for ohmic plasma burn-through. e.g. failed ohmic burn-through at  $n_D^0(0) = 2 \times 10^{17}[m^{-3}]$  ( $\sim p(0) = 7.2 \times 10^{-6}[Torr]$ ), ii) 3MW RF will ensure robust start-up for a broad range of conditions with 5% Be, and iii) however, in the case of C, low  $p(0)$ , low error field, and low carbon content would be required even with 5MW RF power. With the modified ITER size, the ITER physics basis presented plasma burn-through simulations using the SCENPLINT code [5]. It showed that 2[MW] of RF power enables plasma burn-through with the design value of toroidal electric field at a prefill gas

pressure of  $6 \times 10^{-6}$  [Torr].

In the previous simulations, constant value or empirical models were used for particle confinement time without considering parallel transport, which is important at open magnetic field configurations such as the plasma burn-through phase. In addition, the impurity treatments were overly simplified in the previous models. In [6], constant impurity fraction was used, and constants of impurity recycling coefficient (i.e.  $Y_I^I = 1$ ) and impurity recycling time (e.g.  $\tau_{imp} = 100[ms]$ ) were assumed. In order to simulate the evolution of impurity fraction, simple growing fraction model, in which impurity fraction is an exponential function of time, was used in [5].

This chapter provides predictive simulations for the plasma burn-through phase in ITER using the DYON code. Despite the previous simulations for ITER, DYON simulations can make important contributions for ITER due to the facts that;

1. For the first time, the simulation results and initial conditions (assumptions) used have been validated using experimental data; the DYON simulation results show good agreement with the JET experiments with the ITER-like wall.
2. The DYON code has been significantly improved to include key physics aspects in the plasma burn-through phase.
  - The DYON code computes the impurity evolution using self-consistent PWI model (i.e. Physical sputtering model for a beryllium wall).
  - In the DYON simulations, a new confinement time model has been developed; Transonic ambipolar transport along magnetic field lines using dynamic effective connection length  $L_f(t)$  is used for parallel transport model, and Bohm diffusion is adopted for perpendicular transport model.
  - Atomic reaction calculation for all charge states of impurities is sophisticated using the latest atomic data package, ADAS. ([6] did have calculation of all charge states, but it was done assuming constant impurity fraction with old atomic data.)
  - Neutral screening effects are taken into account for all impurity charge states; Only D neutral screening was used in the previous model [6].

- The simulations use the modified ITER size and the ITER operation scenario obtained from F4E (Fusion 4 Energy), which is an European Union's organization for ITER.<sup>1</sup>

For predictive simulations, the design values of ITER such as toroidal loop voltage and magnetic fields are used as input data for the circuit system in the DYON code. In section 7.2, the circuit system used to compute the plasma current is explained. The DYON simulation results of ohmic (unassisted) plasma burn-through in ITER are given in section 7.3. The simulations of RF-assisted plasma burn-through and the estimation of the required RF power for successful burn-through in ITER are presented in section 7.4, followed by the main conclusions and discussion of the results obtained in section 7.5.

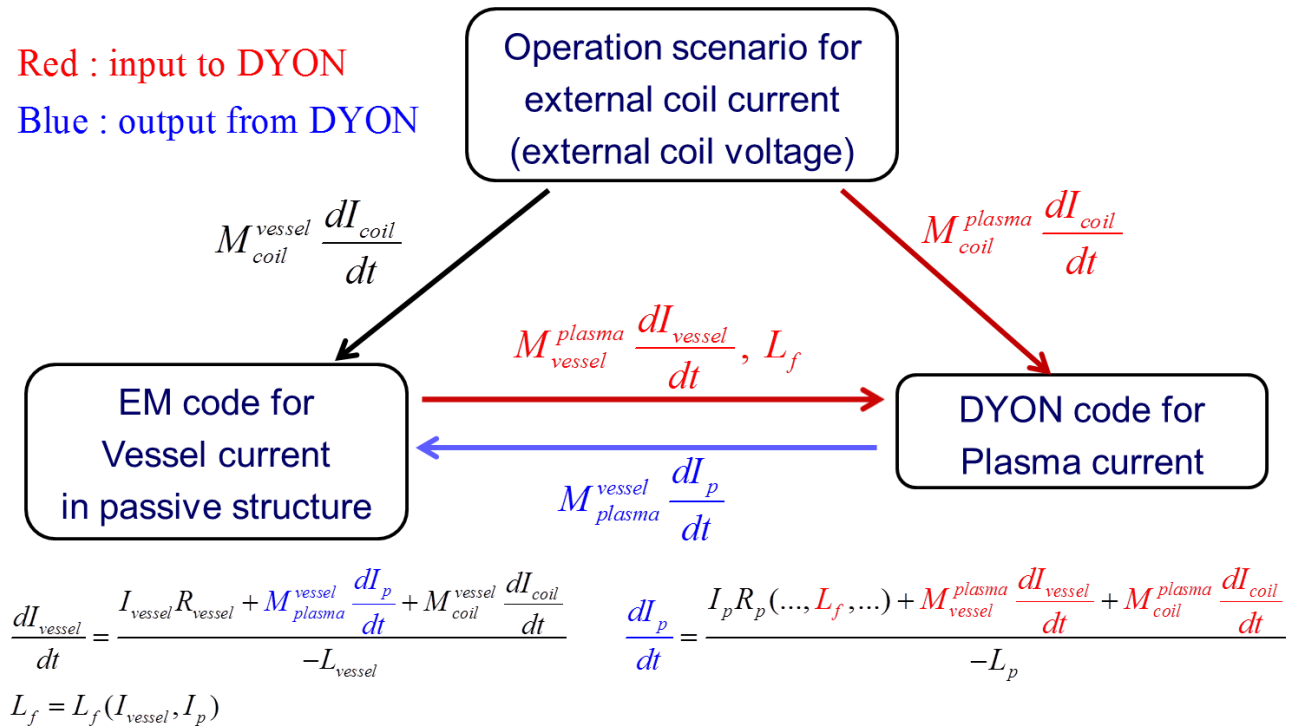


Figure 7.1: Full interactive circuit system.



## 7.2 Circuit system for DYON simulations

In tokamaks, the toroidal loop voltage is induced by the change of current in external coils such as central solenoid and poloidal field coils. The current swing induces eddy currents in the passive structure (e.g. vacuum vessel), thereby resulting in shielding effects of the external magnetic fields. Thus, in order to calculate the toroidal loop voltage on axis in the vessel (i.e. actual voltage driving plasma current), a full circuit system should be computed using mutual inductances  $M$ , which are a function of geometric structure, e.g.  $M_{coil}^{vessel}$  is determined by the relative geometry between vessel and external coils.

Figure 7.1 describes a full interactive circuit system. A preprogrammed operation scenario (evolution of external voltages for the electromagnets in time) determines the currents (or voltage) in external coils. They induce voltage in vessel and on axis e.g.  $M_{coil}^{vessel} \frac{dI_{coil}}{dt}$  and  $M_{coil}^{plasma} \frac{dI_{coil}}{dt}$ , resulting in eddy currents in the vessel  $I_{vessel}$  and a plasma current  $I_p$ . They also induce voltage in each other i.e. interaction between  $I_{vessel}$  and  $I_p$ . In addition, the eddy current contributes to the stray magnetic field near the axis, reducing the effective connection length, which is one of the important parameters in the particle balance in the DYON code. Hence, the circuit equation of eddy current and plasma current should be computed simultaneously. The full circuit equation system is given by

$$\begin{aligned} \frac{dI_{vessel}}{dt} &= \frac{I_{vessel}R_{vessel} + M_{plasma}^{vessel} \frac{dI_p}{dt} + M_{coil}^{vessel} \frac{dI_{coil}}{dt}}{-L_{vessel}} \\ \frac{dI_p}{dt} &= \frac{I_p R_p + M_{vessel}^{plasma} \frac{dI_{vessel}}{dt} + M_{coil}^{plasma} \frac{dI_{coil}}{dt}}{-L_p}. \end{aligned} \quad (7.1)$$

where  $L$  and  $R$  indicate a self inductance and electric resistance, respectively. However, the full circuit equation system requires a significant amount of effort for coding a 3 dimensional passive structure, which is very complicated in tokamaks.

The design values of ITER are calculated by F4E using the CREATE code [55]. F4E provided us with the toroidal loop voltage on axis  $V_{ext}$ , calculated using the current in external coils and the resultant eddy currents in passive structure in ITER,

$$V_{ext} = M_{vessel}^{plasma} \frac{dI_{vessel}}{dt} + M_{coil}^{plasma} \frac{dI_{coil}}{dt}. \quad (7.2)$$

---

<sup>1</sup><http://www.fusionforenergy.europa.eu/>

In addition, CREATE calculations provided the stray field on axis  $B_{stray}$ , which is needed to calculate the effective connection length. Using the design values, the circuit equation of the DYON simulations for ITER can be simplified as

$$\frac{dI_p}{dt} = \frac{I_p R_p(\dots, B_{stray}, \dots) + V_{ext}}{-L_p}. \quad (7.3)$$

It should be noted that plasma current was not taken into account in the simulations from F4E when computing  $V_{ext}$  and  $B_{stray}$ . In other words, the interaction between eddy current and plasma current is ignored in the simulations for ITER.

At 0.9 seconds after the start of the flux swing from the ohmic transformer coil, the toroidal loop voltage reaches a maximum of  $E = U_l/(2\pi R) \sim 0.35$  [V/m] at  $R = 5.65$  [m], which is the centre of the initial plasma [5]. Thus, the plasma break-down (electron avalanche) is assumed to occur at 0.9 second, and the DYON simulations also start from 0.9 second when the electric field reaches a maximum. The toroidal loop voltage is preprogrammed to decrease after 0.9 second (see Figure 7.7 (a)).

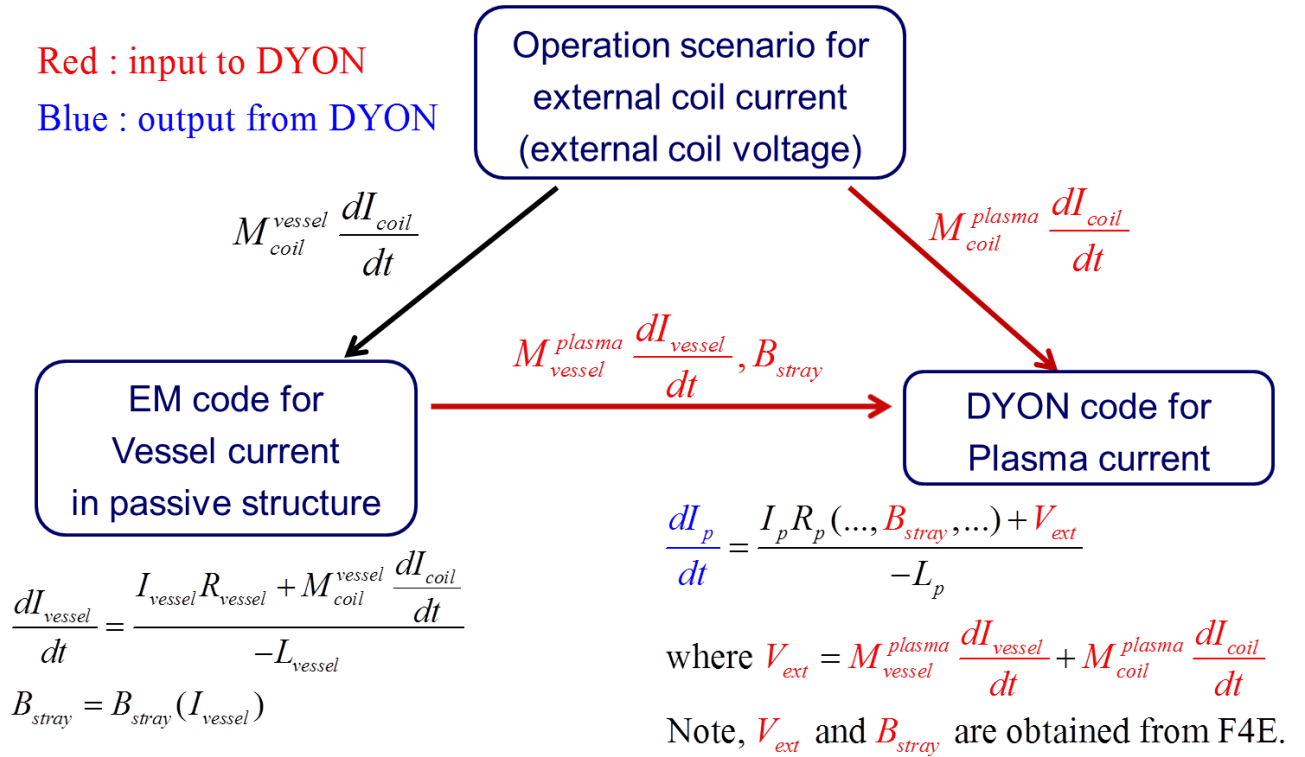


Figure 7.2: Circuit system used in the DYON code for ITER simulations.

## 7.3 Ohmic (unassisted) plasma burn-through

Plasma burn-through simulations for ITER have been performed with a PWI model for a Be wall, including the physical sputtering model as validated with the ITER-like wall in JET. The design values for ITER are used in DYON simulations; i.e. the toroidal loop voltage  $U_l(t)$ , the vertical magnetic field  $B_V(t)$  and radial magnetic field  $B_R(t)$  which are used for the effective connection length, the plasma major  $R(t)$  and minor radius  $a(t)$ , and the vessel volume  $V_V$ . An overview of the parameters is given in Table 7.1. In these simulations of plasma burn-through in ITER, initial concentrations of  $Be$  (1% of  $n_D(0)$ ),  $C$  (0.5% of  $n_D(0)$ ), and  $O$  (0.1% of  $n_D(0)$ ) are used, similar to values used for simulations of JET with the ITER-like wall. Other initial conditions and assumptions e.g.  $T_e(0)$ ,  $T_i(0)$ ,  $J_p(0)$ ,  $Y_D^D$ , and  $l_i$  are listed in Table 7.1.

With the given design values, it is found that very low prefill gas pressures ( $7.2 \times 10^{-6}[Torr]$ ) are required to achieve ohmic plasma burn-through (see Figure 7.3 (a)). Higher prefill gas pressures ( $1.8 \times 10^{-5}[Torr]$ ) used in present day devices (typical  $p(0)$  in JET is  $5 \times 10^{-5}[Torr]$ ) will result in ITER in a failed burn-through, despite ITER having a connection length of 4000 [m] at the start of the simulation ( $t = 0.9[s]$ ). The required time to achieve 1[MA] of plasma current is about 2 seconds (see Figure 7.3 (b)), which is much longer compared to that in JET ( $0.5 \sim 1$  second), due to the low loop voltage available.

Figure 7.3 (d) and (e) show the corresponding  $Be$  evolution in the ITER simulations. The densities for the different charge states of  $Be$  are computed in the DYON code. In the case of a successful plasma burn-through,  $Be^{4+}$  becomes the dominant charge state. However, in the failed case, the initial  $Be$  content does not continue the ionization process and the total content decreases. If plasma burn-through is not successful, plasma temperature does not increase. This results in the incident ion energy below the threshold energy for physical sputtering i.e. no further source of  $Be$ . This is a difference with previous simulations where an assumed Be fraction was used. In the DYON code the PWI process determines the Be erosion; no plasma, no erosion.

Figure 7.4 shows (a) the electron power loss and (b) the radiation power loss for the successful simulation of plasma burn-through in ITER simulation. The electron power loss during the early start-up phase up to 1.5 seconds is dominated by the radiation and ionization power losses (blue in Figure 7.4 (a)). However, towards the end of the plasma burn-through process, the

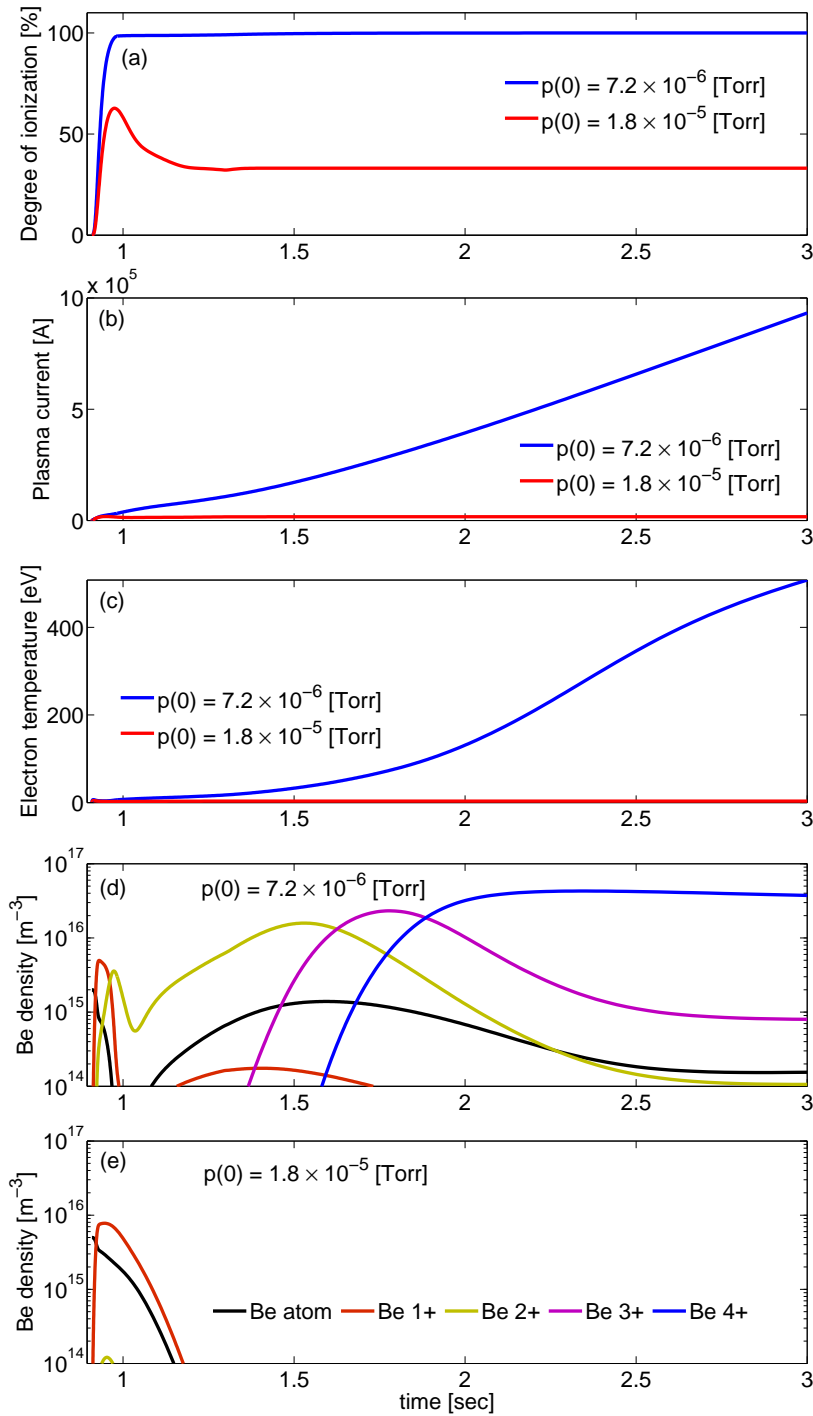


Figure 7.3: Predictive ohmic (No RF assist) plasma burn-through simulations for ITER. Using design values ( $V_L(t)$ ,  $B_v(t)$ ,  $B_R(t)$ ,  $R(t)$ , and  $a(t)$ ), different prefill gas pressures are used;  $p(0) = 7.2 \times 10^{-6}$  [Torr] (Blue) and  $1.8 \times 10^{-5}$  [Torr] (Red) in (a) Degree of ionization, (b) Plasma current, and (c) Electron temperature. (d) Evolution of impurity density (Be) in ITER simulations at  $p(0) = 7.2 \times 10^{-6}$  [Torr], and (e)  $p(0) = 1.8 \times 10^{-5}$  [Torr].

Plasma parameters	Input value
$U_l$ [V]	11.36 at $t = 0.909$ [sec] (see Figure 7.7 (a))
$P_{RF}$ [MW]	0 (Figure 7.3 and 7.4) 4 (Figure 7.7)
$B_v$ [Tesla]	$4.4 \times 10^{-4}$ at $t = 0.909$ [sec]
$B_R$ [Tesla]	$5.1 \times 10^{-5}$ at $t = 0.909$ [sec]
$R$ [m]	5.65
$a$ [m]	1.6
$V_V$ [m <sup>3</sup> ]	1400
$B_\phi$ [Tesla]	5.3
$p(0)$ [Torr]	$7.2 \times 10^{-6}$ (Figure 7.3 and 7.4) $1.8 \times 10^{-5}$ (Figure 7.3) $5 \times 10^{-5}$ (Figure 7.5 and 7.7)
$n_D^0(0)$ [m <sup>-3</sup> ]	$2.78 \times 10^{23} \times p(0)$ [Torr]
$n_{Be}^0(0)$ [m <sup>-3</sup> ]	$0.01 \times n_D^0(0)$ [m <sup>-3</sup> ]
$n_C^0(0)$ [m <sup>-3</sup> ]	$0.005 \times n_D^0(0)$ [m <sup>-3</sup> ]
$n_O^0(0)$ [m <sup>-3</sup> ]	$0.001 \times n_D^0(0)$ [m <sup>-3</sup> ]
$T_e(0)$ [eV]	1
$T_i(0)$ [eV]	0.03
$J_p(0)$ [Am <sup>-2</sup> ]	$382.5 \times E$ [V/m]
$Y_D^D$	1
$\gamma_{iz}(0)$	0.002
$l_i$	0.5

Table 7.1: Input values given to the DYON code for plasma burn-through simulations of ITER

power loss due to the electron transport dominates. Figure 7.4 (b) shows the corresponding radiated power. The sources of the radiation are shown by different colors. The majority of the radiated power during the plasma burn-through phase is  $D$  radiation (black line). The first peak in  $Be$  radiation (red line) at the start of the discharge, results from initial  $Be$  content,

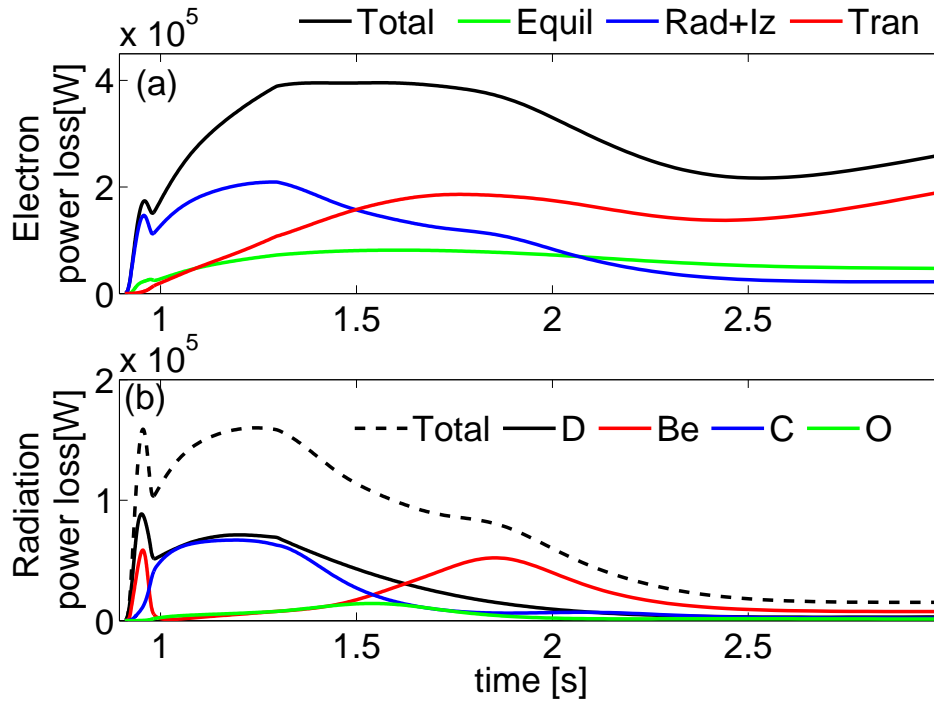


Figure 7.4: Simulated power losses for the simulation of ohmic plasma burn-through at  $p(0) = 7.2 \times 10^{-6}$  [Torr] in Figure 7.3. (a) electron power losses; total electron power loss (black, Electron power loss due to the radiation and ionization (blue), transport power loss (red), and equilibration power loss (green)) and (b) radiation power loss; the total radiated power is indicated by the black dashed line. The contribution to the radiated power are indicated; D(black), Be(red), C(blue), O(green)

which is an assumption validated by JET data. It decreases immediately after the initial radiation peak. The second increase in the *Be* radiation around 1.9 second is due to more *Be* entering the plasma due to physical sputtering. Until the incident ions have reached sufficient temperature (i.e. the incident energy exceeds the physical sputtering threshold) this second *Be* radiation peak is delayed. This evolution (double peak) of the *Be* radiation has been observed

in experiments with the ITER-like wall [52]. The simulations indicate that  $C$  radiation is comparable to the  $D$  radiation for the period  $1 \sim 1.5$  second (see Figure 7.4 (b)). For a higher initial  $C$  content the  $C$  radiation will dominate the radiation barrier.

## 7.4 RF-assisted plasma burn-through

RF power can provide pre-ionization for electron avalanche and additional heating during the plasma burn-through phase. In ITER, RF power will be used to ensure robust start-up. Using the DYON code, RF-assisted plasma burn-through has been simulated for ITER. Here, the RF power is defined as the total absorbed RF power in the plasma i.e.  $V_p \times P_{RF}$ , and the RF power in a unit volume  $P_{RF}[W/m^3]$  is included in the energy balance as shown below (i.e.  $P_{aux} = P_{RF}$ ).

$$P_e = P_{oh} + P_{RF} - P_{Rad+Iz} - P_{equil} - P_{conv} \quad (7.4)$$

If the given RF power is high enough for full ionization of the plasma and to overcome the radiation barrier, the plasma current increases. Figure 7.5 shows the DYON simulation results. There is a critical RF power for plasma burn-through between 3MW and 4MW at prefill pressure of  $5 \times 10^{-5}$  [Torr] (with initial conditions given in Table 7.1). The plasma current ramp-up is not significantly different with higher RF power (6 MW (green) and 8 MW (black) in Figure 7.5). The slightly faster increase in plasma current is due to the additional heating of the RF power, which increases electron temperature, thereby reducing the plasma resistance. Once plasma burn-through is completed, the ramp-up rate of plasma current is mainly determined by the toroidal loop voltage.

The plasma current keeps increasing even if the RF power is switched off. Figure 7.6 shows the simulation result when the RF power is deliberately turned off in the simulation at  $t = 2$  seconds. The electron temperature shows a significant change at  $t = 2$  seconds since the RF power makes contribution to the total electron heating. In contrast, the electron density does not show such a change at  $t = 2$  seconds. This is due to the fact that despite the decrease in electron temperature, it is still high enough for D ionization. Although the electron temperature determines the plasma resistance, plasma current ramp-up also does not change at  $t = 2$  second; the self-inductance of the plasma current maintains the ramp-up rate.

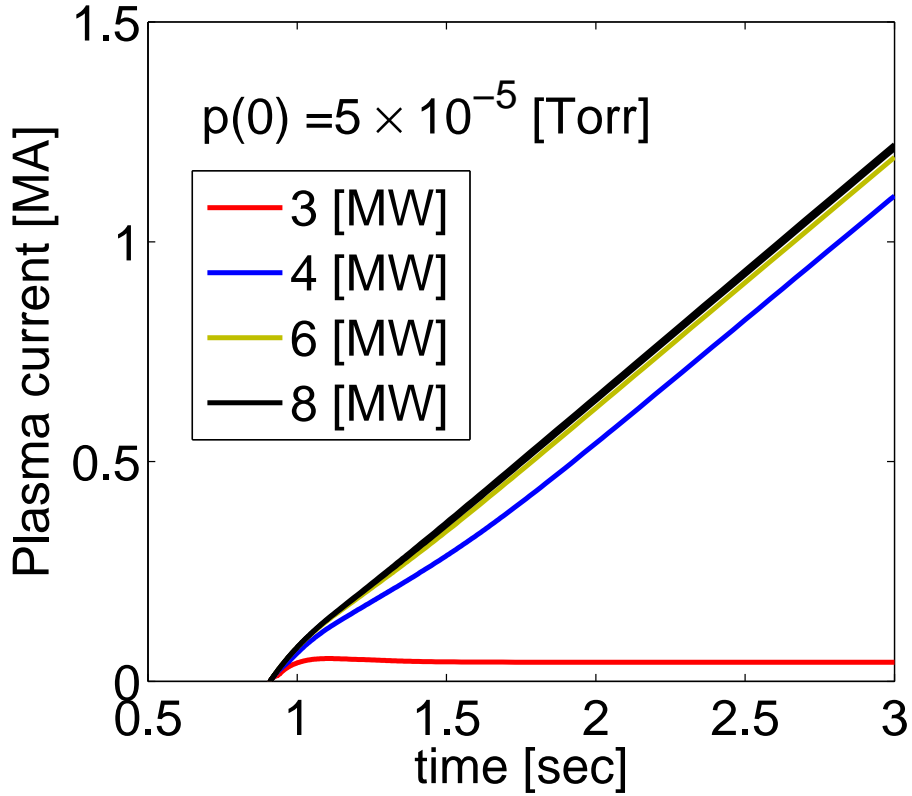


Figure 7.5: Simulated plasma current in RF-assisted plasma burn-through simulations for ITER. With the same prefill gas pressure ( $p(0) = 5 \times 10^{-5}$  [Torr]), the RF power is scanned.

Figure 7.7 shows a DYON simulation of RF-assisted plasma burn-through in ITER. In this simulation, constant 4 [MW] of RF power and the same design values in Table 7.1, including the toroidal loop voltage (see Figure 7.7 (a)), are used. Although the prefill gas pressure used ( $5 \times 10^{-5}$  [Torr]) is much higher than that for ohmic plasma burn-through ( $7.2 \times 10^{-6}$  [Torr]) in Figure 7.3, the plasma current and electron temperature are slightly higher in the simulations of RF-assisted burn-through. Deuterium burn-through is completed instantly as can be seen by the abrupt increase in electron density in Figure 7.7 (d).

Figure 7.7 (e) shows the particle confinement time  $\tau_p$ . In the DYON simulations, the  $\tau_p$  is computed as

$$\frac{1}{\tau_p} = \frac{1}{\tau_{\parallel}} + \frac{1}{\tau_{\perp}} \quad (7.5)$$

where  $\tau_{\parallel}$  is parallel confinement time obtained by the transonic ambipolar transport model,



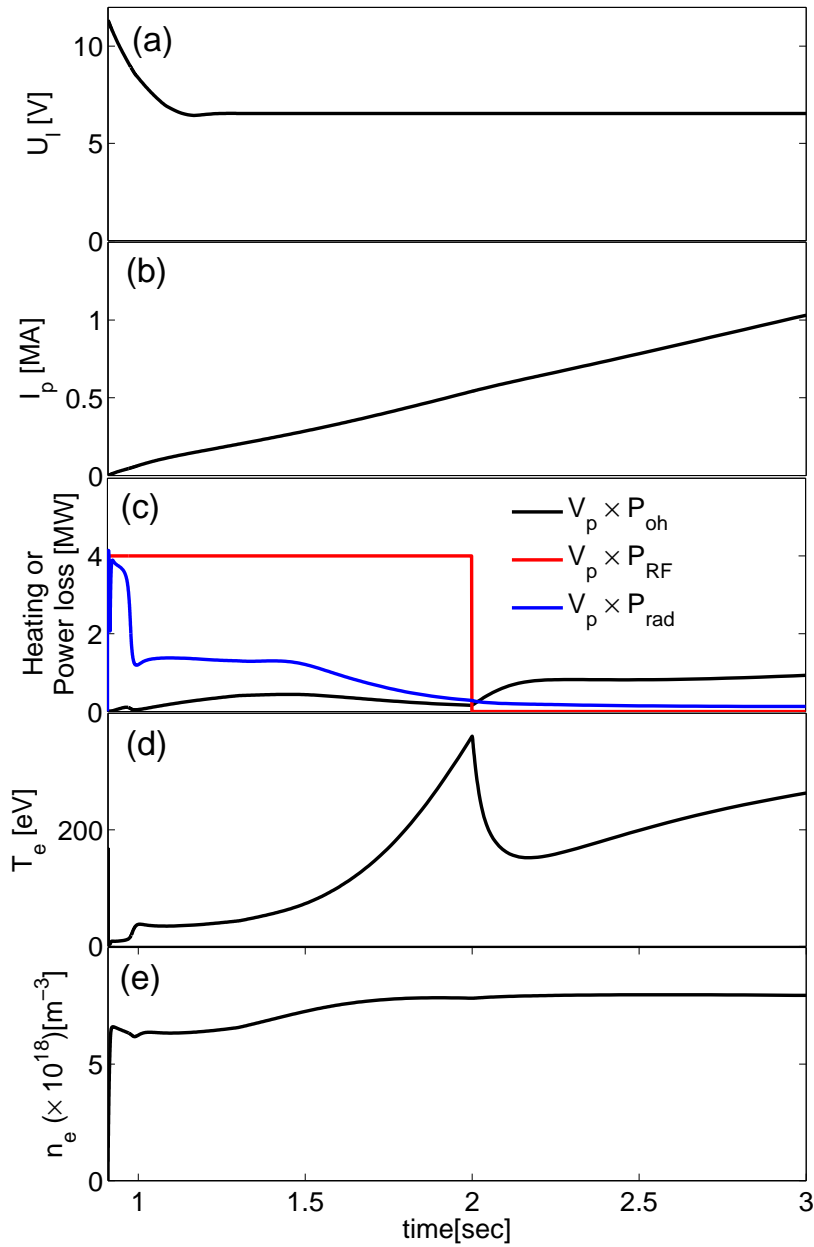


Figure 7.6: Simulation results when 4 MW of RF power is switched off at  $t=2$  second.

and  $\tau_{\perp}$  is perpendicular confinement time calculated by the Bohm diffusion model [36]. At the beginning of the plasma burn-through phase, where the effective connection length is not sufficiently long, particle transport is dominated by the parallel transport along the magnetic field lines. As the plasma current increases, the closed magnetic flux surfaces are formed; the effective connection length approaches infinity. This reduces the parallel transport, and the perpendicular transport becomes dominant (See Figure 7.7 (e)).

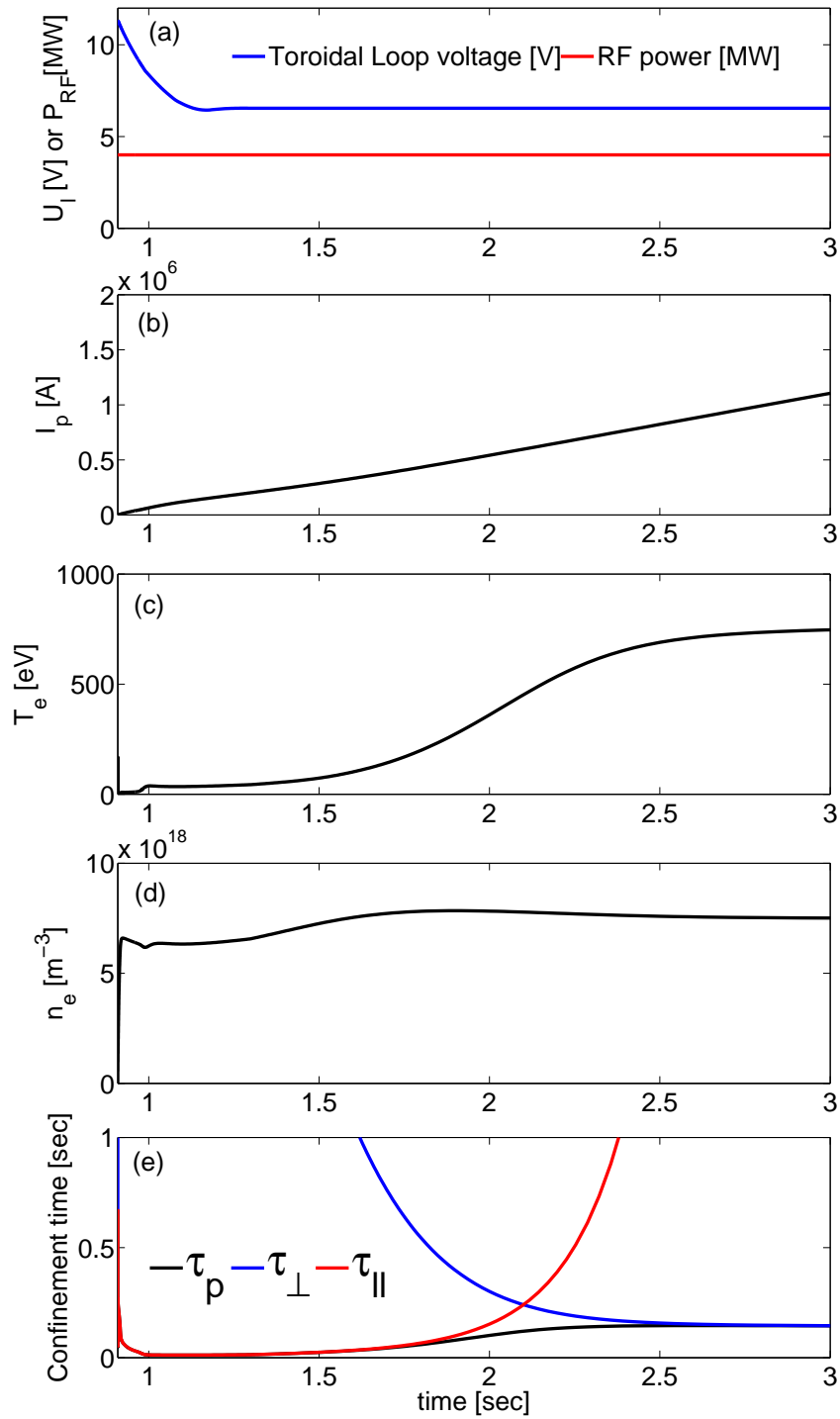


Figure 7.7: Simulation results of RF-assisted plasma burn-through in ITER. (a) toroidal loop voltage (design value obtained from F4E. Note, at ITER  $E_l \sim U_l/40[m]$ ) and RF power, (b) plasma current, (c) electron temperature, (d) electron density, and (e) particle confinement time; perpendicular confinement time (blue), parallel confinement time (red), and the resultant particle confinement time (black).

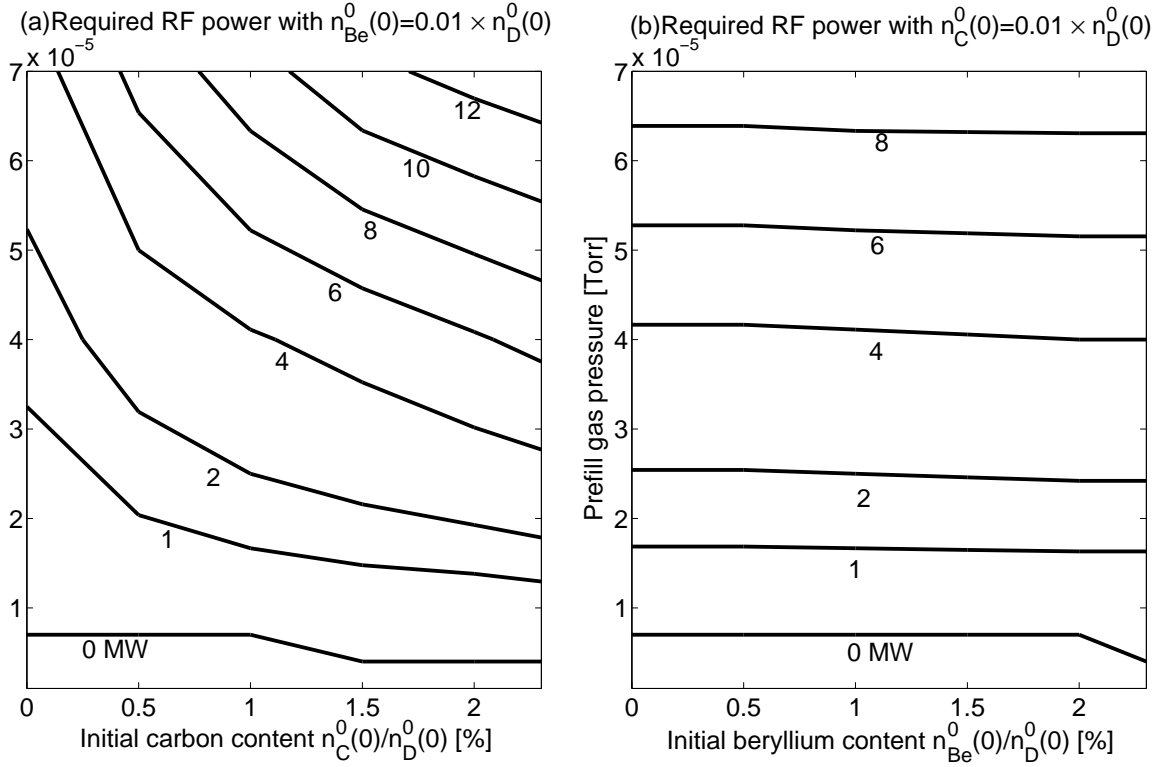


Figure 7.8: Estimation of the required RF power using the DYON simulations for successful plasma burn-through in ITER. (a) initial Be content 1% of  $n_D(0)$  (b) initial C content 1% of  $n_D(0)$ .

The required RF power is subject to operation parameters such as prefill gas pressure and initial impurity content. Figure 7.8 gives the DYON estimation of the required RF power in ITER at various operation parameters, showing the impact of prefill gas pressure  $p(0)$  and initial impurity fraction  $n_I(0)$ . Here, we define successful plasma burn-through as

$$I_p(3sec) > 100[kA] \quad (7.6)$$

$$\frac{dI_p}{dt}(3sec) > 1[kA/sec]. \quad (7.7)$$

In Figure 7.8(a) a scan of initial C fraction is given and a scan of Be fraction is given in (b). Fixed initial Be fraction (1% of  $n_D(0)$ ) and initial C fraction (1% of  $n_D(0)$ ) are used in (a) and (b), respectively. As shown by Figure 7.8 (a) and (b), the initial Be fraction does not impact on the required RF power, but the initial C content results in significant difference in the required RF power. In both cases, without RF assist, plasma burn-through will be possible only at

		(a)	(b)	(c)	(d)	(e)	(f)
Input	$p(0)[Torr]$	$7.2 \times 10^{-6}$	$1 \times 10^{-5}$	$1 \times 10^{-5}$	$5 \times 10^{-5}$	$5 \times 10^{-5}$	$5 \times 10^{-5}$
	$n_{Be}^0/n_D^0 \times 100[\%]$	1	1	1	0.1	1	1
	$n_C^0/n_D^0 \times 100[\%]$	1	1	2.3	0.1	0.1	1
	$V_p \times P_{RF}[MW]$	0	0.2	0.4	2.1	2.3	5.3
Output	$t_{Burn}^D - 0.909[sec]$	0.091	0.051	0.031	0.015	0.071	0.007
	$t_{Burn}^{Be} - 0.909[sec]$	1.291	1.101	1.381	1.211	1.651	0.941
	$t_{Burn}^C - 0.909[sec]$	1.641	1.431	1.681	1.531	1.961	1.201

Table 7.2: Burn-through time of  $D$ ,  $Be$ , and  $C$  in DYON simulations for ITER. According to ITER scenario in F4E, electron avalanche is assumed to occur at 0.909[sec]. The RF power is the minimum power required at the given prefill gas pressure and initial impurity content.

prefill gas pressure below  $1 \times 10^{-5}$  [Torr]. The required RF power increases almost linearly with the prefill gas pressure. This is due to an increase in  $D$  atom density which increases with prefill gas pressure. In addition, since we assume here the fraction of the initial impurity against prefill  $D$  density, the impurity content is also higher with higher  $D$  prefill gas pressure.

It is planned to have RF power up to 8 [MW] available in ITER for burn-through assist. If the initial  $C$  content is smaller than the assumed 1% of prefill  $D$  atoms  $n_D(0)$ , using the RF assist power, plasma burn-through in ITER will be available at around  $5 \times 10^{-5}$  [Torr], which is a typical prefill gas pressure used in present devices including JET. However, it should be noted that the RF power in this section is the absorbed value. If the RF power is not sufficiently absorbed in a plasma, it can result in serious damage to the diagnostic tools in the vessel. Hence, the absorption efficiency of RF power during the plasma burn-through phase should be evaluated quantitatively.

The required time for burn-through is shown in Table 7.2; burn-through time for  $D$ ,  $Be$ , and  $C$  are  $t_{burn}^D$ ,  $t_{burn}^{Be}$ , and  $t_{burn}^C$ , respectively. It can be seen that in all cases after  $D$  burn-through is achieved,  $Be$  and  $C$  are fully ionized in turn. RF power reduces burn-through time significantly even if  $p(0)$  and initial impurity content are much higher (see (a), (d) and (f)). While an initial  $Be$  content delays the burn-through time (see (d) and (e)), the burn-through time is not much extended by the initial  $C$ , even at high fraction (see (b) and (c)).

## 7.5 Summary and Discussion

The DYON code has been used to perform a predictive simulation for ITER. Without RF assist for plasma burn-through, start-up in ITER will be available only at very low prefill gas pressure (at  $p(0) < 10^{-5}[Torr]$ ). At JET with the ITER-like wall such lower prefill gas pressures are not used to avoid having a too slow electron avalanche phase or too low initial plasma density that may cause run-away electrons. However, 4 [MW] of RF assist will make ITER start-up available at prefill gas pressures up to  $5 \times 10^{-5}[Torr]$ , which is in the typical range used at present devices. The RF assist will result in instant deuterium burn-through. Once plasma burn-through is completed, the ramp-up rate of plasma current is not significantly affected by increasing the RF power.

The required RF power is subject to prefill gas pressure and initial impurity content. With prefill gas pressure, the required RF power increases almost linearly. The initial Be content will not impact on plasma burn-through in ITER, but an initial C content can increase the radiated power significantly. Fortunately, in case a full W diverter is installed in ITER, the initial C content in ITER is expected to be much lower than observed in JET experiments with the ITER-like wall ( $0.5 \sim 1\%$  of  $n_D(0)$ ).

# Chapter 8

## Summary and Main Conclusions

### 8.1 Original scope of thesis

The scope of the thesis is to study the physics and the modelling of the plasma burn-through phase in tokamaks, including the review of the basic concepts of the electron avalanche phase (Townsend avalanche theory). The fundamental physics of deuterium burn-through has been investigated, and the models for the treatment of impurities have been developed including plasma wall interaction. These key physics aspects are included in a comprehensive numerical simulator, the DYON code. For the first time the simulation results have been compared with data from experiments in JET, to study the influence of a carbon wall and a beryllium wall on plasma burn-through. Using the (validated) DYON code, predictive simulations for ITER have been performed.

### 8.2 Summary and Conclusions

A gas discharge can be produced by applying an electric field to a gas. The seed electrons are accelerated and via collisions they ionize the neutrals producing more electrons and ions. These new electrons are again accelerated and make further impact ionizations producing an electron avalanche. Moreover, secondary electrons are generated at the cathode by impacting ions, which can generate further electrons through the electron avalanche process. This process maintains

the discharge. The physics of gas discharge formation was first explained by Townsend, and is called a Townsend break-down.

At low temperatures, the plasma is not yet fully ionized. Examples of partially ionized discharges can be found in laboratory plasmas as well as during the start-up phase of fusion devices. Neutrals and partially ionized ions emit line radiation which could result in the loss of a significant part of the (ohmic) heating power. The radiated power is proportional to the product of electron density and neutral density. As ionizations proceed, the electron density increases and the neutral density decreases, resulting in the maximum of radiated power at a certain degree of ionization, which is called the radiation barrier. If the heating power exceeds the radiation barrier, the radiated power loss decreases and the electron temperature can increase.

In fusion research, the most promising device for magnetic confinement is the Tokamak, where the plasma is confined in a toroidal vacuum vessel and kept away from the solid walls by magnetic fields. The so-called effective connection length  $L_f$  is commonly used as a measure of the travelling distance of electrons and ions to the surrounding wall;  $L_f$  is the average length of the magnetic field lines between two contacting points at the vessel wall, and is in the range  $100 [m] \sim 1000 [m]$  (without a plasma current). A toroidal electric field can be applied to a filling gas (typically deuterium, with pressure  $p(0) \sim 5 \times 10^{-5} [Torr]$ ) by the variation of the current in the central solenoid. In present devices the magnitude is of the order of  $1 V/m$ . By this electric field, electron avalanche can occur in the prefill gas, and a plasma current is generated. (Note, for air at standard temperature and pressure, the electric field needed to generate arc between 1 meter gap electrodes is about  $3.4 [MV/m]$ .) If ohmic heating of the plasma current is high enough to overcome the radiation barrier, the ionization process continues, thereby enabling  $T_e$  to increase, i.e. plasma burn-through.

The increase in electron temperature is very important for tokamak start-up. The plasma resistance decreases as electron temperature increases. Hence, the plasma current increases with electron temperature. After plasma burn-through the electron temperature keeps increasing even with much smaller loop voltage. The build-up of plasma current generates poloidal magnetic field, which makes the magnetic field lines closed, thereby resulting in infinite effective connection length. When the effective connection length is not long enough, the parallel transport along the magnetic field lines is the dominant transport mechanism. Thus, the increase

in plasma current improves the plasma confinement in a tokamak.

Plasma burn-through is determined by several parameters: (1) the induced toroidal loop voltage  $U_l$ , (2) the prefill gas pressure  $p(0)$ , (3) the effective connection length  $L_f$ , (4) the initial impurity content of the discharge  $n_I(0)$ , and (5) the ratio of plasma volume  $V_p$  to vessel volume  $V_V$  (determining the neutrals available to the plasma). Computational simulations are required to take into account the effects of these parameters.

The energy flow in a plasma is important to simulate the plasma burn-through phase. Free electrons gain energy from ohmic heating or additional RF power, and lose the energy through three channels: (1) Transport; as free electrons lose their kinetic energy when they escape the plasma, (2) Radiation and Ionization; free electrons lose the energy when they collide with bound electrons in ions or atoms and (3) Equilibration; free electrons lose the energy by temperature equilibration with ions. Thus, equilibration is a heating channel for ions. The ions lose energy by transport and charge exchange.

In order to solve this energy balance, one needs to solve the particle balance simultaneously, since density terms are involved in the energy balance. A prefill gas of the vacuum chamber provides deuterium (D) atoms. The D atoms are ionized, and D ions recombine with free electrons to return to neutrals. Deuterium ions are also transported to the wall, resulting in recycling of D atoms or sputtering of impurity atoms. Impurity atoms are ionized, and can recombine with free electrons reducing their charge state. Impurity ions are also transported to the wall; the impurity wall-sputtering generates additional impurity atoms. The impurity ions can accept an electron from other atoms or ions. In the simulations presented here, it is assumed that only D atoms are an electron donor in charge exchange reactions. All the atomic reactions are functions of plasma temperature, so energy balance should be solved simultaneously.

The DYON code computes the energy balance equations and particle balance equations to determine the evolution of temperature and density in a plasma during the burn-through phase. Impurity densities are calculated for all charge states. Using the computed electron temperature, the plasma resistance is obtained, and a circuit equation calculates plasma current and the resultant ohmic heating. The ohmic heating is included in the energy balance. From this coupled differential equation system, the DYON code computes self-consistent values of the plasma parameters in time.



Impurity effects are essential for computing the radiated power. Most of impurities come from the surrounding wall via Plasma Wall Interactions (PWI) such as sputtering or recycling. A new all metal wall (called the ITER-like wall) has been installed recently in JET, made of Beryllium (Be) in the main chamber (e.g. important for break-down physics) and Tungsten (W) tiles in the lower part of the vessel called divertor. Experiments show a clear difference in the measured radiated power during the plasma burn-through phase with the different wall materials in JET; previous experiments with a Carbon (C) wall have much higher radiated power than the Be wall. The magnitude of radiation barrier was found to be linearly correlated with the calculated impurity influx from the C wall, while such a relation was not found for the Be ITER-like wall.

A PWI model has been included in the DYON code. The ion flux to the wall can be calculated using the plasma volume, the ion density, and the particle confinement time. The ion outflux results in D recycling at the wall which is calculated using the recycling coefficient  $Y_D^D$ . Based on experimental data,  $Y_D^D$  can be adjusted. Simulations use a recycling coefficient ( $> 1$ ) during plasma formation for the C wall, decaying to 1, while for the ILW a recycling coefficient ( $< 1$ ) was used, increasing towards 1. The ion outflux also results in impurity sputtering at the wall. Impurity sputtering can be calculated by using the corresponding sputtering yield. The resultant neutral influx to a plasma is computed. In the case of a Be wall, physical sputtering is dominant due to the low threshold energy. In the case of a carbon wall, chemical sputtering is dominant due to high chemical reactivity of C, resulting in production of hydrocarbon and carbon monoxide at all impact energies.

From the plasma wall interactions, D and impurities enter the plasma, and are ionized in the outer part (shell) of the plasma volume. The shell volume is determined by the mean-free-path for ionization. During the burn-through phase, the mean free path decreases as the electron temperature increases. If the mean-free-path is longer than the plasma size (minor radius), the volume occupied by neutrals within the plasma is equal to the whole plasma volume. If it is shorter than the minor radius, neutrals will be absent in the core. The neutral screening effect determines the neutral volume within the plasma, which is important when calculating atomic reactions. As a result, the volume where D atoms exist is somewhat larger than that of impurity atoms.

Impurity densities in all charge states should be calculated to determine the radiated power.

Since the densities of the different charge states are dependent on each other, they should be solved in a matrix, also taking into account the impurity influx from the wall and the neutral screening effects. In addition to impurities entering the plasma via PWI, a (small) initial impurity fraction  $n_I(0)$  in the residual gas might be present. A possible source could be those impurities only weakly attached to the wall after migration during previous experiments. Starting with these initial impurity fractions, the impurity content during the burn-through phase is calculated self-consistently by the DYON code, using the plasma wall interaction models.

The simulation results have been compared with the measured examples of plasma burn-through obtained in JET experiments with the *C* wall and *Be* wall. Input such as toroidal loop voltage  $U_l$ , prefill gas pressure  $p(0)$ , magnetic fields ( $B_\phi$  and  $B_v$  to calculate  $L_f$ ), and plasma size ( $R$ ,  $a$ , and  $V_p$ ) are obtained from measurement in JET. Initial impurity contents were assumed as 1%  $n_{Be}(0)$  and 0.5%  $n_C(0)$  of  $n_D(0)$ . For the *Be* wall, the D recycling coefficient is assumed to grow from 0.9 to 1 during the burn-through phase. Since not all neutrals in the vessel are accessible to the plasma, effective vessel volume is given as  $100 \text{ m}^3$  (actual vessel volume is  $189 \text{ m}^3$ ).

It was found that the simulated synthetic photon emission data for *D* and impurities ( $Be^{1+}$  and  $C^{2+}$ ) have the same temporal evolution as those measured by photomultiplier tubes. Also, the measured total radiation power and temporal evolution is matched well by the DYON simulations. The electron temperature, density and plasma current from the simulations show good agreement with the measurements. The good agreement between the simulation results and the experimental data implies that important physics aspects of plasma burn-through, and also the dynamics thereof, are well modeled in the simulations.

The DYON code can be used to compute and document the differences between a *C* wall and a *Be* wall. For the *C* wall, the radiation barrier is much higher and dominated by *C* radiation. However, in the *Be* wall, the radiation power loss is much smaller and not dominated by the *Be* radiation. The radiation barrier in the *Be* wall is dominated by the *D* radiation as long as other impurities are not significant.

Using the DYON code, the JET operation space for plasma burn-through can be determined. The required electric field for a range of prefill pressures has been computed. The Townsend criterion provides a first estimate for the required electric field for electron avalanche. The

DYON simulations provide the required electric field for a successful plasma burn-through for a pure  $D$ , and in the presence of either a Be or C wall. The resultant operation spaces are compared. At the range of prefill gas pressure above  $5 \times 10^{-5} [Torr]$ , the required electric fields for plasma burn-through (i.e. burn-through criterion) are higher than the Townsend criterion alone.

With the PWI models, the burn-through criterion increases from that for pure D plasma. While slightly more toroidal electric field is required with a Be wall, the burn-through criterion significantly increases in the presence of a C wall. These predictions are also compared to experimental data, and the majority of the experimental data points with the C wall and the Be wall lie above (or near) the simulated minimum electric field required, again showing good agreement of the simulations with the experiments, over a wide range on conditions. It should be noted that in previous studies determining operation space in tokamaks, only the Townsend criterion was used. However, at high prefill gas pressure, the limitation is set by the burn-through criterion rather than the Townsend criterion. It was observed that the Be wall tends to absorb the fuel at the wall. This can reduce the prefill gas pressure or initial plasma density, thereby resulting in slow electric avalanche (which is not favorable for operation) or run-away electron generation. Hence, the prefill gas pressure used for start-up with the Be wall in JET is higher than that of the C wall.

Previously, plasma burn-through simulations were attempted for International Thermonuclear Experimental Reactor (ITER) using constant impurity fraction or simple exponential function of the impurity content with time. However, those simulations have never been compared against experimental data in present devices. The DYON code is a plasma burn-through simulator developed at JET. It has been validated using JET experiment results.

Predictive simulations for ITER have been performed using the DYON code. The plasma facing components in ITER will be made of Be and W. ITER is two times larger than JET, and the use of superconducting coils restricts the toroidal loop voltage available for plasma initiation. As a result, ITER will have a limitation on toroidal electric field up to 0.35 V/m. This is small compared to the typical toroidal electric field in JET, which is typically 1 [V/m]. This limitation of toroidal electric field will significantly reduce the operation window for burn-through. With the design value of ITER, the requirements for successful ohmic burn-through have been studied. Without RF assist for plasma burn-through, start-up in ITER will be

available only at very low prefill gas pressure (at  $p(0) < 10^{-5}[\text{Torr}]$ ). At JET with the ITER-like wall such lower prefill gas pressures are not used.

For reliable start-up in ITER, additional RF power is planned. Applying additional RF power reduces the required toroidal electric field since it provides seed electrons (i.e. pre-ionization) needed for the electron avalanche. Furthermore, the additional RF heating can assist plasma burn-through as shown in tokamak experiments such as AUG and DIII-D. The simulations of RF-assisted plasma burn-through in ITER are used to estimate the required RF power; 4 [MW] of RF assist will make ITER start-up available at prefill gas pressures up to  $5 \times 10^{-5}[\text{Torr}]$ , which is in the typical range used at present devices. The RF assist will result in instant deuterium burn-through. Once plasma burn-through is completed, the ramp-up rate of plasma current is not significantly affected by increasing the RF power. The required RF power is subject to prefill gas pressure and initial impurity content. With prefill gas pressure, the required RF power increases almost linearly. The initial Be content will not impact on plasma burn-through in ITER, but an initial C content can increase the radiated power significantly. Fortunately, in case a full W divertor is installed in ITER, the initial C content in ITER is expected to be much lower than observed in JET experiments with the ITER-like wall ( $0.5 \sim 1\%$  of  $n_D(0)$ ).

### 8.3 Future Work

The theoretical (simulational) investigation on plasma burn-through has been published only with 0D simulation i.e. no variation of density or temperature with radius in the plasma. Since the closed flux surfaces (CFSs) are not established yet during the plasma burn-through phase at low plasma current, a 2D approach of numerical simulations is extremely difficult. Fortunately, the results of DYON simulations (also 0D), show good agreement with JET data. This implies the assumption of a uniform temperature and density in a numerical simulation is reasonable to compute the gross energy and particle balances during the plasma burn-through phase. Probably, this is due to the open field configurations during the plasma burn-through phase. With the open magnetic field lines, the parallel thermal conduction and particle diffusion would be significantly high, so that variation over the plasma radius (profile) will be small enough to be ignored. Quantitative investigations on the profile effects of temperature and density will be interesting to confirm this.

Although the simulational results show good agreement against JET data, including the effect of plasma profiles into the model would be an improvement. This would allow for quantitative investigation of power balances as both ohmic heating and power losses are functions of plasma parameters which can be different at each position. For more accurate simulations, the profile effect would be also important in particle balance, due to the particle diffusions within a plasma column. Modelling of such a 1D (or 2D) effect would enable the model to describe the details of the burn-through physics as a function of the plasma radius, i.e. burn-through shell, as well as localised heating by microwaves.

For RF-assisted burn-through simulations, we assumed constant absorbed RF power. However, absorption efficiency of RF power at low temperature plasma can be small. In that case, launching excessive RF power can result in serious damage to the diagnostic systems. In addition, non-inductive tokamak start-up, in which an additional heating power is the only heating source, is of crucial importance for a commercial fusion power plant. In order to apply the model to such conditions, there is an urgent need for development of an additional heating module; with better estimates for the absorbed power as function of plasma parameters.

The two ring model used in the circuit equations in the DYON code is a simplified model for JET. Assuming the majority of the eddy currents flow in the MK2 structure (mechanical support ring of divertor in JET), the plasma current can be reproduced showing good agreement with JET data. However, such an assumption might not be valid for all devices. Furthermore, in order to apply the DYON code to the optimization of the operation scenario in ITER, the electromagnetic part, which calculates eddy current in passive structures with given PF coil current scenario, should be improved by integrating them into the equations.

Modification of the points stated above will enable the potential usage of the DYON code to be expanded to various different experiments, while reducing the assumptions made.



# List of Tables

2.1	<i>Constants A and B in the Equation (2.6) at the range of <math>E/p</math> [21]</i> . . . . .	25
2.2	<i>Secondary electron emission coefficients <math>\gamma_{se}</math> [21]</i> . . . . .	28
3.1	<i>Inductances and resistances of a plasma current ring and a MK2 current ring for JET</i> . . . . .	51
3.2	<i>Assumed parameters for the justification of ambipolar transport model for impurities</i> . . . . .	56
3.3	<i>Input and output in the DYON code.</i> . . . . .	62
4.1	<i>Plasma parameters assumed for DYON simulations. (Figure 4.1, 4.2, 4.4, and 4.5)</i> . . . . .	69
5.1	<i>Sputtering yields and recycling coefficients.</i> . . . . .	86
5.2	<i>Parameters for physical sputtering yield of beryllium in the ITER-Like Wall [26],[42]</i> . . . . .	89
5.3	<i>Sputtering yields and recycling coefficients assumed for the plasma burn-through simulation in the ITER-Like Wall</i> . . . . .	91
6.1	<i>Initial conditions for the burn-through simulation in JET.</i> . . . . .	97
6.2	<i>Plasma parameters assumed for the plasma burn-through simulation (#82003) in the ITER-Like Wall</i> . . . . .	111

- 7.1 *Input values given to the DYON code for plasma burn-through simulations of ITER135*
- 7.2 *Burn-through time of D, Be, and C in DYON simulations for ITER. According to ITER scenario in F4E, electron avalanche is assumed to occur at 0.909[sec]. The RF power is the minimum power required at the given prefill gas pressure and initial impurity content. . . . . 142*



# List of Figures

1.1	<i>Basic structure of a tokamak with an iron core . . . . .</i>	4
1.2	<i>Description of the drift motions in tokamaks . . . . .</i>	5
1.3	<i>Stabilization of horizontal displacement of a plasma in tokamaks. The imbalance of the poloidal magnetic field (<math>B_\theta(r_1) - B_\theta(r_2)</math>) is compensated by the vertical magnetic field <math>B_v</math>. . . . .</i>	7
1.4	<i>Stabilization of vertical displacement of a plasma in tokamaks. The concave vertical magnetic field, produced by the shifted outer poloidal field coils, generates the restoring force <math>\vec{F}_R</math>. P3U, P4U, P4L, and P3L correspond to the outer poloidal field coils installed in JET. . . . .</i>	7
1.5	<i>Superconducting central solenoid coil in ITER . . . . .</i>	10
1.6	<i>Joint European Torus (JET) . . . . .</i>	11
1.7	<i>(a) ITER material configuration and (b) material configuration for the JET ITER-like Wall project.[7] . . . . .</i>	12
1.8	<i>JET chamber with indicated main plasma facing components. [8] . . . . .</i>	13
1.9	<i>Schematic description of effective connection length <math>L_f</math> . . . . .</i>	15
1.10	<i>Hexapolar null configuration for plasma break-down in JET [9] . . . . .</i>	16
1.11	<i>Typical experimental data during the plasma burn-through phase measured in JET(#82003); (a) plasma current, (b) toroidal loop voltage, (c) electron density, (d) D alpha line emission, (e) Be<sup>1+</sup> line emission, and (f) C<sup>2+</sup> line emission . .</i>	17

2.1	<i>Visualisation of an electron avalanche, also known as a Townsend discharge. The applied electric field accelerates seed electrons to collide with other neutrals and release further electrons, causing an avalanche. - from WIKIPEDIA . . . . .</i>	22
2.2	<i>Townsend first coefficient <math>\alpha</math> . . . . .</i>	26
2.3	<i>Secondary electron emission . . . . .</i>	27
2.4	<i>Analytical drawing of Equation (2.15); gas : He, Ar, H<sub>2</sub>, N<sub>2</sub>, cathode : W . . . . .</i>	29
2.5	<i>Minimum electric fields for electron avalanche in hydrogen isotope gas (solid lines) and in helium (dashed lines), for various effective connection length <math>L_f</math>. The experimental data for unassisted (ohmic) and RF-assisted start-up in DIII-D [11] and JT-60U [23] are superposed. Proposed parameters for ITER start-up are also indicated. The shaded domain represent the typical parameters for DIII-D start-up. The red dashed line labelled ‘Min.’ is the lowest electric field at which unassisted start-up in DIII-D is possible.[4] . . . . .</i>	34
3.1	<i>Energy flow in a plasma . . . . .</i>	42
3.2	<i>Particle flow in a plasma . . . . .</i>	47
3.3	<i>DYON simulation result of confinement time for a typical discharge in JET. The green line is the parallel confinement time (by Equation (3.49)), and the blue line is perpendicular confinement time (by Equation (3.53)). The black line is a resultant particle confinement time calculated by Equation (3.54). . . . .</i>	54
3.4	<i>Mean free path for ionization for Deuterium, Carbon, and Oxygen. <math>\lambda_{iz} = v_n / (n_e &lt; \sigma v &gt;_{iz})</math> . . . . .</i>	57
3.5	<i>The areas of green and yellow-green indicate a neutral volume of deuterium within a plasma volume <math>V_n^D</math>. The neutral volume of an impurity is indicated by <math>V_n^I</math>, i.e. yellow-green region. The red region represents no neutral region into which neutrals cannot penetrate. The sum of the two green regions and the red area equals the total plasma volume <math>V_p</math>. : (a) ions (b) ions and deuterium neutrals (c) ions and neutrals of an impurity and deuterium (d) neutrals of impurities and deuterium. The grey region (d) represents the vessel volume <math>V_V</math>. . . . .</i>	59

- 4.1 *DYON simulation results for pure deuterium plasmas for two different prefill pressures  $5 \times 10^{-5}$  [Torr] (success) and  $7 \times 10^{-5}$  [Torr] (failure). The colors of lines in (a) and (b) indicate successful  $I_p$  ramp-up (blue) and failure (red). The solid lines represent the net electron heating power  $P_e$ . The dashed lines and the chain lines are the amount of  $P_e$  consumed by increasing  $T_e$  and increasing  $n_e$ , respectively. The corresponding plasma currents  $I_p$  are represented by the blue solid line ( $I_p$  ramp-up) and the red solid line (non-sustained break-down) in (b). In order for  $I_p$  to increase,  $P_e$  must be positive in the  $I_p$  ramp-up phase. . . . .* 67
- 4.2 *DYON simulation results for pure deuterium plasmas for two different prefill pressures  $5 \times 10^{-5}$  [Torr] (success) and  $7 \times 10^{-5}$  [Torr] (failure). The solid lines and the dashed lines in (a) show  $P_{Oh}$  and  $P_{Loss}$  in successful (blue) and failure (red) cases, respectively. (b) is an expanded figure from the burn-through phase in (a). It is determined by  $P_e$  during the plasma burn-through phase whether  $P_e$  is positive for the  $I_p$  ramp-up phase. . . . .* 68
- 4.3 *(a) shows the change of  $n_e(t)n_D^0(t)$  with the normalized  $n_e$ . Since  $n_e(t)n_D^0(t)$  can be substituted by  $n_e(t)(n_D^0(0) - n_e(t))$  in the case of a recycling coefficient(= 1.0), it has a maximum value as  $n_e(t)$  approaches Equation (4.9). (b) indicates electron power loss coefficient due to the radiation and ionization of deuterium,  $\langle \sigma v \rangle_{rad+iz}$ , obtained from ADAS.  $\langle \sigma v \rangle_{rad+iz}$  is strongly dependent on  $T_e$  only. . . . .* 72
- 4.4 *DYON simulation results for pure deuterium plasmas for two different prefill pressures  $5 \times 10^{-5}$  [Torr] (success) and  $7 \times 10^{-5}$  [Torr] (failure). The blue line and the red line indicate the case of successful  $I_p$  ramp-up and failed ramp-up, respectively. (a) shows  $P_{rad+iz}$ . The corresponding degree of ionization is indicated in (b). The critical degree of ionization  $\gamma_{iz}(t_{RIB})$  is 87.1% as calculated using Equation (4.11) where minor radius  $a$  is assumed to be 0.5[m]. Whether or not a degree of ionization can go over  $\gamma_{iz}(t_{RIB})$  is critical for  $I_p$  ramp-up. (c) and (d) show electron temperature and density, respectively. . . . .* 74

- 4.5 *DYON simulation results for a pure deuterium plasma for various prefill pressures. The figures show (a) the plasma current, (b) the degree of ionization, and (c) various electron power losses at different prefill gas pressures,  $1 \times 10^{-5}$ ,  $3 \times 10^{-5}$ ,  $5 \times 10^{-5}$ , and  $7 \times 10^{-5}$  [Torr]. The assumed loop voltage and plasma parameters are shown in Table 4.1. Under the given condition, a critical prefill gas pressure for  $I_p$  ramp-up exists between  $5 \times 10^{-5}$  and  $7 \times 10^{-5}$  [Torr]. Prefill gases are almost fully ionized in the cases of successful  $I_p$  ramp-up while they are not fully ionized in the cases of failure. The colored lines in (c) indicate  $P_{Loss}$  (dashed red),  $P_{equi}$  (dashed green),  $P_{conv}^e$  (dotted cyan), and  $P_{rad+iz}$  (chain blue), respectively. As shown in (c),  $P_{rad+iz}$  is dominant in  $P_{Loss}$  during the burn-through phase, and its peak values coincide the RIB. The RIB increases with prefill gas pressure, thereby increasing  $P_{Loss}$  maximum. That is, the higher the prefill gas pressure, the larger the  $P_{Loss}$  maximum. . . . . 75*
- 5.1 *(a) and (b) show the fractional abundance of  $C^{2+}$  and  $Be^{1+}$ , respectively. In both figures, each line indicates the assumed equilibrium or particle confinement time : solid black (Coronal equilibrium), dashed red ( $\tau_p = 50$ [ms]), and dashed blue ( $\tau_p = 10$ [ms]). . . . . 79*
- 5.2 *(a) shows the radiation barrier at different  $C^{2+}$  influx calculated by the  $T_e(t_{C^{2+}peak}) = 6$ [eV] in the carbon wall JET. The error bars of  $C^{2+}$  influx are for  $T_e(t_{C^{2+}peak}) = 5.2$  or  $6.7$ [eV]. (b) indicates the radiation barrier at different  $Be^{1+}$  influx calculated by the  $T_e(t_{Be^{1+}peak}) = 1.7$ [eV] in the ITER-like wall. The error bars of  $Be^{1+}$  influx are for  $T_e(t_{Be^{1+}peak}) = 1.5$  or  $1.9$ [eV]. The linear correlation coefficients for the carbon wall and the ITER-like wall are 0.89983 and 0.0061026, respectively. . . . . 81*
- 5.3 *(a) D recycling coefficient and (b) Gas fuelling used in the DYON simulations with a carbon wall or ITER-like wall . . . . . 83*

- 5.4 *Particle balance in a plasma during the plasma burn-through phase. CX is charge exchange reaction between D atoms and impurity ions; it is assumed that only D atoms are an electron donor in charge exchange reactions. Iz is impact ionization by free electrons, and Recom is Recombination reaction. Wall is the surrounding plasma facing component; in this study the wall material is carbon or beryllium.* 85
- 5.5 *PWI models used in the DYON simulations with a carbon wall.* . . . . . 86
- 5.6 *PWI models used in DYON simulations with ITER-like wall* . . . . . 89
- 5.7 *Simulation results in the carbon wall and the beryllium wall under the identical conditions are presented: (a) Plasma current, (b) electron density (blue) and deuterium atom density (red), (c) electron temperature (blue) and ion temperature (red), (d) radiation power losses and ohmic heating power (dotted black: total radiation power loss, solid blue: deuterium radiation, solid red: beryllium radiation, solid black: carbon radiation, dashed blue: oxygen radiation, and dashed red: ohmic heating power), (e) sputtering yield (solid black: carbon sputtering due to incident deuterium ion, solid blue: beryllium sputtering due to incident deuterium ion, solid red: self-sputtering yield), (f) impurity densities in each charge state.* . . . . . 90
- 6.1 *(a) cyan circle: The outermost flux surface obtained with EFIT at 109[ms] after plasma initiation, (b) red solid lines: line of sight for interferometry, (c) blue solid lines: line of sight for photomultiplier tubes, (d) black solid line: line of sight for Thomson scattering.* . . . . . 95
- 6.2 *Each figure show simulation results and JET data of (a) Plasma current, (b) Loop voltage, (c) Total radiation power, (d) Plasma temperature, and (e) Plasma density. In all figures, red solid lines indicate JET experimental data and blue solid lines describe the simulation results. The red dotted line in (e) represent electron density measured by interferometry.* . . . . . 99

- 6.3 *The blue solid line in (a) indicates the synthetic data of  $C^{2+}$  line(465[nm]) emission. The red solid line in (a) shows  $C^{2+}$  line(465[nm]) emission measured with the photomultiplier tube in JET. The different units in the simulated data( $[p\ m^{-3}sec^{-1}]$ ) and the measured data( $[p\ m^{-2}sec^{-1}str^{-1}]$ ) are indicated in the left and right y-axis, respectively. The change of  $C^{2+}$  line in the simulation results and the measured data show good agreement, thereby implying that the DYON code computes the impurity evolution reasonably well. (b) shows the simulational evolution of carbon, and (c) represents the enlarged figure between 0 and 0.05 second in (b). . . . . 100*
- 6.4 *The blue chain line and the red dashed line indicate the perpendicular confinement time, Equation (3.53), and the parallel confinement time, Equation (3.49), respectively. The resultant particle confinement time is shown by the black line, Equation (3.54). . . . . 102*
- 6.5 *The red solid lines in each figure show simulation results without the parallel transport model: (a) Plasma current, (b) Total radiation power, (c) Plasma temperature, (d) Plasma density, and (e) the synthetic data of  $C^{2+}$  line(465[nm]) emission. In all figures, the blue solid lines describe the simulation results with the parallel transport model, which is compared with the JET data in Figure 6.2 and 6.3. . . . . 103*
- 6.6 *In (a), the red dashed line shows the effective connection length without the MK2 current model (i.e. single plasma current ring) in the DYON code, and the blue solid line describe the effective connection length with the MK2 current model, i.e. two ring model (plasma current and MK2 current). The red dashed line and the blue solid line in (b) show the particle confinement with and without the MK2 current model, respectively. . . . . 104*
- 6.7 *The red solid lines in each figure show simulation results without the MK2 current(i.e. single plasma current ring): (a) Plasma current, (b) Total radiation power, (c) Plasma temperature, (d) Plasma density, and (e) the synthetic data of  $C^{2+}$  line (465[nm]) emission. In all figures, the blue solid lines describe the simulation results with the two ring model(plasma current and MK2 current), which is compared with the JET data in Figure 6.2 and 6.3. . . . . 105*

- 6.8 *DYON simulation results with the new models for the ITER-like wall and JET data. (a) Plasma current, (b) Loop voltage, (c) Total radiation power (Bolometry), (d) Electron temperature (Thomson scattering), (e) Electron density (Thomson scattering and Interferometry). The red lines (and the black line in (e)) indicate JET data for #82003, and the blue lines are the corresponding DYON simulation results. The the condition given for the simulations is in Table 6.2. . . . . 107*
- 6.9 *The measured photomultiplier tube data and the synthetic photomultiplier tube data: (a) number of photons emitted from  $Be^{1+}$  (527[nm]), (b) number of photons emitted from  $D^0$  (D alpha), and (c) number of photons emitted from  $C^{2+}$  (465[nm]). The red lines are the photomultiplier tube data in JET for #82003, and the blue lines are the synthetic data, calculated by DYON simulations. . . . . 108*
- 6.10 *These figures compare the photomultiplier tube data ( $Be^{1+}$  (527[nm])) between the measured data and the synthetic data, and show the significance of the new models used in the DYON simulations. The red solid lines are the photomultiplier tube data in JET for #82003. The blue solid line in (a) is the synthetic data with the condition given in Table 6.2 (i.e. with physical sputtering model on BeO layer, erosion model of BeO layer, and initial Be content). The black dashed line and solid line in (b) are without initial Be content or any physical sputtering model, respectively. The black solid line in (c) is for pure Be wall. The black solid line in (d) is without erosion model of BeO layer i.e. continuous BeO layer. 110*
- 6.11 *The figures show the effects of the deuterium recycling coefficients. (a) electron density (b) number of photons emitted from  $D^0$  (D alpha) (465[nm]). The red lines are (a) Thomson scattering data (b) the measured photomultiplier tube data in JET (#82003). The blue and black lines are the DYON simulation results with the growing model or decay model of  $Y_D^D$ , respectively. . . . . 113*
- 6.12 *The figures show the effects of deuterium fuelling efficiency applied after 100 [msec]. (a) D atom puffing with the assumed fuelling efficiency (black 30%, blue 10%, and green 0%), (b) electron densities, obtained by DYON simulation (black 30%, blue 10%, and green 0%) and measured by Thomson scattering (red) in JET (#82003). . . . . 115*

- 6.13 *The figures show the effects of  $n_c^0(0)$  on the radiation barrier and the constituent radiated power. (a) bolometry data (red) in JET (#82003), and the simulated radiated power in the DYON simulations (solid black 1%, solid blue 0.5%, and solid green 0% of  $n_c^0(0)$ ). (b) the constituent radiated power (solid blue: total radiated power, dashed red: Be, dashed green: D, dashed black: C, dashed blue: O). For the simulation in (b), the  $n_c^0(0)$  is assumed to be 0.5%, as given for the simulation in Figure 6.8 and 6.9. . . . . 116*
- 6.14 *DYON simulation results using the vessel volume  $V_V = 190 [m^3]$ . . . . . 118*
- 6.15 *The cyan dashed lines show the Townsend criterion at different effective connection lengths, as indicated with 500, 1000, and 2000[m], respectively. The black solid, red dotted, and blue dashed lines indicate the criterion for plasma burn-through, i.e. the minimum electric field for plasma burn-through in the case of a pure deuterium plasma (black solid), beryllium wall (red dotted), and carbon wall (blue dashed), respectively. The wall-sputtering models described in section 5.4 are used for the simulations, and the required plasma parameters are given by Table 4.1. The green chain line indicates the criterion for deuterium burn-through, calculated analytically by Equation (6.12). The area above both the burn-through criterion and Townsend criterion represents the operation space available for successful start-up in JET. . . . . 119*
- 6.16 *DYON simulation results for a pure deuterium plasma or with PWI models i.e. carbon wall or beryllium wall. Each line indicates the electron power losses due to the radiation and ionization: carbon wall(dotted blue), beryllium wall(dashed red), and pure deuterium plasma(solid black). In the case of a carbon wall, the first RIB (mainly from deuterium radiation) is much smaller than the second peak, which results from carbon impurities. . . . . 121*



- 6.17 *Operation space for JET start-up. The green lines indicate the Townsend criterion for electron avalanche with an effective connection length of 200m (pessimistic) and 500m (reasonable), respectively. The black line is the required electric field for pure deuterium burn-through, computed using the DYON code. The red (Be wall) and blue (C wall) lines are the corresponding burn-through criterion and including the different wall models. The circles correspond to the successful plasma burn-through in JET experiments with the ITER-like wall (#80239 ~ #82905, red circles) and the C wall (#70988 ~ #78805, blue circles).* . . . . . 123
- 7.1 *Full interactive circuit system.* . . . . . 130
- 7.2 *Circuit system used in the DYON code for ITER simulations.* . . . . . 132
- 7.3 *Predictive ohmic (No RF assist) plasma burn-through simulations for ITER. Using design values ( $V_L(t)$ ,  $B_v(t)$ ,  $B_R(t)$ ,  $R(t)$ , and  $a(t)$ ), different prefill gas pressures are used;  $p(0) = 7.2 \times 10^{-6}$  [Torr] (Blue) and  $1.8 \times 10^{-5}$  [Torr] (Red) in (a) Degree of ionization, (b) Plasma current, and (c) Electron temperature. (d) Evolution of impurity density (Be) in ITER simulations at  $p(0) = 7.2 \times 10^{-6}$  [Torr], and (e)  $p(0) = 1.8 \times 10^{-5}$  [Torr].* . . . . . 134
- 7.4 *Simulated power losses for the simulation of ohmic plasma burn-through at  $p(0) = 7.2 \times 10^{-6}$  [Torr] in Figure 7.3. (a) electron power losses; total electron power loss (black, Electron power loss due to the radiation and ionization (blue), transport power loss (red), and equilibration power loss (green)) and (b) radiation power loss; the total radiated power is indicated by the black dashed line. The contribution to the radiated power are indicated; D(black), Be(red), C(blue), O(green)* . . . 136
- 7.5 *Simulated plasma current in RF-assisted plasma burn-through simulations for ITER. With the same prefill gas pressure ( $p(0) = 5 \times 10^{-5}$  [Torr]), the RF power is scanned.* . . . . . 138
- 7.6 *Simulation results when 4 MW of RF power is switched off at  $t=2$  second.* . . . 139

- 7.7 *Simulation results of RF-assisted plasma burn-through in ITER. (a) toroidal loop voltage (design value obtained from F4E. Note, at ITER  $E_t \sim U_t/40[m]$ ) and RF power, (b) plasma current, (c) electron temperature, (d) electron density, and (e) particle confinement time; perpendicular confinement time (blue), parallel confinement time (red), and the resultant particle confinement time (black). . . . 140*
- 7.8 *Estimation of the required RF power using the DYON simulations for successful plasma burn-through in ITER. (a) initial Be content 1% of  $n_D(0)$  (b) initial C content 1% of  $n_D(0)$ . . . . . 141*

# Bibliography

- [1] John Wesson. *Tokamaks*. CLARENDON PRESS OXFORD, 2004.
- [2] G. H. Miley D. R. Kingdon A. A. Harms, K. F Schoepf. *Principles of Fusion Energy*. World Scientific, 2000.
- [3] Francis F. Chen. *Introduction to Plasma Physics and Controlled Fusion*. Plenum Press, 1984.
- [4] Plasma Control ITER Physics Basis Expert Group on Disruptions and MHD. Chapter 8: Plasma operation and control. *Nuclear Fusion*, 39(12):2577, 1999.
- [5] Y. Gribov, D. Humphreys, K. Kajiwara, E.A. Lazarus, J.B. Lister, T. Ozeki, A. Portone, M. Shimada, A.C.C. Sips, and J.C. Wesley. Progress in the ITER Physics Basis Chapter 8: Plasma operation and control. *Nuclear Fusion*, 47(6):S385–S403, 2007.
- [6] B Lloyd, P G Carolan, and C D Warrick. ECRH-assisted start-up in ITER. *Plasma Physics and Controlled Fusion*, 38(9):1627, 1996.
- [7] T. Hirai, H. Maier, Ph. Mertens, R. Neu, E. Gauthier, J. Likonen, C. Lungu, G. Maddaluno, G.F. Matthews, R. Mitteau, O. Neubauer, G. Piazza, V. Philipps, B. Riccardi, C. Ruset, I. Uytendhouwen, and JET EFDA. R&D on full tungsten divertor and beryllium wall for JET ITER-like wall project. *Fusion Engineering and Design*, 82:1839–1845, 2007.
- [8] G. Piazza, G.F. Matthews, J. Pamela, H. Altmann, J.P. Coad, T. Hirai, A. Lioure, H. Maier, Ph. Mertens, V. Philipps, V. Riccardo, M. Rubel, and E. Villedieu. R & D on tungsten plasma facing components for the JET ITER-like wall project. *Journal of Nuclear Materials*, 367–370, Part B(0):1438 – 1443, 2007. Proceedings of the 12th International Conference on Fusion Reactor Materials (ICFRM-12).

- [9] F. Maviglia, R. Albanese, A. Alonso, and P.J. Lomas. Electromagnetic analysis of breakdown conditions in JET. *Fusion Engineering and Design*, 86:675 – 679, 2011. Proceedings of the 26th Symposium of Fusion Technology (SOFT-26).
- [10] A. Tanga, P.R. Thomas, J.G. Cordey, J.P. Christiansen, S.Ejima, A. Kellman, E.Lazzaro, P.J.Lomas, P.Morgan, M.F.Nave, P.Noll, and F.C.Schuller. Start-up of the ohmic phase in JET. In Heinz Knoepfel, editor, *Tokamak Start-up*, volume 26, page 159. European Physical Society, Plenum Press, 1986.
- [11] B. Lloyd, G. L. Jackson, T. S. Taylor, E. A. Lazarus, T.C. Luce, and R. Prater. Low voltage ohmic and electron cyclotron heating assisted start-up in DIII-D. *Nuclear Fusion*, 31:2031–2053, 1991.
- [12] P.C. de Vries, A.C.C. Sips, H.T. Kim, P.J. Lomas, F. Maviglia, R. Albanese, I. Coffey, E. Joffrin, M. Lehnen, A. Manzanares, M. OMulane, I. Nunes, G. van Rooij, F.G. Rimini, M.F. Stamp, and JET-EFDA Contributors. Characterisation of plasma breakdown at JET with a carbon and ITER-like wall. *Nuclear Fusion*, 53:053003, 2013.
- [13] J. Stober, G.L. Jackson, E. Ascasibar, Y.-S. Bae, J. Bucalossi, A. Cappa, T. Casper, M.-H. Cho, Y. Gribov, G. Granucci, K. Hanada, J. Hobirk, A.W. Hyatt, S. Ide, J.-H. Jeong, M. Joung, T. Luce, T. Lunt, W. Namkung, S.-I. Park, P.A. Politzer, J. Schweinzer, A.C.C. Sips, the ASDEX Upgrade Team, the TJ-II Team 3, the ITPA integrated Operations Scenarios Group Members, and Experts. ECRH-assisted plasma start-up with toroidally inclined launch: multi-machine comparison and perspectives for ITER. *Nuclear Fusion*, 51(8):083031, 2011.
- [14] G. L. Jackson, P. A. Politzer, D. A. Humphreys, T. A. Casper, A. W. Hyatt, and et al. Understanding and predicting the dynamics of tokamak discharges during startup and rampdown. *Physics of Plasmas*, 17:056116, 2010.
- [15] V.F. Shevchenko, M.R. O'Brien, D. Taylor, A.N. Saveliev, and MAST team. Electron Bernstein wave assisted plasma current start-up in MAST. *Nuclear Fusion*, 50(2):022004, 2010.
- [16] R. Koch, A.Lysoivan, O.Neubauer, B.Giesen, P.Httemann, H.G.Esser, M.Sauer, R.Uhlemann, M.Vervier, W.Biel, P. Dumortier, F.Durodi, I.Entrop, M.Freisinger, G.Fuchs,

- E.Graffmann, R.Jaspers, H.R.Koslowski, A.Krmer-Flecken, H.T.Lambertz, A.M.Messiaen, J.Ongena, I.M.Pankratov, J.Rapp, H.Reimer, W.Schalt, G.Van Oost, and the TEXTOR-94 Team. Low loop voltage start-up of the TEXTOR-94 discharge with ICRF and/or NBI assistance. Maastricht, 1999. 26th EPS Conf. on Contr. Fusion and Plasma Physics.
- [17] R. Koch, P. Dumortier, F. Durodi, S. Huygen, A. Lyssoivan, A. M. Messiaen, P. E. Vandendplas, G. Van Wassenhove, M. Vervier, and R. R. Weynants. Ion cyclotron resonance heating on TEXTOR. *Fusion Science and Technology*, 47(2):97–107, 2005.
- [18] R.J. Hawryluk and J.A. Schmidt. Effects of low-z impurities during the start-up phase of a large tokamak. *Nuclear Fusion*, 16(5):775, 1976.
- [19] V. A. Belyakov, V. I. Vasiliev, K. M. Lobanov, L. P. Makarova, and A. B. Mineev. Analysis of initial stage of plasma discharge in tokamaks: mathematical model formulation, simulation results, comparison with experiments. pages 1025–1034, Washington, DC, USA, 2003. PHYCON '03: Proceedings of the 2003 International Conference on Physics and Control.
- [20] V. A. Belyakov, K. M. Lobanov, L. P. Makarova, A. B. Mineev, and V. I. Vasiliev. Plasma initiation stage analysis in tokamaks with TRANSMAX code. *Plasma Devices and Operations*, 11:193–201, 2003.
- [21] Michael A. Liberman and Allan J. Lichtenberg. *Principles of Plasma Discharges and Materials Processing*. WILEY INTERSCIENCE publication, 2005.
- [22] R. Papoular. The genesis of toroidal discharges. *Nuclear Fusion*, 16:37–45, February 1976.
- [23] R Yoshino and M Seki. Low electric field (0.08 V/m) plasma-current start-up in JT-60U. *Plasma Physics and Controlled Fusion*, 39(1):205, 1997.
- [24] R. J. Goldston and P.H. Rutherford. *Introduction to Plasma Physics*. Taylor & Francis, 1995.
- [25] H P Summers, W J Dickson, M G O'Mullane, N R Badnell, A D Whiteford, D H Brooks, J Lang, S D Loch, and D C Griffin. Ionization state, excited populations and emission of impurities in dynamic finite density plasmas: I. the generalized collisional radiative model for light elements. *Plasma Physics and Controlled Fusion*, 48(2):263, 2006.

- [26] Peter C Stangeby. *The Plasma Boundary of Magnetic Fusion Devices*. Institute of Physics Publishing Bristol and Philadelphia, 1999.
- [27] B.V Mech, A.A Haasz, and J.W Davis. Isotopic effects in hydrocarbon formation due to low-energy H<sup>+</sup>/D<sup>+</sup> impact on graphite. *Journal of Nuclear Materials*, 255(2-3):153 – 164, 1998.
- [28] C. Garcia-Rosales, W. Eckstein, and J. Roth. Revised formulae for sputtering data. *Journal of Nuclear Materials*, 218:8–17, 1994.
- [29] Y. Kudriavtsev, A. Villegas, A. Godines, and R. Asomoza. Calculation of the surface binding energy for ion sputtered particles. *Applied Surface Science*, 239:273–278, 2005.
- [30] T Wauters, A Lysoivan, D Douai, O Marchuk, D Wnderlich, R Koch, G Sergienko, G Van Oost, and M Van Schoor. 0d model of magnetized hydrogen-helium wall conditioning plasmas. *Plasma Physics and Controlled Fusion*, 53(12):125003, 2011.
- [31] Eduardo de la Cal. Theoretical modelling of deuterium ICRF wall conditioning discharges. *Plasma Physics and Controlled Fusion*, 48(10):1455, 2006.
- [32] Spitzer L. *Physics of Fully Ionized Gases 2nd edn*. New York: Wiley, 1962.
- [33] Braginskii S I. *Reviews of Plasma Physics vol 1, ed M A Leontovich*. New York: Consultants Bureau, 1965.
- [34] P.H. Rutherford. *Phys. Fluids*, 17:1782, 1974.
- [35] S. Chapman. *Phys. Soc.*, 72:353, 1958.
- [36] Hyun-Tae Kim, W. Fundamenski, A.C.C. Sips, and EFDA-JET Contributors. Enhancement of plasma burn-through simulation and validation in JET. *Nuclear Fusion*, 52(10):103016, 2012.
- [37] J.W. Davis and A.A. Haasz. Impurity release from low-z materials under light particle bombardment. *Journal of Nuclear Materials*, 241-243:37 – 51, 1997.
- [38] M.F. Stamp, K. Krieger, S. Brezinsek, and JET EFDA contributors. Experience of Beryllium sputtering yields on JET. San Diego, California, USA, May 2010. The 19th International Conference on Conference on Plasma Surface Interactions (<http://www.iop.org/Jet/fulltext/EFDC100513.pdf>).

- [39] D. Kogut, D. Douai, S. Brezinsek, T. Keenan, S. Knipe, U. Kruezi, P. J. Lomas, G. F. Matthews, S. Marsen, I. Nunes, R. A. Pitts, M. Shimada, P. de Vries, and JET EFDA contributors. Study of JET conditioning with ITER-like wall. Stockholm, Sweden, July 2012. 38th EPS conference on plasma physics (<http://www.iop.org/Jet/fulltext/EFDC120427.pdf>).
- [40] M.F. Stamp, K. Krieger, and S. Brezinsek. Measurements of beryllium sputtering yields at JET. *Journal of Nuclear Materials*, 415(1, Supplement):S170 – S173, 2011.
- [41] V. Philipps, T. Loarer, H.G. Esser, S. Vartanian, U. Kruezi, S. Brezinsek, and G. Matthews. Dynamic fuel retention and release under ITER like wall conditions in JET. *Journal of Nuclear Materials*, <http://dx.doi.org/10.1016/j.jnucmat.2013.01.234>, 2013.
- [42] Joachim Roth, Wolfgang Eckstein, and Maria Guseva. Erosion of Be as plasma-facing material. *Fusion Engineering and Design*, 37:465–480, 1997.
- [43] A. D. Barkalov and G. G. Gladush. Numerical simulation of the initial stage of the plasma column formation in JUST-T tokamak. *Plasma Devices and Operations*, 15:185–192, 2007.
- [44] D. Morozov, A. Pshenov, and A. Mineev. ECR heating power modulation as a means to ease the overcoming of the radiation barrier in fusion devices. *Plasma Physics Reports*, 36:447–454, 2010.
- [45] Jayhyun Kim, S.W. Yoon, Y.M. Jeon, J.A. Leuer, N.W. Eidietis, D. Mueller, S. Park, Y.U. Nam, J. Chung, K.D. Lee, S.H. Hahn, Y.S. Bae, W.C. Kim, Y.K. Oh, H.L. Yang, K.R. Park, H.K. Na, and the KSTAR Team. Stable plasma start-up in the KSTAR device under various discharge conditions. *Nuclear Fusion*, 51(8):083034, 2011.
- [46] V. Philipps, Ph. Mertens, G.F. Matthews, and H. Maier. Overview of the JET ITER-like Wall project. *Fusion Engineering and Design*, 85(7-9):1581 – 1586, 2010.
- [47] A. Huber, K. McCormick, P. Andrew, P. Beaumont, S. Dalley, J. Fink, J.C. Fuchs, K. Fullard, W. Fundamenski, L.C. Ingesson, F. Mast, S. Jachmich, G.F. Matthews, Ph. Mertens, V. Philipps, R.A. Pitts, S. Sanders, and W. Zeidner. Upgraded bolometer system on JET for improved radiation measurements. *Fusion Engineering and Design*, 82:1327 – 1334, 2007.

- [48] R. Pasqualotto, P. Nielsen, C. Gowers, M. Beurskens, M. Kempenaars, T. Carlstrom, and D. Johnson. High resolution thomson scattering for joint european torus (JET). *Review of Scientific Instruments*, 75:3891, 2004.
- [49] A. Boboc, L. Zabeo, and A. Murari. Simultaneous Cotton-Mouton and Faraday rotation angle measurements on JET. *Review of Scientific Instruments*, 77:10F324, 2006.
- [50] C.P. Lungu, I. Mustata, V. Zaroschi, A.M. Lungu, A. Anghel, P. Chiru, M. Rubel, P. Coad, G.F. Matthews, and JET-EFDA Contributors. Beryllium coatings on metals for marker tiles at JET: development of process and characterization of layers. *PHYSICA SCRIPTA*, T128:157–161, 2007.
- [51] F. Piccolo, A. Cenedese, D. Ciscato, and F. Sartori. Non linear model of the gas introduction module for plasma density control at JET. *Fusion Engineering and Design*, 6668(0):741 – 747, 2003.
- [52] J.W. Coenen, M. Sertoli, S. Brezinsek, I. Coey, R. Dux, C.Giroud, M. Groth, A. Huber, D. Ivanova, K. Krieger, K. Lawson, S. Marsen, A. Meigs, R. Neu, T.Puetterich, G.J. van Rooij, M.F. Stamp, and JET EFDA contributors. Longterm evolution of the impurity composition and impurity events with the ITER-like wall at JET. *Nuclear Fusion*, <http://www.iop.org/Jet/fulltext/EFDP12036.pdf>, 2012 (submitted).
- [53] R. C. Bissell, P. C. Johnson, and P. C. Stangeby. A review of models for collisionless one-dimensional plasma flow to a boundary. *Phys. Fluids B*, 1:1133, 1989.
- [54] P C de Vries, G Arnoux, A Huber, J Flanagan, M Lehnen, V Riccardo, C Reux, S Jachimich, C Lowry, G Calabro, D Frigione, M Tsalas, N Hartmann, S Brezinsek, M Clever, D Douai, M Groth, T C Hender, E Hodille, E Joffrin, U Kruezi, G F Matthews, J Morris, R Neu, V Philipps, G Sergienko, M Sertoli, and JET EFDA contributors. The impact of the ITER-like wall at JET on disruptions. *Plasma Physics and Controlled Fusion*, 54(12):124032, 2012.
- [55] R. Albanese and F. Villone. The linearized create-1 plasma response model for the control of current, position and shape in tokamaks. *Nuclear Fusion*, 38(5):723, 1998.



# Curriculum Vitae

## Hyun-Tae Kim

Nationality : Republic of Korea

Email: hyun.kim09@imperial.ac.uk, htkim8199@gmail.com

## Professional Experiences

**Culham Centre for Fusion Energy**, Theory and Modelling department *2013 ~*

## Education

**Imperial College London**, PhD, Plasma Physics *2009 ~ 2013*

**Seoul National University**, Master, Nuclear Engineering *2007 ~ 2009*

**Seoul National University**, Bachelor, Nuclear Engineering *2000 ~ 2007*

(2003 ~ 2005 Military service (obligatory))

## Awards

**Best Poster Award**: 2011 PGR Symposium in Imperial College London *2011*

**Kwan-Jeong Scholarship**: Full doctoral funding *2010 ~ 2013*

**Young Scientist Award**: 35th Conference of the Korean Vacuum Society *2009*

**Best Poster Award**: 34th Conference of the Korean Vacuum Society *2008*

## Publications

1. **Hyun-Tae Kim**, A.C.C. Sips, P.C. de Vries, and EFDA-JET contributors, Plasma burn-through simulations using the DYON code and predictions for ITER, Plasma Physics and Controlled Fusion, (2013) Accepted
2. **Hyun-Tae Kim**, A.C.C. Sips, and EFDA-JET contributors, Physics of plasma burn-through and DYON simulations for the ITER-like wall, Nuclear Fusion, 53 (2013) 083024

3. P.C. de Vries, A.C.C. Sips, **Hyun-Tae Kim**, P.J. Lomas, F. Maviglia, R. Albanese, I. Coffey, E. Joffrin, M. Lehnen, A. Manzanares, M. OMulane, I. Nunes, G. van Rooij, F.G. Rimini, M.F. Stamp and EFDA-JET contributors, Characterisation of plasma breakdown at JET with a carbon and ITER-like wall, *Nuclear Fusion*, 53 (2013) 053003
4. **Hyun-Tae Kim**, W. Fundamenski, A.C.C Sips, and EFDA-JET contributors, Enhancement of Plasma Burn-through Simulation and Validation in JET, *Nuclear Fusion*, 52 (2012) 103016
5. **Hyun-Tae Kim**, A.C.C Sips, W. Fundamenski, and EFDA-JET contributors, PSI Effects on Plasma Burn-through in JET, *Journal of Nuclear Materials*, 438 (2013), S1271-S1274
6. **Hyun-Tae Kim**, Yong-shin Park, Choong-Ki Sung, Jae-Ryung Yi, and Yong-Seok Hwang, Design and Characterization of a Microwave Plasma Source using a Rectangular Resonant Cavity, *Journal of Korean Vacuum Society*, 17 (2008) 5